Microchannel plates in astronomy

Gareth James Price

Thesis submitted to the University of Leicester for the degree of Doctor of Philosophy.

September 2001

Space Projects and Instrumentation Group
Department of Physics and Astronomy
Leicester University

Abstract

This thesis describes both round-pore microchannel plates (MCPs) used in energetic photon and particle detectors and their square-pore offspring, micropore optics (MPOs), used to focus x-rays.

A Monte Carlo electron raytracing software package is described that is used to predict the energy and angular distribution of electrons (EDOE and ADOE) in a microchannel electron multiplier's output charge cloud, including saturated operation. The model is shown to agree with experimental evidence. The addition of a micromachined electrostatic lens to the end of a microchannel is modelled and found to have no beneficial effects upon the EDOE and ADOE of the channel.

The current state of the art planar and slumped 'lobster eye' square-packed MPOs are evaluated. The best focus ($5'$ FWHM) from a large format (61mm×56mm), small channel (10μm side length) planar MPO is reported, together with the observation of high energy ($\sim$ 50keV$\rightarrow$ 65keV) x-ray focusing from large (500:1) aspect ratio channels. The alignment of many small lobster eye MPOs to create a large optic for the Lobster-ISS instrument is discussed and the alignment jig constructed for this purpose is used to measure the bias angles of a Lobster specification MPO. The bias angle is found to be $4 \pm 1.5'$.

The concept of the microchannel conic approximation to the Wolter type I and II x-ray lenses is reviewed. A radially-packed twin MPO Wolter approximation is then tested, which while of poor quality, demonstrates true Wolter II imaging with a peak gain greater than unity.

Currently proposed (UK) astronomical instruments that employ MPOs are then discussed in the light of the results from the current generation of MPOs.

Declaration

I hereby declare that no part of this thesis has previously been submitted to this or any other University as part of the requirements for a higher degree. Work described here was conducted by the undersigned except for the contribution of colleagues indicated in the text.

Gareth Price
September 2001

Acknowledgements

I would like to thank my supervisor Prof. George Fraser for his support and guidance throughout the duration of my PhD at Leicester. I would also like to thank my colleagues Adam Brunton, Nigel Bannister, Jim Pearson, John Lees and Adrian Martin for their assistance and support, and also for the welcome they have given me into the group.

Thanks are also due to the engineering, technical and workshop staff of the Space Research Centre and Physics department, without whom the experimental work undertaken would have been impossible. Anyone I've forgotten to mention but has contributed to my enjoyable three years at Leicester, both within and outside of work, is also heartily thanked.

I acknowledge the financial support of a PPARC studentship. The work in chapter 2 was supported in part by a US. government SBIR grant from BMDO/DARPA through NOVA Scientific, Inc., Sturbridge, MA, USA.

List of publications

Some of the results presented in this thesis have been incorporated in the following papers. The chapters to which these papers refer are given in brackets.

1. ‘Novel micro-pore x-ray optics produced with microchannel plate technology’,
   M.W. Beijersbergen, M. Bavdaz, A. Peacock, E. Tomaselli, G. Fraser, A. Brunton, G. Price, M. Krumrey, C. Herrmann, A. Freund, E. Zeigler, A. Souvorov, R. Fairbend, J-P. Boutot and S.O. Flyckt
   Proc. SPIE **4012** (2000) 218 (Chapter 6)

2. ‘High-resolution micro-pore x-ray optics produced with microchannel plate technology’,
   M.W. Beijersbergen, M. Bavdaz, A. Peacock, E. Tomaselli, R. Fairbend, J-P. Boutot, S.O. Flyckt, A. Brunton, G. Price, G. Fraser, C. Herrmann, M. Krumrey, E. Zeigler and A. Freund
   Proc. SPIE **4145** (2000) 188 (Chapter 6).

3. ‘Calculation of the output charge cloud from a microchannel plate’,
   G.J. Price and G.W. Fraser
   Nuclear Instruments and Methods in Physics Research **474** (2001) 188
   (Chapter 2).

4. ‘Wolter focusing with micrchannel plates: Analysis of first full face illumination results’,
   G.J. Price, A.N. Brunton, M.W. Beijersbergen and G.W. Fraser
   In preparation (Chapters 3, 5 and 6).

5. ‘Hard x-ray imaging with micropore optics: Experimental results’,
   G.J. Price, A.N. Brunton and G.W. Fraser
   In preparation (Chapters 3 and 4).

List of acronyms

ADOE	Angular Distribution Of Electrons
ADC	Analogue to Digital Converter
AGN	Active Galactic Nuclei
ASM	All Sky Monitor
AXAF	Advanced X-ray Astrophysics Facility
	(NASA X-ray observatory, now Chandra (1999-))
CCD	Charge Couple Device
CZT	Cadmium Zinc Telluride
DSC	Detector SpaceCraft (one half of XEUS)
EDOE	Energy Distribution Of Electrons
ESA	European Space Agency
ESTEC	European Space Research and Technology Centre
EUV	Extreme Ultra-Violet (xÅ→yÅ)
EXOSAT	European X-ray Observatory Satellite (1983-1986)
ExPA	Express Palette Adapter
FIRST	Far Infra-Red and Submillimetre Telescope
FOV	Field Of View
FWHM	Full Width at Half Maximum
HERMES	High Energy Remote-sensing of MErcury's Surface
HRC	High Resolution Camera (on Chandra)
HRI	High Resolution Imager (on Einstein)
ISS	International Space Station
JPEX	Joint Astrophysical Plasmadynamic Experiment
LEO	Low Earth Orbit
MAXI	Monitor All-sky X-ray Image (planned Japanese ISS payload)
MCP	Microchannel Plate
MPO	Micropore Optic (Microchannel Plate Optic)

MSC	Mirror SpaceCraft (one half of XEUS)
NASA	National Aeronautics and Space Administration
NASDA	National Space Development Agency of Japan
NGST	Next Generation Space Telescope
PPARC	The Particle Physics and Astronomy Research Council
PSF	Point Spread Function
PTFE	Poly Tetra Fluoro Ethylene
QE	Quantum Efficiency
RoSAT	Röntgen Satellite (1990-1999)
RSPP	Radio and Space Plasma Physics group at Leicester University
RXTE	Rossi X-ray Timing Explorer (1995-)
SEE	Secondary Electron Emission
SEM	Scanning Electron Microscope
SMEX	Small Mission Explorer
SPI	Space Projects and Instrumentation group at Leicester University
SPIE	Society of the Photo-optical Instrument Engineers
SRC	Space Research Centre at Leicester University
SuperDARN	Super Dual Auroral Radar Network
TMP	Turbo Molecular Pump
TRP	Technology Research Programme
TTF	Tunnel Test Facility
UHV	Ultra High Vacuum
VTF	Vacuum Test Facility
VUV	Vacuum Ultra-Violet (xÅ→yÅ)
WFC	Wide Field Camera (on RoSAT)
XEUS	X-ray mission for Evolving Universe Spectroscopy
XMM	X-ray Multi Mirror mission (ESA X-ray observatory, now XMM-Newton (1999-))
XRF	X-ray fluorescence

Contents

List of Figures

List of Tables

Chapter 1

Microchannel plates in astronomy

1.1 Introduction

If the birth of X-ray astronomy is taken to be the 18^{th} June 1962, the day that the first extra-solar source was discovered (Giacconi *et al.*, 1962), then the discipline will be nearly forty years old at the publication of this thesis. In that time the instrumentation used to make observations has developed from the simple sounding rocket mounted Geiger counters used by Giacconi *et al.* to the sophisticated NASA Chandra (formerly AXAF) and ESA XMM-Newton X-ray observatories.

Microchannel plates (MCPs), have been at the heart of this evolution since the first dedicated X-ray telescope, *Einstein*, was launched in 1978. The microchannel plate is a descendent of the continuous dynode electron multiplier that originated independently at the Metallurgical Institute of the Academy of Sciences in the Soviet Union (Oschepkov *et al.*, 1960), the Bendix Corporation in the United States (Goodrich and Wiley, 1962) and at the Mullard Research Laboratories in the United Kingdom (Adams and Manley, 1965). It was found that if microscopic multipliers were formed into arrays they could be used as position sensitive photon counting cameras. As such the technology was classified throughout much of the cold war as the military developed them for image intensifier applications. Following their declassification in the late 1960s (Ruggieri, 1972) they found widespread use as photon and particle detectors amongst the scientific community. This was particularly true of X-ray astronomy where, as already mentioned, they formed the basis for the High Resolution Imager (HRI) on the first imaging X-ray observatory.

More recently, much interest has been shown in the potential use of microchannel plates with square channel cross-sections as high energy or wide field of view, low mass X-ray optics.

In the rest of this chapter the manufacturing process and principles of operation of both microchannel plate detectors and, as they have become known, micropore optics (MPOs) will be described. The heritage of MCPs and current proposals for the use of MPOs in X-ray astronomy and related fields will then be presented. A variety of MCPs and MPOs are shown in Figure 1.1.

1.2 Microchannel plate detectors

The idea of using a resistive tube manufactured from a secondary electron emissive material to amplify electronic signals is attributed to Farnsworth (1930). In the channel multiplier, an incident electron at the entrance of the tube excites secondary electrons from the channel surface. An applied voltage accelerates these electrons down the channel where they in turn generate additional secondary electrons as they strike the channel surfaces. In this manner, an exponential growth in current is achieved along the multiplier. The channel must be evacuated to a level where the mean free path of the electrons is of the same magnitude as the flight paths.

The gain of a channel can be controlled by varying the voltage applied across the channel and its aspect ratio. It is the fact that it is the aspect ratio of a channel, not its diameter, that controls its gain that allows channels to be reduced in size and formed into microchannel plates (see chapter 2 for further details). Figure 1.2 shows schematically how a typical electron avalanche would progress in a channel multiplier.

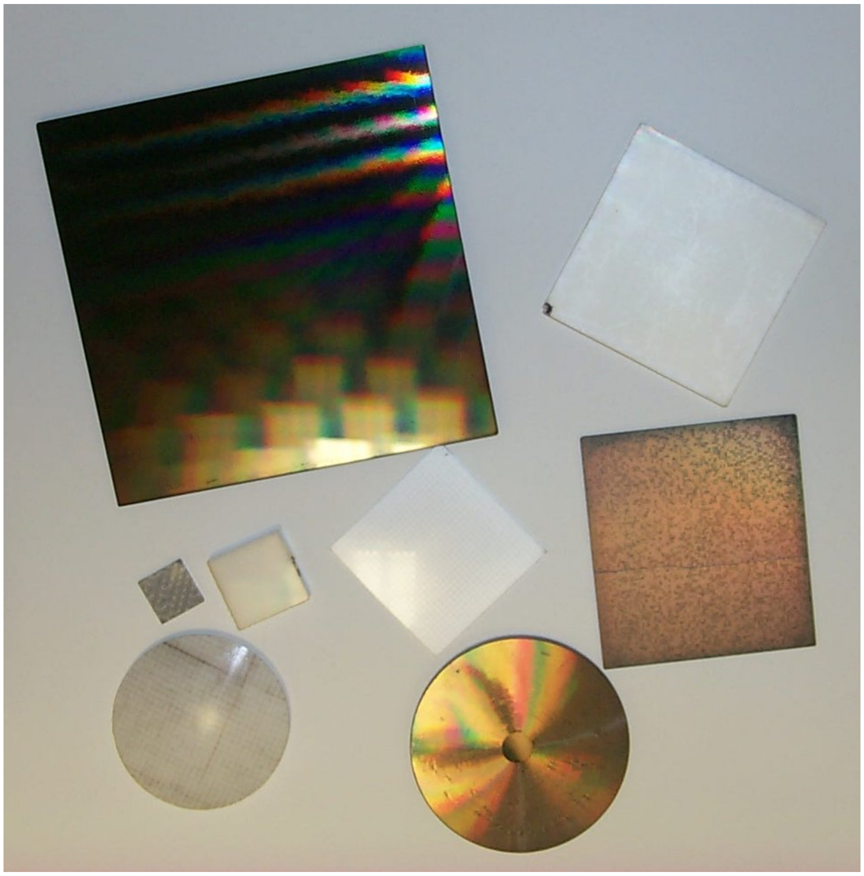

Figure 1.1: A variety of microchannel plates and micropore optics. The large plate in the top left is a Chandra HRC-I type detector plate (dark colour with diffraction patterns). A radially-packed planar MPO (gold) is shown in the foreground with two lobster eye plates in the bottom left and centre (off-white and white). Various other planar square-pack MPOs are show surrounding these. A crack can be seen across the planar MPO on the right of the picture. Scale can be taken from the detector plate (100mm$\times$$100$mm).

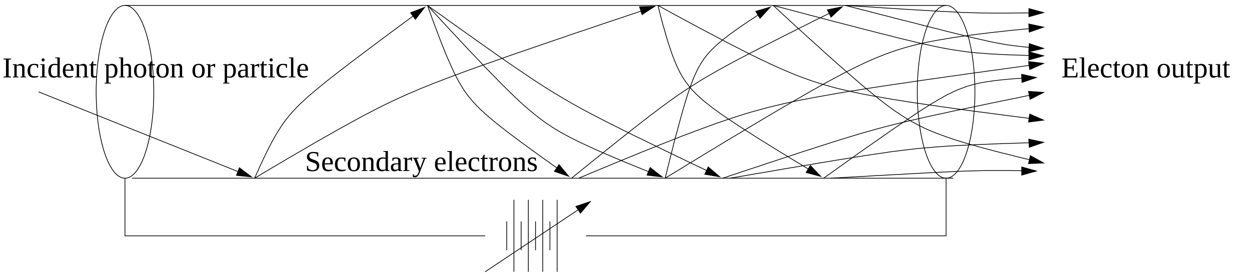

Figure 1.2: An electron avalanche in a typical channel electron multiplier. A photon or particle incident upon the channel wall excites a secondary electron into the channel. This electron is accelerated down the channel by the applied bias until it is incident upon a wall itself, exciting more electrons into the channel. In this way a detectable signal ($\sim 1 \times 10^4$ electrons) can be produced from a single incident event.

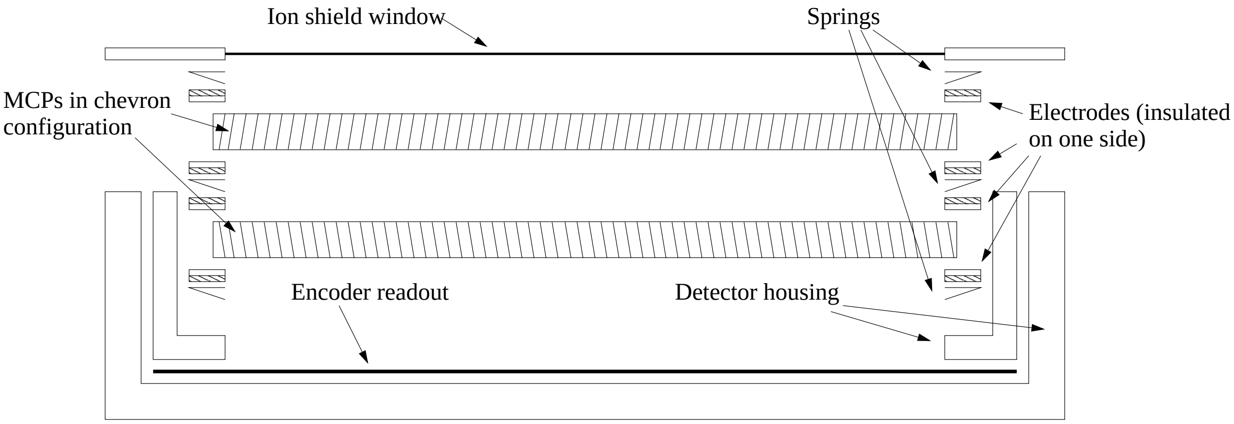

Figure 1.3: A 'chevron' two stage microchannel plate detector. The bias angles of the plates are set opposite each other (in a chevron configuration) to prevent feedback of positive ions.

Figure 1.3 shows how two MCPs, stacked one above the other to provide increase gain, are used to create an MCP camera. The MCPs are usually fabricated with a bias angle on the channels (i.e. the channel axes are not normal to the front surface of the plate, but inclined at an angle, usually 6°→ 13°). In a camera a *chevron* arrangement, where the bias angles of the MCPs are orientated differently, is used to prevent the passage of ions in the opposite direction to the electron avalanche (Figure 1.3). Ions incident near the top of a channel could initiate further high gain avalanches, adding noise to images.

With a resolution theoretically limited only by the channel pitch and a proven durability in the harsh environment of space, microchannel plate detectors have remained a mainstay of high resolution position sensitive detectors in X-ray astronomy since the days of Einstein. The Chandra High Resolution Camera (HRC) plates represent the current state of the art in detector MCPs: 120:1, 12.5μm channels with a CsI photocathode on a pitch of 15μm in a large area format of 100mm×100mm (Winkler *et al.*, 1993; Zombeck *et al.*, 1995a). There are many detailed descriptions of microchannel plate operation in the literature (Wiza, 1979; Fraser, 1989). Chapter 2 describes a Monte Carlo model of avalanche propagation with emphasis on the angular and energy distribution of the electrons in the channel output.

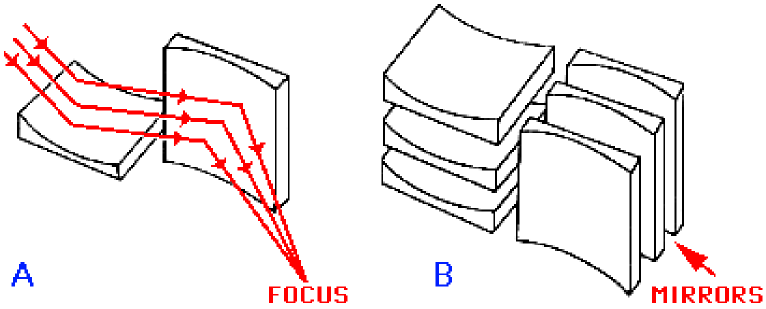

Figure 1.4: The Kirkpatrick-Baez X-ray telescope. A point source reflecting from an ellipsoid is brought to a line focus. Reflections from successive orthogonal ellipsoid surfaces bring the rays to a point focus. The micropore optic approximation to this geometry is shown in Figure 1.5. After Kirkpatrick and Baez (1948).

1.3 Micropore optics

The propagation of X-rays in matter can be described by a complex refractive index of just less than unity. This makes the use of total external reflection at small grazing angles the favoured method of bringing X-rays to a focus (Underwood, 1978; Willingale, 1984).

The idea of using micropore optics (MPOs) to focus X-rays can be traced back to a paper by Schmidt (1975) in which he proposed a wide field of view grazing incidence optic composed of two orthogonal sets of reflecting planes, similar to the Kirkpatrick-Baez (Kirkpatrick and Baez, 1948) arrangement (Figure 1.4). Schmidt suggested that if each set of planes were normal to the surface of a cylinder, a very large field of view optic could be created. This idea was amended by Angel (1979) who, using the example of the squat lobster (Land, 1978), suggested moving the two orthogonal sets of planes together to form an array of square channels, each channel axis normal to the surface of a sphere. This is the *Lobster Eye* optic.

A point source reflecting from an ellipsoid will produce a line focus. The Kirkpatrick-Baez lens system uses reflections from two successive orthogonal ellipsoid mirrors to bring X-rays to a point focus. It was realised (Wilkins *et al.*, 1989) that if microchannel plates could be made with the necessary square cross-section they would provide an array of

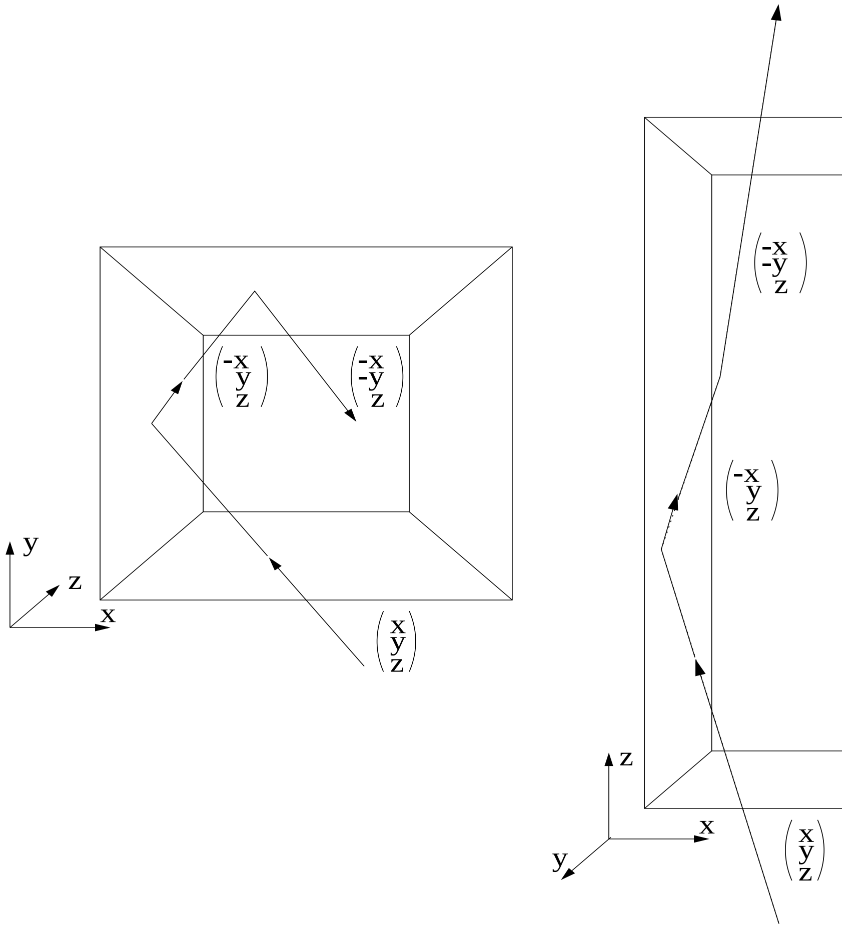

Figure 1.5: Internal reflections from a square cross-section channel. Two successive reflections from orthogonal surfaces reverse the direction of two components of the rays velocity. This property enables the channels to be used in focusing systems.

channels that approximate the Kirkpatrick-Baez system. Although not of ellipsoid profile, the channels are so short that the broadening of the focus is small. Chapman *et al.* (1991) show that a channel of length L will produce a depth of focus equal to $2L$. The array of channels provide many Kirkpatrick-Baez optics in a small area, increasing the reflecting surface visible to the source, and hence the effective area of an optic of given size (Wilkins *et al.*, 1989; Chapman *et al.*, 1991). Figure 1.5 shows how reflections from two orthogonal walls aligned along the z-axis will reverse the x and y components of velocity. If the walls are equidistant between the X-ray source and the image plane (i.e. $L_S = L_I$) the MPO can thus be used for point-to-point imaging, as shown in Figure 1.6.

Square channel plates had, if fact, already been supplied to Leicester and Columbia Uni-

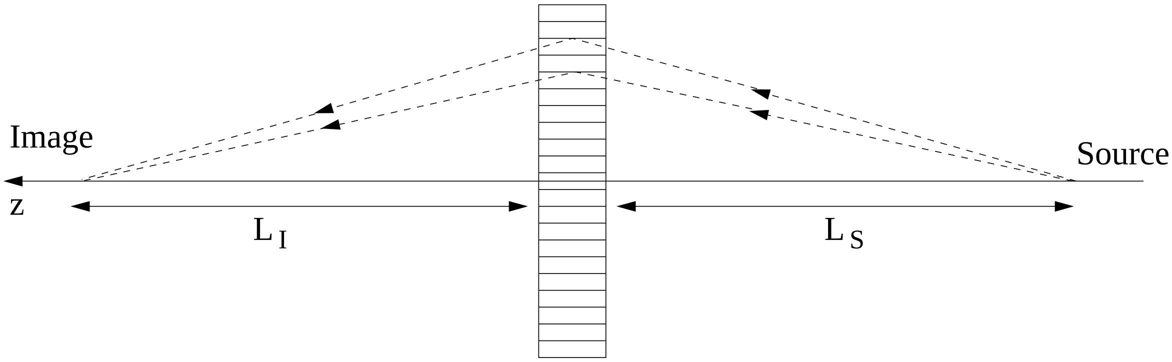

Figure 1.6: Point-to-point focusing. If two successive reflections from orthogonal walls occur within a channel equidistant between a source and image plane, point-to-point imaging in two dimensions is observed.

versities for use both as collimators and, in a detector format, for polarimetry (Fraser *et al.*, 1991a). The first observations of focusing by square pore microchannel plates were reported in 1991 (Fraser *et al.*, 1991b; Kaaret and Geissbuhler, 1991), with the cruxiform structure described by Chapman *et al.* (1991) first measured by Fraser *et al.* (1993b).

If a micropore optic can be slumped such that the channel axes are perpendicular to the surface of a sphere, the optic can be used to focus X-rays from infinity to an image surface positioned half the sphere's radius from the centre of the plate. This is the MPO version of the lobster eye optic proposed by Angel and is shown in Figure 1.7. It can be shown (Chapman *et al.* (1991); section 4.2) that a micropore optic slumped to a spherical surface of radius, R, obeys the lens equation

$$\frac{2}{R} = \frac{1}{L_I} - \frac{1}{L_S} \tag{1.1}$$

where the radius is taken to be positive if the source is on the convex side of the MPO and vice versa.

Slumping measurements were first made with round pore channel plates (Fraser *et al.*, 1993a), the first true lobster eye microchannel plate images were reported by Brunton *et al.* (1995).

As well as the lobster eye micropore optic, an approximation to the Wolter type I (Wolter, 1952) grazing incidence lens has been proposed (Fraser *et al.*, 1993c; Willingale *et al.*,

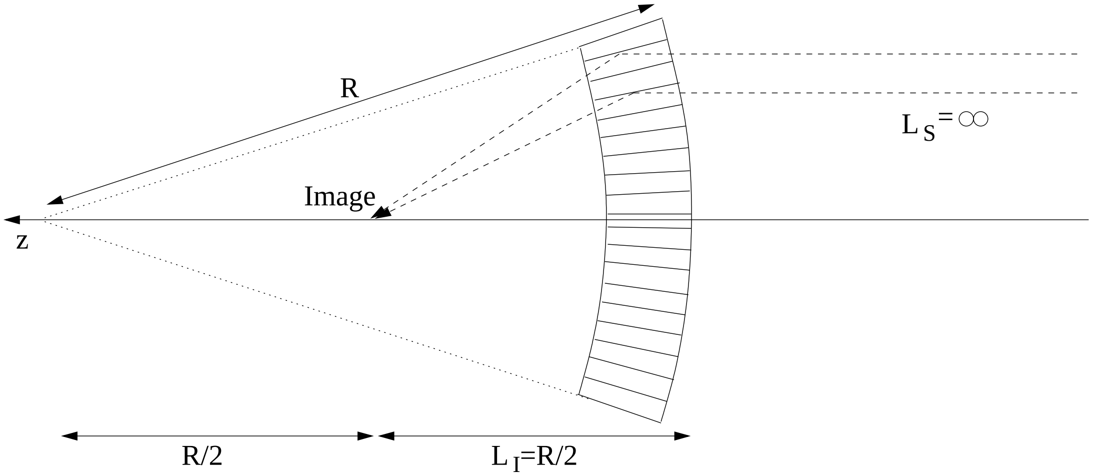

Figure 1.7: A slumped MPO with a radius of curvature, R, forms a lobster eye optic capable of focusing X-rays from infinity. The MPO obeys the lens equation (1.1). If the source is at infinity (as in the case for an astronomical source), $L_I = R/2$.

1998). This is shown in Figure 1.8. The resolution of the Wolter approximation is ultimately limited by the flat wall approximations to the true Wolter geometry, but the MPO realisation of it offers the advantages of very low mass and improved high energy efficiency. Fraser (1997) defines a figure of merit, F, for any X-ray telescope as the ratio of its effective area in cm^2 to mass in kg. For a conventional Wolter type I mirror system $F \simeq 1 \rightarrow 10$; the proposed microchannel Wolter optic for the BepiColombo mission (sections 1.5.2 and 6.7) has $F \simeq 200$ while the Lobster-ISS All Sky Monitor (section 1.5.2 and chapter 7) has a value of $F \simeq 1000$. If the MPOs are produced with large aspect ratio channels, they provide an increased probability of reflection at low grazing angles, and hence an enhanced high energy efficiency.

The lobster eye and Wolter approximation micropore optics find different applications in X-ray astronomy. While the Wolter I approximation discussed in chapters 5 and 6 provides true imaging, it has only a limited field of view (FOV). The lobster eye lens (chapter 4) has no preferable optical axis and a theoretical FOV of 4πsr.

In 1996 a European Space Agency (ESA) Technology Research Programme (TRP) for the development of microchannel plates was initiated by Leicester (contract number 12193/96/NL/SB). Deliverables from the optics part of this programme (both square-

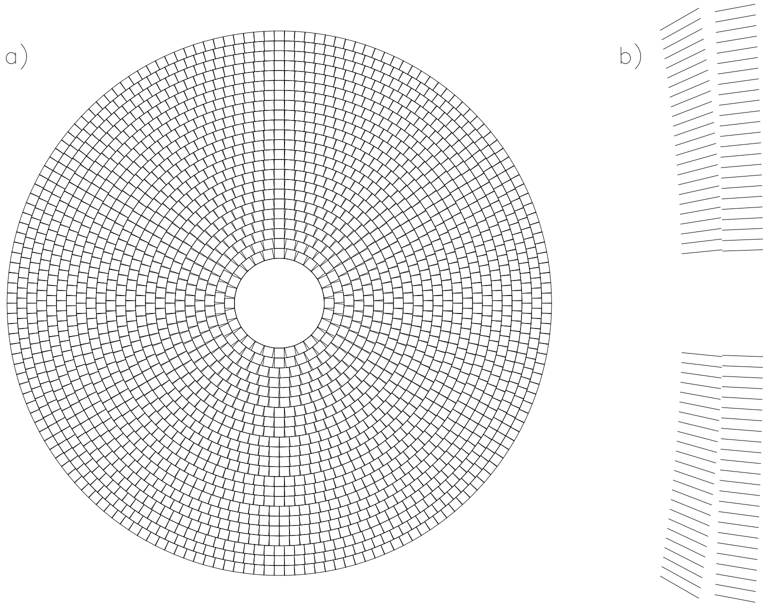

Figure 1.8: Diagram showing (a) the radial-packing of square multifibres around a circular solid core and (b) how two successive radially-packed MPOs would be slumped relative to each other in a microchannel Wolter optic. The input X-ray beam is assumed to enter from the right in (b).

packed lobster eye and Wolter approximation MPOs) are discussed in detail in the respective chapters.

1.4 MCP Manufacturing process

The manufacturing process for both round-pore detector and square-pore optic microchannel plates is essentially the same. In brief, a hollow tube of cladding glass of the cross-section shape required has a core glass inserted into it to provide support during fabrication. The combined cladding and core glass, known as a *couple*, is now hung in a drawing tower where it is heated and drawn so that fibres of approximately 1mm in width are produced, this is cut every 500mm or so yielding the first draw fibres. These fibres are then stacked into *multifibre* bundles (different stacking geometries depending on the fibre cross-section) and drawn again to provide the multifibres $\sim$ 300mm long. This process can be repeated several times to reduce the channel size as necessary.

Once multifibres consisting of channels of the required size have been produced, they are stacked into what is known as a *boule*. The stacking geometry is dependent upon both the multifibre cross-section and the overall design of the MCP. The boule is fused at high temperature and pressure. In the case of square profile boules (called *blocks*) the pressure is applied mechanically and is known as *ram fusion*. Where the boule is otherwise shaped in cross-section the air pressure in the furnace is increased to several atmospheres, this process is called *bomb fusion*. Individual MCPs (or MPOs depending upon the type of boule produced) can then be sliced off using a diamond saw. The attack angle of the saw can be controlled (to $\sim \pm 0.1^\circ$) and hence the bias angle of the plate created. The individual plates are then polished and etched, the core glass being far more susceptible to acid (or alkali depending upon the actual glass composition) than the cladding.

In the case of planar micropore optics the complete process is described above. If the MPO is to be in a lobster eye or Wolter configuration then it must be slumped to the correct radius. If it is MCP detector plates that have been produced, they need to be reduced in hydrogen to provide the secondary electron emissive surface and then have electrodes applied to both faces. A detector MCP may also be required to have a suitable photocathode applied at the entrance to the channels. Brunton (1994) and Martin (2000) provide more detail of the manufacturing process, shown diagrammatically in Figure 1.9. Electron micrographs of a round-pore detector array and square-pore optic array are shown in Figure 1.10.

The TRP contract required the drawing and stacking of fibres into boules or blocks to be refined so as to reduce as far as possible alignment errors between channels. In detector plates this should reduce the frequency of defects within and between multifibres that can lead to ‘black spots’. In optic plates, better channel alignment leads to improved imaging quality.

1.4.1 MPO slumping

In order to realise both the lobster eye optic proposed by Angel (1979) and the conic approximation of a Wolter I lens in MPO format, slumping of the flat plates resulting

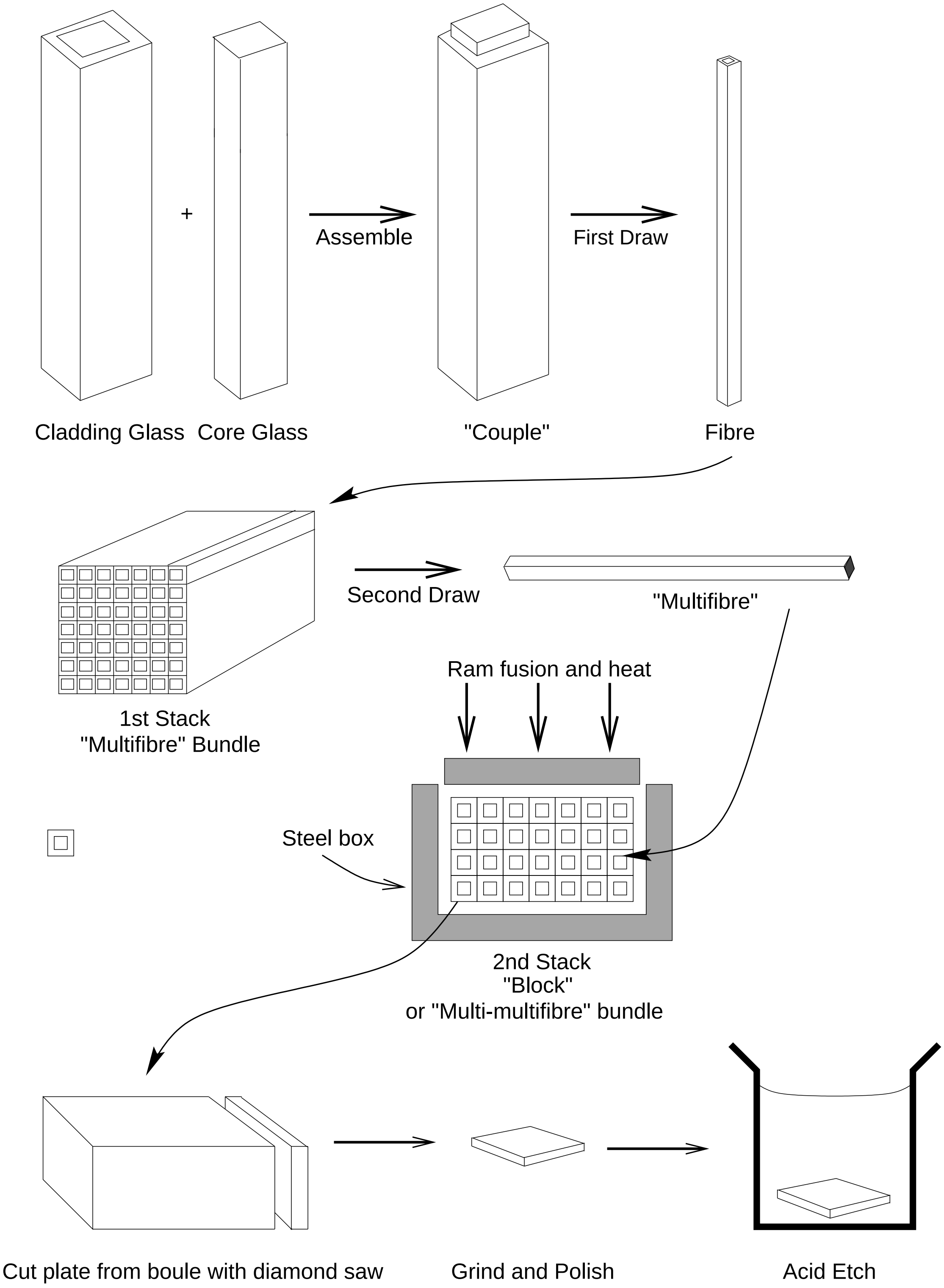

Figure 1.9: Manufacture of a square-pore square-packed MPO. The multifibre production technique is exactly the same for a radially-packed MPO, except that the multifibres are then stacked in a different manner prior to fusion. In the production of a detector MCP, the core and cladding glass are round in cross-section to produce round-pore channels that can be stacked in a hexagonal structure. The multifibres may also be stacked and drawn more than once if necessary. From Martin (2000).

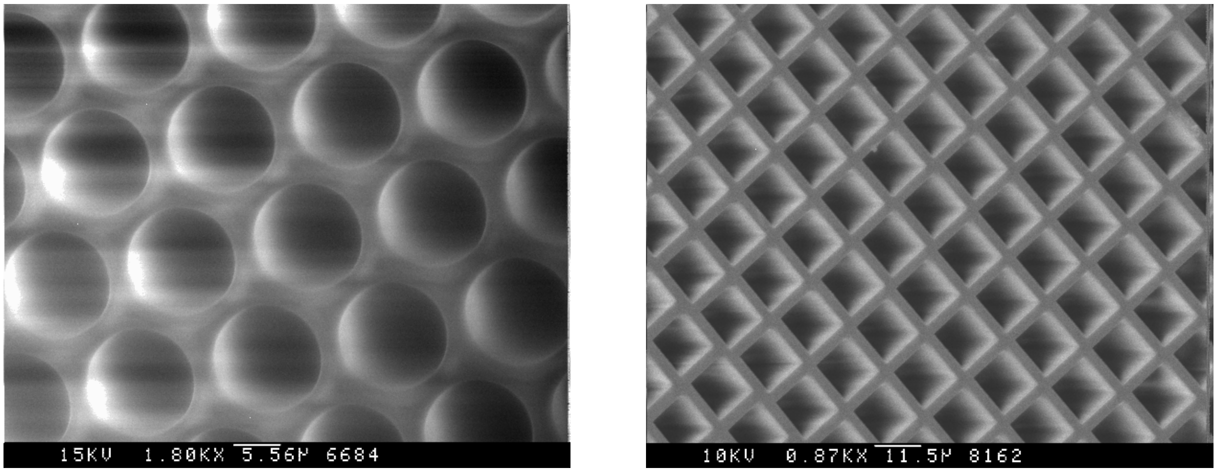

Figure 1.10: Electron micrographs of round-pore detector MCP (left) and square-pore MPO (right). Scale is indicated by the bar in each case.

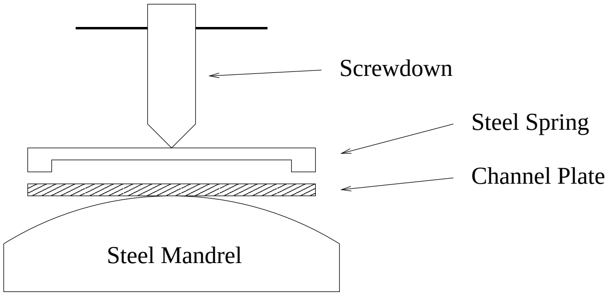

Figure 1.11: Emberson's slumping equipment (Martin, 2000).

from the process described in Figure 1.9 is necessary.

Glass strips have been elastically bent in order to focus X-rays since the idea was first suggested by Ehrenberg (1949). Bending MPOs and then annealing them at high temperature to remove the elastic stresses in the cladding glass was first carried out experimentally at Photonis SAS (then Philips Photonics) (Emberson, 1994). This was achieved by slumping the plate over a steel mandrel as shown in Figure 1.11. Martin covers the subject in more depth in his thesis (Martin, 2000).

A second solution consisting of using positive and negative formers for the required radii is currently being implemented. Results from slumped square-pore square-packed optics manufactured in this method are presented in chapter 4. The results from the two radially-packed MPOs slumped to produce a microchannel Wolter optic are presented in chapter 6.

In a perfectly slumped plate, the radial component of a channel's tilt varies linearly with distance from the centre of the MPO, in this way all the channel axes point to a common centre. The 'trick' is keep the fibres from shearing so that although the MPO has the correct profile, the channels are not perpendicular to the spherical surface. This presents a demanding challenge.

1.5 Astronomical applications of microchannel plates

1.5.1 Detectors

Microchannel plate detectors held the position as the high resolution "detector of choice" in X-ray astronomy for twenty years. The intrinsic energy resolution of MCP detectors, however, is either non-existent, or in the case of those possessing a photocathode, crude ($\delta E/E = 1$ at 1keV, Zombeck *et al.* 1995a,b). This has seen them fall from favour as they have been superseded by CCD cameras and other pixel arrays with both spatial and spectral resolution.

When used in combination with a dispersive element such as a crystal diffraction grating or, in the case of JPEX (Bannister *et al.*, 1999), normal incidence multilayer gratings MCP detectors can be used in a spectroscopic nature. Newly developed progressive geometry vernier readouts (Lapington *et al.*, 1998) have pushed the spatial resolution of MCP detectors to near the theoretical channel pitch resolution ($\sim 15\mu$m resolution has been reported by Lapington *et al.*). The combination of very high detector resolution and diffraction grating technology has enabled previously unseen resolving powers ($\lambda/\delta\lambda = 5000$ at 235Å in the JPEX sounding rocket experiment) to be achieved.

Research into microchannel plates is very much active; lithographically produced silicon MCPs, for example, have been developed to a point where they demonstrate gains comparable to similar lead glass plates, but with 95% open area fractions (Beetz *et al.*, 2000). While still widely used in UV imaging (e.g. the Auroral Imager, section 1.5.2) and spectroscopic readout (e.g. JPEX), new applications have arisen for conventional MCPs in fields such as gamma ray (Shikhaliev, 2001) and neutron (Feller *et al.*, 2000) detection. The imaging X-ray detector of choice may have become the CCD, but the microchannel plate remains an important detector and still has much to contribute to astronomy.

1.5.2 Micropore optics

Since micropore optics are a new technology only just starting to reach a mature state, there are several mission concepts in various stages of development. As the majority of this thesis is concerned with the MPO, I will devote a little space to each of the proposals in astronomy and related fields.

BepiColombo

Named after Prof. Giuseppe Colombo who calculated the orbital manoeuvre that enabled Mariner 10 to pass over Mercury 3 times in 1974-5, BepiColombo is an ESA cornerstone mission to return to the planet nearest the sun. The mission hopes to vastly increase the amount of data available about Mercury (currently the least well known of the terrestrial planets) and clear up unanswered questions raised by the Mariner 10 flybys. This includes a complete mapping of the planet (only $\sim 45\%$ covered by Mariner 10), knowledge of the structure of both the core and crust of the planet and a detailed investigation of the magnetic field. Due to its proximity to the sun, a precise knowledge of Mercury's orbit can also be used to set constraints on general relativity (e.g. the prediction of it's precession).

In order to achieve these scientific aims a three module spacecraft has been envisaged comprising a Mercury Planetary Orbiter, a Mercury Magnetospheric Orbiter and a lander. The orbiter will be a three axis stabilised nadir pointing remote sensing satellite comprising a variety of different wavelength spectrometers and cameras as well as an accelerometer and altimeter. The magnetospheric orbiter will be placed in an eccentric orbit about the planet and will contain electric/magnetic field and wave instruments as well as

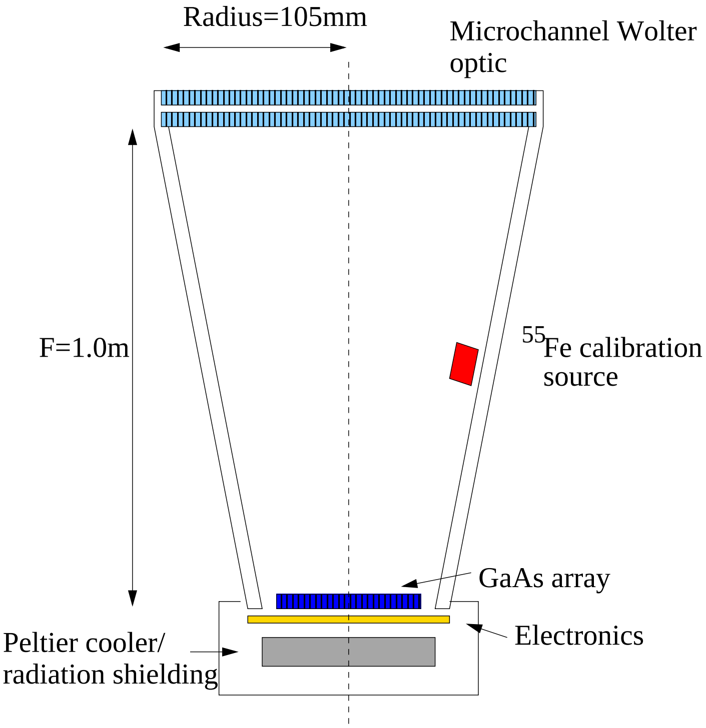

Figure 1.12: HERMES-X, the imaging X-ray fluorescence spectrometer being developed for proposal to the Mercury Planetary Orbiter spacecraft.

a complement of particle detectors. The lander will perform chemical and mineralogical observations of the surface to serve as a "ground truth" reference for the remote sensing instruments.

An imaging X-ray fluorescence spectrometer, the High Energy Remote-sensing of Mercury's Surface (HERMES-X) experiment, is being developed by a consortium of universities led by Leicester for proposal as a payload on the planetary orbiter (Fraser *et al.*, 2001b). HERMES-X will be composed of a 210mm diameter, 1m focal length microchannel Wolter optic imaging onto a GaAs pixel array (Figure 1.12).

The instrument will be sensitive over the energy range 0.5keV→ 10keV with an expected energy resolution of $\sim$ 250eV at 5.9keV. This allows the elements in the range Na→Fe to be identified from their K_α X-ray lines. An angular resolution of $2'$ will give a surface resolution of $\sim$ 200m at 400km periherm, enabling an accurate elemental map of the top few microns of the regolith to be constructed. This will permit different rock classes to be distinguished between, crucial to understanding the planet's tectonic/volcanic history and the evolution of the inner solar system.

The Wolter optic has a field of view $\sim 2^\circ$ and an on-axis effective area of $\sim 100\text{cm}^2$ up to 2keV. Analysis of the solar X-ray and proton induced fluorescent X-ray flux during the expected 2 year lifetime of the orbiter (Owens *et al.*, 2001; Brunton, 2001) indicates the following numbers of counts per 7km^2 ground 'pixel': Mg - ~ 1200, Al - ~ 1100 and Si - ~ 2000. During solar flares, the detector can be switched to a higher resolution mode to achieve statistically significant spectral data from the 200m maximum resolution of the telescope.

A complementary gamma-ray spectrometer, HERMES-G, will explore Mercury's elemental distribution, at depths up to ~ 30cm, through the detection of naturally occurring and cosmic ray induced gamma-ray emissions.

The telescope for HERMES-X has a very similar specification to that of RoSAT's X-ray telescope (100cm^2 effective area at 2keV (Aschenbach, 1987)). The telescope could, thus, be used for significant X-ray astronomy during the ~ 2 year cruise phase to the planet.

The microchannel Wolter optic of HERMES-X is described in greater detail in section 6.7. BepiColombo the mission has been baselined for launch subject to an appropriate window around 2010. HERMES has been pre-proposed to PPARC and an 'intention to propose' document has been submitted to ESA (Fraser *et al.*, 2001b).

XEUS

The X-ray Evolving Universe Spectroscopy Mission (XEUS) is currently being promoted as the follow on to ESA's XMM-Newton X-ray observatory.

Cosmology and the study of the evolution and structure of the universe requires the observation of the youngest, and hence most distant, sources available. Missions such as the Next Generation Space Telescope (NGST) and Herschel (formerly the Far Infrared and Submillimetre Telescope - FIRST) will observe cold matter at infrared and submillimetre

Parameter		Specification
Energy range		0.05keV→ 30keV
Mirror collecting area	@ 1keV	30m^2
	@ 8keV	3m^2
Spatial resolution		$5''$ (goal $2''$)
Field of view		$5'$→ $10'$
Energy resolution	@ 1keV	40eV
Mission lifetime		25 years

Table 1.1: Mission specifications for XEUS.

wavelengths; a high throughput, high resolution X-ray telescope is required to study hot matter. The goal of XEUS is to be able to detect the first black holes, believed to have formed at redshifts of 10 → 20 and take detailed spectra of the most luminous ones (Bavdaz *et al.*, 1999). The specifications arrived at to realise this aim, listed in Table 1.1, amount to the most ambitious X-ray mission ever attempted.

A two spacecraft mission is proposed (Bavdaz *et al.*, 1999) to meet the XEUS requirements; a Mirror SpaceCraft (MSC) being flown in formation with the Detector SpaceCraft (DSC) at a distance of 50m. In a Low Earth Orbit (LEO) near the International Space Station (ISS) the mirror module will begin operation after launch as a 4.5m diameter (6m^2 effective area) Wolter type I optic. The Wolter shells are to be produced using the mandrel replication technique used to fabricate the XMM mirrors (de Chambure *et al.*, 1996). After a period of observation, the robotic arm capability of the ISS will be used to add mirror module 'petals' to the original, increasing its size to the full 10m diameter, 30m^2 effective area specification. The mission scenario is summarised in Figure 1.13.

Although not officially included as a specification, micropore optics (specifically the microchannel conic approximation to a Wolter type I optic) are being considered as a possible high energy extension to the mission. Placed at the centre of the MSC and taking advantage of high L/D channel ratios, they could extend the upper energy limit of the mission from 30keV to 100keV. There are numerous publications detailing the status of XEUS (Bavdaz *et al.*, 2000; Verhoeve *et al.*, 1999), currently under review at ESA as a mission

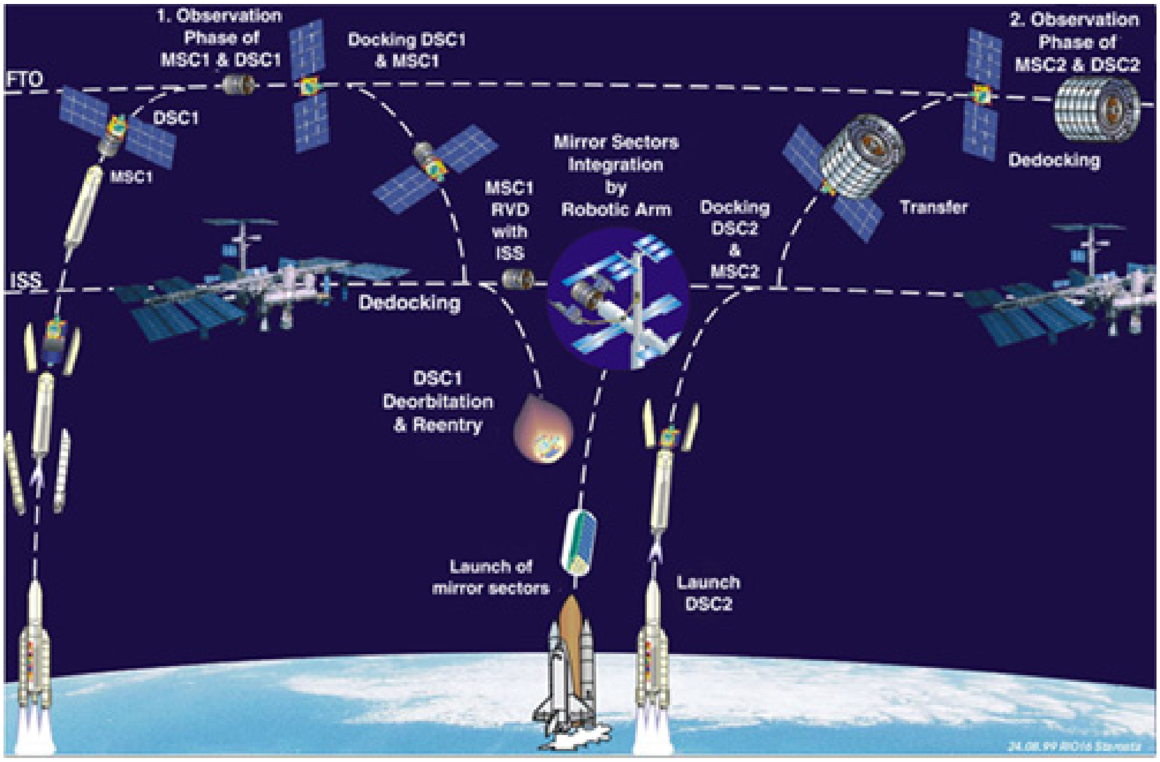

Figure 1.13: The XEUS mission concept. Following launch of the initial Mirror SpaceCraft (MSC) and Detector SpaceCraft (DSC), a period of $4-6$ years is spent observing. The MSC is then docked with the ISS where the mirror is increased in size (from a $6\mathrm{m}^2$ effective area to $30\mathrm{m}^2$). A new generation DSC is then launched and observations begin again. This process can be repeated, providing an active life of up to 20 years. Image from XEUS web page.

concept. Microchannel Wolter optics and their current state of development are discussed more fully in chapters 5 and 6.

Auroral Imager

The Auroral Imager concept has arisen from a joint study carried out by the Space Project and Instrumentation (SPI) and Radio and Space Plasma Physics (RSPP) groups at Leicester. The RSPP group is concerned with the interaction of the solar wind and Earth's magnetic field. As partners in the Super Dual Auroral Radar Network (SuperDARN), they have access to data from the network which images the plasma flow in the polar ionosphere (Greenwald *et al.*, 1995; Lester *et al.*, 1998). Through combining data from this radar network and auroral imagers, much insight can be gained into the relationships between particle currents and electromagnetic fields in the magnetosphere.

Previous auroral imagers such as Freja (Adema, 1993) and POLAR (Frank *et al.*, 1995) have small fields of view (25° and 20° respectivly) and thus can only provide true auroral imaging from high orbits ($h \geq 3000$km). The aim with the Auroral Imager project is to provide similar coverage from a low earth orbit ($h \simeq 800$km). If this is to be the case, a large field of view will be required.

It has been proposed (Lees *et al.*, 1999; Cowley *et al.*, 2000) that micropore lobster eye optics, with a FOV of $90^\circ \times 90^\circ$ could be used to observe all of the aurora from LEO. As the observations are in the VUV (6eV$\rightarrow$ 10eV, 1240Å$\rightarrow$ 2000Å) an MPO would be perfect as the reflectivity is high to large grazing angles of incidence but diffraction effects are not yet significant. A photograph of the type of MPO proposed for the auroral imager (an 85μm square-pore, lobster eye MPO with a 7cm slump radius, Lees *et al.* 1999) is shown in Figure 1.14.

As well as using micropore optics, it has also been proposed that a microchannel plate detector, profiled to the focal surface, is flown as the focal plane instrument. This would be of the type used in the RoSAT Wide Field Camera (WFC) (Wells, 1985), but with a

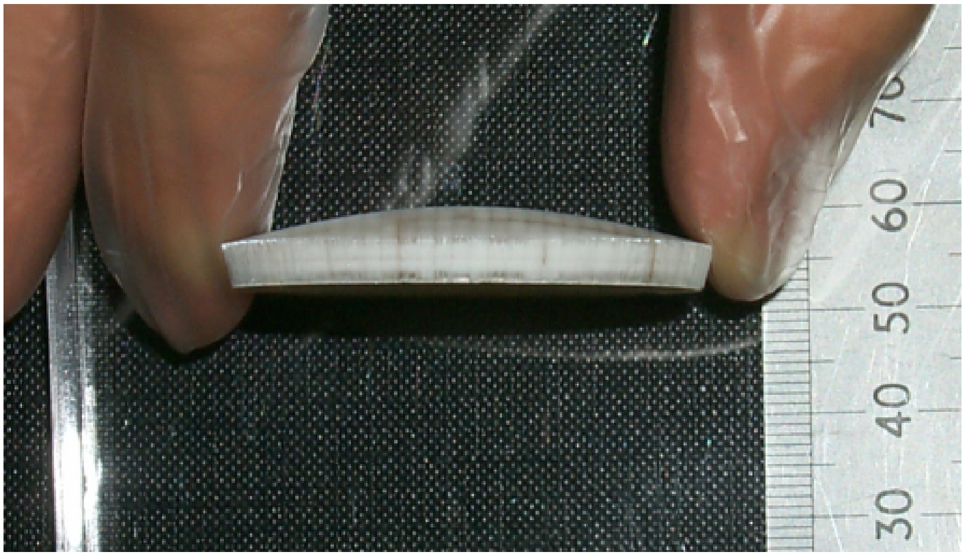

Figure 1.14: A lobster eye MPO of the specifications proposed for the Auroral imager (85μm square-pore, square-packed MPO slumped to a radius of 7cm).

convex, not concave profile.

Figure 1.15 shows a schematic of a single module (*a*) and how these fit together to form a wide FOV multi-module telescope (*b*).

Lobster

Taking advantage of the unlimited field of view of lobster eye optics, an All Sky Monitor (ASM) based upon micropore optics has been proposed (Fraser *et al.*, 2000). Composed of eighteen modules with a total FOV of 2.2sr, Lobster was first proposed as a free flying satellite in the 1997 NASA Small Explorer missions (SMEX) round (Priedhorsky *et al.*, 1997). Here the need for an imaging ASM of Lobster's capability was acknowledged but the instrument rejected on terms of the technical immaturity of the micropore optics and microstrip gas proportional counter detector. Following the ESA TRP contract, Lobster was reproposed as an attached payload for the International Space Station (ISS) in response to the ESA Flexi-missions F2 and F3 rounds (Fraser *et al.*, 2000). Lobster-ISS, as it is now known, has been approved for launch in 2008/9 subject to technical reviews and is about to start a phase A concept study (December 2001).

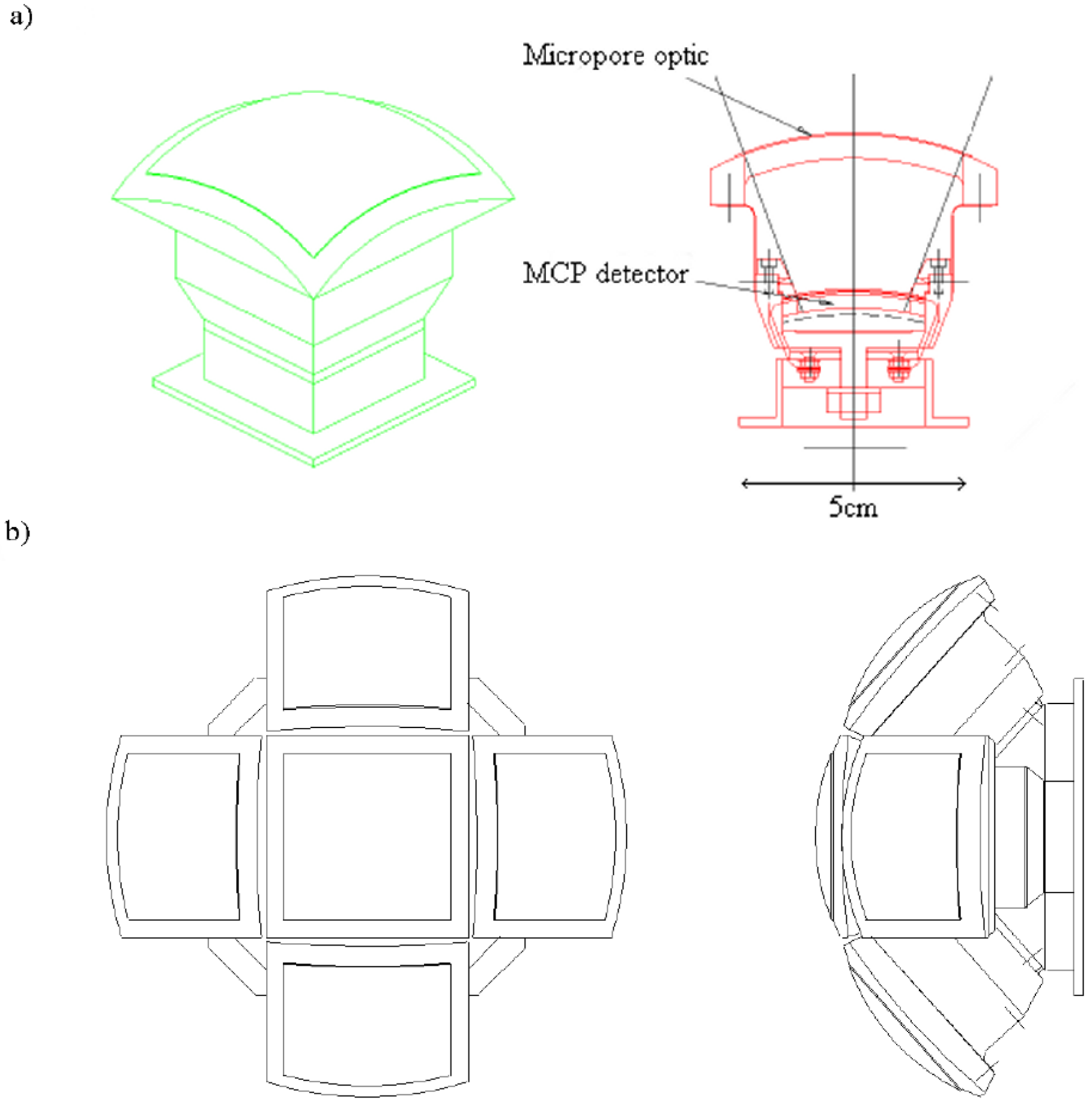

Figure 1.15: (*a*) a single module of the Auroral Imager composed of a lobster eye micropore optic and a convex microchannel plate detector. Scale is indicated by the 5cm bar. (*b*) shows how these may be fitted together to provide a wide FOV multi-module telescope.

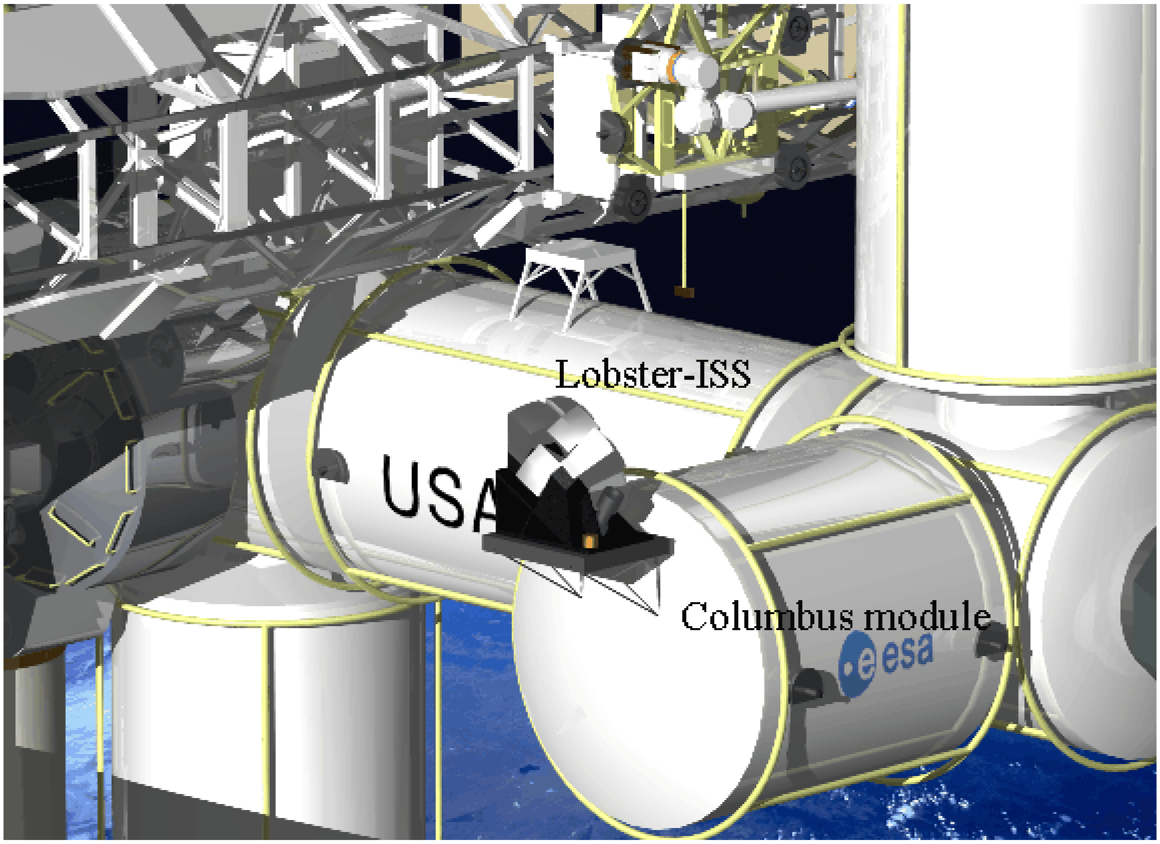

Figure 1.16: The Lobster-ISS ASM as it will look when mounted at the zenith exposed payload facility of the European Columbus module of the ISS.

Lobster-ISS will be mounted externally on the ESA Columbus pressurised module of the ISS and is comprised of six $27° \times 22.5°$ FOV modules. These provide an instantaneous FOV of 162° by 22.5°. As the ISS orbits the Earth every 90 minutes, the Lobster modules will see the entire X-ray sky, any regions of reduced exposure are smoothed out by the precession of the ISS's orbit. Lobster-ISS is shown in its mounting position at the zenith exposed payload facility of the ESA Columbus module in Figure 1.16. The mission is discussed in detail in chapter 7.

1.6 Overview

In the rest of this thesis, I report work that I have undertaken in the three years of my Ph.D. at Leicester University (starting October 1998).

Chapter 2 describes a Monte Carlo model of a detector microchannel I constructed at the suggestion of my supervisor, Prof. George Fraser (Fraser, 1998). Chapter 3 then describes the X-ray test facilities and analysis tools that I have helped to develop and have used extensively during my time at Leicester. A large percentage of both my time and that of my colleagues has been consumed in the continued evolution of the vacuum test systems, without which the full face MPO exposures described in chapters 4 and 6 could not have taken place. The Monte Carlo raytrace model that I extended and used in all MPO analysis (section 3.6) was inherited from Dr Adam Brunton who also had much input during its modification.

Chapters 4, 5 and 6 then describe the latest X-ray focusing results obtained with square channel micropore optics in both square-packed and radial/Wolter configurations. All square-pack images of chapter 4 were recorded by either myself or Dr Brunton, the radial-pack and Wolter MPO images in chapter 6 during several experimental runs on the TTF high energy long beamline (section 3.2.2) by myself, Dr Brunton and Dr Marco Beijersbergen of ESA/ESTEC.

Chapter 7 then discusses a method of co-aligning multiple lobster eye MPOs. I undertook the commissioning of an 'alignment jig' constructed for this purpose. The driving software for the jig was written in house by Kevin Turner. The jig is used to determine the bias angle of a planar MPO.

In the final chapter both the immediate (next few months and years) and long term (next decade) future of the technology are discussed.

Chapter 2

Simulation of a detector microchannel

2.1 Introduction

This chapter explores the principles of operation of microchannel plate (MCP) multipliers in greater detail. Specifically, it is concerned with an electron raytrace computer model of a single microchannel developed to determine the output charge cloud characteristics; the angular and energy distributions of the electrons (ADOE and EDOE respectively). This is a self contained chapter, although it is interesting in relation to the rest of this thesis as it allows the reader to understand more fully the heritage of the micropore optic. It is also a reminder that although the microchannel plate amplifier is a mature technology, research is still very much active in the field in an effort to refine and enhance MCP properties and to find further applications.

The microchannel plate, as described in section 1.2, works through the generation of an avalanche of electrons in a channel with secondary electron emitting properties. In this way a single incident particle or photon produces a detectable signal. An array of microchannels can thus provide a position sensitive detector with a limiting spatial resolution equal to the pitch of the channels (i.e. the distance between the centres of adjacent channels). The spatial resolution and image linearity of microchannel plate imaging detectors using 'progressive geometry' position encoders, however, are also dependent on the ADOE and EDOE of electrons in the output charge cloud. The charge 'footprint' on the readout element must be matched to the repeat pattern of the encoder in order to avoid distortion. Energetic electrons in the charge cloud may also reduce image quality by enlarging and distorting the footprint through secondary electron emission from the anode (Edgar *et al.*, 1989; Lapington, 1997; Lapington and Worth, 1998). A recently suggested application also dependent on the ADOE and EDOE of MCPs, in fact a motive in undertaking this work, is electron beam lithography. Here, microchannel plates are used to multiply and, operating in a saturated mode (section 2.4.2), stabilise the current from a field emitter. This allows bulk exposure of resists, increasing lithographic throughput compared to conventional single beam writing techniques (Haar, 2001).

An analytical model of a single microchannel is first described (section 2.2.1), followed by the development of a Monte Carlo computer simulation (section 2.2.2 onwards). The available experimental data is reviewed and compared with results from the computer model. Potential applications of the modelling, including the possibility of incorporating an electrostatic lens at the exit of a microchannel are then discussed.

2.2 MCP model

A microchannel plate electron multiplier is based on secondary electron emission (SEE). A charged particle or energetic photon incident on a channel wall near the channel entrance will excite secondary electrons into vacuum. A bias applied along the length of the channel then accelerates these secondary electrons down the channel where they themselves will strike the wall. Provided the electron collision energy K_c exceeds eV_1 where V_1 ($\sim$30V) is the first cross-over potential (where the secondary electron yield δ, the mean number of secondary electrons emitted per incident primary, is equal to one), an avalanche propagates, as indicated in Figure 2.1.

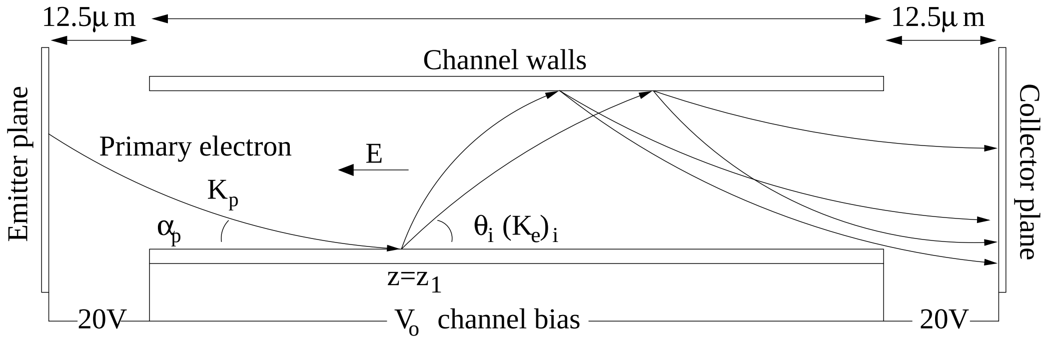

Figure 2.1: Signal amplification in a microchannel. K_p and α_p are the energy and grazing angle for the incident primary electron initiating the avalanche. θ_i ($i = 1, 2\ldots$ in the schematic shown here) and $(K_e)_i$ are the emission angles and energies of the emitted secondaries, α_i and $(K_c)_i$ are the corresponding collision angles and energies.

The potential bias across a microchannel plate is applied via an electrode coating on either side of the channel array. This coating, generally inconel or nichrome, both alloys of nickel, extends to a small distance ($\sim$ 1 channel diameter, D) down the channels (Figure 2.2). This acts to perturb the electric field around the channel entrance/exit to some degree (section 2.2.4).

A model of the working channel has two elements: the representation of the electron emission process from the channel wall (sections 2.2.1-2.2.3) and the calculation of the channel electric field (section 2.2.4) in which electron trajectories are tracked (section 2.2.5).

2.2.1 Secondary electron yield δ

According to the two dimensional channel model of Adams and Manley (1966) the collision energy of an emitted electron can be calculated as

$$K_c = \frac{V_o^2 e^2}{4 K_e \sin^2\theta} \frac{D^2}{L^2} \tag{2.1}$$

where K_e is the secondary electron emission energy and θ is the angle of emission of the electron with respect to the channel surface. L/D is the channel length to diameter ratio, V_o is the potential applied across the channel and e is the electron charge. To zeroth

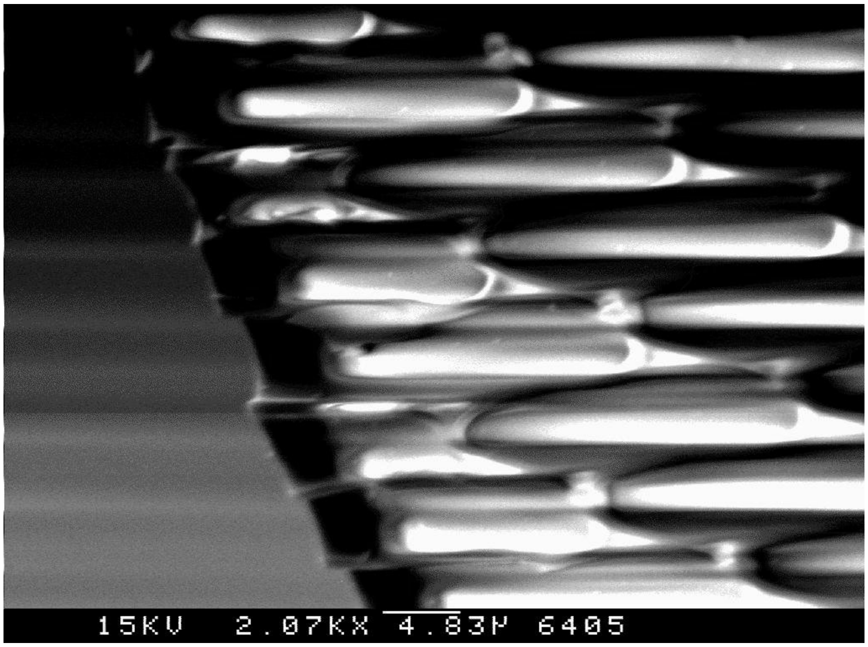

Figure 2.2: An SEM image of a cleaved 6μm pore microchannel plate showing nichrome penetration (dark areas) into channels. Scale is indicated by the bar.

order, K_c is a measure of the maximum electron energy in the EDOE. Assuming electron emission normal to the wall, K_c and α, the incident electron grazing angle, are constants and the channel gain G is given by

$$G = \delta(K_c, \alpha)^{\frac{eV_O}{K_c}} \tag{2.2}$$

where δ is the secondary electron yield coefficient of the surface.

The semi-empirical models of Burke (1977), Dekker (1958) and Hill (1976) suggest that the yield for normal incidence primaries is

$$\delta(K_c, \frac{\pi}{2}) = P_s(0)\frac{K_c}{\epsilon}\frac{L_s}{R_p}(1 - \exp(\frac{-R_p}{L_s})) \tag{2.3}$$

where $P_s(0)$ is the surface escape probability, ϵ is the energy required to create a secondary electron in the material, L_s is the secondary electron escape length and R_p is the range of the primary in the glass. Fraser (1983) has previously derived values for the material constants of lead silicate glass by comparison with the measurements of Hill (1976) and Authinarayanan and Dudding (1976); $P_s(0) = 0.15$, $L_s = 33$Å, $\epsilon = 10$eV. For nickel, representing the nichrome or inconel end-spoiling electrodes, an analysis of the ion-induced

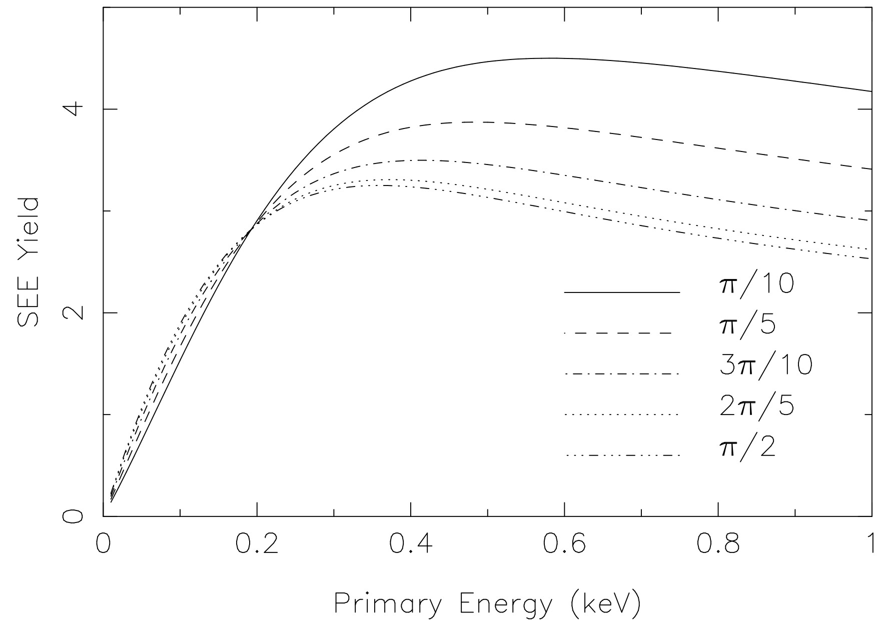

Figure 2.3: SEE yield as a function of primary electron energy for five different primary grazing angles of incidence α.

secondary electron yield data of Von Gemmingen (1982) gives; $P_s(0) = 0.024$, $L_s = 20\text{Å}$, $\epsilon = 6.65\text{eV}$.

The increase of δ with decreasing grazing angle of incidence α comes from a reduction in the distance below the surface that the secondaries are created. Guest (1971) and Bouchard and Carette (1979) suggest that

$$\delta(K_c, \alpha) = \delta(K_c, \frac{\pi}{2}) \exp[p(K_c)(1 - \sin\alpha)] \tag{2.4}$$

where $p(K_c) = 0.7664 - 1.533\exp(-3.598K_c)$, with K_c in keV (derived using a least squares fitting method to experimental data). Figure 2.3 shows the resulting secondary electron yield function for MCP glass.

A fraction R of the incident primaries is elastically scattered back into the vacuum. The lead glass data of Goff and Hendee (1967) indicate that R$\ll \delta$ (R=0.17 for α=20°and a primary energy of 51eV; R=0.05 for α=90°and an energy of 300eV) and so backscattering is neglected in the calculations below.

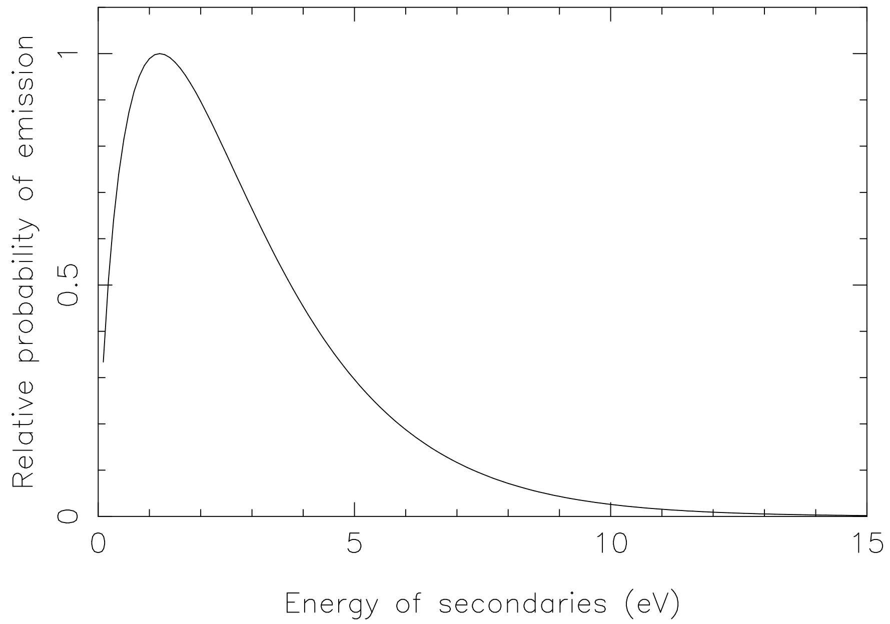

Figure 2.4: **Energy distribution of secondary electrons for lead glass.**

2.2.2 Electron emission energies

The energy distribution of the secondaries produced by primary electron bombardment of lead silicate glass has been thoroughly investigated experimentally (Hill, 1976; Authinarayanan and Dudding, 1976). The relative probability of electron emission at an energy K_e can be expressed by the empirical formula (Petrovna and Flegontov, 1988)

$$f(K_e) = C(\frac{K_e}{K_{av}})^\beta \exp(\frac{-\gamma K_e}{K_{av}}) \tag{2.5}$$

where C is a normalisation factor, K_{av} is the average secondary energy at emission, and β and γ are fit parameters. From comparisons with the data of Hill (1976) for lead silicate glass, the fit parameters are $\beta = 0.7$ and $\gamma = 7$. The resulting distribution, used in the computer model described below, is shown in Figure 2.4.

2.2.3 Electron emission angles

The angular distribution of secondary electrons produced by grazing incidence electron impact on amorphous solids is not well known. The distribution is generally assumed to be of an azimuth independent cosine form (Suzuki and Konno, 1993; Kawarabayashi *et al.*,

1994) where, if ϕ is the angle of emission (to the normal of the surface) then the probability of emission is

$$P(\phi) = \cos\phi \tag{2.6}$$

A physical basis for this distribution is the large number of collisions undergone by secondary electrons during transport from their generation site to the surface. This hypothesis is supported by Monte Carlo simulations of the SEE process (Kawata *et al.*, 1992; Kawata and Ohya, 1997).

Some experimental evidence points to a deviation from the distribution of equation (2.6) as the grazing angle of the primary electrons decreases. Goff and Hendee (1967) state that the greatest probability of secondary electron emission is back towards the direction of the incident electron beam. This back-skewing is attributed to an increase in the probability of inelastic backscattering. There is, however, no available data on the energy dependence of this back-skewing so that in the calculations described below, the secondary electron emission distribution is unchanged from equation (2.6).

In the absence of specific experimental data, the electron energy and angle emission distributions of the nickel electrodes are assumed to be the same as those of the channel glass.

2.2.4 Electric field calculation

The channel electrostatic potential distribution $V(y,z)$ is solved, in the presence of electrode end-spoiling and other perturbations, by finite difference methods. The two dimensional potential matrix is first seeded with a potential linearly increasing in z and then Laplace's equation ($\nabla^2 V = 0$) is solved by four-point Newtonian relaxation (equation 2.7, as reported by Fraser *et al.* (1984)).

$$V_{i+1}(z,y) = \frac{V_i((z-1),y) + V_i((z+1),y) + V_i(z,(y-1)) + V_i(z,(y+1))}{4} \tag{2.7}$$

Iteration continues until either a tolerance of $\nabla^2 V \leq 1 \times 10^{-2}\mathrm{Vm}^{-2}$ is reached or the number of iterations exceeds a preset value. The maximum number of iterations is set

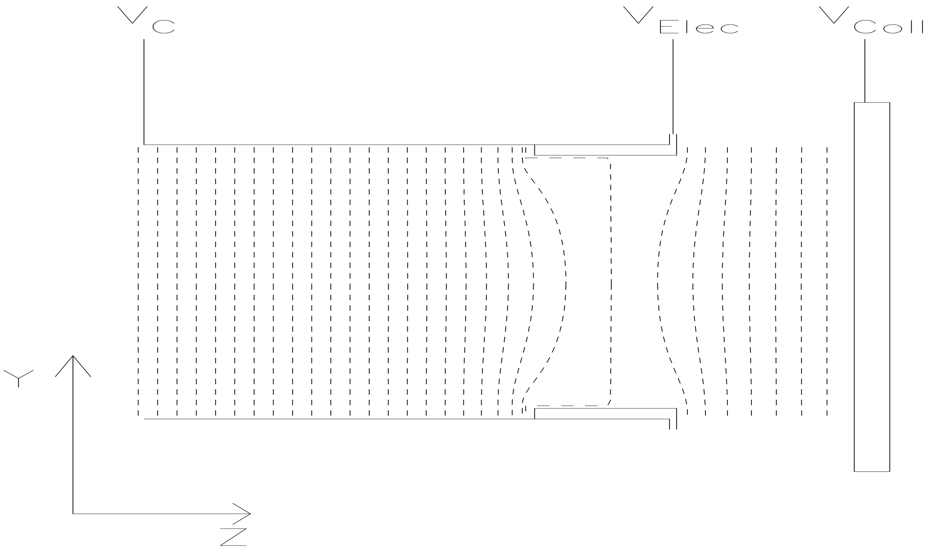

Figure 2.5: Equipotentials near the exit of an end-spoiled channel. $V_c = -75$V; electrode potential $V_{Elec} = -20$V; collector potential $V_{Coll} = 0$V. Contours are separated by 2.5V.

as the multiple of the z and y dimensions of the potential matrix, to do otherwise could lead to exorbitant execution times. At this number of iterations, $\nabla^2 V$ approaches the tolerance level ($\sim$several$\times 10^{-2}$Vm^{-2}) and so accuracy is not excessively sacrificed.

The array elements are separated by 0.25μm in z and y so that in a typical geometry (D = 12μm, L/D=100:1), the potential is stored in a 5000 $\times$ 80 element array. Using a 433MHz Dec Alpha workstation, a typical potential generation takes $\sim$ 8 hours. An example is shown in Figure 2.5.

2.2.5 Electron transport

Each avalanche is initiated by a single primary electron of random energy K_p in the range 100eV→ 600eV and incident angle α_p randomly selected within the channel entrance cone. The model assumes a 20V electron accelerating potential between the emitter plane and channel entrance plane (and between the exit and collector planes). It has been confirmed that the calculated EDOE and ADOE are independent of the starting conditions (as is the channel gain to a large extent, hence the limited X-ray energy resolution of an MCP detector).

The grazing angle of the primary is calculated at the position of first strike ($z = z_1$ in Figure 2.1) and a value of δ calculated from equations (2.3) and (2.4). The number of emitted secondaries is then chosen randomly from a Poissonian distribution with mean δ. For each secondary, an emission angle and energy are assigned from the distributions described by equations (2.5) and (2.6) respectively. The individual electrons are traced in the potential distribution $V(y,z)$ until they next strike the channel wall (lead silicate glass or nickel electrode) or they exit the channel. The equations of motion are solved at $\Delta t = 0.1$ps intervals (the transit time of an electron avalanche in a microchannel is typically 100ps) using the formulae of Klemperer and Barnett (1971). The position of an electron traced through an electric field $V(y,z)$ from a starting position (y_0, z_0) is given by

$$y_1 = y_0 + \left(\frac{dy}{d\tau}\right)_0 \Delta\tau + \frac{1}{4}\left(\frac{\partial V}{\partial y}\right)_0 \Delta\tau^2 + \frac{1}{12}\left[\left(\frac{\partial^2 V}{\partial y^2}\right)_0 \left(\frac{dy}{d\tau}\right)_0 + \left(\frac{\partial^2 V}{\partial y \partial z}\right)_0 \left(\frac{dz}{d\tau}\right)_0\right] \Delta\tau^3 \tag{2.8}$$

$$z_1 = z_0 + \left(\frac{dz}{d\tau}\right)_0 \Delta\tau + \frac{1}{4}\left(\frac{\partial V}{\partial z}\right)_0 \Delta\tau^2 + \frac{1}{12}\left[\left(\frac{\partial^2 V}{\partial z^2}\right)_0 \left(\frac{dz}{d\tau}\right)_0 + \left(\frac{\partial^2 V}{\partial z \partial y}\right)_0 \left(\frac{dy}{d\tau}\right)_0\right] \Delta\tau^3 \tag{2.9}$$

where $\Delta\tau = (2e/m)^{1/2}\Delta t$, e/m is the electron charge to mass ratio. The new velocity is then given by

$$\left(\frac{dy}{d\tau}\right)_1 = \left(\frac{dy}{d\tau}\right)_0 + \frac{1}{2}\left(\frac{\partial V}{\partial y}\right)_0 \Delta\tau + \frac{1}{4}\left[\left(\frac{\partial^2 V}{\partial y^2}\right)_0 \left(\frac{dy}{d\tau}\right)_0 + \left(\frac{\partial^2 V}{\partial y \partial z}\right)_0 \left(\frac{dz}{d\tau}\right)_0\right] \Delta\tau^2 \tag{2.10}$$

$$\left(\frac{dz}{d\tau}\right)_1 = \left(\frac{dz}{d\tau}\right)_0 + \frac{1}{2}\left(\frac{\partial V}{\partial z}\right)_0 \Delta\tau + \frac{1}{4}\left[\left(\frac{\partial^2 V}{\partial z^2}\right)_0 \left(\frac{dz}{d\tau}\right)_0 + \left(\frac{\partial^2 V}{\partial z \partial y}\right)_0 \left(\frac{dy}{d\tau}\right)_0\right] \Delta\tau^2 \tag{2.11}$$

The calculated ADOE and EDOE typically contain ~ 20 electrons and thus a statistically meaningful distribution requires many input electrons. The low gain is an artefact of the model being two dimensional. Electrons must cross the entire channel diameter before being incident on a wall, this is not the case in a real three dimensional channel. The result is that fewer electron generating collisions take place, and consequently the exponential increase in signal current I_c occurs at a reduced rate.

2.3 Experimental data

MCP electron energy distributions may be measured by varying the retarding electric field between a collector plate and the MCP output surface and recording the MCP output current (Koshida and Yoshida, 1979; Koshida *et al.*, 1980, 1985; Koshida and Hosobuchi, 1985). Angular distributions may be obtained by moving a small ($\sim 1 \times 10^{-4}$sr) detector-analyser through a range of solid angles around the output of the active channel (Tyutikov and Tsoi, 1976; Bronshteyn *et al.*, 1979). The available experimental data, however, is sparse. In summary

i) For a fixed channel geometry (pore diameter D, channel length L) Bronshteyn *et al.* (1979) report that the width of the ADOE increases with MCP bias voltage V_o; Tyutikov and Tsoi (1976) find the contrary dependence.

ii) The width of the ADOE decreases slowly with the depth of the nickel-based electrode penetration ('endspoiling') into the channel from the exit face.

iii) The high energy tail of the EDOE is suppressed by operation in current saturation mode where the signal current I_c is a significant fraction of I_s, the standing current in the plate.

The data of Koshida *et al.* (1985) is shown in Figure 2.6 and that of Tyutikov and Tsoi (1976) in Figure 2.7

Regarding previous simulations, the early results of Guest (1971) give a good approximation to EDOE data, but make no angular predictions. More recently Antonov *et al.* (1996), Suzuki and Konno (1993) and Choi and Kim (2000) have reported Monte Carlo avalanche simulations. Choi and Kim do not report any EDOE or ADOE data; Suzuki and Konno describe ADOE measurements for a parallel plate electron multiplier, while Antonov *et al.* report only qualitative ADOE calculations with no EDOE data. The many analytical studies of MCP gain (Adams and Manley, 1966; Harris, 1971; Eberhardt, 1979; Csorba, 1980; Eberhardt, 1981; Funsten *et al.*, 1996) yield no information on ADOE or

EDOE.

2.4 Comparison of model with experiment

2.4.1 Non-saturated operation

Figures 2.6 and 2.7 compare experimental EDOE (Koshida *et al.*, 1985) and ADOE (Tyutikov and Tsoi, 1976) datasets with distributions calculated using the described model. The model channels had the same parameters as those used experimentally. The calculated EDOE shows very good agreement at low energy, the fit deviating at higher energy. The calculated ADOE has the same width and shape as the measured distribution, but is shifted by $-1.0°$ with respect to the results of Tyutikov and Tsoi. This offset, removed from Figure 2.7 so that the otherwise excellent fit can be clearly seen, is another artefact of the two dimensional model. The long electron flight times in the two dimensional model allow for greater axial acceleration. This decreases the electrons' angles to the channel axis and provides the shift in distribution observed in the model ADOE. In a real channel, the probability of long electron trajectories (and hence large axial accelerations) is greatly reduced. Despite this two dimensional nature of the Monte Carlo model and the consequent under-estimation of the number of collisions at small α/high δ, the salient features of the measured distributions are reproduced.

Further calculations in 'simple' channel geometries show that increasing the channel electric field strength (decreasing the aspect ratio L/D or increasing the applied bias V_o) increases the number of low energy divergent electrons produced by a channel and vice-versa. In other words, the trend for ADOE to *broaden* with increased V_o (Bronshteyn *et al.*, 1979) is confirmed.

According to Bronshteyn *et al.* (1979), the half-width of the ADOE peak decreases slowly with the degree of end-spoiling h/D. The angular half-widths measured by these authors lie in the range $5° \rightarrow 15°$. Figure 2.8 shows the calculated EDOEs/ADOEs which result

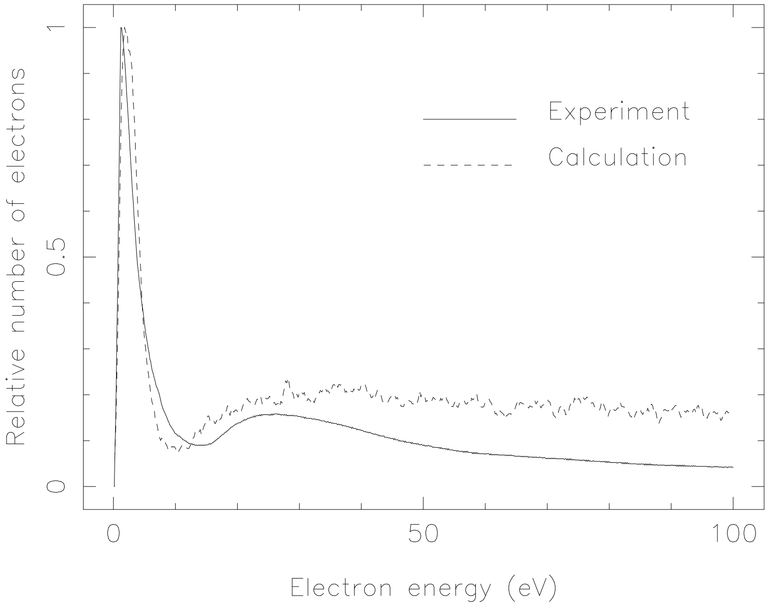

Figure 2.6: Calculated and measured (Koshida *et al.*, 1985) EDOEs, normalised to the low energy peak. $D = 12.5\mu$m; L/D=40:1; $V_o = 1000$V; h/D=0.9. The 20V offset in calculated data due to the model collecting field has been removed in this figure. The maximum emission energy indicated by equation (2.1) is 156eV for $K_e = 1$eV and $\theta = \pi/2$.

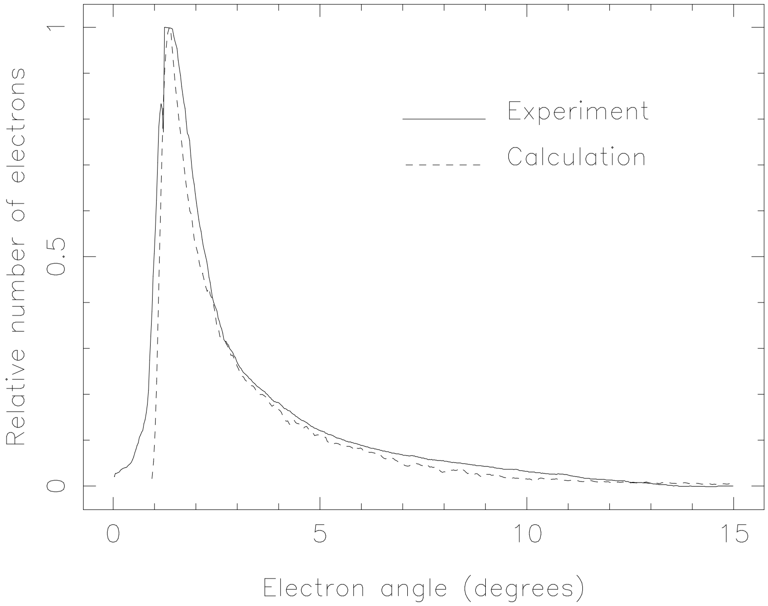

Figure 2.7: Calculated and measured (Tyutikov and Tsoi, 1976) ADOEs. $D = 20\mu$m; L/D=60:1; $V_o = 1000$V; h/D=1.0. A $-1.0°$ offset of the calculated distribution with respect to the measured one, an artefact of the two dimensional nature of the model, is removed in this figure.

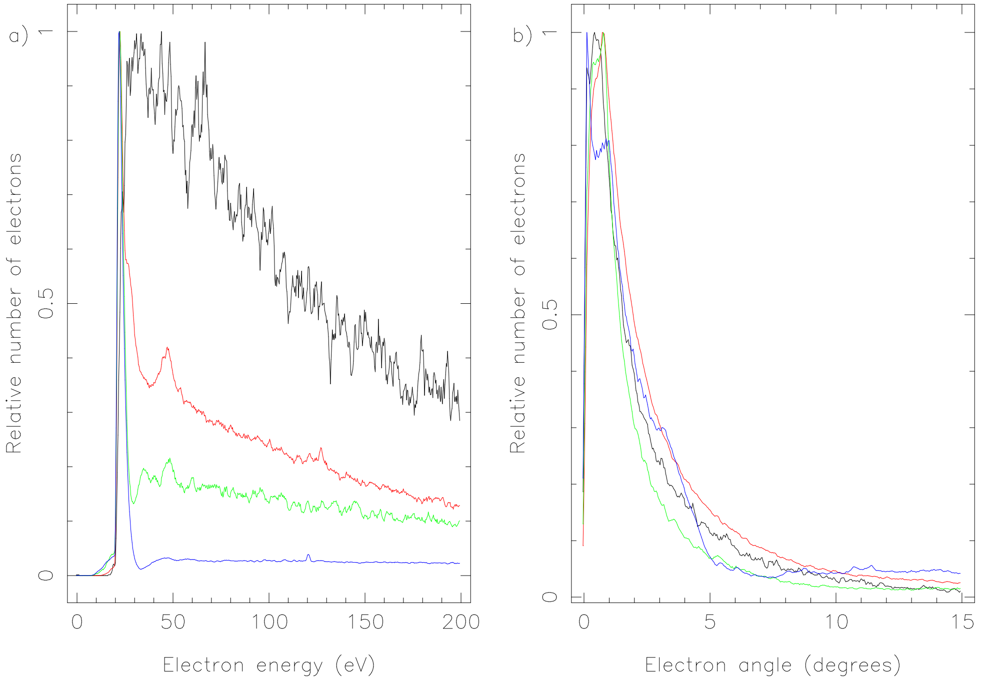

Figure 2.8: EDOEs (a) and ADOEs (b) for a 12μm, 40:1 channel at 800V with various degrees of end-spoiling. The black, red, green and blue lines correspond to h/D=0, 0.5, 1 and 3 respectively. The 20V offset corresponds to the collector field.

from the variation of h/D in a standard channel geometry.

Our ADOEs are narrower than those of Bronshteyn *et al.* (1979), and show no systematic variation with h/D. Increasing the degree of end-spoiling in the model has, however, a marked effect on the EDOE, progressively suppressing the tail of the distribution until, for h/D= 3, the electron energy distribution consists mainly of a sub-10eV spike. This suppression of high energy electrons is observed experimentally by Koshida (1986) for h/D= 1,1.5 and 2.0. Koshida speculated and the model confirms that the electrons in the EDOE peak originate in the constant potential region at the channel exit. Changing $P_s(0)$ for the electrode material in the model, for example, directly influences the relative weights of the EDOE spike and tail.

2.4.2 Operation in current saturation

In the previous section it was assumed that the input current and channel gain are both low, so that the electric field in the channel is determined only by the applied voltage and the electrode penetration. For high gains, positive wall charging (Fraser *et al.*, 1983), due to the failure of the channel to replace charge emitted from the wall during the avalanche, acts to reduce the electric field strength at the channel exit.

When the output current I_c is a significant fraction of the standing current, $I_s = V_o/R_{MCP}$, space charge effects also diminish the electric field. Here, R_{MCP} is the resistance of a microchannel plate.

The microchannel model has been extended to include current saturation, where the formulae of Harris (1971) can be used to estimate the variation of the electric field along the channel axis as I_c/I_s is increased.

It is not realistic to exactly model such a process, since the channel potential would have to be re-calculated after each secondary electron emission step in the avalanche. Instead, the steady state potential in the channel is estimated and then the trajectory of a single electron is traced in the field of many others.

Harris (1971) has derived an equation that allows the calculation of the required channel potential. By considering the total current in a channel (wall current plus space current) as a conserved quantity and considering changes in wall conductivity as the avalanche progresses it can be shown that

$$\frac{dE_R(z)}{dz} = -\frac{4K_e}{E_o E_R(z) D^2} \frac{(1 - E_R(z))(\delta - 1)}{(1 + 2AeE_o^2 E_R(z) \frac{(1-E_R(z))}{(1+AeE_o^2 E_R(z)^2)})} \tag{2.12}$$

where $E_R(z)$ is the relative field strength, E_o is the field strength at the entrance of the channel, δ is the secondary electron yield and A is a proportionality constant relating the induced wall conductivity to incident current density.

The actual wall current only flows near the surface of the channel where the lead glass has been reduced to a semi-conducting state. Bombardment of this layer of reduced glass with electrons will increase its conductivity via the creation of mobile electrons (secondary electrons that have not yet migrated to the surface and been emitted) and the corresponding holes. A must thus be proportional to $1/\epsilon$, where $\epsilon = 10$eV is the energy required to create a secondary electron in the material (Fraser, 1983).

Harris uses a constant, s, with a value between 0 and 50 to represent AeE_o^2; $s = 0$ for highly saturated channels, the saturation level, I_c/I_s, decreasing as s increases. The space current to standing current ratio at a depth z in the channel is

$$\frac{I_c(z)}{I_s} = \frac{1 - E_R(z)}{1 + AeE_o^2 E_R^2(z)} \tag{2.13}$$

In a strongly saturated channel (i.e. high gain or large input current), $AeE_o^2 \ll 1$ and $I_c/I_s \simeq 1 - E_R(L)$ where $E_R(L)$ is the relative electric field strength at the channel exit. Figure 2.9 shows the potential and electric field strength as functions of the distance along a uniform channel calculated using equation (2.12). $I_c/I_s \sim 0.6$ at $z = L$ in this example.

To calculate a saturated potential field, the matrix $V(y, z)$ is seeded with a potential that varies in z as described by equation (2.12). The channel electric field is then solved as described for a linear potential seed (section 2.2.4).

Experimentally, Koshida *et al.* (1985) have found that as I_c/I_s increases, the fraction of electrons with output energies in excess of 50eV decreases. Figure 2.10 compares in detail the measured (Koshida *et al.*, 1985) and calculated EDOEs for a non-saturated and saturated microchannel. The standing current I_s in the data of Koshida *et al.* has been estimated from another paper (Koshida, 1986) in which he uses similar MCPs with $R_{MCP} = 140\text{M}\Omega$. Reasonable agreement is seen between the two sets of data. The experimentally observed trend for the fraction of electrons with energies below 50eV to increase is replicated. The saturation level does not match exactly due to a simplistic approach in modelling the induced wall conductivity. It is known that the relationship between induced conductivity and wall bombardment current is not linearly proportional as assumed in the model (Harris, 1971). However, without having to resort to a very complicated model, the important trends in the output electron cloud EDOE and ADOE as a microchannel becomes saturated have been reproduced.

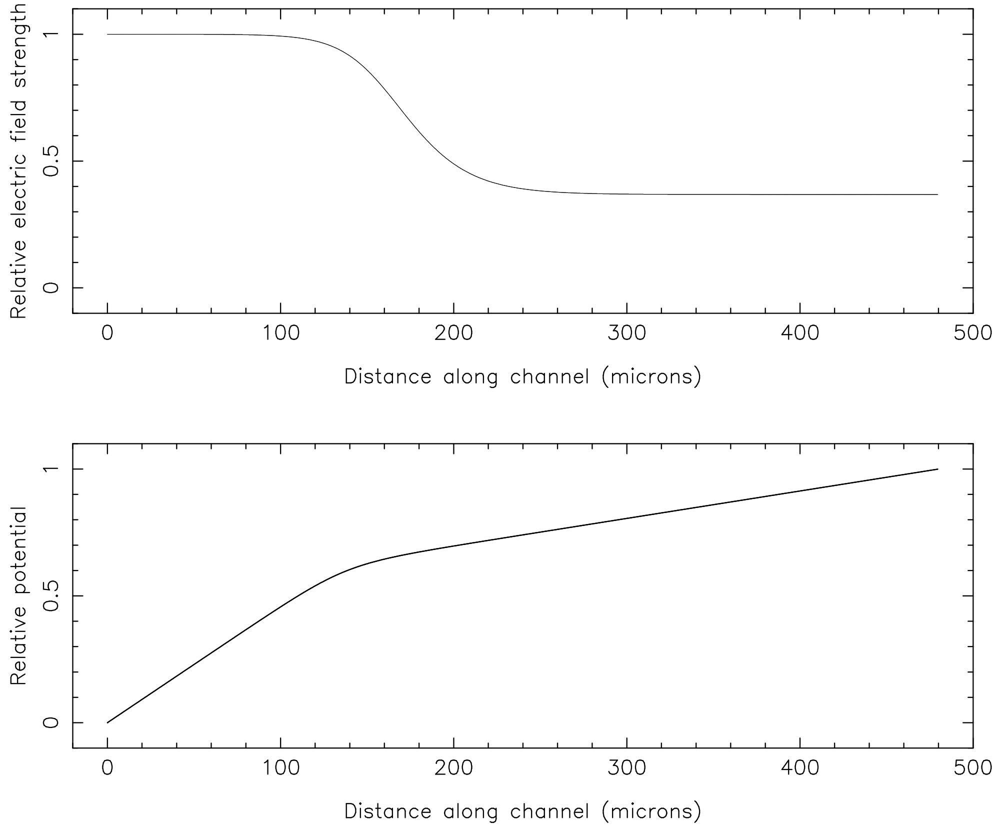

Figure 2.9: Relative potential (bottom) and electric field strength (top) as a function of distance along a 12μm, 40:1 channel biased with 800V and with h/D$= 0.9$. Calculated from equation (2.12). $I_c/I_s \sim 0.6$ at $z = L$ in this example.

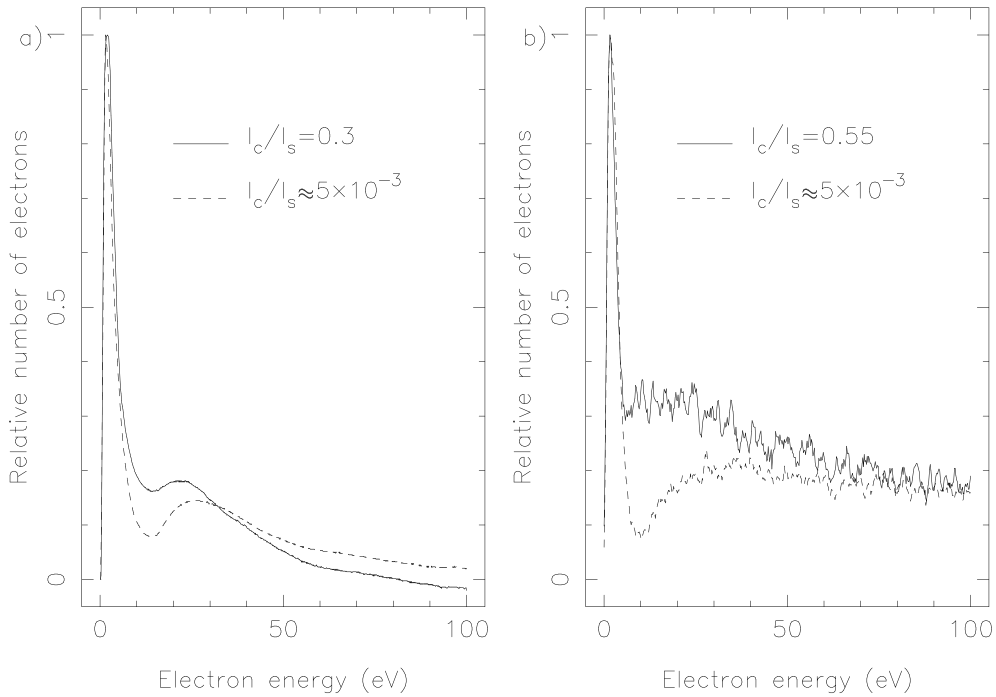

Figure 2.10: **Measured (Koshida *et al.*, 1985) (a) and calculated (b) changes in EDOE with degree of current saturation. $D = 12\mu$m; L/D=40:1; $V_o = 1000$V and h/D=0.9.**

2.5 Applications of the model

The model, although only two dimensional, produces good agreement with the available experimental data and can thus be used to predict the EDOE and ADOE of unknown channel geometries with some degree of confidence (provided the secondary electron yield parameters of the channel walls are known). Examples of interest include

i) The influence of alkali halide coatings on the channel walls (Koshida *et al.*, 1985)

ii) Etched silicon MCPs (Beetz *et al.*, 2000)

Proposed channel modifications can be appraised before costly experimental runs. The model also allows encoders to be matched to MCPs with an appropriate output charge cloud for maximum resolution. A third example, the addition of an electron lens to the microchannel output, that may be of benefit in high throughput electron beam lithography, is discussed below.

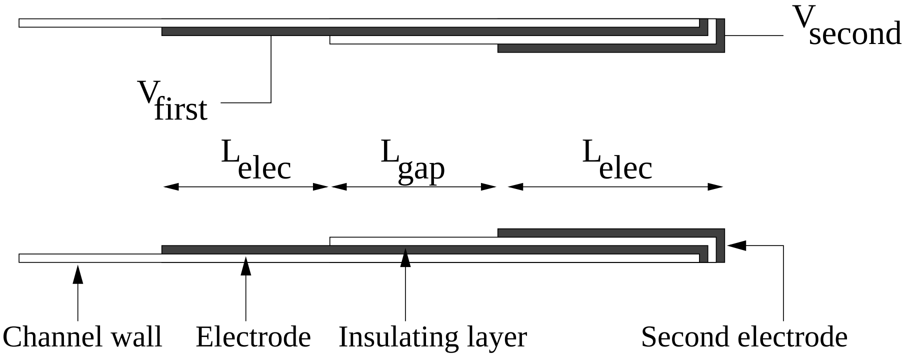

Figure 2.11: Channel exit lens (Floryan, 1996). A conducting electrode is evaporated onto the channel in the normal way to a depth of $2L_{elec} + L_{gap}$. An SiO_2 insulating over-layer of length $L_{elec} + L_{gap}$ is then deposited, and the finally a second electrode of length L_{elec}. The applied potentials are V_{first} and V_{second}.

2.5.1 Electron lens

The addition of micro-fabricated electrostatic lenses to the output of each channel on a microchannel plate has been suggested as a means of narrowing the ADOE (Floryan, 1996) for image intensifier applications. The lens structure is shown schematically in Figure 2.11. No experimental data is available.

Figure 2.12 shows the potential distribution, calculated using the method described in section 2.2.4 with the extra set of electrodes included, in such a lens system. Electrons initially parallel to the channel axis have been traced through the potential and weak focusing is indeed observed.

In this calculation the first and second electrodes were separated by 150V; it is not clear if it is possible to implement the electrode structure with such a large voltage across the insulating structure. Raytraces run with lower potential differences indicate a lack of focusing; for electrode potential differences of 70V or less, mild dispersion is observed.

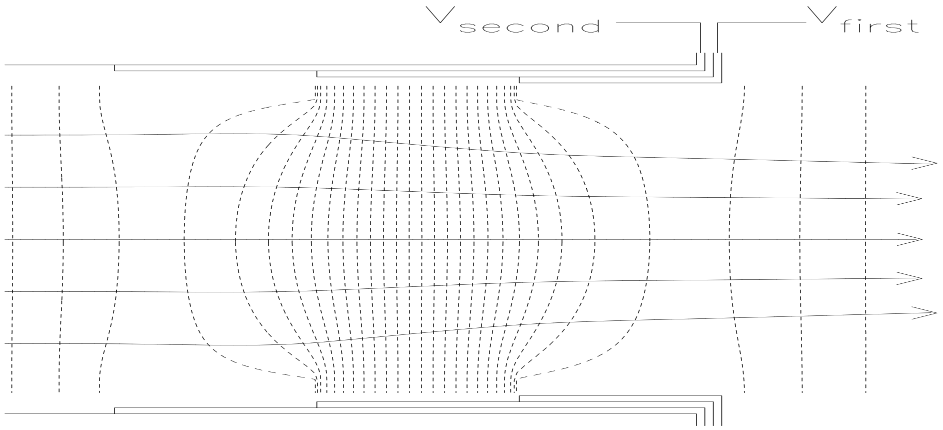

Figure 2.12: Equipotential map of an electrostatic lens mounted at a microchannel exit. The trajectories of electrons with velocities initially parallel to the channel axis are shown. Contours are $5.5V$ apart; $D = 12\mu m$; L/D=40:1; $L_{elec} = 12\mu m$; $L_{gap} = 12\mu m$; $V_{first} = -20V$ and $V_{second} = -170V$.

2.5.2 Results

The EDOE and ADOE resulting from avalanche calculations with the lens system in place are shown in Figure 2.13. The ADOEs show there is, unfortunately, no discernible focusing effect from the lenses. The EDOEs exhibit a suppressed intermediate-energy region relating to the electrode gap, with electron emission seen from the constant potential regions of both the lens electrodes.

Although it seems that the micromachined electrostatic lenses will not offer any benefits, the power of the Monte Carlo model described above in evaluating new structures has been demonstrated.

2.6 Conclusions

A two dimensional model of a single microchannel amplifier has been developed, including current saturation mode. The energy and angular distributions of electrons in the output charge cloud have been calculated and these agree well with experimental evidence.

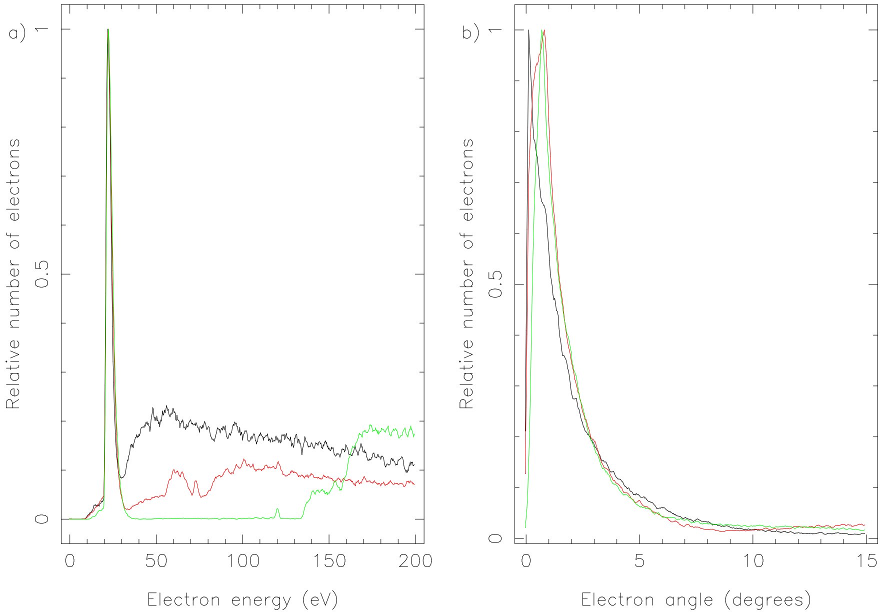

Figure 2.13: EDOEs (a) and ADOEs (b) for a 12μm, 40:1 channel with and without an electron lens. The black represents a normal channel (h/D=0.9, $V_o = 1000$V). The red and green lines correspond to channels with an electron lens ($L_{elec} = 12\mu$m; $L_{gap} = 12\mu$m; $V_{first} = -20$V) and $V_{second} = -90$V and -170V respectively.

The important influence of electrode endspoiling on the EDOE and ADOE of a microchannel has been confirmed. Otherwise the distributions are rather robust; that is, largely independent of channel parameters.

Chapter 3

Test facilities

3.1 Introduction

As the remainder of this thesis is concerned with the development of micropore optics, it is necessary to introduce the facilities used in their evaluation. First, the hardware used to test the optics - detectors, vacuum test systems and X-ray sources will be described. The software developed to calculate the MPO responses, a rigorous Monte Carlo raytrace model, will then be detailed.

3.2 Vacuum test systems

There are two vacuum test systems dedicated to the testing of micropore optics at Leicester University, both of which have recently undergone major upgrades. These are the Vacuum Test Facility (VTF) and the Long Beamline (known as the TTF or Tunnel Test Facility because of its location - a tunnel beneath the Leicester University Physics department).

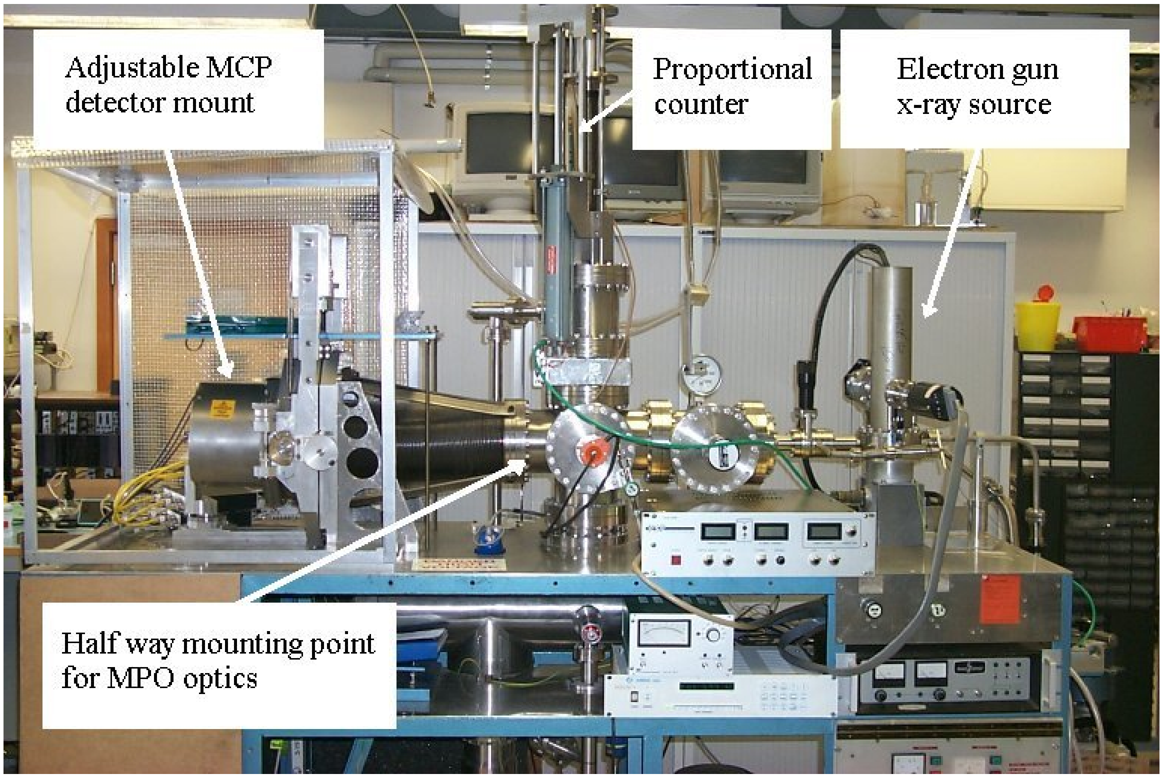

Figure 3.1: The Vacuum Test Facility (VTF) based in the MCP research laboratory at the Space Research Centre (SRC), Leicester.

3.2.1 The Vacuum Test Facility

The VTF is located in the MCP research laboratory of the Space Research Centre (SRC) at Leicester University. The system was first constructed in the summer of 1981 in order to test rapidly developing MCP multipliers (Pearson, 1984). It has since been involved in many important milestones in the development of MCPs and MPOs, including the development of low noise detector glass (Fraser *et al.*, 1987, 1988) and the first observation of square-pore, square-packed MPO cruxiform image structure (Fraser *et al.*, 1993b). The VTF is shown in Figures 3.1 (photograph) and 3.2 (dimensioned sketch).

Composed mainly of stainless steel vacuum sections with copper gasket sealed conflat flanges, the VTF is capable of UHV operation ($< 1 \times 10^{-10}$mbar). However, even very soft ($\sim$ 100eV) X-rays have a transmission of almost unity in pressures as high as 1×10^{-3}mbar over the length (i.e. source-detector separation) of the VTF (1382mm). The main requirement for low pressure operation comes from the MCP detector, whose high

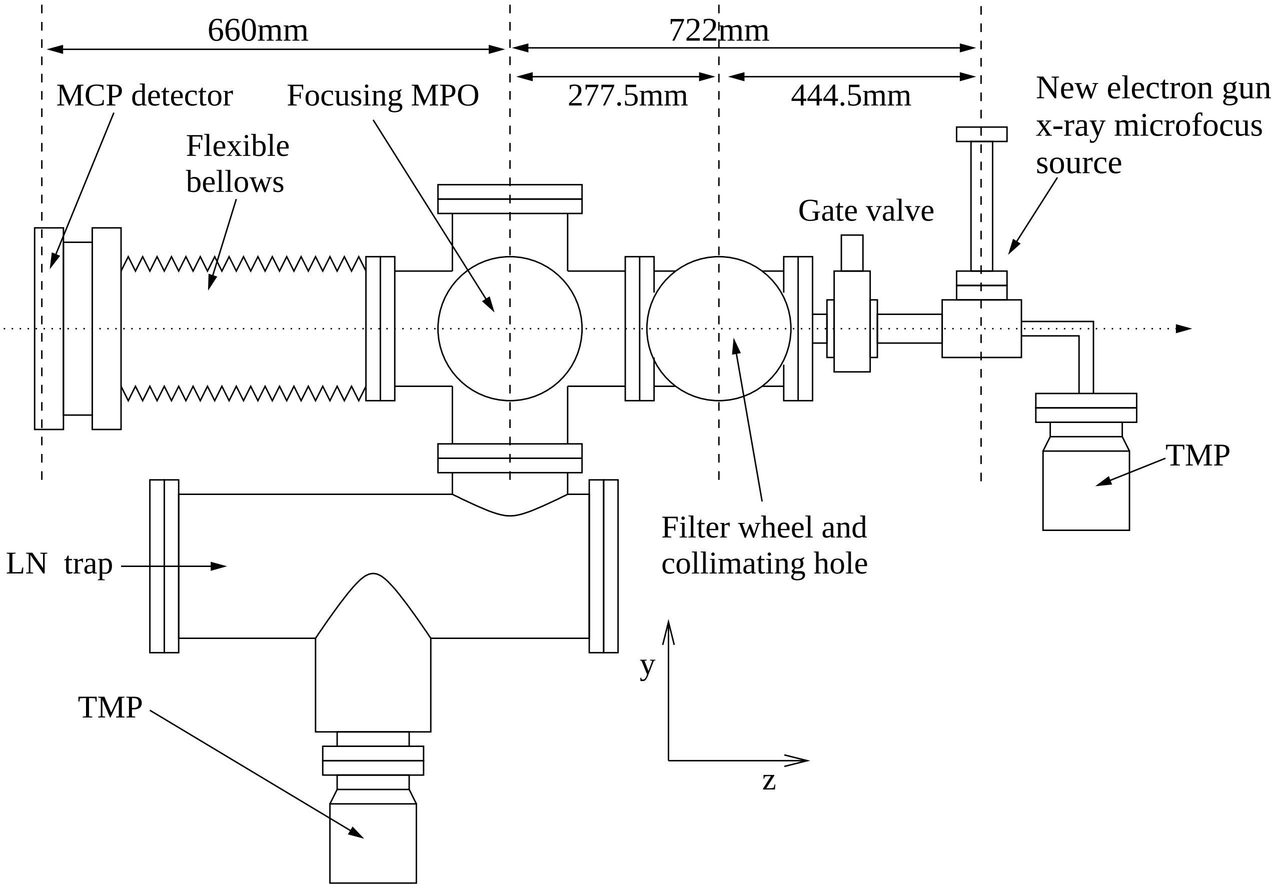

Figure 3.2: Diagram showing the important elements and dimensions of the VTF. The MPO holding jig can be driven 31mm towards the source along the optical axis so that flat MPOs can be used in point- to-point focusing mode ($L_S = L_I = 691$mm).

voltages and requirement for feedback-free operation set a pressure constraint $P \leq 5 \times 10^{-5}$mbar. The VTF main chamber is operated in the pressure range 1×10^{-7}mbar$\rightarrow$ 1×10^{-6}mbar. This is provided via a roughing-pump-backed Turbo Molecular Pump (TMP).

The filter wheel mounted between the source and MPO holding jig (section 3.4) allows up to four filters to be placed in the beam without having to break vacuum. A 1mm diameter collimating hole may be driven into the beam at the same location so that only a small area of the MPO or detector is illuminated. The detector mount at the opposite end of the system may be driven along the x and y axes (keeping the convention that the optical axis is the z-axis) by ±50mm and tilted around the (horizontal) x-axis by $\pm 10^{\circ}$.

X-rays were provided, up to the start of 2001, by a Leicester-built electron bombardment source. Here thermionically emitted electrons are accelerated through a ground plane onto a copper anode. A variable voltage of up to 5000V can be applied to the anode with an emission stabilised filament current. A 15° take-off angle on the anode coupled with a 1.1mm diameter collimating hole provided a source size calculated to be $5.4'$ (hole diameter/MPO-source distance) visible to all of a large format (54mm×54mm) MPO at the centre point. Combinations of different anode voltages and filters (mounted between the source and MPO) provide different X-ray energy bands. Pearson (1984) and Brunton (1994) give a more thorough treatment of this old arrangement.

The problem with this X-ray source, for the purposes of this thesis, was that the quality of the micropore optics being tested were improving to the point at which the source size was becoming the limiting factor in the determination of their angular resolution. If a smaller collimating hole is introduced in front of the electron spot on the anode, the angular size of the source is decreased, but large ($>$ 20mm diameter) MPOs are no longer fully uniformly illuminated. Work was undertaken to increase the electron spot size on the anode through manipulating the ground plane electric field, but this proved futile. To this end it was decided that an upgrade of the VTF X-ray source was required.

Beam energy	0eV→ 5000eV
Beam current	10nA→ 30μA
Minimum spot size	$<$ 25μm diameter @ 1μA
	$<$ 100μm diameter @ 30μA

Table 3.1: Parameters of the ELS-5000 electron beam gun acquired from PSP Vacuum Technology Ltd. for the microfocus X-ray source upgrade to the VTF.

Microfocus X-ray source

The method of X-ray production in a microfocus X-ray source is identical to that in a conventional electron bombardment source, i.e. a bremsstrahlung continuum dependent on the electron impact energy plus characteristic X-ray line emission from the anode. The difference is that instead of free electrons being attracted towards the HT anode, an electron gun is used to shoot highly focused electrons onto an earthed target. X-rays will only be generated in the electron impact area and hence with sufficient focusing, an extremely small X-ray source that emits into 2πsr (and will thus uniformly illuminate all of the MPO) can be provided.

In order to realise this improvement within budgetary constraints, it was decided that rather than purchase an off-the-shelf microfocus source, we would acquire an electron gun and modify the current source chamber to suit. The electron gun (an ELS-5000) was purchased from PSP Vacuum Technology Ltd. of Macclesfield. The gun parameters are given in Table 3.1. It should be noted that the gun is manufactured in such a way that focusing voltages scale with the kinetic energy of the beam making the parameters energy independent.

The main engineering problem in fitting the electron gun was that it was designed with surface science applications in mind, and hence has to be run in UHV conditions. The VTF source chamber is separated from the main chamber by a 2μm polycarbonate (Lexan) window with 0.4μm aluminium evaporated onto it to prevent charging. The window will hold a large pressure differential, enabling UHV conditions to be held in the source chamber without having to worry about the main chamber. The addition of a gate valve allows either side to be vented independently. As well as requiring UHV conditions (involving a 24 hour bakeout), the electron gun also outgasses strongly when in operation (due to electron bombardment of gun elements and surfaces), creating the need for a high pumping speed.

This need was originally catered for by the ion pump attached to the old source chamber which, while rather slow, could produce a vacuum $\sim 1 \times 10^{-9}$mbar. The requirements were further complicated, however, when the ELS-5000 beam was switched on for the first time and no X-rays resulted - it transpired that the large magnetic field of the ion pump's magnets were bending the electron beam to such an extent that it was no longer incident on the anode.

After several rethinks, the configuration eventually settled on was another roughing pump backed TMP with a pumping speed (after connections have been taken into account) of approximately $50\ell\mathrm{s}^{-1}$. With a suitable bakeout this gives an ultimate vacuum of $\sim 1 \times 10^{-9}$mbar and an operating vacuum (with electron gun on) of $\sim 5 \times 10^{-8}$mbar.

The electron gun turned out to be very sensitive to magnetic fields, requiring the removal of all possible sources from its immediate vicinity (TMP controller, Penning gauges, even the mild steel frame that supports the VTF) and the addition of a mu-metal sheath over the gun (the sheath can be seen in Figure 3.1 covering the gun). The stainless steel making up the source chamber is, unfortunately, itself magnetic so that although the sensitive region where the electrons are accelerated is protected by the mu-metal, the source's ultimate performance is degraded. The addition of a new, high permeability, stainless steel chamber is hoped to improve the resolution considerably. Simple pinhole camera analysis of the source spot gives an angular source size at the MPO of $< 1.0'$ FWHM, a factor of 5 better than the old source with full face illumination possible and plenty of flux available. The camera measurements were made with a 100μm diameter hole 40mm from the source spot. An ellipse 8.6mm$\times$4.5mm FWHM was observed on the detector, equating to a $150\mu\mathrm{m}\times 30\mu$m X-ray emitting spot at the anode. The anode was re-manufactured in copper with a 30° take-off angle to make the spot, as seen by the optic, less elliptical. With this taken into account, the focal spot is $150\mu\mathrm{m}\times 60\mu$m, the

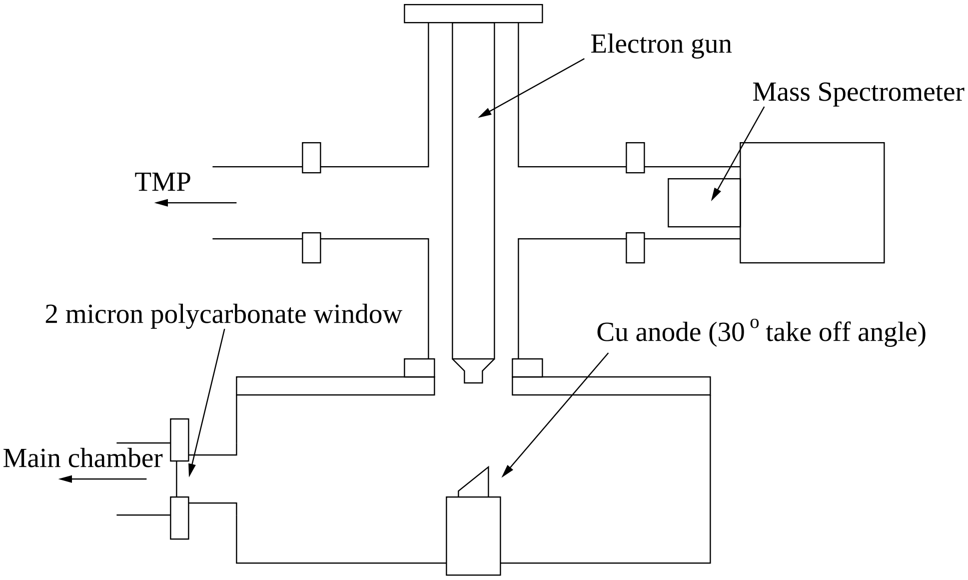

Figure 3.3: The microfocus X-ray source attached to the VTF.

anisotropy a result of the magnetic fields in the source chamber. Figure 3.3 shows the microfocus source chamber.

The calculated X-ray spectrum (section 3.6.2) of the electron gun source with the most commonly used settings (2kV accelerating voltage with a 4μm aluminium filter in addition to the Lexan source window (Figure 3.3)) is shown in Figure 3.15.

3.2.2 The Long Beamline Facility

The Tunnel Test Facility (TTF) is a 20m long beamline dating back to the early 1970s when it was used for Ariel-V and VI collimated proportional counter detector testing. There have since been several major modifications including the addition of a large test chamber, 1.5m long by 1.25m diameter, to test the EXOSAT medium energy detector array (MEDA) in the late 1970s (Turner and Smith, 1981).

The TTF is currently configured for use as a high energy, high angular resolution test facility for micropore optics. Using several ports along the beamline, both planar and slumped MPOs may be tested, short focal length optics ($R_{slump} \leq 1$m) being accommodated in the tank. The tank and beamline are pumped by a single large liquid helium cryo-pump yielding an ultimate vacuum of $\sim 1 \times 10^{-6}$mbar. The source chamber may be isolated from the beamline via a gate valve and is pumped independently by a roughing-pump-backed TMP (limiting pressure - as for VTF main chamber $\sim 1 \times 10^{-7}$mbar).

One of the ESA TRP aims is to use large aspect ratio channels (L/D >500:1) to provide efficient X-ray focusing at hard ($>$ 50keV) X-ray energies. To enable testing at such energies a Philips PW-2184/00 (100kV/3kW) X-ray tube was fitted within a modified source chamber. In order to provide a safe radiation environment with such a powerful source the 20m high-vacuum stainless steel beamline was plated with $\sim$ 5mm of lead and the beam divergence limited with the use of baffles at the exit of the source chamber and midway between the source and central optic mounting port. The source chamber itself was surrounded with a lead lined ($>$ 1cm thick) enclosure and the large access flange of the tank coated with thick lead (again $\sim$ 1cm thick) where necessary. The result is a 20m beamline that can be safely operated at 100kV/3kW (i.e. with leakage count rates undetectable above background). Figure 3.4 shows photographs of the source chamber, beamline and tank. Figure 3.5 is a dimensioned sketch of the TTF.

The X-ray camera is mounted on a movable carriage that allows it to be driven 800mm forwards (along the z-axis) from the main chamber flange. This equates to approximately 400mm either side of the 10m point from the central MPO mounting port. This flexibility not only allows the best focus of MPOs to be found, it also makes the test chamber accessible to a larger variety of slump radii plates.

TTF X-ray source

Using different filter and source energy combinations, it is possible to produce a variety of X-ray energy bands. A low energy (5kV) copper anode electron bombardment X-ray tube (similar to the old VTF source, built in house) can be interchanged with the 100kV/3kW tungsten anode high energy source. Table 3.2 lists the commonly used filter and energy combinations.

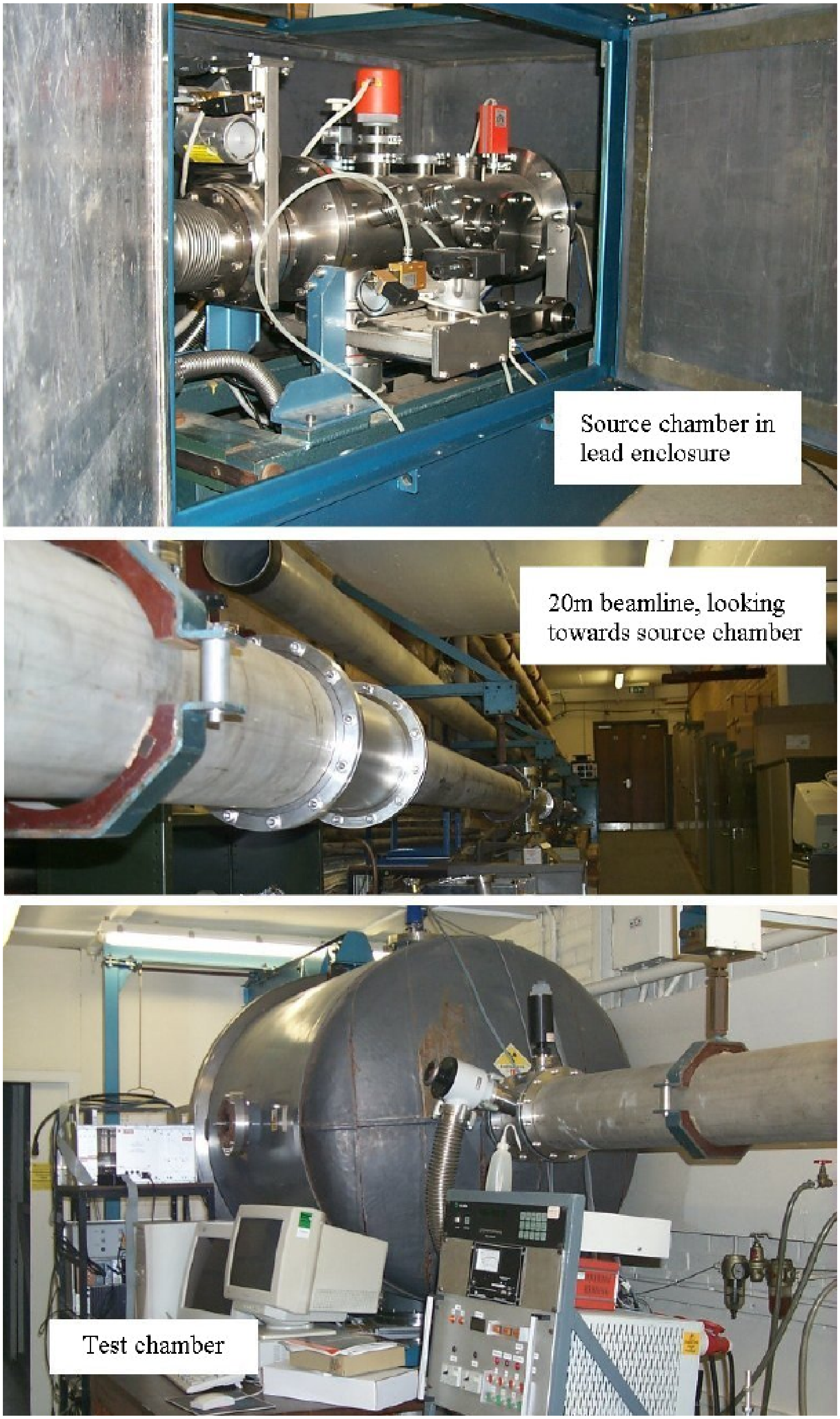

Figure 3.4: The Tunnel Test Facility (TTF) high energy long beamline located in the Leicester University Physics building basement.

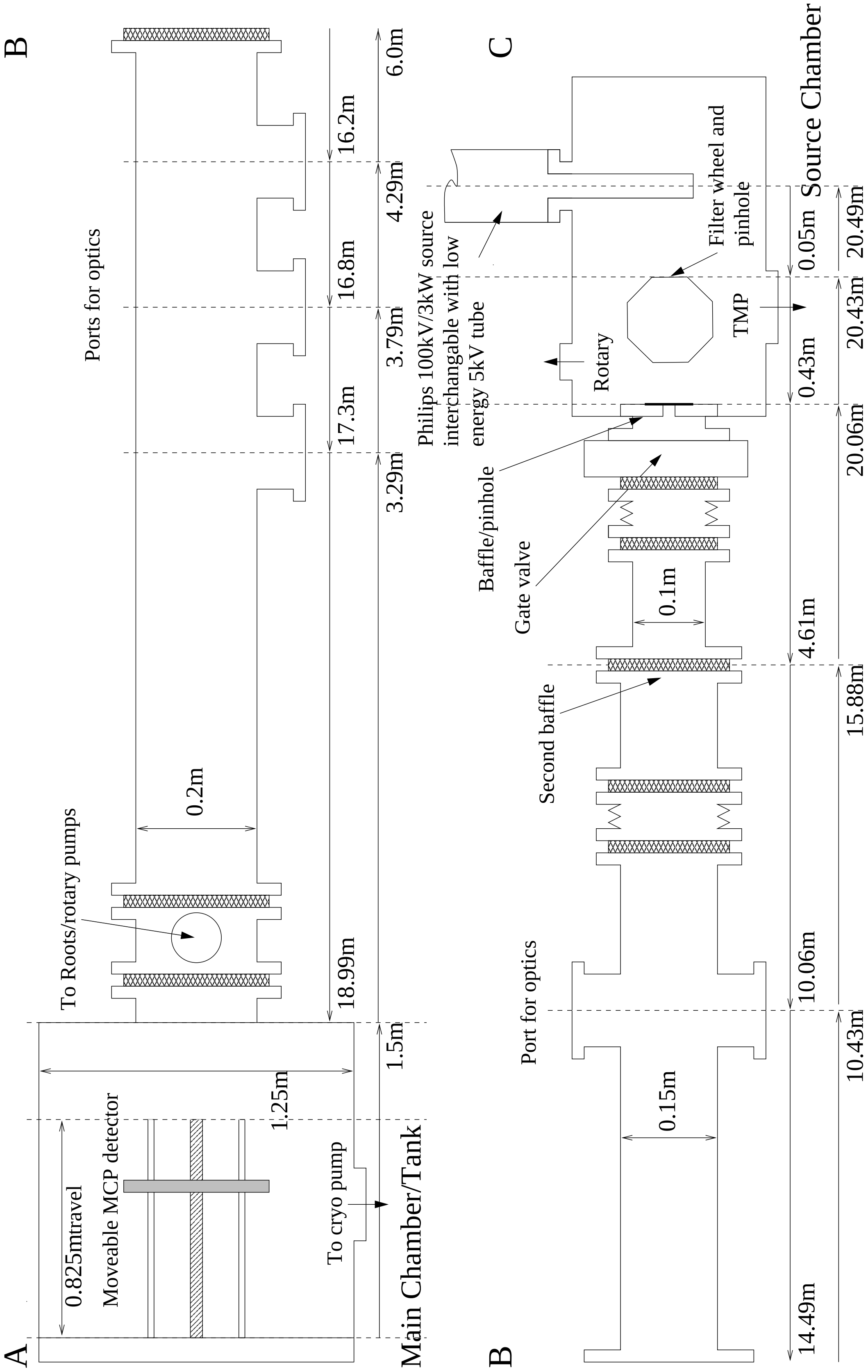

Figure 3.5: Diagram showing the important elements and dimensions of the TTF. The total length (AC) is 20.49m.

X-ray tube	Accelerating Voltage	Filter
Low energy source	5kV	4μm polycarbonate
		0.4μm aluminium
Philips PW-2184/00	20kV	100μm copper
	25kV	200μm molybdenum
	45kV	500μm tin
	80kV	500μm tantalum

Table 3.2: Commonly used X-ray tube voltage and filter combinations in the TTF.

Source collimation is provided via a 1mm diameter pinhole attached to each filter. This provides a calculated $20''$ source (seen at the central MPO mounting port) that fully illuminates the largest format MPOs currently available ($\sim$ 60mm diameter). As the source is so far from the MPOs, X-rays are incident upon channel walls at much lower grazing angles than in the VTF, as required for their operation at high energy. The pinholes are drilled through 1mm thick stainless steel sheets in all cases except for the highest (Ta filter) energy setting. Here a 1mm thick sheet of silver is required to provide the necessary attenuation for 60keV→ 80keV X-rays.

A Cadmium Zinc Telluride (CZT) single pixel X-ray spectrometer (Bale, 2001) was used to measure the spectral output at each source setting in Table 3.2. These results are presented in section 3.6.2 where they are compared with calculated X-ray spectra.

3.3 Microchannel plate X-ray camera

The same X-ray camera, a large area microchannel plate detector with resistive anode readout, is used to record the focal plane intensity distributions in both vacuum systems. The 100mm×100mm format MCPs were originally developed for the AXAF (now Chandra) High Resolution Camera (HRC) programme (Zombeck *et al.*, 1995a) and are now finding non-astronomical applications in areas such as medical and biological imaging (Lees and Pearson, 1996). The plates have 120:1 12.5μm diameter circular channels on a 15μm pitch with a 6° bias angle and are manufactured in low-noise glass. Two identical plates are mounted in a chevron configuration and the output encoded through charge division from a resistive anode. The active area of the detector, limited by the rear electrode, is 93mm$\times$93mm.

The charge deposited on the resistive anode from an event is read out by four charge sensitive pre-amps attached to its corners. The signals are then fed into an 11-bit Analogue to Digital Converter (ADC), via filter amplifiers, for digitisation and recording on an Acorn Archimedes computer. The resistive anode method of collecting the charge output leads to read-out distortion (Fraser and Mathieson, 1981). A linearization table is created from an image of precisely known points (using a mask of 100μm holes in front of the detector) for each set-up, as slightly varying the electronic settings can alter the exact read-out errors. Events are then repositioned according to this table, hence removing the distortion (Barstow and Samsom, 1990).

The ADC provides a theoretical resolution of 75μm over the diagonal length of the resistive sheet ($\sqrt{2} \times$ 110mm), although in practice this is only achieved near the centre of the detector. Charge saturation in the pre-amps degrades performance in events occurring close to the edge of the resistive anode to several hundred microns. The data we are interested in (the central foci of micropore optics) will always be recorded at the centre of the detector and hence will still be at high resolution.

A new set of Photonis HRC specification channel plates, were fitted to the camera in August 2000. The quantum efficiency of the old plates had become degraded through prolonged operation so that it varied significantly from channel to channel (known as the "chicken wire effect" (Barstow *et al.*, 1990; Pearson *et al.*, 2000)) making the recorded images unreliable.

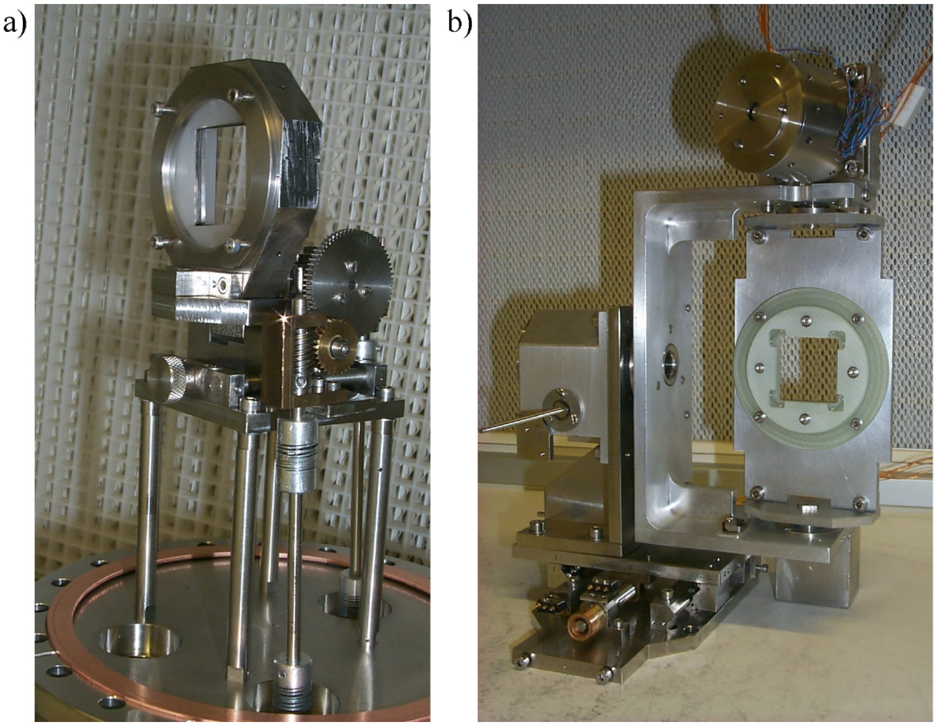

Figure 3.6: The beamline port (a) and tank test chamber (b) MPO holding jigs. The jigs support MPOs in the X-ray beam and allow manipulation about two orthogonal axes. The beamline jig is manipulated manually via vacuum sealed rotary drives, the tank jig via computer controlled stepper motors.

3.4 MPO holding jigs

Micropore optics are mounted in the two systems via the MPO holding jigs. There are two jigs, one that fits a standard 8inch conflat port (mid-point on the VTF and all beamline ports on the TTF) and one that is mounted in the tank test chamber of the TTF. Figure 3.6 shows photographs of the two jigs.

The MPOs are secured in the jig heads with PCTFE (Poly-Chloro-Tetra-Fluoro-Ethylene) spacers and stainless steel springs. Care is taken to ensure that bolts are only nipped shut so as not to place any stress on the MPO that may distort it. The tank jig (figure 3.6(b)) is only used for slumped optics. Consequently, the MPO is mounted between concave and convex spacers of the correct radius of curvature.

The MPOs can be manipulated about the x and y axes of the system. The beamline jig has a range of motion of +7°to −6° about the x-axis ($0.066 \pm 0.004°$ per turn on rotary drive) and ±9° about the y-axis ($0.44 \pm 0.03°$ per turn on rotary drive) (Brunton, 1994). The tank jig has a 360° range of motion about both axes with an accuracy limited by the gearing ratio on the stepper motors (400 steps per motor revolution with a 1/80 worm to wheel gear ratio gives $40''$ per step).

3.5 Quantitative measurement of MPO foci

In order to quantitatively analyse MPO responses, the focal resolution, effective area and gain can be measured. The focal resolution will be quoted as the Full Width at Half Maximum (FWHM) in this thesis unless otherwise stated. Calculating the Poissonian uncertainty in the number of peak channel counts ($\sqrt{N}$ where N is the number of counts) in a large image file ($\sim 1 \times 10^6$ counts) and propagating this through the FWHM calculations yields a statistically negligible error, hence FWHM measurements are quoted without errors.

In order to calculate the effective area of the MPO, the counts in the focus are divided by the intensity of counts on the MCP detector with no MPO present under otherwise identical conditions. Approximating the focal point spread function (PSF) as a Gaussian allows us to calculate the standard deviation ($\sigma = 0.424\mathrm{FWHM}$) of the distribution. Including all events occurring within a 3σ radius of the focal maximum gives a 99.7% confidence limit that all relevant counts have been included. Approximating as a Gaussian is not unreasonable if the tilt errors that inevitably broaden the focal PSF are assumed to come from a Gaussian distribution (this is true, at least, in the raytrace model described in section 3.6 below). Uncertainty is introduced to the measurement as a result of the Poissonian statistics that apply to such count-rate measurements and errors in accurately determining the X-ray source intensities.

The gain measurements quoted will be peak channel gains. The maximum number of counts per pixel in the focus is divided by the average number of counts per pixel with no

Vacuum system/source	Voltage	Current	Filter	Count rate
VTF/Microfocus	2kV	2.35A e^- beam	4μm Al	3500 ± 350cts/s
		2.45A e^- beam		11100 ± 1000cts/s
		2.55A e^- beam		15400 ± 1500cts/s
TTF/Low energy	2.5kV	1.5mA emission	Makrofol	22000 ± 500cts/s
TTF/	20kV	40mA emission	100μm Cu	1200 ± 40cts/s
Philips PW-2184/00	30kV	25mA emission	200μm Mo	1300 ± 50cts/s
	45kV	65mA emission	500μm Sn	7200 ± 150cts/s
	80kV	15mA emission	500μm Ta	72000 ± 1500cts/s

Table 3.3: Full illumination detector count rates with no MPO present. The settings shown are those relevant to experiments reported in this thesis. Count rates were found through illuminating a small area of the detector via a pinhole and scaling up the solid angle.

MPO present. Uncertainties arise as for the effective area measurements shown above.

The X-ray source intensities were determined through illuminating the MCP detector in the absence of an MPO. A pinhole was inserted in the beam to reduce the total count rate to one similar to that seen with an MPO (500cts/s→ 1000cts/s). If the full detector is illuminated at the source intensities used in MPO experiments, the electronics become saturated and a representative intensity is not recorded. Table 3.3 lists source settings and filter combinations relevant to this work with the measured intensities on the MCP detector (scaled up to full detector area).

The large uncertainties associated with the VTF microfocus source ($\sim 10\%$) arise as the electronic are not emission stabilised, an improvement that is planned. In addition, a reference X-ray diode calibrated to the MCP detector count rates, is to be installed in both systems. This should greatly improve the accuracy of effective area and gain measurements.

3.6 Raytrace model of micropore optics

The need to be able to model the expected performance and observed defects of the first generation of micropore optics led to a Monte Carlo raytrace simulation being developed by Brunton (1994; Brunton *et al.* 1997). This software package has been modified by the present author to allow the calculation of the properties of radially-packed and Wolter micropore optics and to extend its use to the hard X-ray region. These modifications are described below.

3.6.1 Basic model

X-rays in vacuo travel in straight lines, allowing the use of simple geometric identities to define a photon's path. Given a cartesian origin, **a**, and a unit vector direction, **b**, the path of a ray is described as

$$\boldsymbol{r} = \boldsymbol{a} + t\boldsymbol{b} \tag{3.1}$$

where t is a scalar. The co-ordinates are arranged so that the z-axis is along the optical axis with the origin at the centre of the MPO in the case of flat MPOs, and at the centre of curvature in the case of slumped MPOs. These co-ordinate systems are shown in Figure 3.7.

A ray is generated at the source within specified area and angular constraints and traced to the point of interception with the optic. Rays can be made to come from infinity by increasing the area of emission to the same as the MPO and setting the angular divergence to zero. To trace a ray to a flat plate we find the interception of the generated ray, $\boldsymbol{r}$,with the front of the optic (defined by the unit vector normal to that plane, $\hat{\mathbf{n}}$)

$$\boldsymbol{r}.\hat{\boldsymbol{n}} = \frac{L}{2} \tag{3.2}$$

where L is the channel length. In the case of slumped plates, the intersection of the ray with a sphere of the slump radius, R_{slump}, is calculated from

$$\boldsymbol{r}.\boldsymbol{r} = R_{slump}^2 \tag{3.3}$$

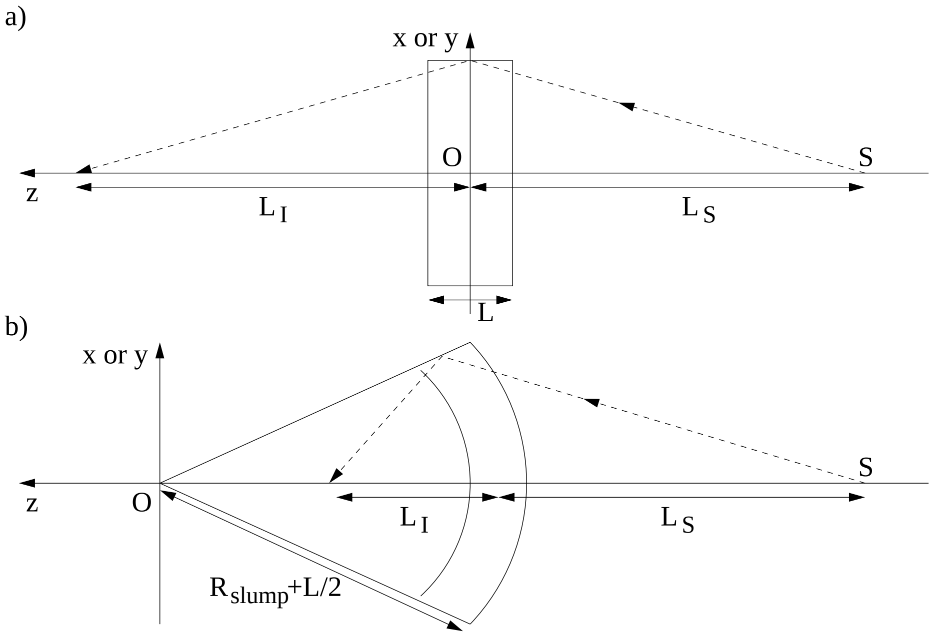

Figure 3.7: The co-ordinate systems used in the raytrace model in the (a) flat and (b) slumped plate cases. Point O is the origin, S the source position and L the MPO thickness. Typical ray paths are indicated by the broken lines.

Whether the incident ray has entered a channel or struck the inter-channel web is then determined from the specified MPO geometry (open area fraction, multifibre size, packing style). Rays that strike the web were, in the original model, considered absorbed. This is no longer the case as described in the next section. If a ray has entered a channel, its co-ordinates are recorded and the channel is transformed to the optical axis of the system. This is done to make the reflection subroutine universal and is achieved by translation (in the case of flat square-packed plates) and rotation about the origin (in the case of radially packed and slumped plates).

Once within a channel the ray undergoes a specular reflection from a channel wall to form a new ray characterised by $\boldsymbol{r} = \boldsymbol{c} + s\boldsymbol{d}$ where $\boldsymbol{c}$ is the point of reflection, $\boldsymbol{d}$ is calculated from the wall normal and incident direction and s is a scalar.

$$\boldsymbol{d} = 2\hat{\boldsymbol{n}} \cos\theta_{inc} + \boldsymbol{b} \tag{3.4}$$

θ_{inc} is the incident angle (as opposed to grazing angle) determined from $-\hat{\boldsymbol{n}}.\boldsymbol{b} = \cos\theta_{inc}$.

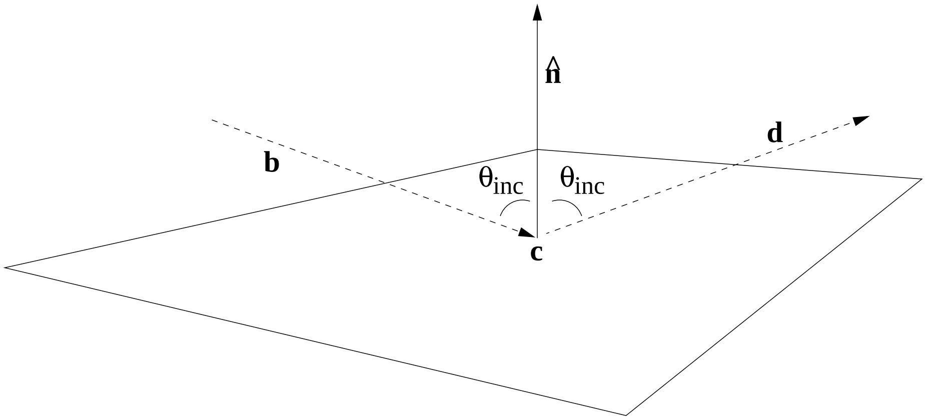

Figure 3.8: Specular reflection from a plane surface.

The wall normals are given by the standard unit vectors in the x and y axes, **i** and **j**. The ray is followed from reflection to reflection until it leaves the channel. Figure 3.8 shows the vector representation of a specular reflection from a plane surface.

Every-time a ray is incident on a channel wall, the probability of reflection taking place is calculated (see section 3.6.2 for details) and the Monte Carlo process decides if it occurs or not. Rays not reflected, as for those incident on the web, were considered to be absorbed in the original code.

Finally, when a ray emerges from a channel it is traced to the detector plane (the normal to the detector plane being the unit vector along the optical axis, **k**). When incident on the detector plane the event is binned in x and y co-ordinates as if for an 11 bit ADC in a detector the same size as that used experimentally (section 3.3). The images can then be quantitatively analysed using the same techniques as described for real images in section 3.5. As the exact number of rays to have struck the MPO in the model is well known, the error in effective area and gain calculations is insignificant. Raytrace model results are thus quoted with no errors.

3.6.2 Modifications to original model

The advent of radially-packed micropore optics and microchannel Wolter optics for use at X-ray energies up to 100keV, not available when the original code was written, motivated changes to the model. The major modifications are:

i) The extension of the model to incorporate new multifibre packing geometries.

ii) The inclusion of transmission through the inter-channel glass septa.

iii) A more advanced multi-layer reflection algorithm.

iv) New input spectrum files (both calculated and measured) to accurately represent the test systems' X-ray sources.

Geometric modification

In order to calculate whether a ray has entered a channel or hit the channel web, the multifibre distribution over the MPO surface and the channel distribution within each multifibre are required.

First, the specific multifibre is determined. In the case of a square-pore, square-packed optic this is as simple as sorting the incident x and y co-ordinates into bins of the correct size (Np where $N \times N$ is the number of channels in a multifibre and p is the channel pitch). The process is more complicated in the slumped case as the multifibre boundaries follow great arcs of radius R_{slump} centred on the origin instead of straight lines, but is still easily solved.

In the case of radially-packed plates, the multifibre is defined by the ring number from the centre of the optic and the azimuth angle from the x-axis about the optical (z) axis. In this case, because the packing of the multifibres is imperfect, there will also be occasions when the ray will strike an area between multifibres (Figure 3.9). As in the square-packed case, slumping the optic changes the multifibre boundaries from straight lines to great arcs. Both of these problems can be solved with the careful use of logic in the computer code.

As all TRP multifibres are the same (55×55 bundles of 10μm side length square-pore,

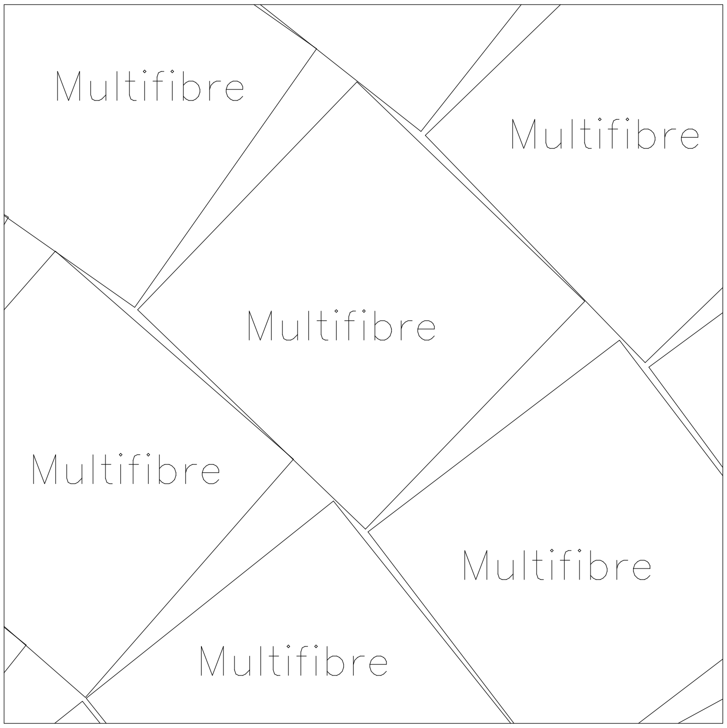

Figure 3.9: Spaces between adjacent square multifibres packed about a circular core. These are either voids or filled with glass in real-life MPOs manufactured by Photonis SAS.

square-packed channels) finding the channel a ray has entered within a multifibre is trivial. The multifibre is split into bins of side p and thus the channel cell that the ray falls in is calculated in the same manner as for flat and slumped square-packed optics. If the ray has an x or y co-ordinate that falls in the range $\frac{|D|}{2} \rightarrow \frac{|p|}{2}$ then it is considered to have struck the channel web, where D is the channel side length.

To model the twin MPO microchannel Wolter optics (chapters 5 and 6) the same code, with the correct radius of curvature passed to it as an argument, can be used for each MPO in the pair.

Transmission of X-rays

If a ray intersected the inter-multifibre area or the channel web within a multifibre it was considered absorbed in the old model. For X-ray energies less than 5keV this is a fair assumption as even a few microns of lead silicate glass will be essentially opaque. The extension of the model to include spectra generated by the high energy Philips source (photon energies up to 100keV), however, should obviously include transmission (the probability of transmission through the inter-channel septa approaches unity at such energies).

In the modified code, any ray that is incident upon the channel/multifibre web or isn't reflected within a channel is traced through the channel matrix until it either emerges into a channel or reaches the back of the plate. The distance of this path is calculated and another Monte Carlo calculation determines whether the ray is transmitted or absorbed.

The probability of transmission is calculated from the dielectric constant of the bulk channel plate glass (considered to be $Si_6O_{17}KPb_2$ at a density of 4gcm^{-3}; Willingale *et al.* 1998; Martin 2000). From Henke (1981) we see that the linear absorption co-efficient, μ_{ab} can be written in terms of the complex refractive index, $n = 1 - \delta - i\beta$

$$\mu_{ab} = \frac{4\pi\beta}{\lambda} \tag{3.5}$$

where λ is the X-ray wavelength. When the index decrements δ and β are small compared with unity, as is the case for X-rays in the bandgap we are concerned with, the dielectric constant, $\kappa = 1 - \alpha - i\gamma$, is related to the refractive index by the simple relations $\delta = \frac{\alpha}{2}$ and $\beta = \frac{\gamma}{2}$. This allows the linear absorption (in μm^{-1}) to be written in terms of energy, E, (in keV) and the complex components of the dielectric constant as

$$\mu_{ab} = \frac{2\pi\gamma E}{1.24 \times 10^{-3}} \tag{3.6}$$

The probability of transmission for lead glass of thickness t is then calculated from the well known absorption formula (Beer's law)

$$\frac{I}{I_o} = e^{-\mu_{ab}t} \tag{3.7}$$

The complex constants are calculated using a computer program Xopt (Willingale, 1994), from theoretically calculated atomic scattering cross-sections of electron orbitals (Cromer and Liberman, 1970).

A ray that is transmitted continues as any other ray until it is incident upon a channel wall where it may be either reflected, transmitted or absorbed, or until it reaches the detector plane.

It has recently become clear that it is not realistic to use a simple single layer reflectivity model with low surface roughness micropore optics (Brunton *et al.*, 1999; Martin, 2000), as can be seen in Figure 3.10. It has been found that during the etching of the core glass from channel plates, a lead free region of silicon dioxide is formed next to the channel surface. Many authors agree that this layer is 100Å→ 500Å thick (Hill, 1976; Siddiqui, 1977; Praček and Kern, 1993). Interference is observed between reflections from the SiO_2 vacuum surface and the interface between the silica and lead glass, leading to the Kiessig fringes (Kiessig, 1931) seen in Figure 3.10. Brunton *et al.* (1999) have produced a very good fit to experimental data using a 359Å SiO_2 layer with an rms surface roughness of 11.3Å on top of the bulk channel plate glass with an interface roughness of 25.5Å rms (Figure 3.11).

To include this physical complexity in the raytrace model, the reflection algorithm used by Brunton *el al.* to fit the data of Figure 3.11 was imported. This comes from the computer program Rex (Crabb *et al.*, 1993) which in turn uses the multi-layer reflectivity formulae of Parratt (1954). For plane parallel interfaces between homogeneous layers, $(n-1, n, n+1)$ the reflectivity coefficient is

$$R_{n-1,n} = a_{n-1}^4 \left(\frac{R_{n,n+1} + F_{n-1,n}}{R_{n,n+1} F_{n-1,n} + 1} \right) \tag{3.8}$$

where

$$F_{n-1,n} = \frac{f_{n-1} - f_n}{f_{n-1} + f_n} \tag{3.9}$$

and

$$f_n = (\phi^2 - 2\alpha_n - 2i\gamma_n)^{1/2} \tag{3.10}$$

Here α and γ are the real and imaginary dielectric constant index decrements, calculated as in the case of transmission, by the computer program Xopt. ϕ is the grazing angle. The quantity a_n is the amplitude reduction factor defined as

$$a_n = \exp\left(-i \frac{\pi f_n d_n}{\lambda} \right) \tag{3.11}$$

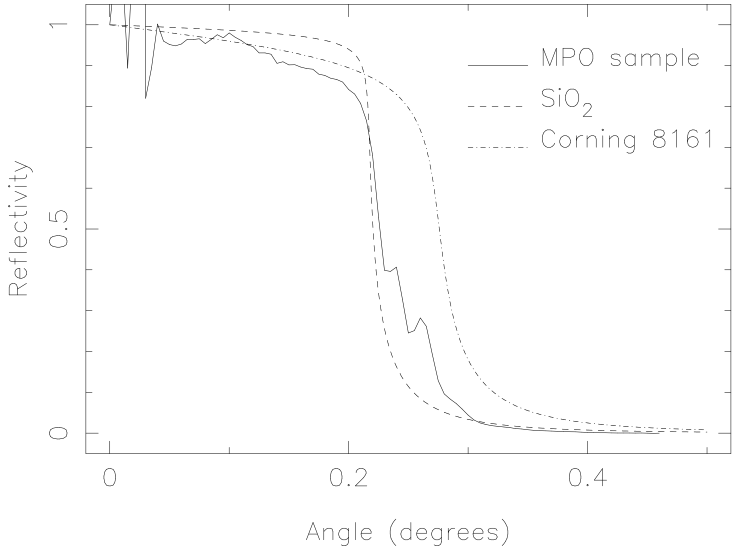

Figure 3.10: Theoretical reflectivity verses grazing angle curves of silicon dioxide and Corning 8161 channel plate glass compared with a measured reflectivity curve of an actual MPO at 8keV. The Kiessig fringes resulting from multi-layer reflections can be seen in the experimental data (Martin, 2000).

where d_n is the thickness of layer n. Surface roughness is accounted for using the scalar theory of Beckmann and Spizzichino (1963). Here the Fresnel coefficient is modified by a Debye-Waller factor to give

$$F'_{n-1,n} = F_{n-1,n} \exp -\frac{1}{2}\left(\frac{4\pi\sigma\sin(\phi)}{\lambda}\right)^2 \tag{3.12}$$

where σ is the rms surface roughness and λ the X-ray wavelength (both in Å). The perturbation from the specular direction is randomly selected from a Gaussian distribution with an rms magnitude (in radians) of

$$\psi_{scatter} = \frac{\lambda}{\tau\sin(\phi)} \tag{3.13}$$

where τ is the correlation length of the surface roughness (treating the roughness as a sinusoidal variation in height) (Church *et al.*, 1978).

Input spectra

In the original version of the raytracing code only a single input X-ray energy was specified. This code was then altered to be able to include 100 point normalised source spectra files.

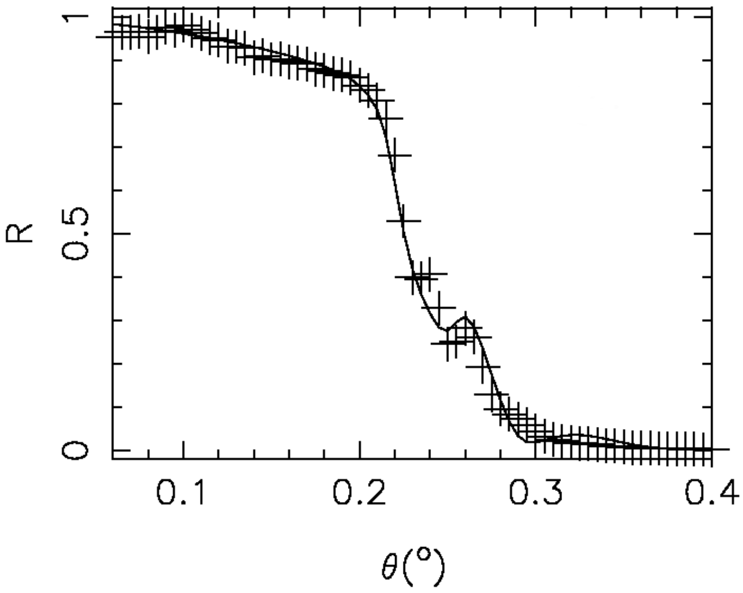

Figure 3.11: Experimental reflectivity measurements and the calculated fit (solid line) as a function of grazing angle. The data was taken at 8keV for Nova Scientific MPOs manufactured in Corning 8161 glass and hydrogen reduced so that a layer of SiO_2 is formed at the surface. The fit is produced using the parameters described in the text. From Brunton *et al.* (1999).

Much recent work, however, has been dedicated to both measuring and calculating input spectra for the VTF and TTF sources.

CZT measurements of TTF source

A single pixel Cadmium Zinc Telluride detector was mounted in the TTF in place of the MCP detector. The CZT detector, a 5mm×5mm×2mm three stage peltier cooled (-40°C) crystal, is described in detail by Bale (2001) and references therein. The CZT detector has a quantum efficiency of $\sim$ 100% at energies in the range 10keV$\rightarrow$ 100keV, becoming slightly suppressed below 10keV. The electronic component of the energy resolution is $\sim$ 400eV FWHM, measured using a pulsar when operating in the TTF environment.

Figure 3.12 shows the normalised intensity plot recorded for each of the Philips source settings shown in Table 3.2. An unfiltered 60keV spectrum is also shown in Figure 3.13(a). It should be noted that these spectra contain detector artefacts. Not only will the lines

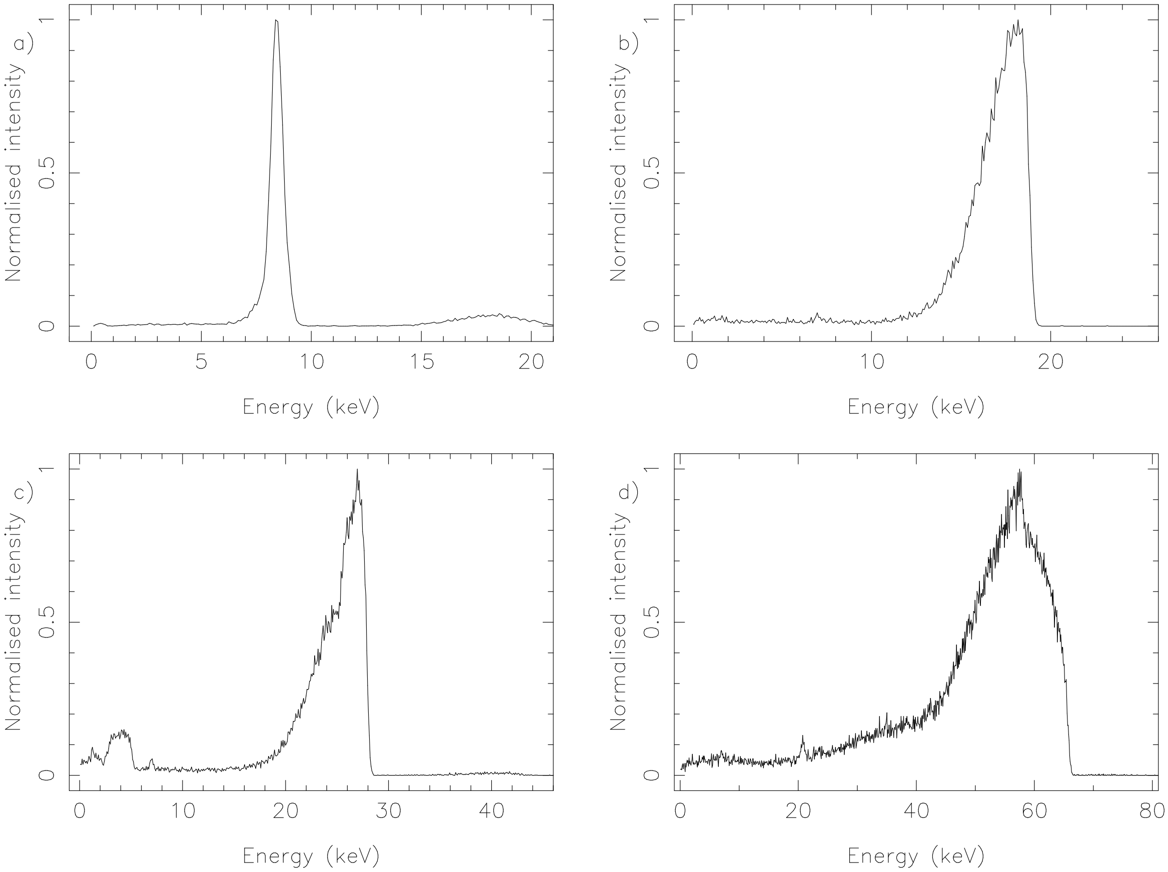

Figure 3.12: TTF source spectra recorded with a CZT detector for anode voltage/filter combinations of (*a*) 20kV and 100μm Cu, (*b*) 25kV and 200μm Mo, (*c*) 45kV and 500μm Sn and (*d*) 80kV with 500μm Ta.

be broadened by noise, but absorption edges and fluorescent escape peaks associated with the detector materials are observed. This is most clearly seen in Figure 3.12(*c*), where the Cd-K edge can be seen at 26.7keV with the corresponding Cd-K_α and Cd-K_β escape peaks at 3.5keV to 6.0keV and 0.6keV to 3.1keV respectively.

Calculation of source spectra

An X-ray source spectrum may be altered by changing the accelerating voltage, anode composition/take-off angle and filter material/thickness. It would be impractical to re-measure the spectrum each time a change is made in any of these parameters. Spectra measured (say) with a CZT diode are also not exact measurements of the source spectra; to obtain 'true' MPO input spectra, a detailed model of the detector would have to be

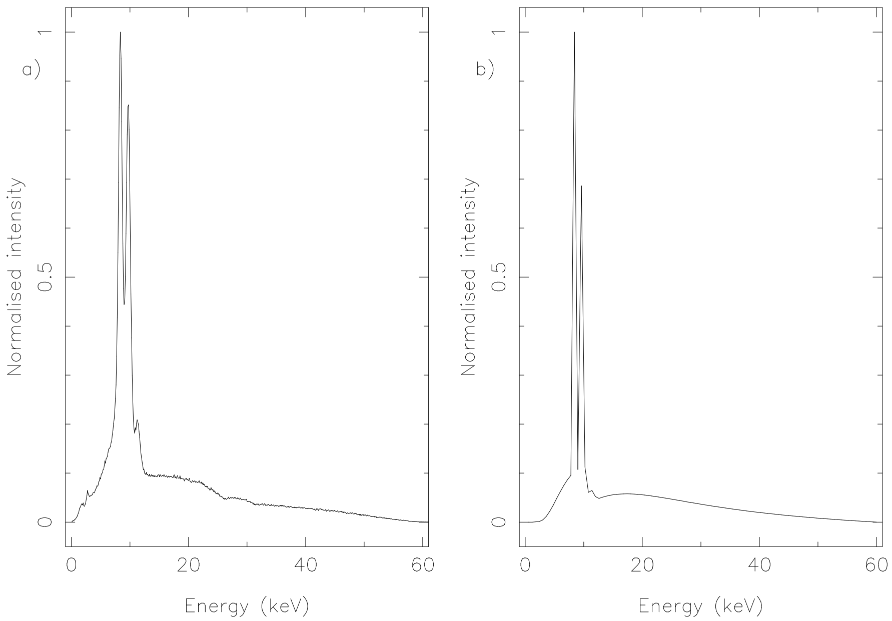

Figure 3.13: **Measured (a) and calculated (b) unfiltered TTF source spectra at 60kV. Detector resolution not included in calculation.**

built up to calculate artefacts accurately so that they could be removed (Bale, 2001).

An accurate *ab initio* model of an electron bombardment X-ray source is thus highly valuable. To this end the model of Pella *et al.* (1985) was adopted, where the bremsstrahlung emission from, and self absorption in, the target can be expressed (in units of photons/electron/sr/keV) as

$$N_{cont}(E) = \frac{K_e Z}{4\pi}\left(\frac{E_o}{E}-1\right)\left[\left(1+a\left(E_o^{1.65}-E^{1.65}\right)\right)\mu_t\frac{1}{sin\psi}\right]^{-2} \qquad (3.14)$$

where E is the photon energy, E_o is the electron bombardment energy, Z is the atomic number of the target, μ_t is the mass absorption co-efficient of the target, ψ is the target take-off angle and $K_e = 2.76 \times 10^{-6}$ and $a = 1.2 \times 10^{-6}$ are constants.

The line-to-continuum ratios can be calculated at the line wavelengths using the empirical formula

$$\frac{N_{line}(\lambda)}{N_{cont}(\lambda)} = \exp\left(-0.5\left(\frac{U_o-1}{1.17U_o+3.2}\right)^2\right)\left(\frac{a}{b+Z^4}+d\right)\left(\frac{U_o\ln\left(U_o\right)}{U_o-1}-1\right) \qquad (3.15)$$

where a, b and d are a set of constants that change depending upon the particular line. Values for the K and L series are contained in the previously mentioned reference (Pella *et al.*, 1985), those for the M series in a later paper (Pella *et al.*, 1991). U_o is the "overvoltage", defined as the ratio of the electron bombardment energy to the line energy.

The ratio in equation (3.15) has the units of Ångstroms, the line intensity being an absolute measurement (photons/electron/sr) with the continuum intensity being an integral (photons/electron/s/Å). To convert to units of energy (keV) we use the relation

$$N(E) = N(\lambda)\frac{d\lambda}{dE} = N(\lambda)\frac{\lambda^2}{12.4} \tag{3.16}$$

The line intensities are finally divided by their bin size (in keV) to get the final integral in the proper units of (photons/electron/sr/keV). A calculated source spectrum for the tungsten anode Philips source at 60keV is shown together with a measured spectrum in Figure 3.13(*b*). The calculated spectrum includes absorption due to a 0.5mm thick beryllium window that is an integral part of the tube.

Transmissions are calculated as for the raytrace model via equations (3.6) and (3.7). Figure 3.14 shows the calculated Philips source spectra, multiplied by the relevant filter transmissions, from Table 3.2. Comparison with the measured data of Figure 3.12 shows satisfactory agreement.

The calculated spectrum from the modified VTF source chamber is shown in Figure 3.15, both with and without a 4μm Al filter.

3.7 Conclusions

A description of the micropore optic vacuum test systems at Leicester University has been presented. The Vacuum Test Facility offers a very small ($< 1'$) low energy ($<$ 5keV) highly divergent ($> 2^\circ$) X-ray source in a system that allows large off-axis angles to be subtended at the optic. The Long Beamline Tunnel Test Facility allows MPOs to be tested with hard X-rays (up to 100keV) at small grazing angle of incidence ($< 10'$) to a high resolution ($20''$). The TTF also offers numerous optic mounting options to accommodate a wide range of slump radii and Wolter optics. All experimental images in the rest of this

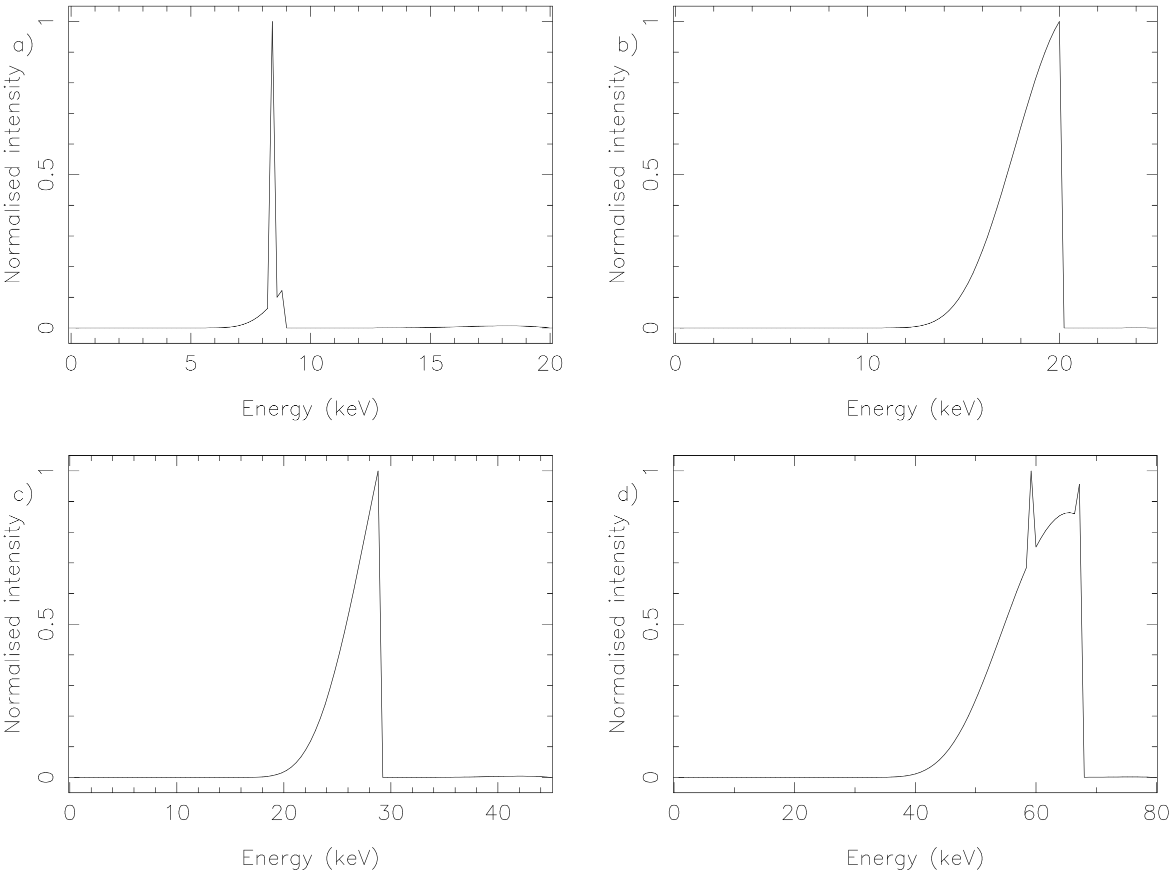

Figure 3.14: Calculated TTF source spectra for anode voltage/filter combinations of (a) 20kV and 100μm Cu, (b) 25kV and 200μm Mo, (c) 45kV and 500μm Sn and (d) 80kV and 500μm Ta. Comparison with the measured spectra in Figure 3.12 shows reasonable agreement.

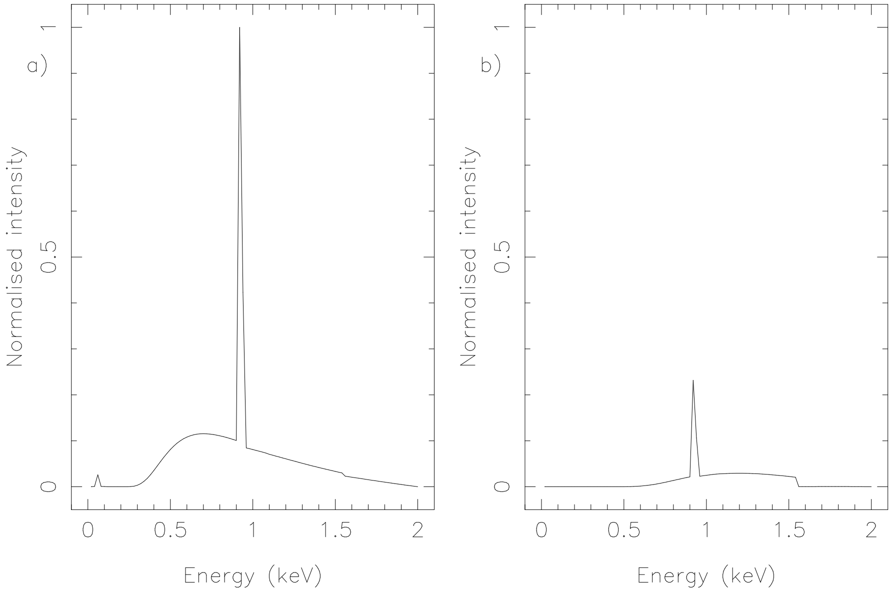

Figure 3.15: Calculated VTF source spectra (a) filtered through the Lexan window separating the source and main chambers (b) with an additional 4μm Al filter in place.

thesis have been obtained in one of these two test systems.

The raytrace model of Brunton (1994) has been extended to allow the calculation of the high energy response of micropore optics in square-pack, radial-pack and Wolter-pack configurations. The inclusion of a more realistic reflection algorithm and precisely calculated source input spectra has further improved the accuracy of the model. This is used to both predict and model the response of tested optics throughout the rest of this work.

Chapter 4

Square-packed micropore optics

4.1 Introduction

Since it was realised that square-pore square-packed micropore optics could be used to produce low mass, high effective area Kirkpatrick-Baez (Kirkpatrick and Baez, 1948) and lobster eye (Schmidt, 1975; Angel, 1979) optics, various institutions have initiated programmes to develop the idea. The ESA TRP programme initiated by Leicester to develop micropore optic technology included the initial production of three square-pore, square-packed blocks in order to refine the production techniques necessary for the fabrication of large format MPOs with smaller pores, increased aspect ratios and low surface roughness prior to attempting the manufacture of radially-packed Wolter elements.

The programme has led to several major milestones in the development of MPO technology:

i) The point-to-point focusing of high energy ($\sim$ 50keV$\rightarrow$ 65keV) X-rays.

ii) Production of large format (56mm$\times$61mm) flat square-packed MPOs with the best ever observed focus ($5.2'$ square) from an MPO of this size.

iii) Large (40mm square) format slumped square-packed MPOs with foci comparable to that of flat plates.

After discussing the principles of operation of square-packed MPOs and modifications to the manufacturing techniques, these achievements will be more fully addressed in this chapter. The Monte Carlo raytracing software described in section 3.6 will be used to model the optics and deduce the quality of channel alignment.

4.2 Principles of operation of square-packed micropore optics

The nature of the focus expected from a square-pore square-packed micropore optic is determined by the geometry of the optic and the size and position of the source relative to the MPO's optical axis. As described in section 1.3, successive reflections from orthogonal walls parallel to the channel (z) axis will reverse the x and y components of velocity of the photon (Figure 1.5).

If the MPO is planar and the channel axes are parallel to the optical axis of the system, photons from an on-axis source will be focussed to an on-axis position the same distance behind the optic as the source is in front of it (i.e. the source distance, L_S, is equal to the image distance, L_I). This geometry is illustrated in Figure 1.6.

If the channel axes are normal to the surface of a sphere centred on the system optic axis, then analysis of the ray diagram in Figure 4.1 yields the lens equation

$$\begin{aligned} \phi &= \theta + \alpha_{ref} && (4.1) \\ &= \theta + \alpha && (4.2) \\ &= 2\theta + \delta && (4.3) \end{aligned}$$

where δ is the incident ray's angle to the optical axis, θ is the slump angle of the channel the ray strikes a distance y from the optical axis, α is the incident grazing angle of the ray to the channel wall and ϕ is the angle to the optical axis of the emergent ray. As $y \ll L_S$,

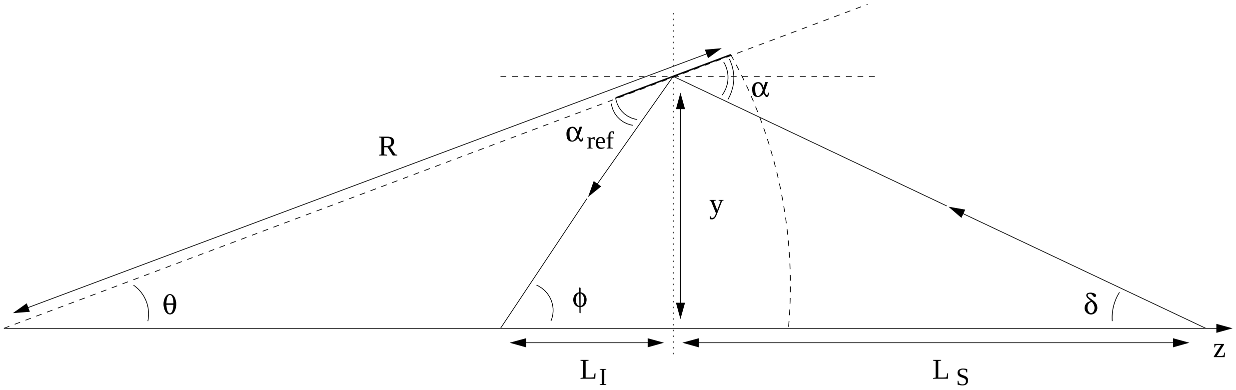

Figure 4.1: Ray diagram showing the focusing principle of a lobster eye micropore optic.

L_I and the slump radius of curvature, R, we can use the small angle approximations $\sin a = a$ and $\tan a = a$. The angles can thus be written in terms of the height of the incident ray above the MPO's optical axis as; $\delta = \frac{y}{L_S}$, $\theta = \frac{y}{R}$ and $\phi = \frac{y}{L_I}$. Substituting into equation (4.3) we can write

$$\frac{1}{L_I} = \frac{2}{R} + \frac{1}{L_S} \tag{4.4}$$

In the limit $L_S \to \infty$ this reduces to $L_I = \frac{R}{2}$. However, not all rays will be reflected once from orthogonal walls, and not all sources are on-axis.

4.2.1 Reflection modes

As the reflections occur from channel walls, not single reflective surfaces, it is possible to get multiple reflections down channels. As Figure 4.2 shows, a photon undergoing an odd number of reflections from opposite walls of a channel will leave with the component velocity normal to those walls reversed. A photon undergoing an even number of reflections will leave the channel with the same velocity components that it entered with.

There are thus five possible outcomes for a photon entering a square channel:

i) It passes through completely unreflected in either x or y directions.

ii) It undergoes an even number of reflections in both directions.

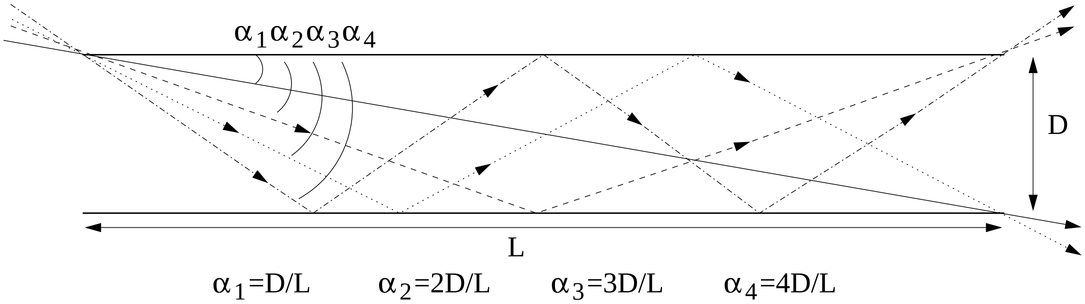

Figure 4.2: Maximum allowable angles as a function of the number of reflections occurring in a channel of length L and side length D. Rays undergoing an odd number of reflections emerge with the component of velocity normal to the walls reversed, those undergoing an even number do not.

iii) It undergoes an odd number of reflections in the x direction and an even number in the y.

iv) It undergoes an even number of reflections in the x direction and an odd number in the y.

v) It undergoes an odd number of reflections in both directions.

From Figure 4.2 it can be seen that the number of reflections a photon will undergo in either direction is a function of the incident angle (and hence position of the channel relative to the source) and the channel's aspect ratio. Figure 4.3 shows schematically the focus that results from these different reflections. The unreflected component of the focus has a pyramidal intensity distribution of base length $2L_S D/L$, resulting from the maximum transmission angle (α_1 in Figure 4.2) of D/L.

Photons undergoing an odd number of reflections from orthogonal channel walls (odd-odd) form the (pyramidal) intensity distribution of the central focus. This has a base length of $2D$ if only single reflections contribute to the focus, increasing to $6D$ for triples, $10D$ for quintuples etc. (Brunton *et al.*, 1997). The probability of a photon emerging from a channel decreases with increasing grazing angle and number of reflections so in most cases a single reflection approximation holds.

Photons suffering odd numbers of reflections from one set of parallel walls and an even number from the orthogonal set (odd-even), thus only having one component of their velocity reversed, will be focused into a line. The orthogonal line foci are the *cross-arms* of the structure.

Analysis of the reflection angles in Figure 4.2 shows that the structure due to odd-even and even-even (reflected rays undergoing no focusing effect) reflections is periodic. Areas in an image containing no events are those whose position relative to the source subtend an angle such that rays emitted in that direction suffer an odd number of reflections at the MPO, redirecting them to either the focus or cross-arms. Figure 4.4 shows an image calculated using the raytrace model described in section 3.6, the MPO is perfectly aligned and the *chequerboard* periodic structure can be seen. A roll-off in intensity is expected towards the edges of the MPO as the reflectivity decreases with increasing incident grazing angle.

In a lobster eye optic, the focus accumulates in the same manner with the exception that the image size is reduced. It can be shown (Chapman *et al.*, 1991) that the transverse magnification of a lobster eye MPO is $M_T = L_I/L_S$. The base length of the central focus becomes $D(1 + M_T)$ and the base length of the unreflected intensity is $(2L_S D/L)R/(R + L_S)$.

4.2.2 Off-axis sources

If the source is off-axis then a point-to-point imaging optic will act as if the optical axis of the MPO has moved to a position where the source is on-axis. This will be seen in the image plane as the cruxiform focus centred about a point displaced from the original optical axis by the same distance and in the same direction as the source has been moved by. In a lobster eye optic the same behaviour is exhibited with the exception that the central focus displacement is magnified by the transverse magnification defined above ($M_T = L_I/L_S$).

A key advantage with square-packed MPOs is that there is no defined optical axis, this is defined by the system into which they are placed. In the true lobster eye configuration,

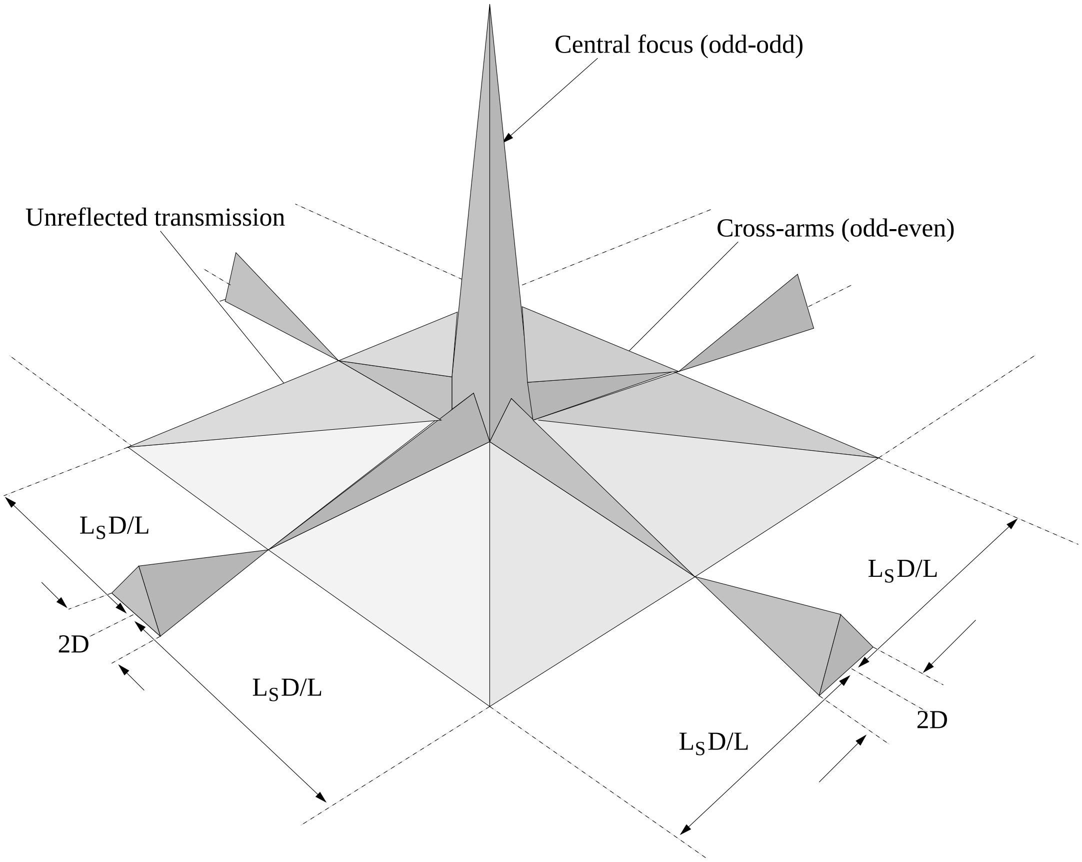

Figure 4.3: The cruxiform focal structure of a planar square-pore square-packed micropore optic. The central focus is comprised of photons reflected an odd number of times from orthogonal walls, the base of the pyramid is $2D$ resulting from the non-ellipsoid profile of the channel walls. The unreflected component has a base size $2L_SD/L$, resulting from the maximum transmission angle of the channels being D/L. The cross-arms result from odd-even reflections from the orthogonal walls.

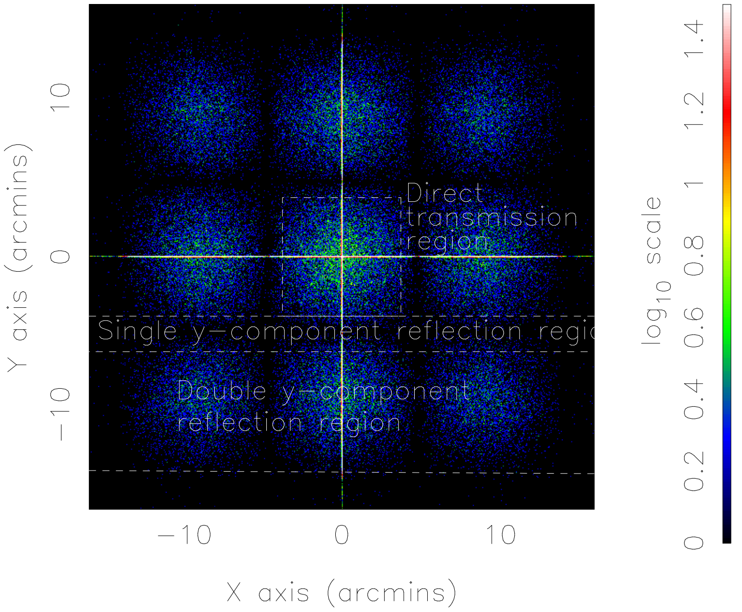

Figure 4.4: Calculated image of a perfectly aligned MPO with 10μm, 100:1 channel on a 12μm pitch. The periodic *chequerboard* nature of the odd-even and even-even reflections from orthogonal channel walls can be seen as well as the central focus of odd-odd reflections and line foci of odd-even reflections. The annotated areas are symmetrical about the central focus.

rays from infinity are focused onto a spherical image plane of radius $R/2$ centred at the slump origin (R is the slump radius). This configuration (shown in Figure 4.5) can view 4πsr and will theoretically focus rays incident from one direction, within an acceptance area given by the critical reflection angle θ_c and slump radius R of $4R^2\theta_c^2$, to a point on the image plane. This principle behind the Lobster-ISS All Sky Monitor (chapter 7).

4.3 Pre-TRP MPO quality

Before the initiation of the TRP programme (1996), micropore optics tested at Leicester were produced by Phillips Photonics (now Photonis SAS following a management buy-out in 1998) of Brive, France and Galileo Electro-Optics (now Burle Electro-Optics) of Sturbridge MA, USA. Square-pore channel plates have been acquired elsewhere by other groups, Melbourne University having tested those from Schott Fibre-Optics, USA for example.

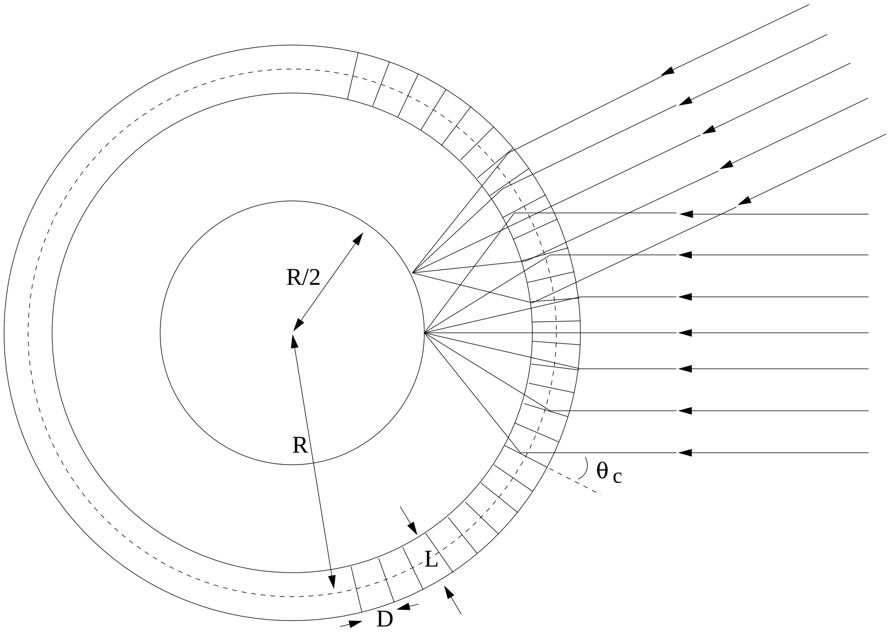

Figure 4.5: The true lobster eye configuration, where rays from infinity are focussed onto a spherical image plane of radius $R/2$ centred at the origin of the MPO slump. The acceptance area is defined by the critical angle θ_c at which the probability of grazing X-ray reflection becomes very small.

The best results from these older plates are presented by Brunton *et al.* (1997) and Peele *et al.* (1996). Brunton *et al.* illuminated a 33mm diameter Galileo Electro-Optic MPO of aspect ratio 56:1, channel side length 85μm and channel pitch 122μm with Si-K X-rays ($1.74keV$) in the Leicester VTF. They obtained a FWHM focus of $7.4' \times 10.3'$ from a $0.5'$ source size (a 100μm collimating hole used in front of the old VTF electron bombardment source; note that the illumination problems described with this set-up in section 3.2.1 were not encountered due to the small size of the MPO). The peak gain of the MPO focus was calculated to be 28 ± 3.7. Peele *et al.* exposed a 15mm square Schott Fibre-Optics MPO with a channel side length of 200μm, channel pitch of 240μm and aspect ratio 30:1 to a Al filtered laser plasma source (90% flux within boundaries 1.36keV→ 1.56keV). They obtained a $3.3'$ FWHM focus from a $2.2'$ source with a gain within the FWHM of 21 ± 4.

Modelling and metrology by various methods (Scanning Electron Microscope (SEM), Atomic Force Microscope (AFM) and X-ray scattering) led to Brunton *et al.* and Peele *et al.* deducing channel misalignments and deformations listed in Table 4.1 and shown in

Type of misalignment	Magnitude	
	Brunton *et al*	Peele *et al*
Pincushion	$g/D = 0.0045$	Not stated
Radiusing	$R_{corner}/D = 0.035$	Not stated
Inter-channel tilt error	$5'$ rms	$6'$ rms
Channel rotation error	$0.84°$ rms	Not stated
Inter-multifibre tilt error	$8'$ rms	$7'$ rms
Multifibre rotation error	$1.3°$ rms	$3.15°$ rms
Surface roughness	30Å	20Å

Table 4.1: MPO misalignments deduced from modelling and metrology for square-pore square-packed pre-TRP plates. Pincushion and radiusing effects are shown in Figure 4.6.

Figure 4.6.

4.4 Photonis TRP MPOs

Several aspects of MPO geometry were identified in the TRP programme as requiring attention. These were essentially the need for larger aspect ratios channels with low surface roughness and the requirement to improve the regularity of the square-pore channels and channel stacking.

In order to tackle stacking errors and channel regularity, the manufacturing process outlined in section 1.4 needs to be carefully controlled from the build of the core and cladding couple to the drawing rate, stacking procedure and fusion pressure/temperature. In order to make possible large L/D ratios (in excess of 500:1) and smooth channel surfaces, the etching process must be optimised so that the core glass is removed completely with the minimum of damage to the cladding.

During the programme the drawing processes have been optimised such that the square-pore single fibre and multifibre sizes can be controlled to within 3μm ($\sim 0.5\%$). The etching conditions have also been improved to the point that 500:1 aspect ratio MPOs have

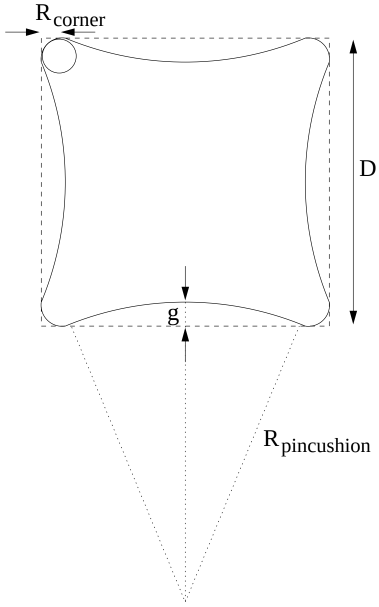

Figure 4.6: Diagram of the pincushion distortion and vertex radiusing of square-pore channels commonly found in pre-TRP MPOs.

regularly been produced with surface roughnesses of the order of 10Å→ 20Å (Boutot *et al.*, 2000). The original combination of cladding/core glass (Corning 8161 and Circon ACMI RE695 respectively), chosen for its high lead content (and hence improved X-ray reflectivity characteristics) was found to be susceptible to weakening during the severe acid etches required to clean such large aspect ratios (Boutot *et al.*, 2000). This resulted in MPOs from several blocks manufactured with these glasses either cracking or, after long etches, disintegrating. To remedy this situation some blocks were also made with a Philips 297 cladding and Philips 274 core. This combination proved more resistant to the etching process. Figure 4.7 shows electron micrographs of square-pore MPO channels resulting from the TRP programme. Note the absence of any visible channel pincushion effect and very low vertex radiusing (so low that it can be discounted as a problem).

It was decided that the standard multifibres used in the TRP programme would be 55×55 arrays of 10μm square channels. The small pore size acts to increase the effective area of an optic of given geometrical size and makes possible reasonable thickness MPOs with large aspect ratios.

Measurements by Beijersbergen *et al.* (1999) at both the Physikalisch-Technische Bunde-

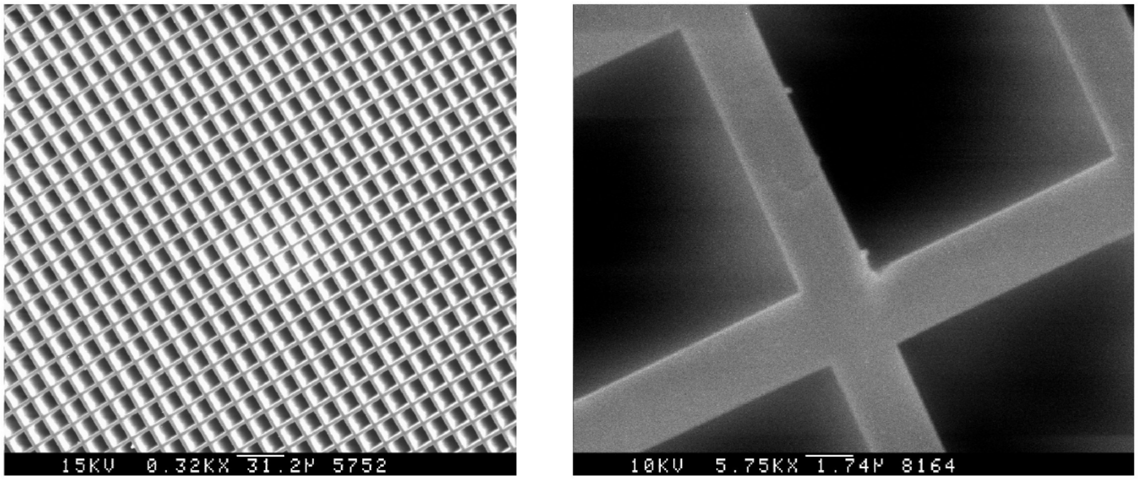

Figure 4.7: Electron micrographs of square-pore MPO channels from the ESA TRP programme showing their regularity and the absence of both pincushion distortion and vertex radiusing. Scale is indicated by the bar in both cases.

sanstalt (PTB) laboratory at Bessy II, Berlin, and at the European Synchrotron Radiation Facility (ESRF), Grenoble, have yielded data on the alignment of multifibre channels. Reflection measurements of individual and multiple channels show that a best image quality of 20″ can be obtained, but this is dependent upon which set of walls are illuminated. This dependence is found to be a result of differing wall roughnesses (Beijersbergen, 2000a), an effect that must originate with the MPO orientation during etching or fusion (the channels are randomly stacked). The surface roughness of channel walls is found to be 15Å rms. The multifibres yield image qualities between 1′ and 2′.

4.5 Square-packed results

In the following sections the three milestones described in the introduction will be presented. The experimental data will be described in each case before modelling the optic X-ray response with the raytrace software described in section 3.6. All quantitative calculations are performed in the method described in section 3.5.

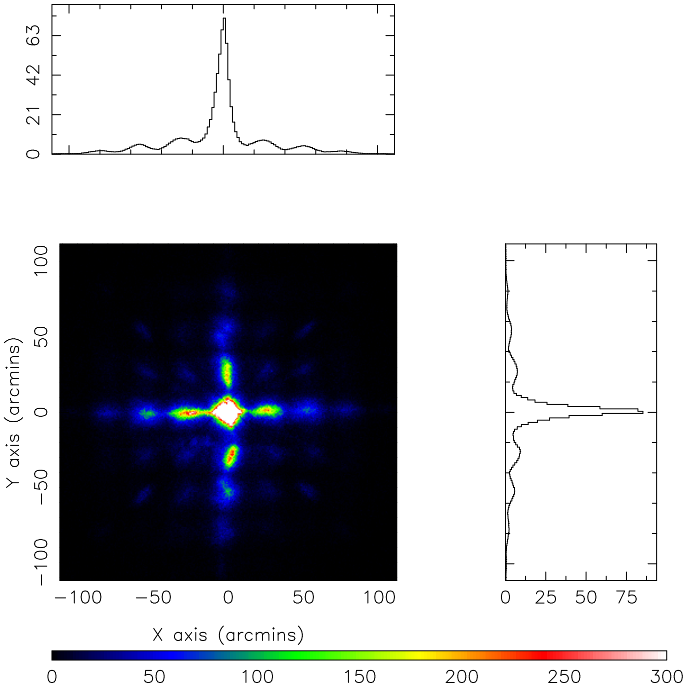

Figure 4.8: Full face illumination of the 500:1 square-packed MPO FB-001-A3 in the VTF with Cu-L (0.93keV) X-rays. The FWHM cuts through the focus horizontally and vertically show the central focus to be $5.2'$ square. The effective area within 3σ of maximum is 0.38 ± 0.07cm^2 and the peak gain is 20 ± 4.

4.5.1 High energy X-ray imaging

A thick (5mm) plate cut from block B, a 54mm×54mm format Philips 297/274 combination, was chosen for testing at hard X-ray energies. The restricted single reflection angles due to the large (500:1) aspect ratio were predicted to allow operation of the optic up to X-ray energies of around 100keV.

The MPO, serial number FB-001-A3, was tested at both low energy (0.93keV) in the VTF and at higher energy ($\sim$ 50keV$\rightarrow$ 65keV) in the TTF (section 3.6.2 gives precise details of the X-ray spectra in the different energy modes). Figure 4.8 shows the image and axial cuts through the focus for a full face illumination with Cu-L (0.93keV) X-rays in the VTF. The FWHM focus is $5.2'$ square. The effective area is calculated to be 0.38 ± 0.07cm^2 with a peak intensity gain of 20 ± 4.

Figure 4.9 shows the image and cuts when the MPO was illuminated with a tantalum-

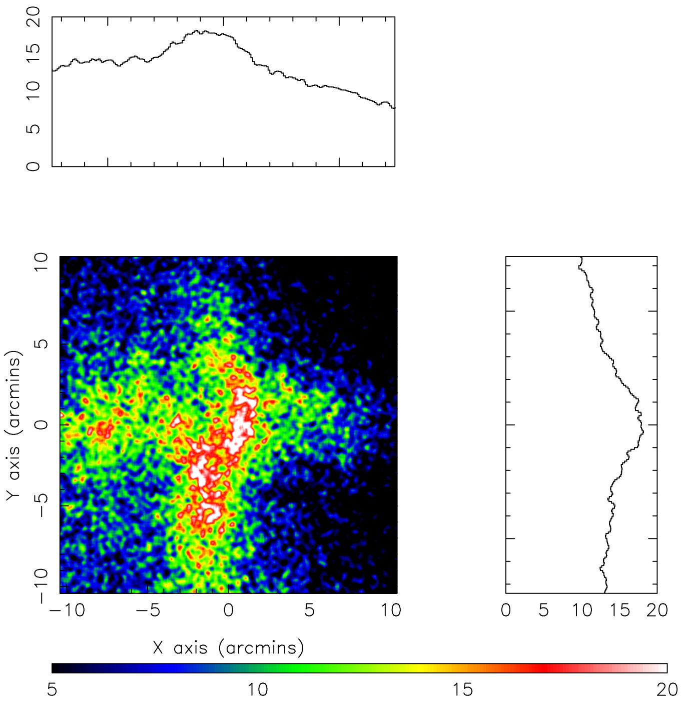

Figure 4.9: Full face illumination of the 500:1 square-packed MPO FB-001-A3 in the TTF with a tantalum-filtered 80kV X-ray continuum (∼ 50keV→ 65keV). The FWHM cuts through the focus horizontally and vertically show the central focus to be $6.0' \times 5.5'$. The effective area is calculated to be $0.11 \pm 0.02\text{cm}^2$ with a peak gain of 0.7 ± 0.2.

filtered 80kV X-ray continuum (∼ 50keV→ 65keV). The TTF source size when this image was recorded was larger than is currently the case at $\sim 1.2'$. The focus is obscured in Figure 4.9 due to the transparency of the MPO at hard X-ray energies, making it difficult to take an accurate measurement of the focal size or effective area. After subtracting the transmitted background from the data, cuts across the entire image yield a source size of $6.0' \times 5.5'$, in agreement with the low energy measurements. The effective area is measured at $0.11 \pm 0.02\text{cm}^2$ with a depressed peak gain of 0.7 ± 0.2.

Figure 4.10 shows the off-axis image created by tilting the MPO such that the focus is formed in the top left hand corner of the detector. This confirms that the datasets in Figures 4.9 and 4.10 show a real focus which is sensitive to the off-axis angle of the source.

In a perfectly aligned MPO with the same parameters, the FWHM resolution is limited by the source size and the effective areas, calculated with the raytrace model, are: 0.7cm^2 with a peak gain of 7508 in the VTF with Cu-L (0.93keV) X-rays and 0.1cm^2 with a peak

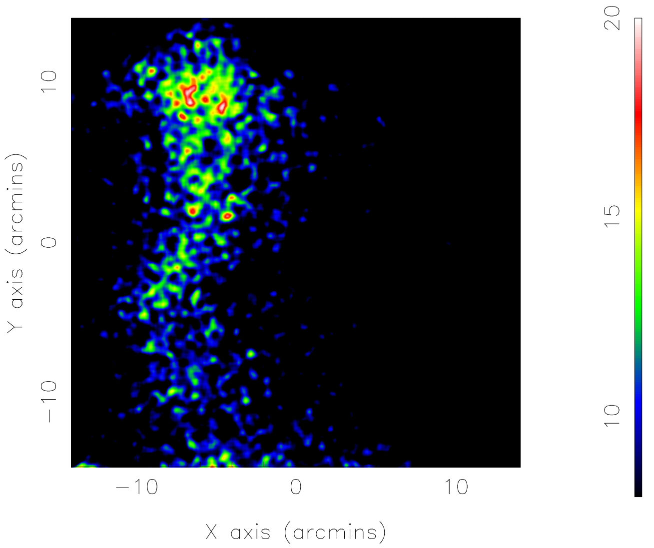

Figure 4.10: **Full face illumination of FB-001-A3 in the TTF with a tantalum-filtered 80kV X-ray continuum (∼ 50keV→ 65keV). The MPO was tilted so that an off-axis focus is formed, proving that the focus seen in Figure 4.9 is a true focus formed through reflections from orthogonal walls.**

gain of 11 in the TTF with the tantalum-filtered 80kV X-ray continuum. Effective area curves for a perfectly aligned version of MPO FB-001-A3 in the VTF and TTF are shown in Figure 4.11.

To roughly model the experimental results, it is possible to include random small magnitude rms tilt and rotation errors between the channels in the computer model. However, close analysis of Figure 4.8 shows that the cross-arms of the cruxiform structure are not exactly orthogonal. The vertical arm is ∼ 1° from vertical *in opposite directions* either side of the focus, whilst the horizontal arm shows a 1° departure from the true horizontal. Such behaviour has been observed before (Peele *et al.*, 1998) and is attributed to a gradual systematic shearing of channels across the MPO (shown in Figure 4.12).

It has been demonstrated (Beijersbergen *et al.*, 1999) that the channels in the individual multifibres used to assemble these MPOs are aligned to an accuracy of between $20''$ and $1'$. It seems that large scale misalignments between multifibres must be responsible for the degraded imaging seen. In order to model this, a misalignment map is created in which the alignment error of each multifibre may be specified.

The channels within multifibres are modelled with a 15Å rms roughness on a 1μm cor-

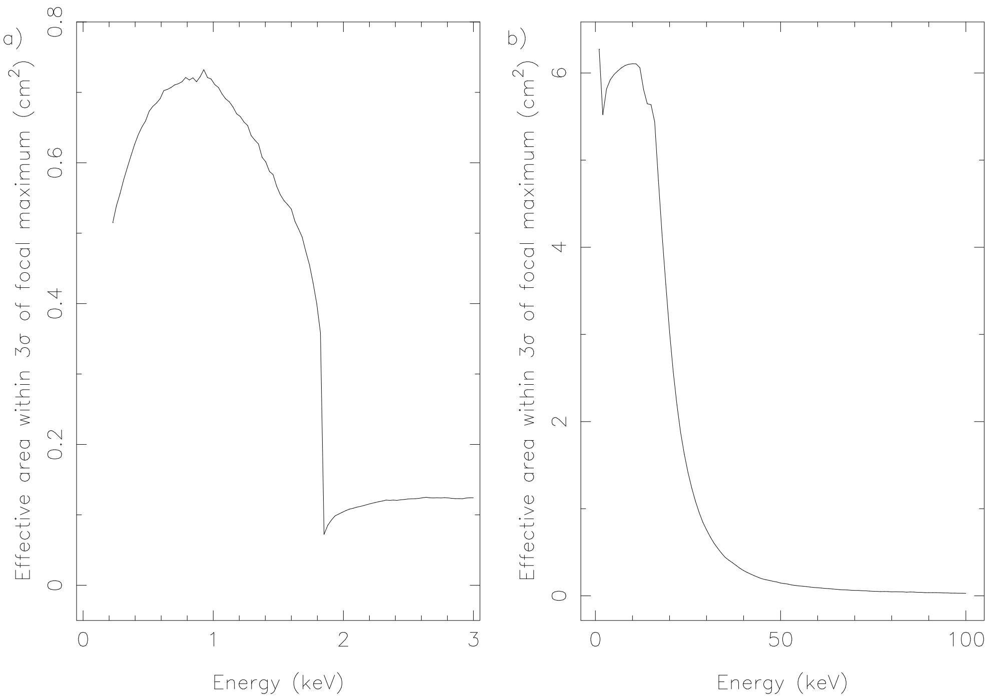

Figure 4.11: The effective area curves as a function of energy for a perfectly aligned MPO with the same parameters as FB-001-A3 in (a) the low energy test chamber (VTF) and (b) the high energy long beamline (TTF). The X-ray sources are on-axis.

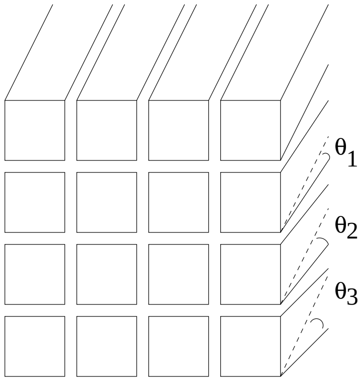

Figure 4.12: The gradual shearing of successive layers of multifibres creates the non-orthogonal cross-arms seen in the MPO FB-001-A3 image of Figure 4.8.

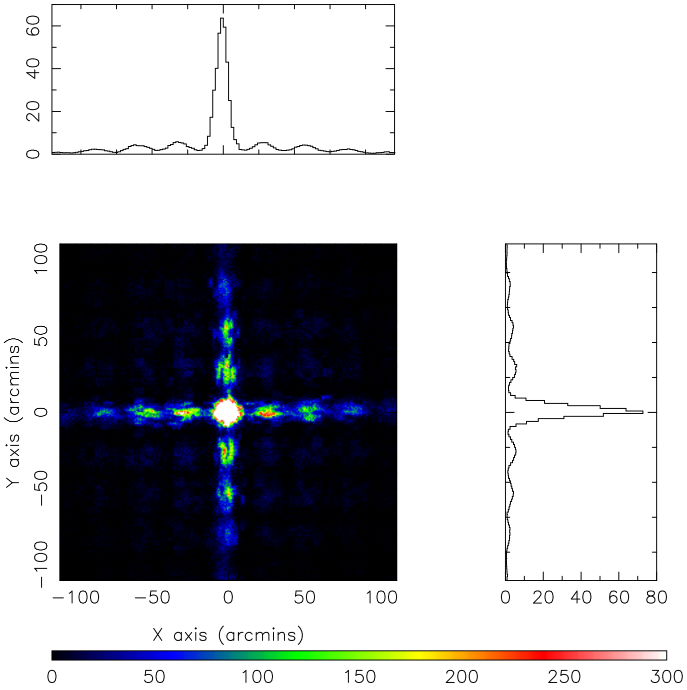

Figure 4.13: Raytraced image of MPO FB-001-A3 illuminated with Cu-L (0.93keV) X-rays in the VTF. The model used a tilemap with a gradual $7'$ twist in each direction to produce slightly non-orthogonal cross-arms. Additional $1'$ rms tilt and $1.1°$ rms rotation errors between the multifibres provide a FWHM focus of $5.5'$ square. The effective area is 0.51cm^2 with a peak gain of 18.

relation length with $20''$ rms tilt misalignments and $34'$ rms rotation errors. The multis suffer a gradual twisting of $7'$ across the MPO and $3.5'$ above and below the centre in opposite directions to result in the non-orthogonal cross-arms seen. There are additional $1'$ rms tilt and $1.1°$ rms rotation errors between the multifibres. The resulting images are shown in Figures 4.13 and 4.14 for the low energy and 80kV tantalum-filtered continuum illuminations respectively.

The raytraced images shows a strong correlation with the observed (Figures 4.8 and 4.9). This suggests that the imperfections used in the model are of the correct magnitude and type. Analysis of the production process at Photonis (Brunton *et al.*, 2000) has found that the misalignments are most probably introduced during the fusion of individual multifibres into a block. It has been proposed that problems may arise as a result of the glass expanding at a different rate to the mould used to apply pressure during ram fusion, or due to the moulds deforming slightly as a result of repeated thermal cycling.

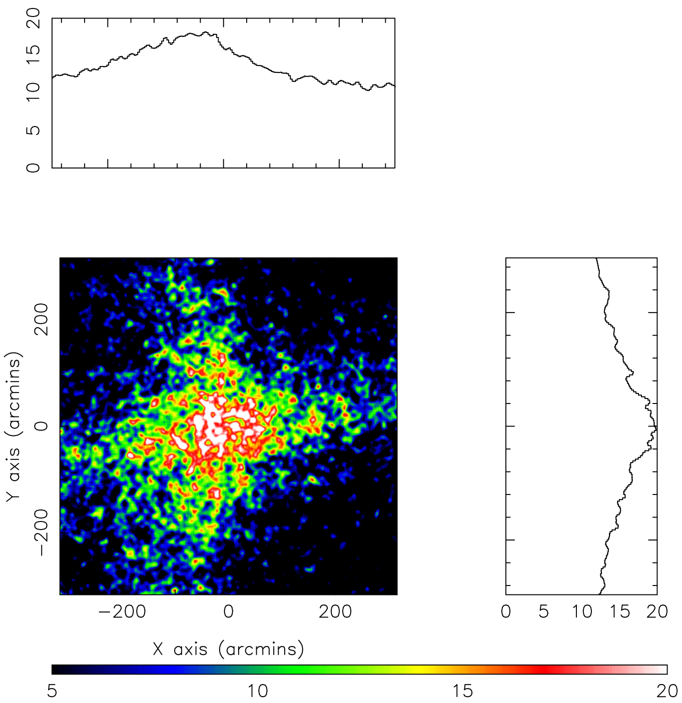

Figure 4.14: Raytraced image of MPO FB-001-A3 illuminated in the TTF with a tantalum-filtered 80kV X-ray continuum (~ 50keV$\rightarrow 65$keV). The model used a tilemap with a gradual $7'$ twist in each direction to produce slightly non-orthogonal cross-arms. The previously quoted inter-channel misalignments were included with additional $1'$ rms tilt and $1.1°$ rms rotation errors between the multifibres. The focus has a FWHM resolution of $\sim 5.5'$ square. The effective area is 0.1cm^2 with a peak gain of 0.9. Compare with Figure 4.9.

Even with the flagged problems, high energy micropore optic X-ray focusing has been demonstrated for the first time. The focus is to a reasonably high resolution ($5.2'$ square at low energy, increasing to $6.0' \times 5.5'$ at higher energies) but the gain and effective area are suppressed at higher energies as the focus is swamped by transmitted rays. This would make the optics of no practical use. To improve the high energy response, the fusion process needs to be refined in order to eliminate alignment errors introduced at this stage, coupled with work to make the glass more opaque or extend the channel aspect ratio. Using the raytrace model of MPO FB-001-A3 with perfectly smooth walls and perfectly aligned channels illuminated with the tantalum-filtered source spectrum in the TTF, a peak gain of 11 is demonstrated with channel aspect ratios of 500:1, 29 with 1000:1 and 73 with 2000:1.

4.5.2 Largest-format micropore optic

The largest format micropore optic tested in full face illumination thus far is the 56mm×61mm block C plate FD-001-C1. Block C was assembled using a slightly modified process following feedback about the performance of MPOs from blocks A and B (Brunton *et al.*, 2000). The mould spacers used for the ram fusion process were machined from stainless steel chosen to provide a composite thermal expansivity that should match that of the MPOs. It should also be noted that block C was compacted to a smaller (0.35%) degree than A and B ($\sim 2\%$). FD-001-C1 is a 100:1 MPO with otherwise identical characteristics to the other TRP MPOs (10μm side channels on a 12μm pitch stacked into 55×55 multifibre arrays.

Figure 4.15 shows an image taken in the VTF with Cu-L (0.93keV) X-rays. The FWHM focus is $5.2'$ square with an effective area of $0.94 \pm 0.13\text{cm}^2$ and a peak gain of 44 ± 5. As the cross-arms in this image are essentially orthogonal it seems that the gradual shearing of channels across the MPO has been eliminated and the image can be modelled using simple random alignment errors. Figure 4.16 shows a raytraced image with inter-channel alignment errors as found experimentally for the other TRP multifibres (Beijersbergen *et al.*,

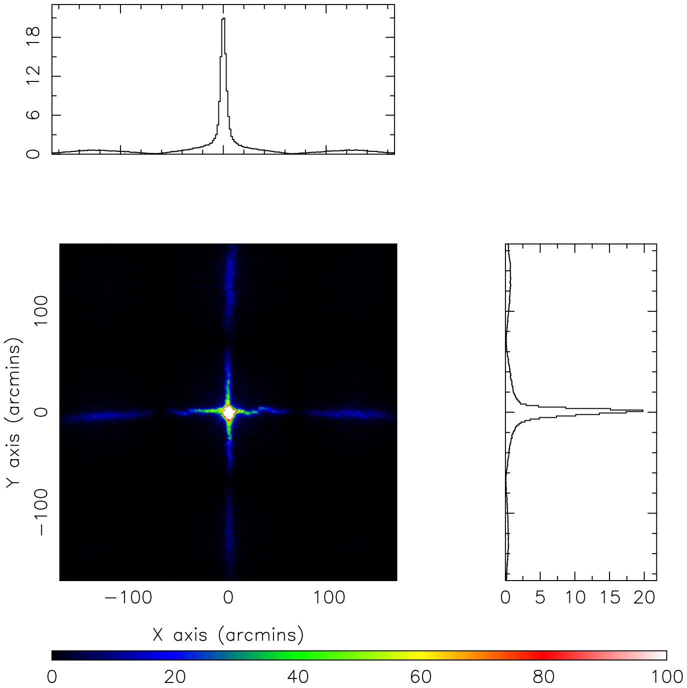

Figure 4.15: Full face illumination of MPO FD-001-C1 with Cu-L (0.93keV) X-rays. Taken in the VTF with a sub arcminute source the FWHM focus is 5.2′ square. The effective area is 0.94±0.13cm^2 with a peak gain of 44 ± 5..

1999) and rms inter-multifibre tilt and rotation errors of 1′ and 1.1° respectively.

From this data, it seems that the trouble taken trying to match the fusion mould thermal expansion co-efficients to those of the glass was worth the effort as the gradual shearing has been eliminated. The lower compression could conceivably result in a less stressed MPO with the possible effect of better aligned multifibres.

An interesting result discovered with MPO FD-001-C1 is the degrading effects of humidity on micropore optics. The initial tests of FD-001-C1 took place on 01/09/2000, before the modifications to the VTF described in section 3.2.1. This exposure yielded a 5.9′ square focus from a 5.4′ source, possibly a source size limited result. Following the modification of the VTF to the sub-arcminute fine-focus source, the MPO was re-tested on 23/04/2001. The MPO focus quality was found to have become degraded to 8.2′ square. After investigating all possible sources of error, it was decided that the actual MPO must have become deformed from its original figure. Discussions with Photonis revealed that the glass used in the manufacture of these plates (Corning 8161) can absorb water vapour.

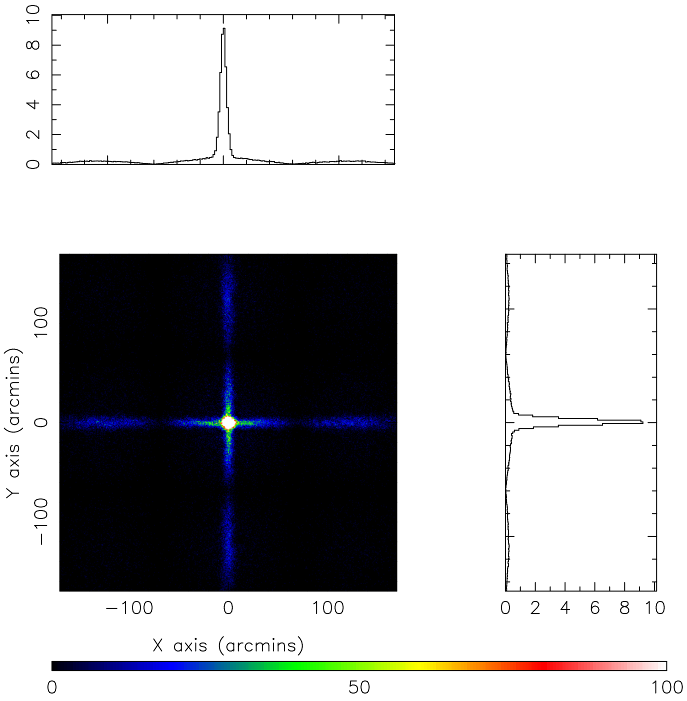

Figure 4.16: Raytraced image of the full face illumination of MPO FD-001-C1 with Cu-L (0.93keV) X-rays in the VTF. The multifibres had $1'$ rms tilt errors between them with $1.1°$ rms rotation errors in addition to the standard inter-channel alignment errors. The FWHM focus is $5.3'$ square with an effective area of 1.45cm^2 and a peak gain of 72.

It was therefore hypothesised that as the plate had been left exposed to atmosphere for six months, it had absorbed water causing it to warp slightly, enough to degrade its performance. To test this theory, the MPO was baked at 280°C under vacuum for 72 hours to allow outgassing of the water molecules. When re-tested following this procedure it was found that the MPO had recovered its original focus and was even slightly improved ($5.2'$ square), as would be expected with a smaller source size.

This episode highlights the fact that special care must be taken with micropore optics, especially thin plates of low aspect ratio that are more susceptible to warping. Warping due to absorption of water into the MPO glass is recoverable, although this may not have been complete. It also shows how sensitive the focal resolution of thin micropore optics are to any form of stress placed upon them. All MPOs at Leicester are now stored in dry conditions (relative humidity of $\sim 15\%$ maintained with regularly replaced self indicating silica gel crystals).

4.5.3 Best lobster eye focus

Several block A (40mm×40mm) MPOs were slumped at Photonis. These were tested at Leicester in early 2000. The MPO format and slump radius were chosen to be the same as those originally proposed for the Lobster-ISS project (chapter 7); 10μm channels on a 12μm pitch with an aspect ratio of 50:1 and a slump radius of 75cm.

Evaluation of the slumped MPO lens equation (Eqn. (4.4)) shows that this can be accommodated in direct focus in the TTF (L_S = 19.625m, L_I = 0.3675m). In order to ensure all channels are sampled in such a low aspect ratio, small MPO, it must be tilted so that an off-axis image is formed (on-axis only the 12mm about the perimeter of the MPO definitely reflect X-rays). Figure 4.17 shows the image formed with one such MPO, serial number EK-001-B5, in this manner.

The poor quality focus of this image, measured with a FWHM focal resolution of $12'$ in the vertical cut and a split $30'$ in the horizontal, can be simulated by assuming large

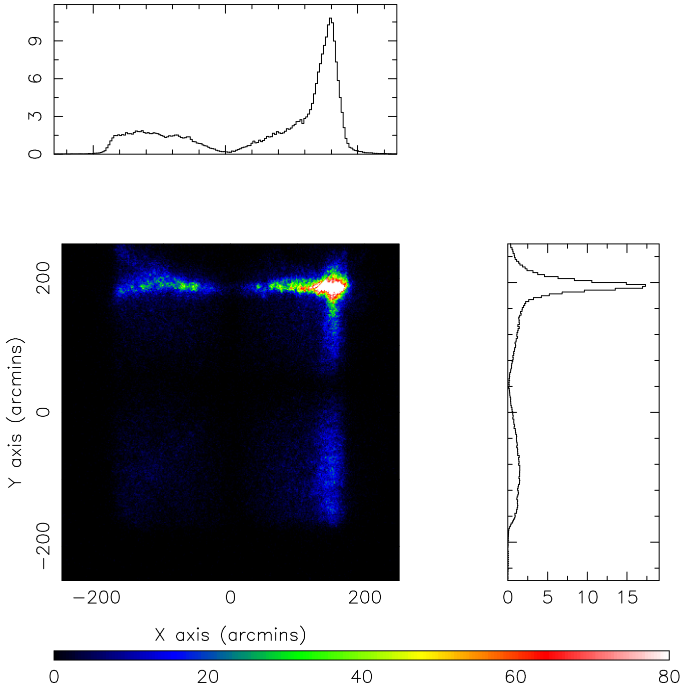

Figure 4.17: Full face illumination of the slumped 50:1 square-packed MPO EK-001-B5 illuminated in the TTF with Cu-L (0.93keV) X-rays. Cuts through the focus horizontally and vertically show the central focus to be $12' \times 30'$. The effective area is 1.13 ± 0.25cm^2 with a peak gain of 14 ± 3.

inter-multifibre rms tilt errors ($3'$) together with different slump radii in the x and y axes. The y-axis slump, forming the horizontal cross-arm, is of the correct 75cm, whilst that in the x-axis is of 90cm radius. The image formed with these misalignments is shown in Figure 4.18.

These errors have been attributed to the pre-etch slumping method (current work at Photonis favours slumping post-etch) and poor bias control when the plates were cut from the block. The maximum slump angle expected in such an MPO is $1.5°$, so any bias angle of the order of $\sim 1°$ would have a major detrimental effect on the post-slump quality. Other MPOs from the same batch had equivalent or worse foci and all broke when attempting to use them with the Lobster alignment jig described in section 7.4.2. It seems that the mechanical strength of 0.5mm thick slumped MPOs is very low, to the point where larger channels (20μm side length instead of 10μm) and hence thicker plates are now baselined for the Lobster-ISS project.

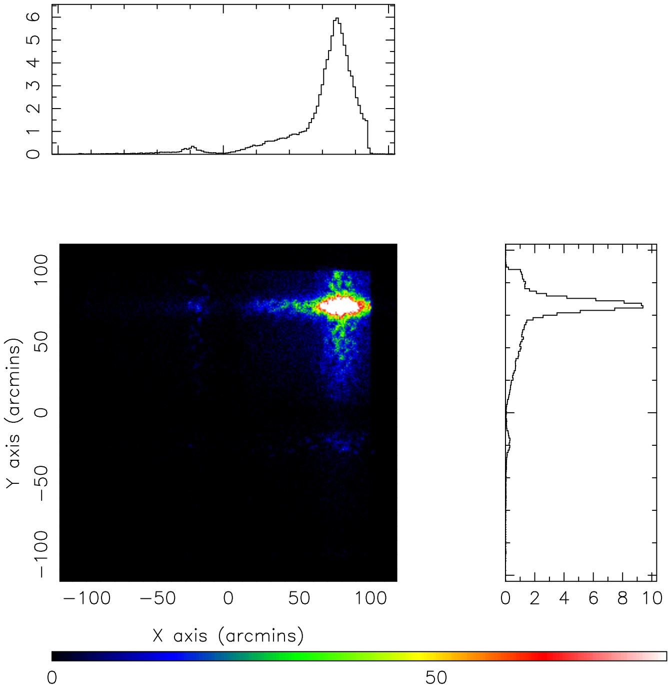

Figure 4.18: Raytraced off-axis full face illumination image of the square-packed MPO EK-001-B5 with Cu-L (0.93keV) X-rays. Together with the inter-channel misalignments used in all simulations, EK-001-B5 has $3'$ rms inter-multifibre tilt errors and different slump radii in the x (correct 75cm)and y (90cm) axes. The FWHM resolution of the focus is $12.9' \times 21.5'$ with an effective area of 1.25cm^2 and a peak gain of 23.

4.6 Conclusions

Planar square-pore square-packed MPOs are approaching a point of maturity where they may become a useful new technology. High resolution ($\sim 5'$) large format micropore optics have been demonstrated that are capable of focusing up to high ($\sim$ 65keV) energies. To improve the high energy response and resolution of planar optics, higher aspect ratio channels with lower inter-multifibre alignment errors are required.

Most alignment errors are introduced during the fusion process and hence it is proposed that it is this section of the production process that requires attention, as demonstrated by the improvement of block C MPOs over those from blocks A and B. It has also been noted that thin (low aspect ratio) MPOs are extremely sensitive to any stresses placed upon them and must, therefore, be mounted and handled very carefully. To prevent contamination that can induce such stresses in plates, they must be stored in clean, dry conditions (preferably under vacuum).

Large format (40mm square) slumped MPOs with reasonable foci have been observed for the first time, although the slumping process still needs greatly improving. Stricter control over bias angles introduced during the slicing of individual MPOs from a block also need to be observed if lobster eye optics of the quality needed for satellite missions are to be created. Several improvements in the slumping process have been made since the testing of MPO EK-001-B5. Chapter 7 reports bias angle measurements from new ($D = 20\mu$m) plates carefully cut at Photonis. New slumped optics created from these MPOs are currently at Leicester, awaiting testing.

Chapter 5

Microchannel Wolter optics: Theory

5.1 Introduction

The concept of using micropore optics in a radial-packing arrangement was first raised in the Hard X-ray Telescope (HXT) proposal for the ESA M3 announcement of opportunity (Fraser *et al.*, 1993c). In a subsequent publication (Willingale *et al.*, 1998), it was noted that this packing geometry had several advantages over the more traditional lobster eye configuration (notably non-cruxiform point spread functions and larger effective/geometric area ratios). The ESA TRP programme listed as one of its objectives the "manufacture of a series of test optics culminating in the production of slumped radially-packed Wolter MCP arrays" (ESA Internal report, 1995).

This chapter describes the basic principles of operation, supported by raytrace models, of the conic approximations to the Wolter type I and type II mirror systems, and their translation into MPO format.

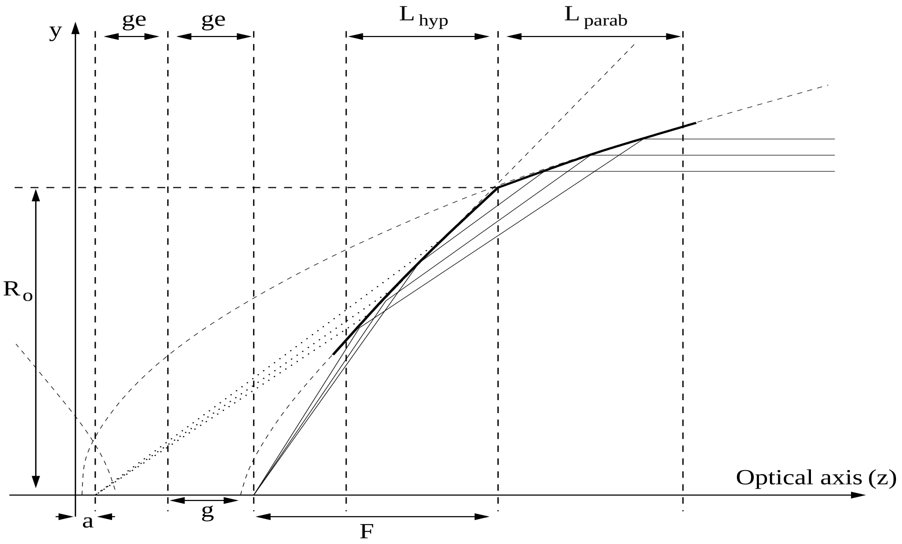

Figure 5.1: Wolter I telescope. F is the focal length of the telescope; a the focal length of the parabola and ge is the focal length of the hyperbola. L_{parab} and L_{hyp} are the lengths of the parabola and hyperbola mirror sections respectively and R_o is the mirror radius where they join.

5.2 Wolter X-ray optics

The idea of using coaxial, confocal conic sections to form grazing incidence X-ray imaging systems was first proposed by Wolter (1952). Of the three systems he proposed, the type I, which forms images with successive reflections from the internal surfaces of a parabaloid and hyperbaloid of revolution, has formed the basis of all high resolution X-ray telescopes flown to date. The state of the art telescopes in terms of angular resolution and effective area are currently Chandra ($0.5''$ resolution) and XMM-Newton (1550cm^2 effective area at 1keV per telescope, 4650cm^2 total).

The type II Wolter telescope focuses rays by reflections from the internal surface of a parabaloid and then from the *external* surface of a hyperbaloid, the type III via reflections from the external surface of a parabaloid and then the internal surface of an ellipsoid. The type I and II systems are shown in Figures 5.1 and 5.2 respectively.

To increase the effective area of Wolter I optics, coaxial mirror shells are nested within each other. The XMM mirror modules each have 58 shells (Gondoin *et al.*, 1994; de Chambure *et al.*, 1998). The difficulties of fabricating many mirrors to have exact conic section

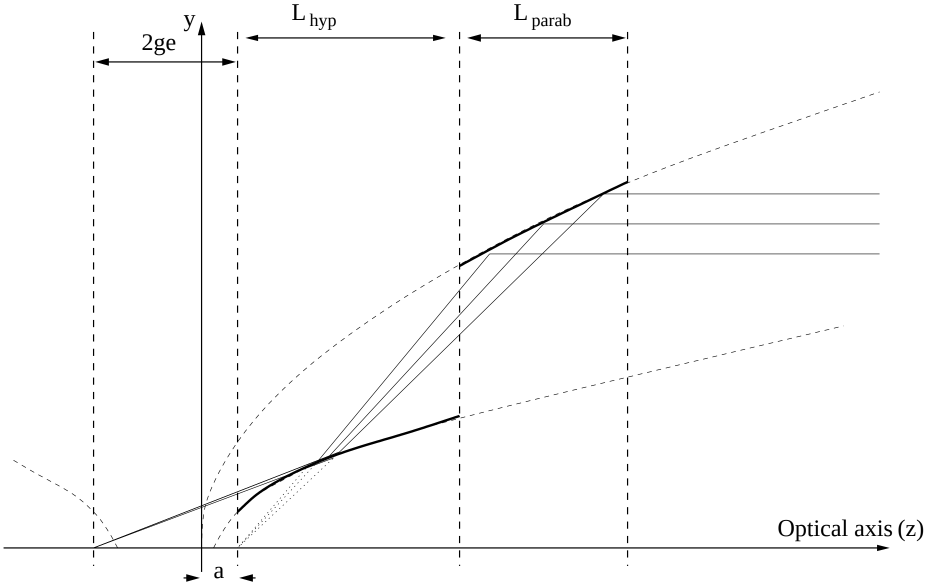

Figure 5.2: Wolter type II telescope. Here, the secondary reflection occurs from the outside surface of a coaxial, confocal hyperbola instead of from the inside as in a Wolter I optic. X-rays are focused to the further focal point of the hyperbola.

profiles are thus compounded by the need to co-align them all. In order to simplify this task, the conical section mirrors of high throughput telescopes are sometimes approximated by cones (e.g. the Broad Band X-Ray Telescope BBXRT (Petre *et al.*, 1991) and the Advanced Satellite for Cosmology and Astrophysics, ASCA (Tanaka *et al.*, 1994)).

A microchannel Wolter optic consists of two coaxial radially-packed micropore optics, each slumped such that the concentric rings of channels form conical approximations to the true Wolter geometry. The microscopic dimensions of the ring spacing in the optics effectively provide an enormous number of nested shells for a low geometric area and mass. Figure 1.8 in chapter 1 shows schematically the radial-packing pattern and the relative slump radii of the two successive MPOs in a Wolter type I approximation.

5.2.1 Wolter geometry

There are many publications detailing the mathematical treatment of the Wolter I geometry (Mangus and Underwood, 1969; VanSpeybroeck and Chase, 1972). The Wolter I mirror system shown in Figure 5.1 has the origin of the co-ordinate system and the

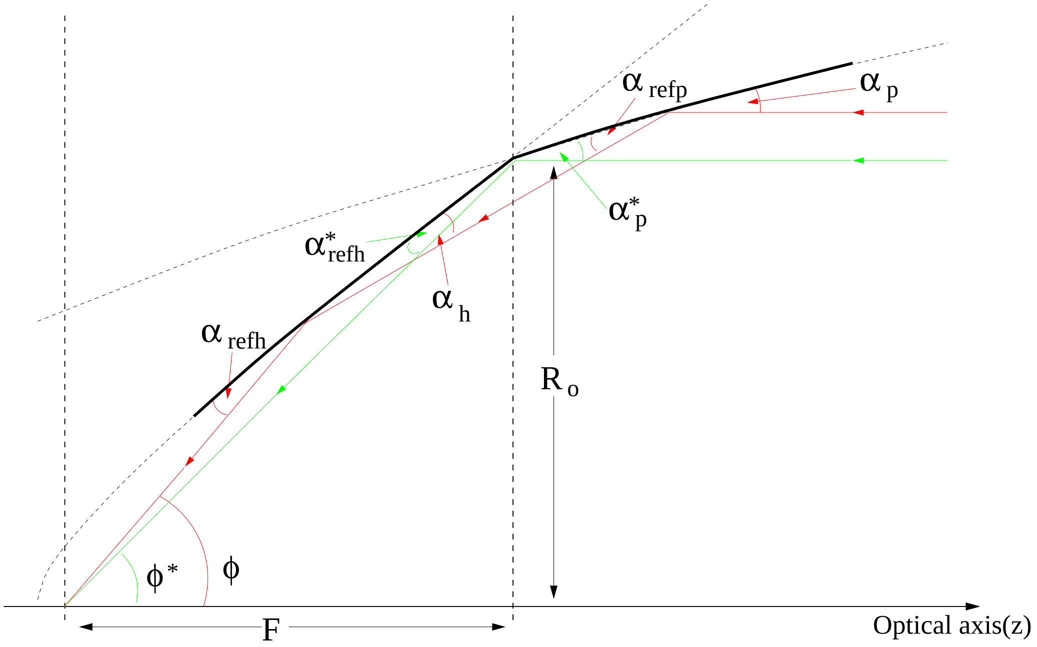

Figure 5.3: Ray path through a Wolter type I mirror system. The star superscript refers to reflections occurring an infinitesimal distance from the parabola/hyperbola interface (green ray).

parabola coincident. The equations describing the confocal parabola and hyperbola are then

$$y_{parabola}(z) = \sqrt{4az} \tag{5.1}$$

$$y_{hyperbola}(z) = \sqrt{(1-e^2)((z-ge-a)^2-g^2)} \tag{5.2}$$

where a is the focal length of the parabola, g is the distance between the centre and vertices of the hyperbola and ge is the focal length of the hyperbola. From the point where the parabola and hyperbola intersect, we can define the focal length, F, of the system and its radius, R_o.

By considering the incident and reflected angles of a ray passing through the mirror system (Figure 5.3) we can derive formulae for the mirror parameters. In this derivation, θ represents the angle between the tangent to a mirror section and the optical (z) axis; α the grazing angle a ray makes with the mirror section tangents and ϕ the angle between a ray and the optical axis.

Considering a ray from a source at infinity striking the parabola at some point (red ray in figure 5.3), its angle of reflection relative to the optical axis will be

$$\phi_{refp} = \alpha_{refp} + \theta_p = \alpha_p + \theta_p \tag{5.3}$$

where θ_p is the angle between the tangent to the parabola and the optical axis at the incident position. Since the ray is from infinity, $\theta_p = \alpha_p$ so that

$$\phi_{refp} = 2\alpha_p = 2\theta_p \tag{5.4}$$

The next reflection will occur on the hyperbola, where the grazing angle of incidence α_h is given by

$$\begin{aligned} \alpha_h &= \theta_h - \phi_{refp} && (5.5) \\ &= \theta_h - 2\alpha_p && (5.6) \\ &= \theta_h - 2\theta_p && (5.7) \end{aligned}$$

Here, θ_h is the angle between the tangent to the hyperbola and the optical axis at the incident position. The angle that the emergent ray makes with the optical axis is thus

$$\begin{aligned} \phi &= \theta_h + \alpha_{refh} && (5.8) \\ &= \theta_h + \alpha_h && (5.9) \\ &= 2\theta_h - 2\theta_p && (5.10) \end{aligned}$$

If we consider a pair of reflections occurring an infinitesimal distance either side of the join between the parabola and hyperbola (the green ray at the dashed vertical line in Figure 5.3), we can write the focal length in terms of the final reflected angle and mirror radius

$$F = \frac{R_o}{\tan \phi^\star} \tag{5.11}$$

The $\star$ superscript refers to reflections taking place at the parabola/hyperbola boundary. VanSpeybroeck and Chase (1972) find that if the mirror parameters are such that the incident angles on both the parabola and hyperbola at the boundary are equal (i.e. $\alpha_p^\star = \alpha_h^\star = \alpha^\star$), then the collecting area of the system and X-ray reflectivities at short wavelengths are maximised for a given diameter to focal length ratio, with very little loss in angular resolution. As $\theta_p = \alpha_p$, we are able to write equation (5.7) as

$$\theta_h^\star = \alpha_h^\star + 2\alpha_p^\star = 3\alpha^\star \tag{5.12}$$

Hence we know that at the boundary between the parabola and hyperbola

$$\theta_h^\star = 3\theta_p^\star \tag{5.13}$$

Thus, from equation (5.10), the final reflected angle is found to be $\phi^\star = 4\alpha^\star$ and the focal length can be written as

$$F = \frac{R_o}{\tan 4\alpha^\star} \tag{5.14}$$

where $\alpha^\star$ is the incident angle of the ray at the parabola/hyperbola boundary.

5.2.2 Microchannel conic approximations

In a conic approximation to the Wolter I geometry, the angles of the two cones are chosen to maximise effective area and resolution. In the case of the microchannel Wolter optic, where the lengths of the two sections (L_{parab} and L_{hyp} in Figure 5.1) are small and there will be little deviation from the ideal conic section, the ratio of angles at the cone intersection described by equation (5.13) is maintained (i.e. $3\theta_p = \theta_h$).

With this in mind it is possible to analyse the path of rays through the microchannels and derive lens equations for the system. Figure 5.4 shows the reflections made by a ray in the conic approximation to a Wolter type I optic.

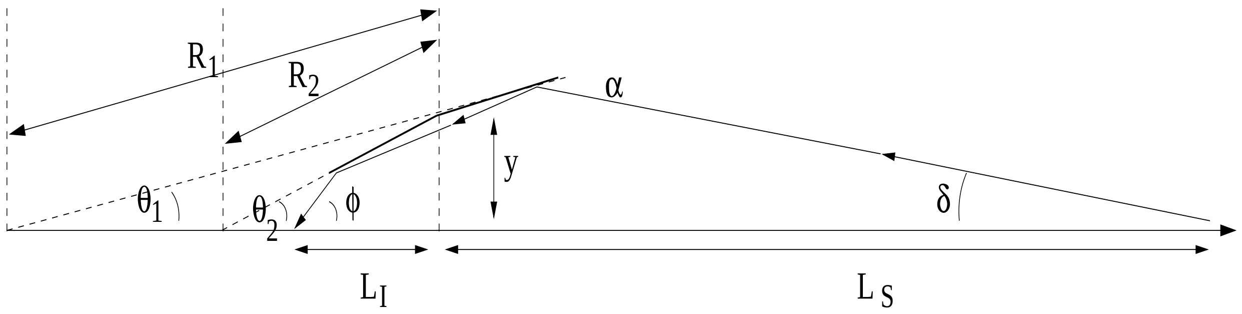

Figure 5.4: Reflection of an X-ray from a single Microchannel Wolter optic surface. Here L_S is the source distance and L_I the image distance. R_1 and R_2 are the slump radii of the two successive micropore optics. θ_1, θ_2, ϕ and δ are angles subtended to the optical axis by the first and second conic sections and by the emergent and incident rays respectively.

The ray, from a source at a finite distance, L_S, from the optic strikes it a radial distance y from the optical axis. Here L_S is the source distance from the centre of the optic

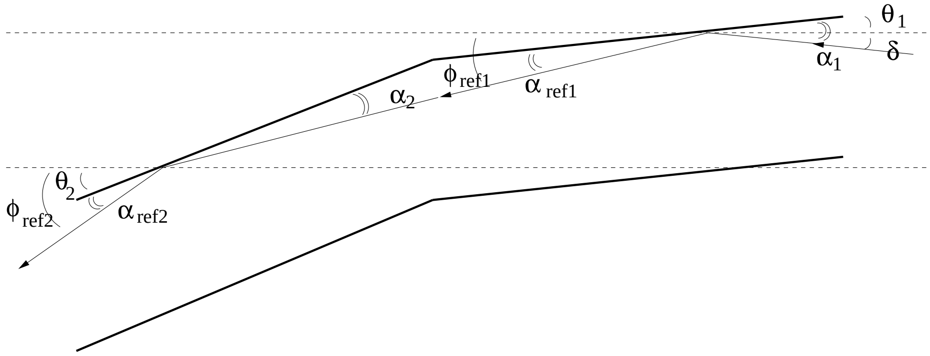

Figure 5.5: Reflection of a ray through a microchannel conic approximation to a Wolter type I optic.

(i.e. the intersection between parabola and hyperbola) and L_I the image distance. In a microchannel Wolter optic, the two successive MPOs are slumped to radii of R_1 and R_2 respectively. As the angles made with the optical axis (θ_1 and θ_2) are small, the change in y between the reflections can be considered as negligible and we can adopt the small angle approximations; $\sin a = a$ and $\tan a = a$ (i.e. $\phi = \frac{y}{L_I}$, $\delta = \frac{y}{L_S}$, $\theta_1 = \frac{y}{R_1}$ and $\theta_2 = \frac{y}{R_2}$). The relation of equation (5.13) can then be written in terms of the slump radii of the MPOs

$$R_1 = 3R_2 \tag{5.15}$$

Figure 5.5 shows, in detail, the path of the ray through two microchannels in a Wolter I optic arrangement. The first grazing reflection angle, α_1 is the sum of the conic section angle and the incident angle of the ray, $\alpha_1 = \delta + \theta_1$. The reflected angle to the optical axis is then

$$\phi_{ref1} = 2\theta_1 + \delta \tag{5.16}$$

The incident grazing angle in the second conic section is

$$\begin{aligned} \alpha_2 &= \theta_2 - \phi_{ref1} && (5.17) \\ &= \theta_2 - 2\theta_1 - \delta && (5.18) \end{aligned}$$

Thus, the angle the emergent ray makes to the optical axis is

$$\begin{aligned} \phi_{ref2} &= \theta_2 + \alpha_{ref2} && (5.19) \\ &= 2\theta_2 - 2\theta_1 - \delta && (5.20) \end{aligned}$$

Using the definitions of the angles from above, the angle formula can be written in terms of distances along the optical axis

$$\frac{1}{L_I} = \frac{2}{R_2} - \frac{2}{R_1} - \frac{1}{L_S} \tag{5.21}$$

This gives a focal length, when viewing an infinitely distant source (i.e. $1/L_S = 0$), of $R_1/4$. There is, however, a constraint that applies to this mode of operation. The ray reflected from the first surface (parabaloid approximation) must strike the second (hyperbaloid approximation). This constraint can be expressed as

$$\begin{aligned} \phi_{ref1} &< \theta_2 && (5.22) \\ 2\theta_1 + \delta &< \theta_2 && (5.23) \end{aligned}$$

Knowing that $\theta_2 = 3\theta_1$ this can be written

$$\delta < \theta_1 \tag{5.24}$$

or

$$R_1 < L_S \tag{5.25}$$

In the event of the incident angle exceeding this boundary condition, then the ray can be incident upon the opposite side of the channel in the second micropore optic (Figure 5.6). In this mode, the microchannel system is approximating not the type I Wolter optic, but the type II (shown in Figure 5.2). Analysis of the angles in Fig. 5.6 leads to the following lens equations

$$\begin{aligned} \phi_{ref2} &= 2\theta_2 - 2\theta_1 - \delta && (5.26) \\ \frac{1}{L_I} &= \frac{2}{R_2} - \frac{2}{R_1} - \frac{1}{L_S} && (5.27) \end{aligned}$$

In summary, the microchannel Wolter optic, because it has close-packed, parallel reflective walls can operate in both Wolter type I and Wolter type II modes. The lens equation remains the same, the mode changing when the primary incident angle becomes larger than the angle the first cone makes with the optical axis.

There are, of course, other reflection modes as the angle of the primary incident ray changes. For sources a long way off-axis (i.e. for large δ), there will be the possibility of

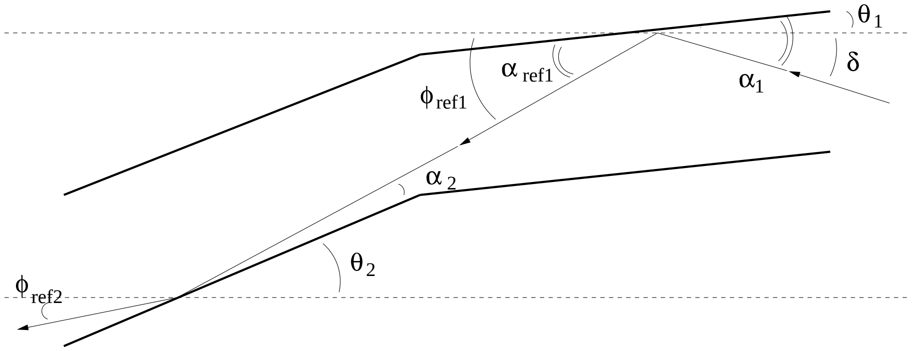

Figure 5.6: Microchannel conic approximation to a Wolter type II optic.

more than two reflections occurring through the system, adding complicated artefacts to the image. It is easier to deal with these problems within a computer model instead of seeking analytical solutions. Section 3.6 describes the raytrace model developed for such applications.

In the following sections, a theoretical investigation of both a planar point-to-point focusing MPO and a microchannel Wolter optic supplied by Photonis SAS as part of the ESA TRP programme is undertaken.

5.3 The micropore optics

One of the deliverables of the ESA TRP contract at Photonis was a series of radially-packed boules of square-pore square-packed multifibres. These were to start as planar radially-packed optics and culminate in the production of a slumped Wolter pair. Ideally, the multifibres would be of trapezoidal cross-section to minimise free space between adjacent fibres. However, it was decided that due to difficulties in drawing and stacking such shapes it would be better to first attempt this procedure with standard square-pack multifibres (Boutot *et al.*, 2000).

In spring 2000, Leicester took delivery of several planar radially-packed plates from boule A, a 50mm diameter boule packed around an 8mm diameter solid lead glass centre. These were manufactured with a cladding/core glass combination of Corning 8161 and Circon

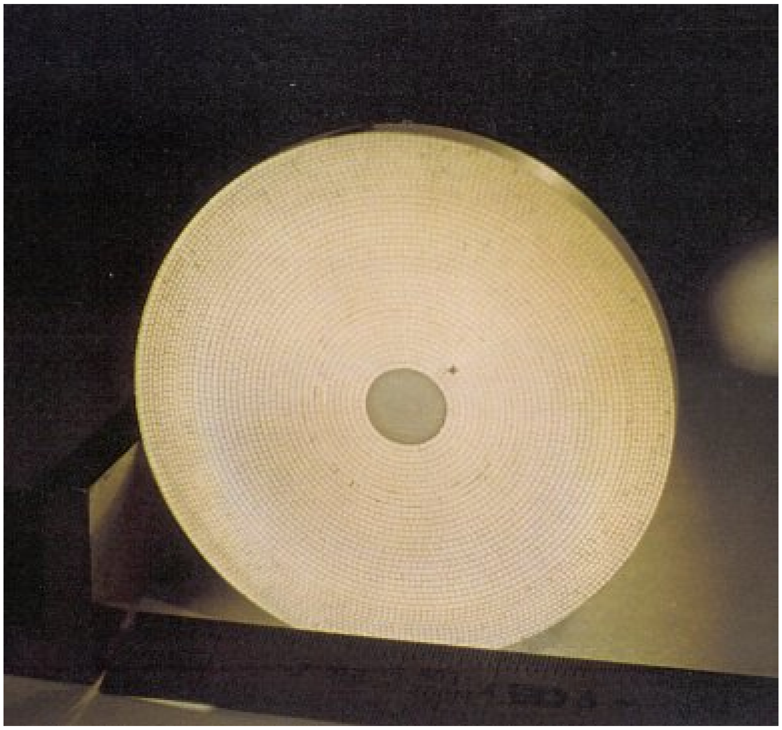

Figure 5.7: A solid core flat radially-packed micropore optic of the type tested at Leicester (From Boutot *et al.* (2000)).

ACMI RE695 respectively. A photograph of a solid core flat radially-packed micropore optic is shown in Figure 5.7.

The final deliverables of the TRP programme, a twin set of radially-packed slumped plates that together made up a conic approximation to a Wolter type I optic, arrived in autumn of the same year. These MPOs came from boule E, a 60mm diameter boule manufactured as for A with the following two important differences:

i) A thermal expansion co-efficient mismatch between the core glass and channel glass induced stresses that caused MPOs cut from boule A to disintegrate. In boule E, the solid core was omitted, a hexagonal fibre from a conventional round-pore microchannel detector plate was used as the boule centre.

ii) As stated in section 4.4, it was thought that the high lead content of Corning 8161 glass would result in the production of more reflective MPOs at high X-ray energies. In practice it was found that during the long etching processes required to

Description	Boule	Serial number	Slump radius	L/D	Diameter
Planar MPO	A	FE-001-R4	∞	500:1	50mm
First Wolter MPO	E	GB-001-R4	20m	500:1	60mm
Second Wolter MPO	E	GB-001-R3	6.67m	500:1	60mm

Table 5.1: Properties of the radially-packed MPOs evaluated in this thesis.

clean large aspect ratio channels of the core glass to the necessary finish, the glass became degraded. This contributed in part, along with the stresses induced by the thermal mismatch, to the mechanical fragility of the MPOs from boule A. Boule E was manufactured from a cladding/core combination of Philips 297 and 274 glasses respectively.

The microchannel Wolter optic was fabricated with a focal length of 5m ($R_1 = 20$m and $R_2 = 6.67$m from equations (5.15) and (5.27)). Table 5.1 summarises the properties of radially-packed optics that appear in this thesis.

The multifibres are common to those used throughout the rest of the TRP micropore optic programme (square-packed bundles of 55×55 square channels of 10μm side length on a 12μm pitch). Synchrotron measurements (Beijersbergen *et al.*, 2000b,a) find the image quality of individual channels and multifibres to concur with those from square-packed MPOs. The surface roughness of the channels walls is 15Å rms with multifibre image quality varying between $20''$ and $2'$.

5.4 Raytrace models of the optics

Using the computer model described in section 3.6, rigorous raytracing simulations can be run to predict the response of a micropore optic. This section predicts the behaviour of the planar radially-packed and Wolter MPOs described in section 5.3 for three cases:

i) Perfectly aligned fibres and multifibres, perfectly smooth channel walls

ii) Perfectly aligned multifibres. Channel roughnesses and inter-channel alignment errors as found experimentally (Beijersbergen *et al.*, 1999, 2000b,a) and described in section 5.3.

iii) Inter-channel alignment errors as in (ii). Multifibres randomly misaligned with an rms magnitude of $2'$.

The results are calculated with on and off-axis sources. To create the off-axis effect, the MPOs are tilted by $3.44'$ (1mrad) about the vertical (y) axis with respect to the beam, as it is done experimentally (chapter 6). The quantitative MPO responses are calculated as described for all MPO images in section 3.5.

5.4.1 Planar radially-packed micropore optics

A radially-packed MPO displays symmetry about its optical axis and hence its behaviour is easy to analyse with an on-axis source. In the planar point-to-point focusing format, the optic will obey the simple relation $L_I = L_S$, i.e. the MPO is equidistant between the source and image. The cruxiform structure that defines a lobster eye focus will be absent as a result of the symmetry about the optical axis.

However, when the source moves off-axis with respect to the MPO severe coma will result, as would be expected for reflections from the inside of a cylinder (Figure 5.8).

Raytraced images from MPO FE-001-R4, situated at the TTF mid-point ($L_S = L_I =$ 10m), are shown in Figure 5.9 for the different alignment models with the source both on and off-axis. Images (a) and (d) are for perfectly aligned optics with perfectly smooth channel walls, (b) and (e) with inter-channel alignment errors described above (ii) and (c) and (f) with the additional inter-multifibre tilts (iii). It can be seen that with a modest misalignment the focus and comatic circle broaden, and as the errors approach the magnitude of the tilt angle the circle becomes so blurred the results become virtually indistinguishable. As can be seen, even very small misalignments radically alter the

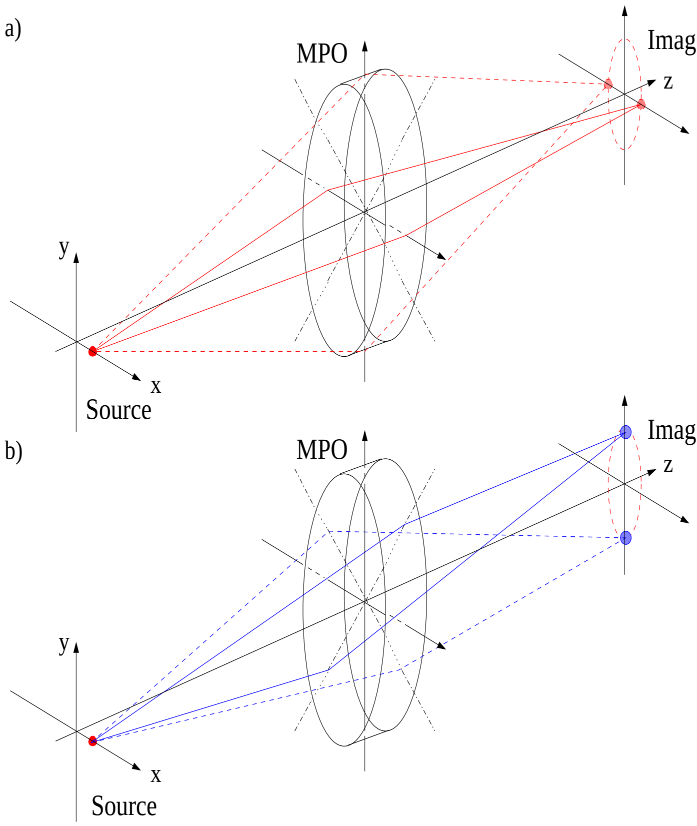

Figure 5.8: Reflections from the inside wall of a cylinder give rise to coma when the source is off-axis. Reflections from opposite sides of the cylinder give rise to points on the image plane. (a) shows how the opposite image point arise on the horizontal axis (b) on the vertical. If this is integrated all the way around the cylinder, a comatic circle will result in the image plane.

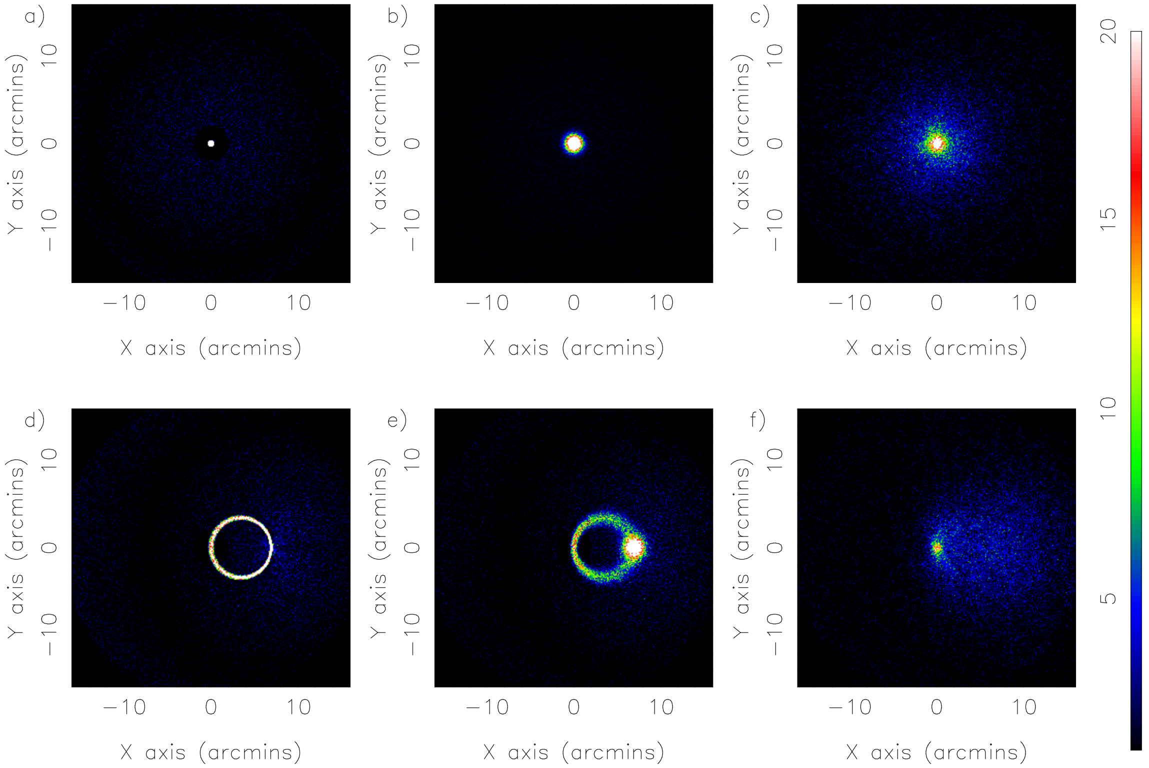

Figure 5.9: Raytraced images of the planar radially-packed MPO FE-001-R4 illuminated in the TTF with W-L (8.4keV) X-rays. In images (a) to (c) the source is on-axis and in (d) to (f) the optic is tilted by $3.44'$ about the vertical axis. (a) and (d) have all channels perfectly aligned, (b) and (e) have 15Å surface roughness (1μm correlation length) and $20''$ rms channel misalignment within multifibres, while (c) and (f) have an additional $2'$ rms inter-multifibre misalignment. $1'$ corresponds to 2.9mm on the detector.

performance of a micropore optic.

A useful way of looking at both the effective area and resolution of an image is to view the encircled fraction of the total flux in the image and the cumulative intensity as a function of the radius of the encircled area on the detector. Figure 5.10 shows the encircled flux and cumulative intensity as a function of radius for the on-axis data shown in Figure 5.9.

The on-axis effective area and resolution curves for FE-001-R4 are shown in Figure 5.11. All three alignment scenarios outlined above are included. A qualitatively similar X-ray optical response to that shown in Figure 5.9 is expected for all flat, radially-packed MPOs, the quantitative performance changing with channel aspect ratio, multifibre size, MPO diameter etc.

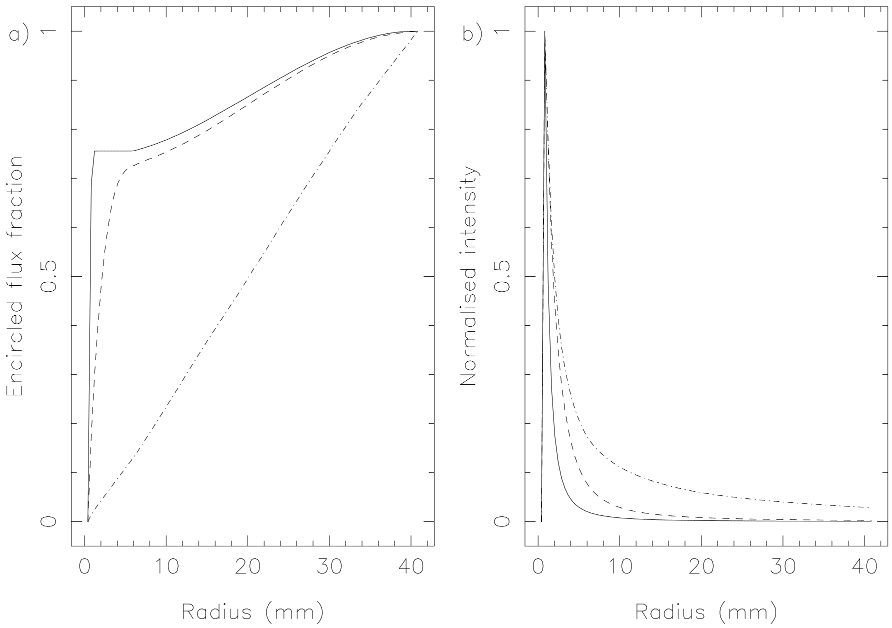

Figure 5.10: (a) the encircled flux and (b) cumulative intensity as a function of radius for the calculated on-axis point spread functions of MPO FE-001-R4 when illuminated with W-L $(8.4$keV$)$ X-rays in the TTF. The perfectly aligned (solid line), weakly (dashed) and strongly misaligned (dash-dot) data comes from the datasets shown in Figure 5.9(a, b, c).

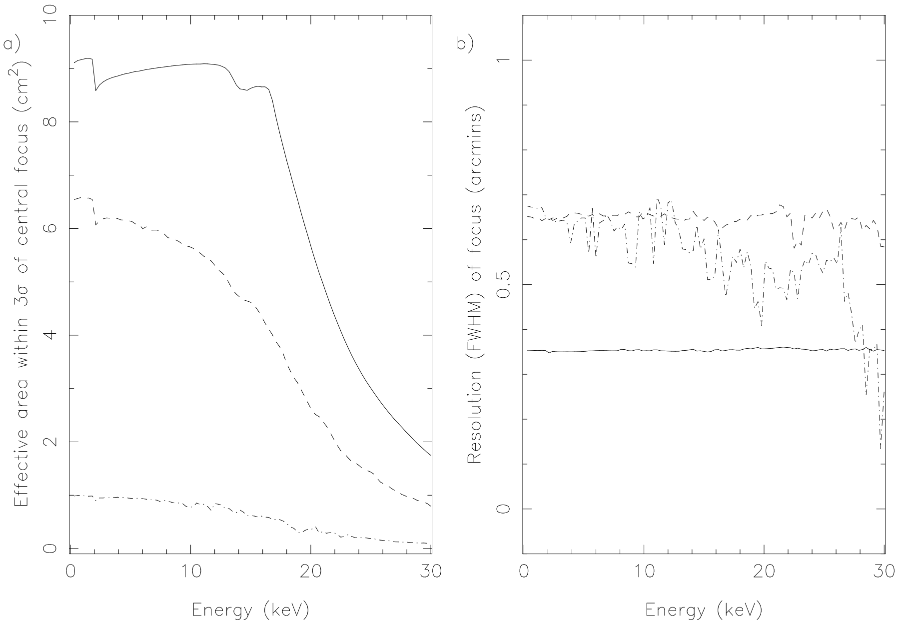

Figure 5.11: (a) the effective area and (b) resolution curves for MPO FE-001-R4 when illuminated with on-axis X-rays in the TTF. The solid lines are for a perfect optic, dashed correspond to channels with 15Å roughness on a 1μm correlation length and $20''$ rms misalignment. The Dash-dot lines show an additional $2'$ rms inter-multifibre misalignment.

5.4.2 Microchannel Wolter optics

Analysis of the Wolter lens equation (Eqn. (5.27)) with respect to the possible configurations of the TTF (section 3.2.2) showed the only combination of source and image distances that allowed the optic to be accommodated in direct focus to be $L_S = L_I = 10$m. In this position the requirement for Wolter type I operation, as specified in equation (5.25), is not satisfied. When tested in the TTF, the microchannel Wolter optic was *operating in a Wolter type II mode* as shown in Figure 5.6. A brief comparison of the optic's response to X-rays from infinity (i.e. when operating in Wolter I mode with $L_I = 5$m) and when in the TTF with $L_S = L_I = 10$m is given in this section.

Raytraced images with the source at infinity are shown in Figure 5.12. Both on and off-axis datasets are shown for all three alignment scenarios described above. The images calculated using exactly the same alignment and tilt parameters, but with the optic located at the mid-point of the TTF are shown in Figure 5.13.

As in the case of a simple lens, a Wolter optic produces an inverted image in which the angle subtended between a source point and the optical axis at the optic and the corresponding image point and optical axis at the optic are identical. As an optic is tilted the focus is, therefore, expected to remain in the centre of the image, as is seen in the figures.

The effective area of the optic as functions of energy and off-axis angle when illuminated with X-rays from both an infinite source and in the TTF are shown in Figures 5.14 and 5.15 respectively.

The small effective area when on-axis and perfectly aligned results from a combination of the small optic diameter and low L/D ratio together with the large slump radius of the first MPO. This means that only a small proportion of the X-rays incident upon the front MPO will undergo a reflection and exit with the correct angle to be incident upon the second MPO's outer channel surfaces. If the optic is tilted (or imperfections tilt individual channels), the angles subtended by incident rays on the front MPO's channel

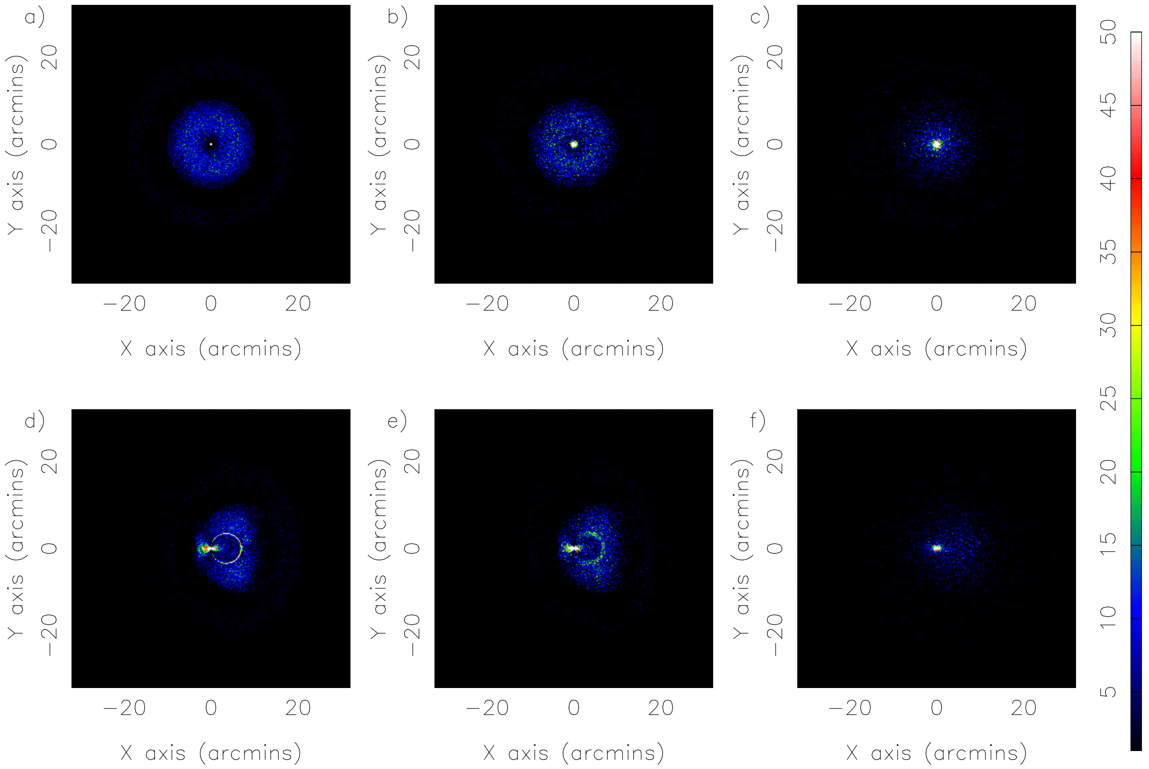

Figure 5.12: Raytraced images of the microchannel Wolter optic illuminated with W-L (8.4keV) X-rays from infinity (operating in Wolter type I mode). In images (a) to (c) the source is on-axis and in (d) to (f) the optic is tilted by $3.44'$ about the vertical axis. (a) and (d) have all channels perfectly aligned, (b) and (e) have 15Å surface roughness (1μm correlation length) and $20''$ rms channel misalignment within multifibres, while (c) and (f) have an additional $2'$ rms inter-multifibre misalignment. $1'$ corresponds to 1.45mm on the detector.

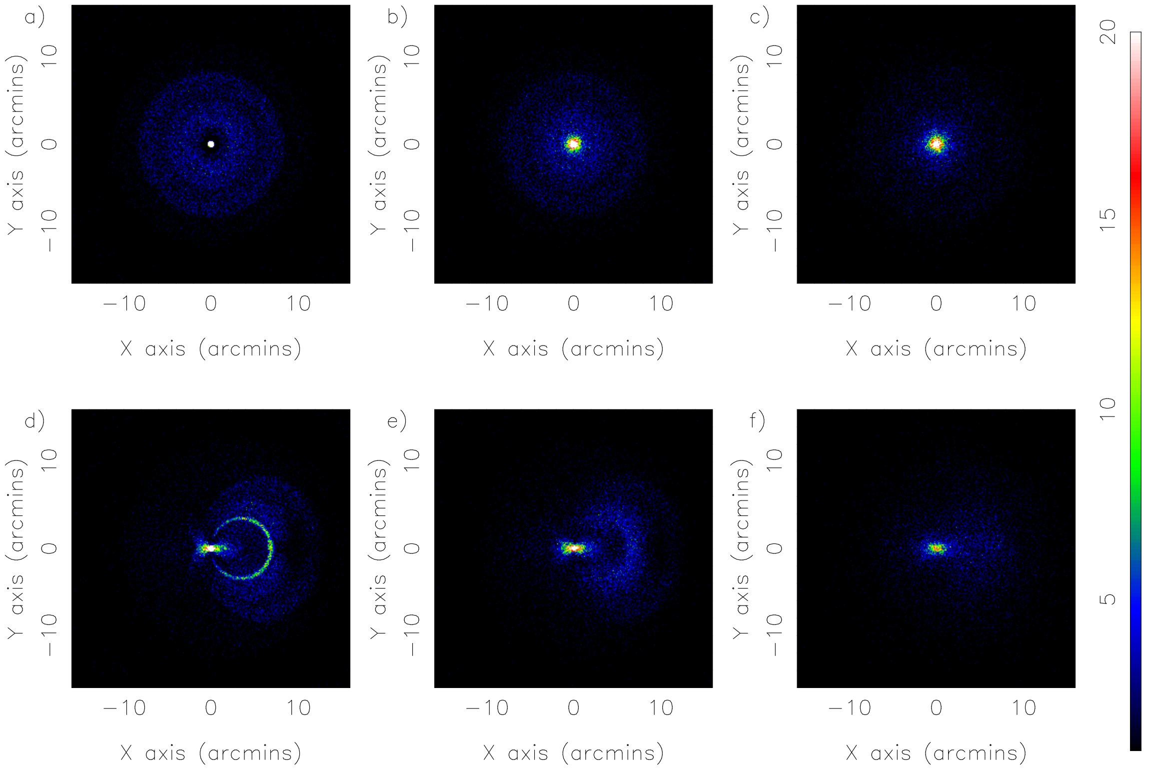

Figure 5.13: Raytraced images of the microchannel Wolter optic illuminated with W-L (8.4keV) X-rays at the mid-point of the TTF ($L_S = L_I = 10$m, operating in Wolter type II mode). In images (a) to (c) the source is on-axis and in (d) to (f) the optic is tilted by $3.44'$ about the vertical axis. (a) and (d) have all channels perfectly aligned, (b) and (e) have 15Å surface roughness (1μm correlation length) and $20''$ rms channel misalignment within multifibres, while (c) and (f) have an additional $2'$ rms inter-multifibre misalignment. $1'$ corresponds to 2.9mm on the detector.

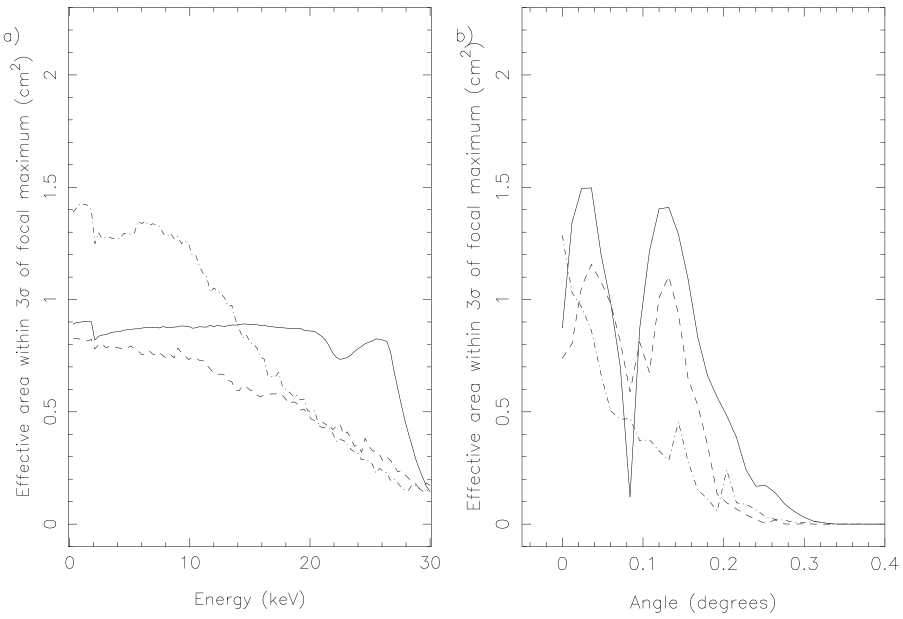

Figure 5.14: **Calculated effective area curves for the microchannel Wolter optic with the source at infinity. The on-axis response as a function of energy is shown in** (*a*) **and as a function of off-axis angle at** 8.4**keV in** (*b*). **The solid line corresponds to a perfect plate; dashed line - rms inter-channel misalignment of** $20''$ **and surface roughness of** 15Å **rms; dash-dot line an additional** $2'$ **rms inter-multifibre misalignment.**

surfaces increase this proportion and, therefore, the effective area. In order to get larger effective areas with the same slump radii, larger channel aspect ratios or bigger diameter optics are required. When located in the TTF, the finite source distance means that larger angles are subtended at the channel entrances and consequently larger effective areas are seen.

The effective area is low compared to that calculated by Willingale *et al.* (1998). This is attributed to a change in the channel geometry (Willingale *et al.* use 12.5μm channels on a 15μm pitch), a reduced open area fraction (0.61 c.f. 0.69) as a result of packing square multifibres in a radial pattern in TRP optics and only including events within 3σ of the focal maximum instead of 10mm. If these changes are included in the model, the data of Willingale *et al.* is recreated.

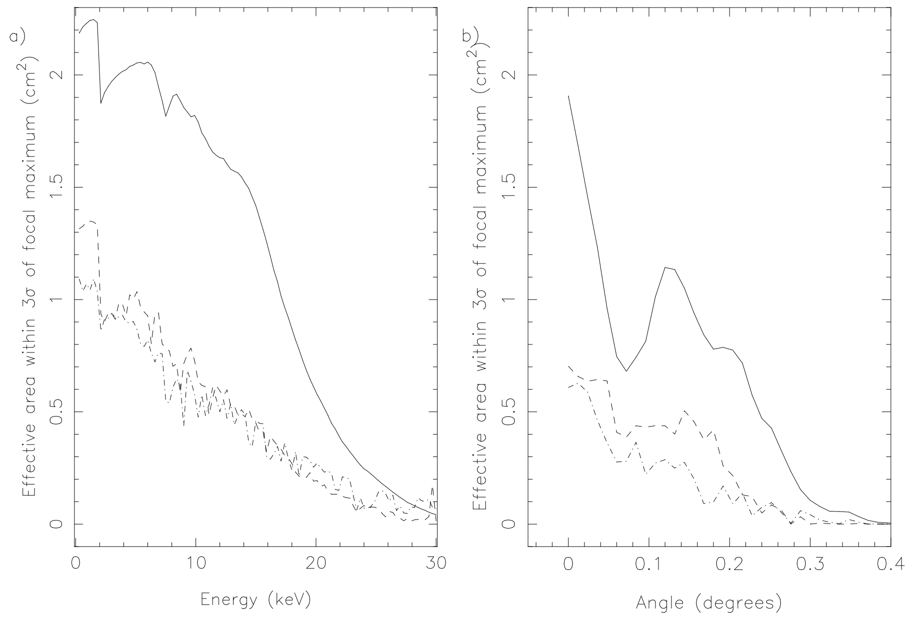

Figure 5.15: Calculated effective area curves for the microchannel Wolter optic at mid-point of the TTF ($L_S = L_I = 10$m). The on-axis response as a function of energy is shown in (a) and as a function of off-axis angle at 8.4keV in (b). The solid line corresponds to a perfect plate; dashed line - rms inter-channel misalignment of $20''$ and surface roughness of 15Å rms; dash-dot line an additional $2'$ rms inter-multifibre misalignment.

5.5 Conclusions

The micropore optic realisation of the conic approximation to the Wolter type I and II grazing incidence X-ray optics has been introduced. The optic moves smoothly between the two modes of operation, obeying the same lens equation either side of the transition point.

Raytrace models of both a microchannel Wolter optic and a single planar radially-packed MPO have shown how they are expected to behave when perfectly aligned and with alignment errors randomly selected from Gaussian distributions. These show that single radially-packed MPOs are unlikely to have any practical application as any off-axis movement results in severe comatic distortion. The conic Wolter approximation, however, has shown that it is capable of true imaging with reasonable resolution and effective area but with the advantage of very low mass.

Chapter 6

Microchannel Wolter optics: Experiment

6.1 Introduction

Following the theoretical introduction of the microchannel Wolter optic in the previous chapter, the experimentally observed responses are now described. The observed full face illumination images of the single planar MPO FE-001-R4 and Wolter pair GB-001-R3 and GB-001-R4 are first described. The raytrace model is then used to model the misalignments in each optic. The proposed Wolter type I optics for the High Energy Remote-sensing of Mercury's Surface (HERMES) X-ray imaging fluorescent spectrometer on ESA's BepiColombo Mercury orbiter (section 1.5.2) is then discussed in the light of the current status of radial/Wolter pack MPOs.

6.2 Experimental set-up

Both the planar radially-packed MPO and the Wolter pair were tested in the TTF (section 3.2.2). Both were also located at the mid-point port of the beamline ($L_S = L_I = 10$m).

This satisfies the point-to-point focusing conditions of the planar optic and, as described in section 5.4, allows the accommodation of the Wolter approximation in direct focus (operating, however, in type II mode). The procedure for each optic followed the same path:

i) The plate is aligned mechanically by reflecting laser light from the centre of the detector flange off the MPO centre and back to its origin. This method is illustrated in Figure 6.1.

ii) The MPO is then finely aligned so that the source is on-axis using X-rays. This is done through both the maximisation of the count rate falling on the detector and visual inspection of images formed on the MCP detector.

iv) The detector is driven through the focus of the MPO along the z-axis to determine the best focus (range ±400mm - section 3.2.2). This is more appropriate to short focal length slumped MPOs as optics at the mid-point have a large focal depth (a 400mm drive corresponds to 1mm maximum increase on detector in perfect optic).

iii) The plate is rotated about the x and y axes to determine its off-axis response.

v) If appropriate, the MPO is illuminated with the different energy bands described in section 3.6.2.

Effective areas, gains and resolutions are calculated as described in section 3.5. The images were captured using the MCP detector described in section 3.3.

6.3 Planar radially-packed MPO FE-001-R4 results

The radially-packed MPO FE-001-R4 is described in section 5.3. Figure 6.2 shows a deep on-axis image taken with W-L (8.4keV) X-rays following alignment of the optic. The first thing to note is the presence of a focus at the centre of the image. This is certainly a true focus as the 8mm diameter, 5mm thick lead glass core of the optic will prevent any

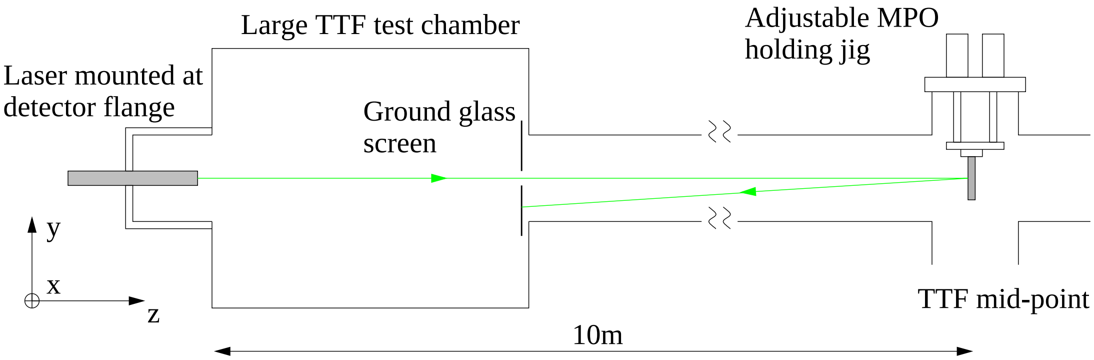

Figure 6.1: To mechanically align the MPO perpendicular to the optical axis of the TTF, a laser is used. First the optical axis is determined by aligning the laser beam from the centre of the detector flange with the centre of a ground glass screen at the far end of the test chamber and the centre of the MPO manipulator at the TTF mid-point. The MPO is then rotated about the x and y axes until the laser beam is reflected back to the centre of the ground glass screen.

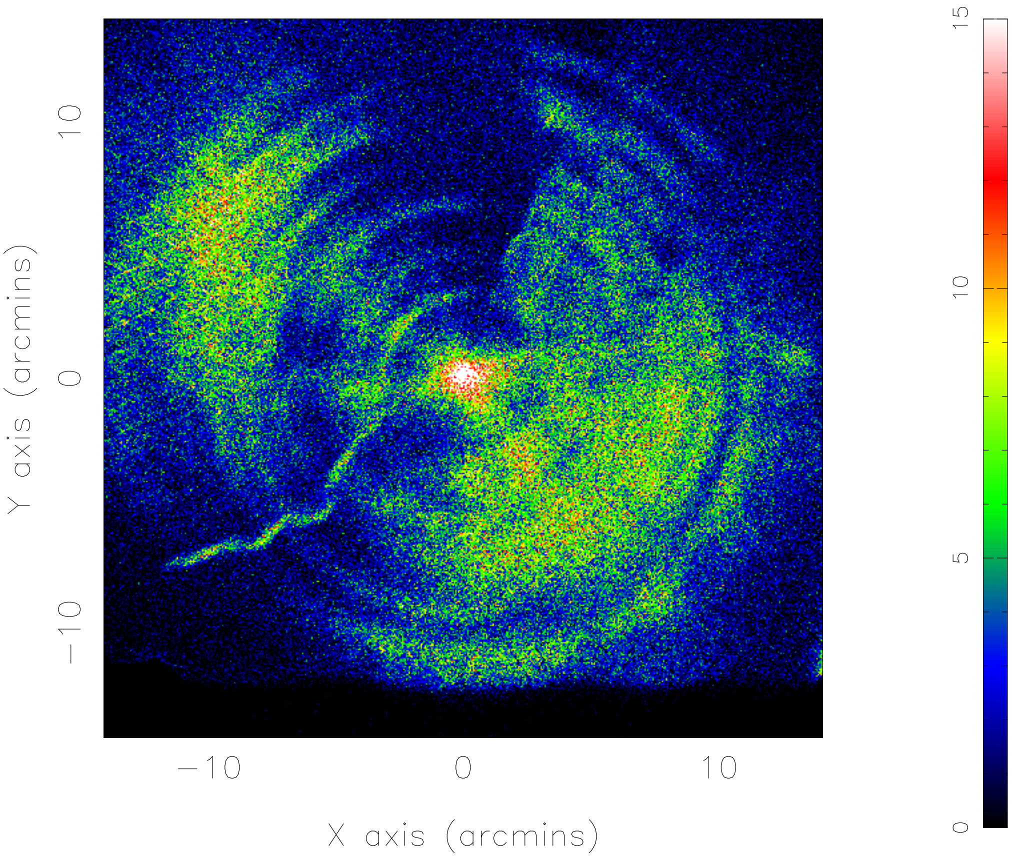

Figure 6.2: Linerarized deep (1×10^6 counts) on-axis image of MPO FE-001-R4 illuminated in the TTF with W-L (8.4keV) X-rays. The cross hatching to the left of the image is an artefact of the linearization process. The line starting in the bottom left hand corner and propagating to the centre of the image is a crack in the MPO itself.

Off-axis angle (Degrees)	FWHM resolution (arcmins)	Effective area (cm^2)	Peak gain
on-axis	1.6	0.67 ± 0.1	4.9 ± 1.5
0.033 ± 0.01	1.2	0.21 ± 0.04	3.6 ± 1.2
0.066 ± 0.01	1.7	0.15 ± 0.03	3.6 ± 1.2
0.100 ± 0.01	1.4	0.16 ± 0.03	2.7 ± 1.0
0.165 ± 0.01	0.6	0.046 ± 0.008	1.9 ± 0.6
0.231 ± 0.01	N/A	N/A	N/A

Table 6.1: The measured resolution, effective area and peak gain of the radially-packed planar MPO FE-001-R4 when illuminated in the TTF with W-L (8.4keV) X-rays at various tilt angles. The corresponding images are shown in Figure 6.3.

unreflected transmission into this region. The simultaneous presence of what appear to be partial comatic circles and a central focus suggest the presence of large scale multifibre misalignments in the optic. The concentric rings surrounding the focus are most likely due to uneven transmission through different multifibre rings, suggesting misalignment errors between each ring. The fact that some sectors of the MPO exhibit very little transmission points towards the presence of large scale azimuthal misalignments. This hypothesis is further supported by the fact that the MPO has several physical cracks running across it, as can be seen via the leaked X-rays in Figure 6.2.

The off-axis response of the MPO as it is tilted in the X-ray beam is shown in Figure 6.3. This figure only shows one tilt direction, but the behaviour is symmetric in either direction about both tilt axes. The resolutions, effective areas and peak channel gains of the images in Figure 6.3 are shown in Table 6.1. Table 6.2 lists the on-axis values for a variety of illumination spectra together with perfect optic values, calculated with the raytrace code, for comparison.

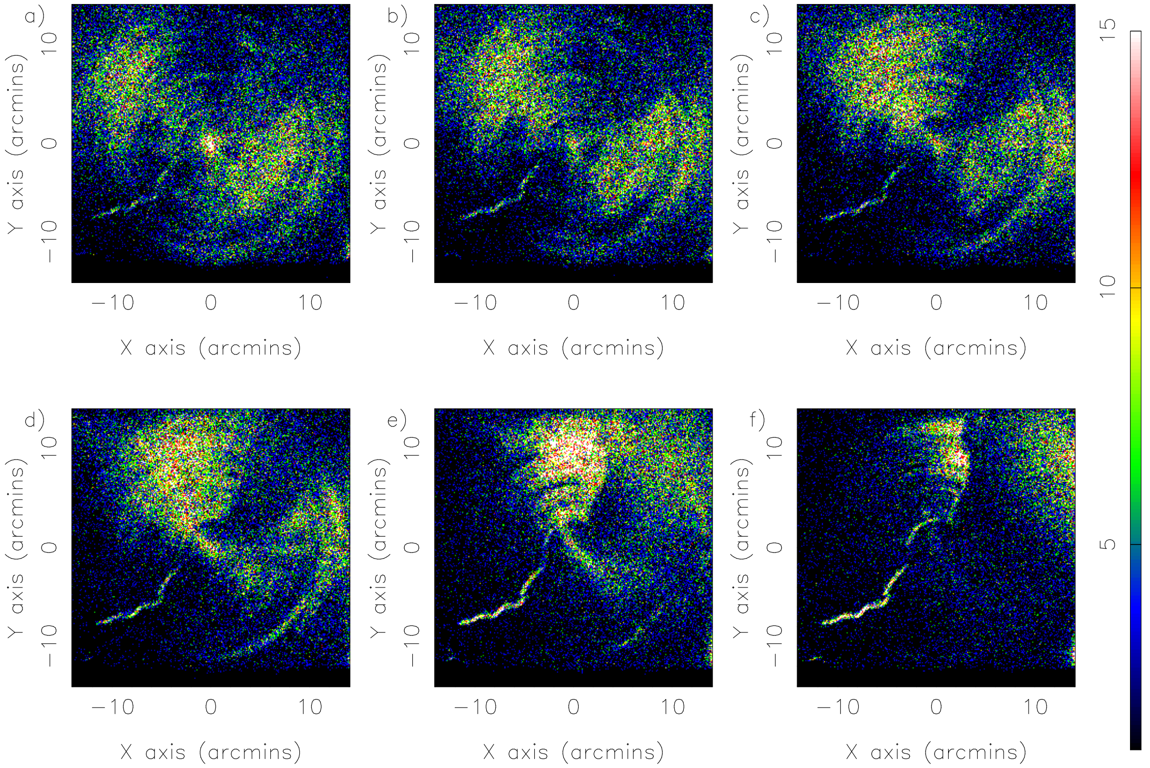

Figure 6.3: Series of linerarized images showing the MPO FE-001-R4 response as it is tilted in the W-L (8.4keV) X-ray beam. Image (a) is on-axis, (b) has a 0.033° tilt, (c) 0.066°, (d) 0.1°, (e) 0.165° and (f) 0.231°. The line originating in the bottom left hand corner corresponds to a crack in the MPO. In these images the plate was rotated about its horizontal (x) axis in a clockwise direction, but the behaviour is symmetric as it is tilted about the other axis.

X-ray energy (keV)	Measured (FE-001-R4)			Calculated (perfect MPO)		
	Res	Area	Gain	Res	Area	Gain
8.40 (W-L)	1.6	0.67 ± 0.1	4.9 ± 1.5	0.36	9.4	931
17.44 (Mo-K)	1.56	0.26 ± 0.04	2.4 ± 0.9	0.36	6.6	687
25.27 (Sn-K)	0.6	0.03 ± 0.006	1.7 ± 0.8	0.36	2.3	231

Table 6.2: The measured on-axis resolution, effective area and peak channel gain of MPO FE-001-R4 at different TTF energy settings. The resolutions are in arcminutes and effective areas in square centimetres. Perfect MPO calculations are shown on the right for comparison.

Off-axis angle (Degrees)	FWHM resolution (arcmins)	Effective area (cm^2)	Peak gain
on-axis	1.60	0.27 ± 0.05	2.7 ± 0.9
0.060 ± 0.01	1.32	0.42 ± 0.07	3.8 ± 1.2
0.086 ± 0.01	1.22	0.33 ± 0.06	3.3 ± 1.1
0.104 ± 0.01	0.90	0.23 ± 0.04	2.3 ± 0.8
0.128 ± 0.01	0.75	0.10 ± 0.02	2.3 ± 0.8
0.177 ± 0.01	1.20	0.10 ± 0.02	1.7 ± 0.6

Table 6.3: The measured resolution, effective area and peak gain of the microchannel Wolter optic when illuminated in the TTF with W-L (8.4keV) X-rays at various tilt angles.

6.4 Microchannel Wolter optic results

The dual MPO Wolter optic is composed of MPOs GB-001-R4 and GB-001-R3, both described in section 5.3. The MPOs arrived at Leicester pre-aligned in a fixture that was attached to the MPO holding jig head to allow them to be inserted in the X-ray beam. The method of packing the multifibres about a hexagonal round-pore detector multifibre leads to a lot of holes at the centre of the optics. To ensure that transmission through these holes could not be confused with the focus a 10mm diameter, 200μm thick molybdenum disk was taped into position over the centre multifibres.

A deep on-axis image of the microchannel Wolter optic illuminated with W-L (8.4keV) X-rays in the TTF is shown in Figure 6.4. Figure 6.5 shows the images formed as the optic is tilted through $11'$ from the on-axis position. The resolutions, effective areas and peak gains are shown in Table 6.3.

The most important result is the presence of a focus at the centre of the image. This shows that some channels must be correctly aligned. The fact that the focus remains at the centre of the image as the optic is tilted confirms that true Wolter II imaging has been demonstrated in, at least, parts of the optic. The higher energy Sn-K ($\sim$ 25.3keV) on-axis response of the Wolter optic is listed in Table 6.4 together with that of a perfect optic.

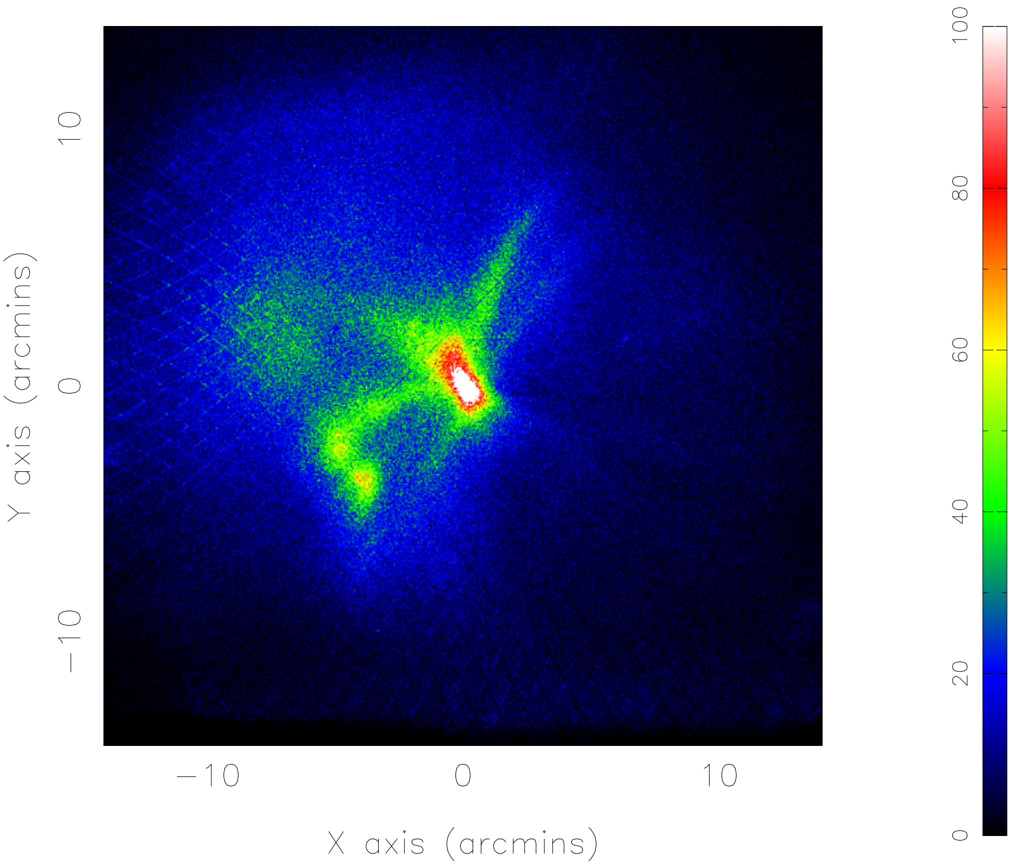

Figure 6.4: Linerarized deep (3×10^6 counts) on-axis image of the microchannel Wolter optic illuminated in the TTF with W-L (8.4keV) X-rays. The cross hatching to the left of the image is an artefact of the linearization process.

X-ray energy (keV)	Measured (FE-001-R4)			Calculated (perfect MPO)		
	Res	Area	Gain	Res	Area	Gain
8.40 (W-L)	1.6	0.27 ± 0.1	2.7 ± 0.9	0.36	1.7	183
25.27 (Sn-K)	0.6	0.02 ± 0.001	0.4 ± 0.1	0.36	0.1	13

Table 6.4: The measured on-axis resolution, effective area and peak gain of the microchannel Wolter optic at different TTF energy settings. The resolutions are in arcminutes and effective areas in square centimetres. Perfect MPO calculations are shown on the right for comparison.

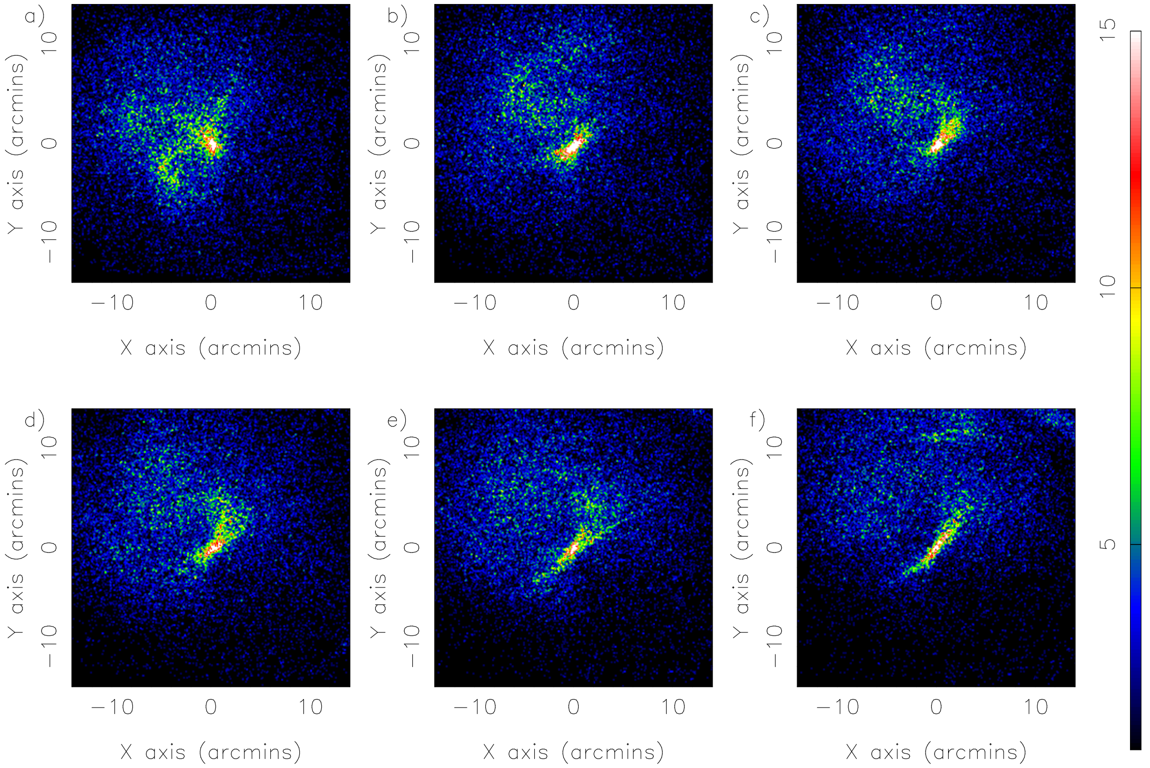

Figure 6.5: Series of images showing the microchannel Wolter optic's response as it is tilted in the W-L (8.4keV) X-ray beam. (a) is on-axis, (b) has a $0.06°$ tilt, (c) $0.086°$, (d) $0.104°$, (e) $0.128°$ and (f) has a $0.177°$ tilt.

6.5 Misalignment models

A comparison of the results for both the single, planar, MPO and the microchannel Wolter optic with those predicted using a perfect or randomly distorted optic (section 5.4) shows little agreement. This suggests that the misalignment errors present in the real MPO are systematic. The experimental evidence of Beijersbergen *et al.* (1999, 2000b,a) shows that the stacking errors incurred during the fusion of individual fibres into multifibres are essentially randomised within the parameter space previously presented (section 5.3). The large scale systematic errors must, therefore, occur between multifibres. Misalignment maps, introduced in section 4.5, in which the alignment errors of every multifibre can be specified are thus used to model these errors.

6.5.1 Planar radially-packed MPO FE-001-R4

The severe comatic distortion that results when an off-axis source is imaged with a planar radially-packed MPO mean that the effective area in the central focus should be zero the moment this occurs. Different portions of the MPO must, therefore, contribute to the focus observed as the optic is tilted. It can also be deduced that sections of the optic must be aligned to a reasonably high degree as partial coma are observed (small random errors cause the blurring out of the comatic circle - section 5.4). This, as well as the uneven transmission through adjacent multifibre rings, can be explained by introducing a constant misalignment to each multifibre in the same ring, but with different errors in each ring.

The difference in tilt angle between sectors of the MPO separated by large scale azimuthal misalignments can be found by tilting the MPO and noting the angles at which adjacent sectors allow transmission. This is seen between Figures 6.3(a) and (d), the relative alignment is $\sim 6'$. A multifibre misalignment map was thus setup for FE-001-R4:

i) The multifibres within each ring are well aligned. However, there are random $\sim 6'$

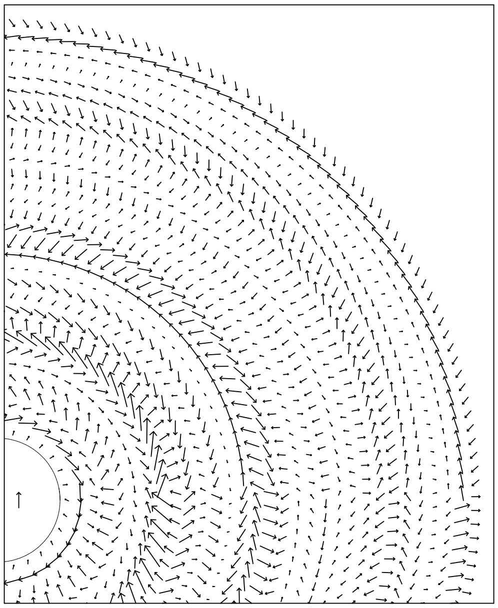

Figure 6.6: Multifibre misalignment map generated to simulate MPO FE-001-R4. The arrows are centred on multifibre positions and give the alignment error direction and magnitude (arrow length). A $10'$ arrow is in the bottom left hand corner for comparison.

rms alignment errors between adjacent rings.

ii) An additional $\sim 6'$ rms misalignment is included that varies as a function of the azimuth angle about the MPOs' optical axis. This has been divided into 4 sectors or 'slices'.

The misalignment map is presented in Figure 6.6, here the arrows are centred on multifibres, the arrows direction and length indicating the misalignment direction and magnitude.

The raytraced MPO responses moving from an on-axis position through the same tilts as used experimentally (Figure 6.3) are shown in Figure 6.7. Effective areas, resolutions and peak gains are listed in Table 6.5 for comparison with the experimental data in Tables 6.1 and 6.2. A plot of the on-axis measured and simulated encircled flux fraction and cumulative intensity at 8.4keV are shown in Figure 6.8. In all cases we see reasonable agreement between model and experiment.

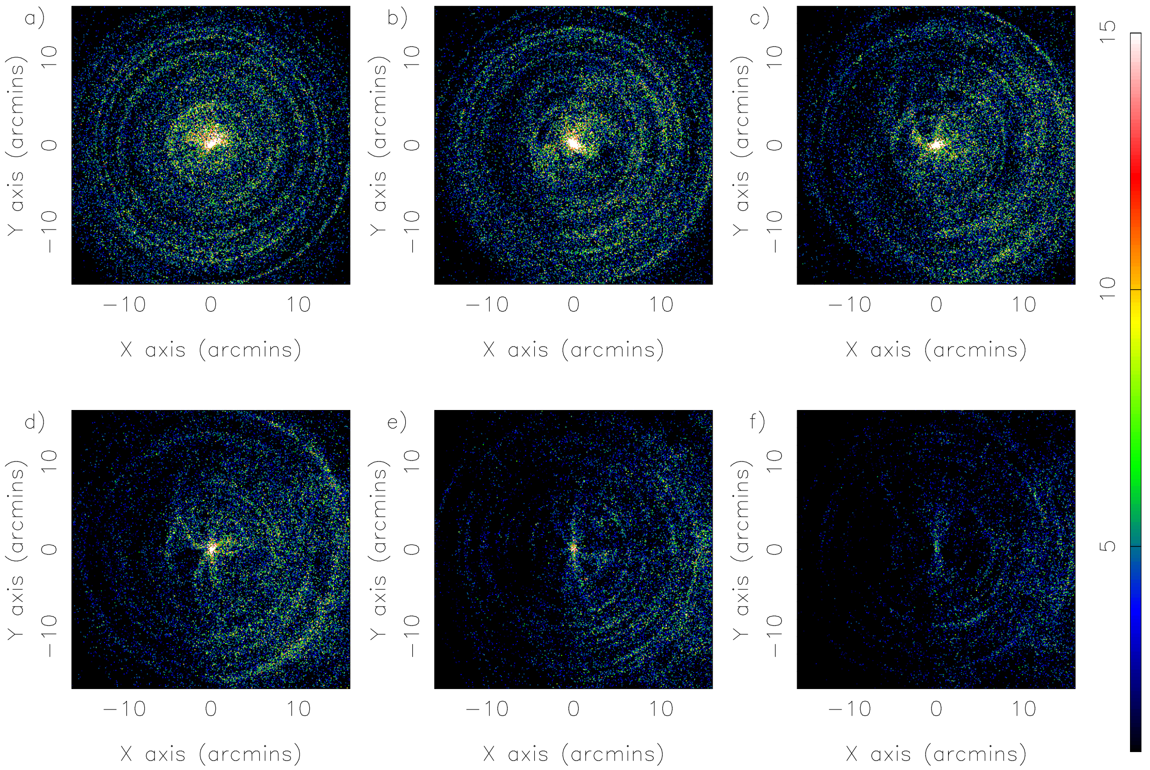

Figure 6.7: A series of raytraced images using the multifibre misalignment model developed for MPO FE-001-R4 illuminated with W-L (8.4keV) X-rays in the TTF. Image (*a*) is on-axis, (*b*) has a 0.033° tilt, (*c*) has a 0.066° tilt, (*d*) has a 0.1° tilt, (*e*) has a 0.165° tilt and (*f*) has a 0.231° tilt. Comparison with the experimental data in Figure 6.3 shows a reasonable match.

Off-axis angle (Degrees)	FWHM resolution (arcmins)	Effective area (cm^2)	Peak gain
on-axis	0.66	0.15	6.4
0.033	0.65	0.22	7.3
0.066	0.70	0.16	6.2
0.1	0.63	0.12	5.5
0.165	0.80	0.06	4.5
0.231	N/A	N/A	N/A
on-axis (Mo-K)	~ 1.0	0.06	5.0
on-axis (Sn-K)	~ 1.0	0.01	2.0

Table 6.5: The resolutions, effective areas and peak gains calculated using the model of the planar radially-packed MPO situated in the TTF and illuminated with W-L (8.4keV) X-rays.

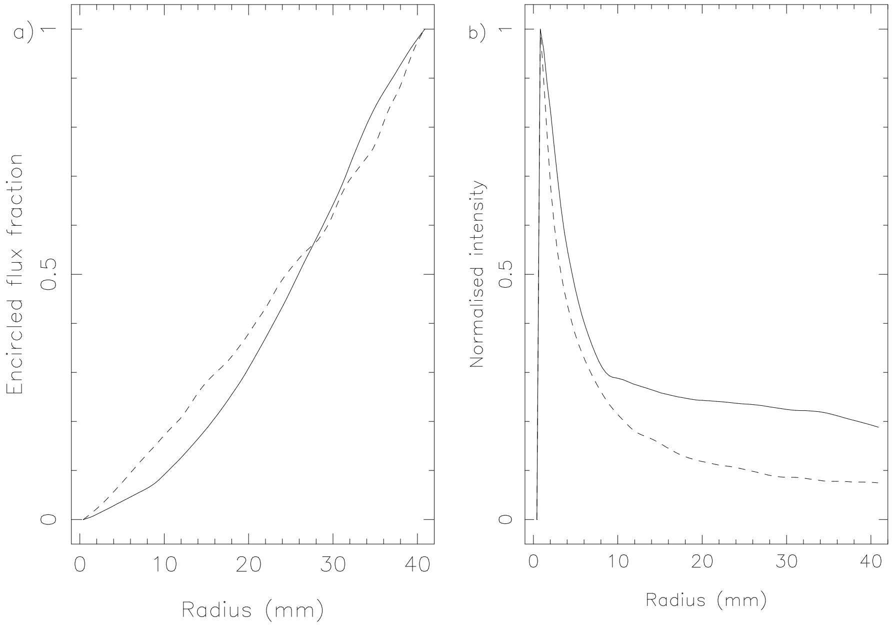

Figure 6.8: The encircled on-axis (a) flux fraction and (b) cumulative intensity as a function of the encircled area radius for the MPO FE-001-R4 illuminated in the TTF with W-L (8.4keV) X-rays. The solid lines show the experimental data displayed in Figure 6.2, the dashed line the raytraced dataset shown in Figure 6.7(a).

6.5.2 Microchannel Wolter optic

The MPOs that made up the Wolter optic were cut from next to each other on boule E and, as such, would be expected to share very similar alignment errors. This should lead to the *relative* alignment between channels at any point on the two MPOs remaining the same. A microchannel Wolter optic is expected to focus to the centre of the detector no matter what its orientation is in the beam (within boundaries dictated by the critical reflection angle). If the channels at all points on the optic had the same relative alignment, the entire optic would be expected to contribute to the focus at all tilt angles. As this is not the case, additional tilt errors must be introduced to each MPO during the slumping process that lead to the relative alignment of channels violating the Wolter approximation condition, $3\theta_1 = \theta_2$.

As the plates were untested with X-rays before slumping and etching, it is not possible to directly test how the slumping process affected them. However, measurements made with a 100μm$\times$$100\mu$m, 10keV X-ray beam at the Bessy-II synchrotron facility in Berlin

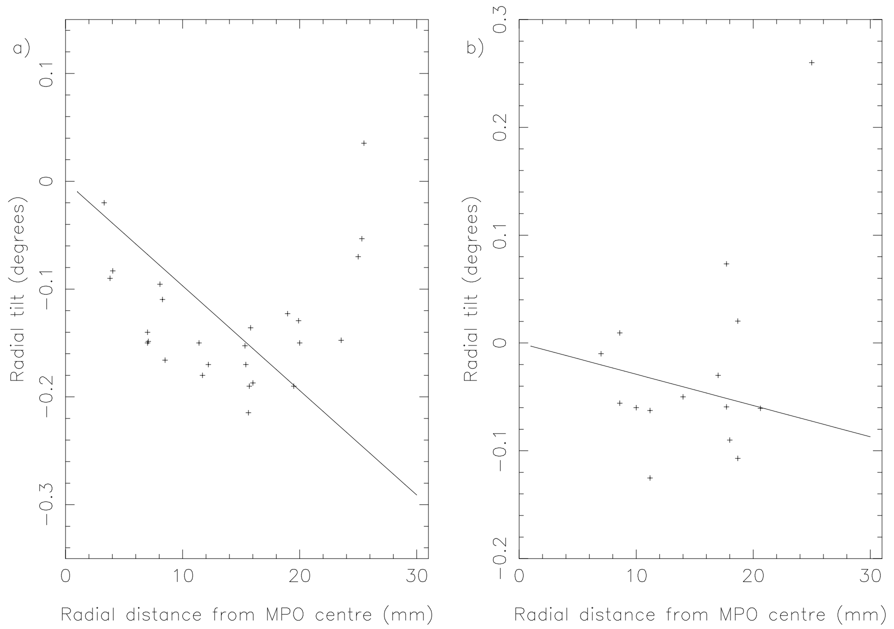

Figure 6.9: **Radial tilt components of** (*a*) **MPO GB-001-R3, the** 6.67**m radius slumped plate from the Wolter optic and** (*b*) **MPO GB-001-R4, the** 20**m radius slump plate. The solid line is the perfect tilt for this radius slumping. Data obtained by Beijersbergen (2000b) at Bessy-II synchrotron in Berlin.**

(Beijersbergen, 2000b) have determined the tilt of multifibres in various positions on each slumped MPO. From this data, both plots of the radial tilt as a function of the distance from the centre of the plate and the random tilt magnitude can be obtained. Figure 6.9 shows the actual radial tilt components of channels as a function of their distance from the MPO centre, together with the tilts expected in perfectly slumped plates.

The radial tilts show a reasonable fit to the slump profile up to a radius of ∼ 20mm, where they deviate from the perfect profile severely. Fibres in MPO GB-001-R3 have an average tilt error of 0.046° while those in GB-001-R4 exhibit an error of 0.040°.

Metrology of the slumped plates show that the actual profile, post etching, is accurate to within several microns across the entire MPO (Boutot *et al.*, 2000). Hence, at radii larger than ∼ 20mm the channels must shear instead of tilting to point to a common centre.

The manufacturing process between the production of boule A and E did not change enormously, and so it is reasonable to assume that similar alignment errors would exist in the pre-slumping MPOs cut from this boule as in FE-001-R4. The misalignment map used to simulate MPO FE-001-R4 was thus used as the basis of that for GB-001-R3 and GB-001-R4. Extra misalignments were added at radial distances greater than 20mm to simulate the shearing of channels and the map was then manually adjusted to provide a fit to the experimental data. The final maps were as follows:

i) Random $\sim 2'$rms alignment errors between adjacent rings.

ii) An additional $\sim 7'$ rms misalignment that varies as a function of the azimuth angle about the MPOs' optical axes.

iii) Simulated shearing of multifibres preventing the channels from pointing to a common centre at radii greater than 20mm from the optical axis. This is modelled through the *addition* of a $10'$ rms error to all multifibres located outside this boundary.

Figure 6.10 shows the radial tilt errors used in the tilemap of MPO GB-001-R3 (6.67m slump radius). Note the similarity with the experimentally obtained data of Figure 6.9(a). The images from the simulation of the Wolter optic, starting on-axis and moving through the same off-axis angles as used in experiment (Figure 6.5) are shown in Figure 6.11.

The spatial resolutions, effective areas and peak gains of all the simulated datasets are shown in Table 6.6 for comparison with those in Tables 6.3 and 6.4. The encircled flux fraction and cumulative radial intensity from the measured (Figure 6.4) and modelled (Figure 6.11(a)) on-axis images are shown in Figure 6.12.

6.6 Summary

Both a focus from a single, planar, radially-packed micropore optic and a true Wolter II focus from a microchannel Wolter optic have been demonstrated with foci $\sim 1'$. Stacking errors between multifibres, however, have reduced the effective areas and gains so that they have no real use as practical optics.

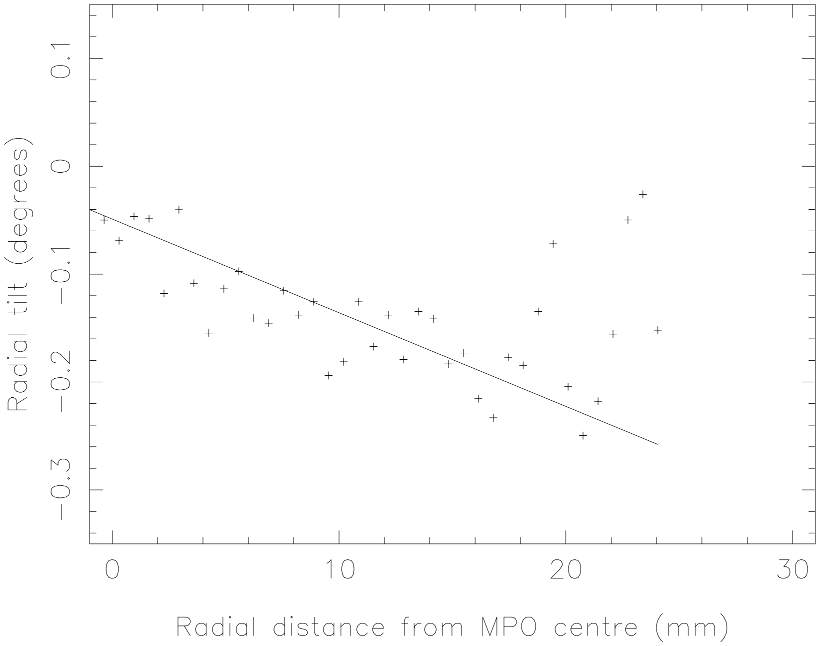

Figure 6.10: The radial tilt components of the tilemap used to simulate MPO GB-001-R3 (6.67m slump radius). The solid line shows the tilts expected for a perfectly slumped plate. Comparison with the experimental data of Figure 6.9(a) shows strong agreement.

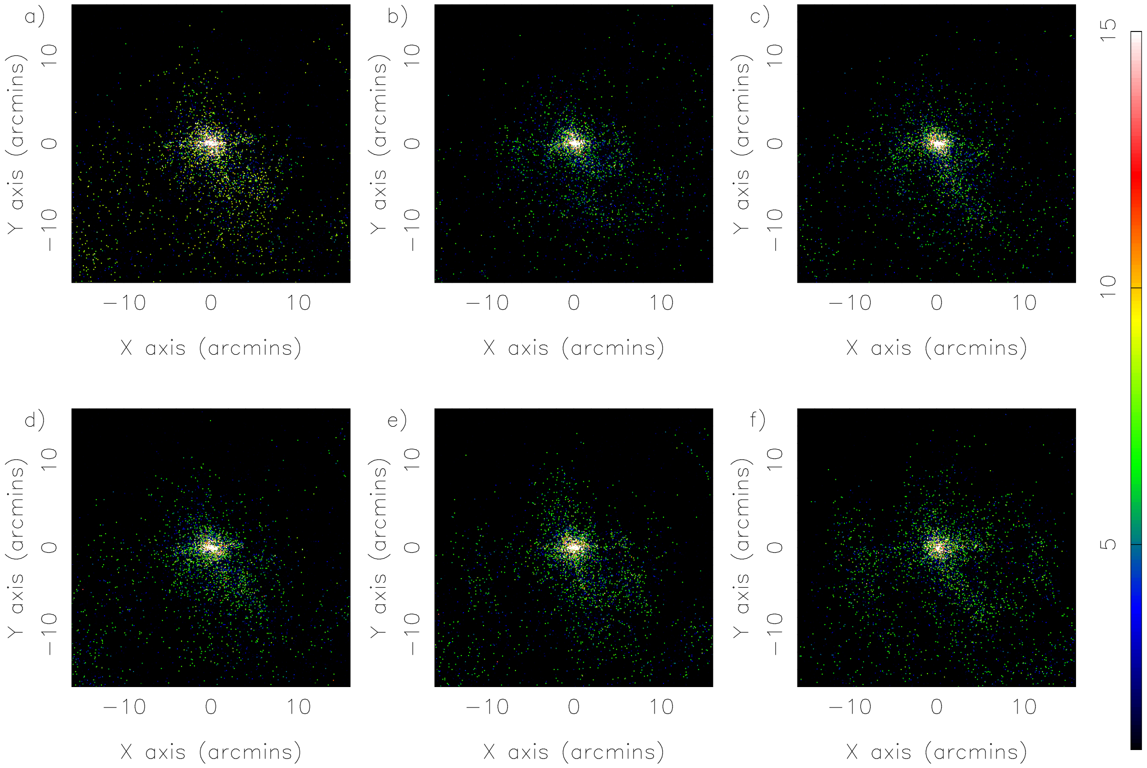

Figure 6.11: Series of raytraced images showing the microchannel Wolter optic's response as it is tilted in the W-L (8.4keV) X-ray beam. (a) is on-axis, (b) has a 0.06° tilt, (c) has a 0.086° tilt, (d) has a 0.104° tilt, (e) has a 0.128° tilt and (f) has a 0.177° tilt.

Off-axis angle (Degrees)	FWHM resolution (arcmins)	Effective area (cm^2)	Peak gain
on-axis	0.64	0.15	5.6
0.06	0.59	0.10	5.8
0.086	0.73	0.12	7.5
0.104	0.70	0.10	5.9
0.128	0.79	0.16	5.3
0.177	1.03	0.10	6.2
on-axis (Sn-K)	1.0	0.003	1.3

Table 6.6: The resolutions, effective areas and peak gains calculated using the model of the microchannel Wolter optic situated in the TTF and illuminated with X-rays. All X-rays are W-L (8.4keV) unless otherwise stated.

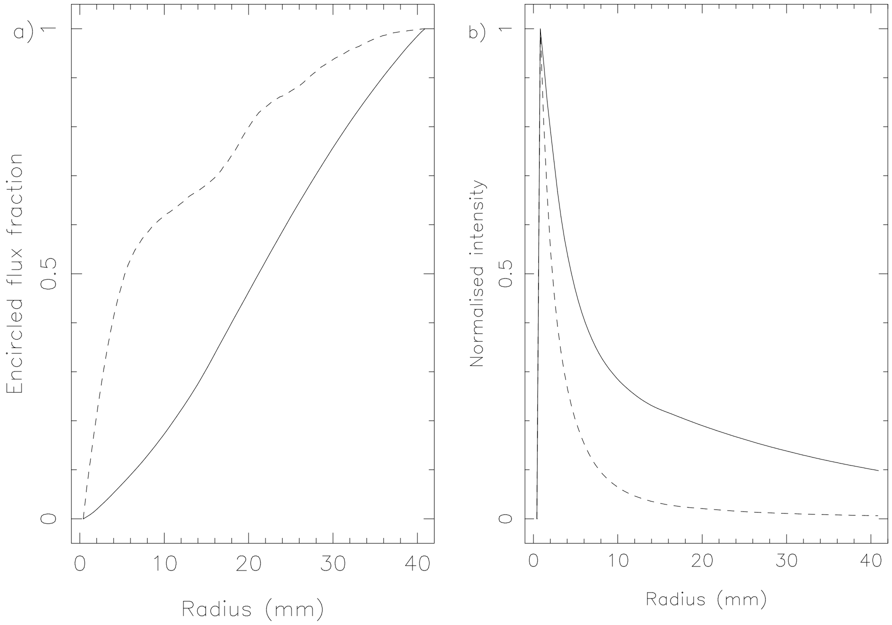

Figure 6.12: The on-axis encircled (a) flux fraction and (b) cumulative intensity as a function of the encircled area radius for the microchannel Wolter optic illuminated in the TTF with W-L (8.4keV) X-rays. The solid lines show the experimental data from dataset displayed in Figure 6.4, the dashed line the raytraced dataset shown in Figure 6.11.

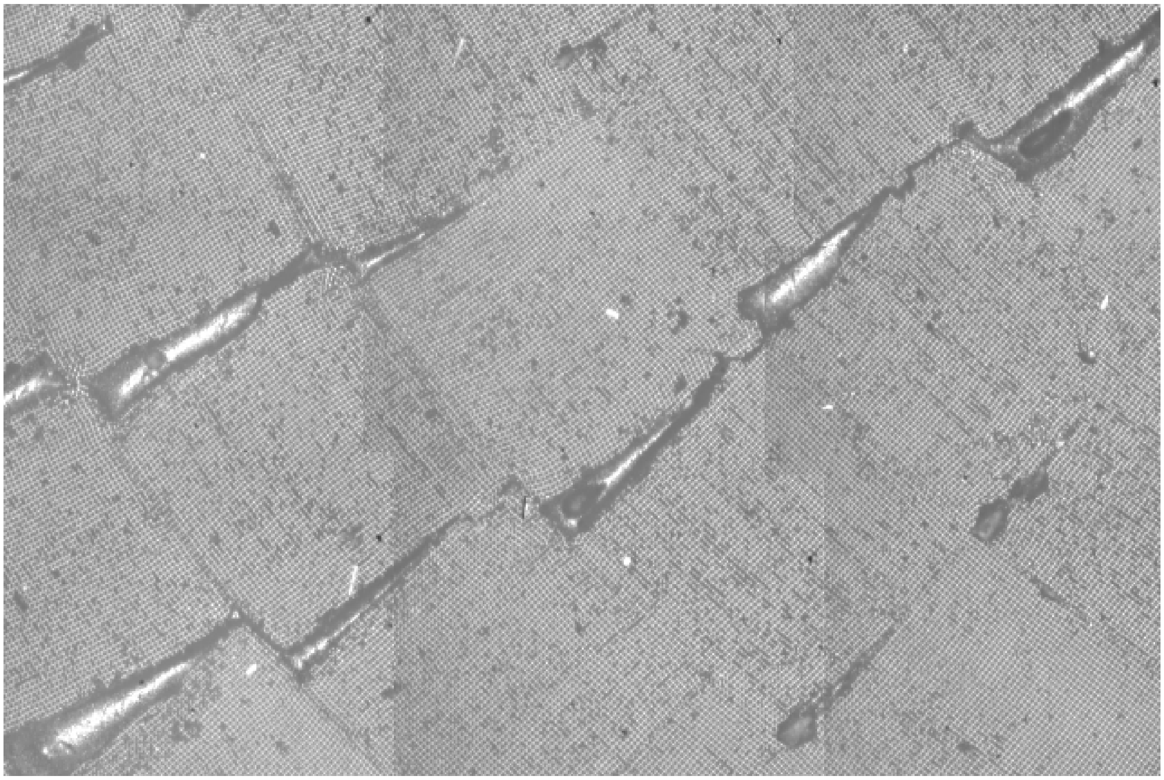

Figure 6.13: Montage of optical microscope images (×60 magnification) showing the different free space sizes between multifibres in successive multifibre rings (MPO FE-001-R4).

Using the raytrace model described in section 3.6 with multifibre misalignment maps developed from the available evidence, the tilt errors between multifibres have been modelled. These models have, without having to individually manipulate the ~ 6000 multifibres, reproduced the salient features of the experimental data. The resolutions, effective areas and gains are to order of magnitude accuracy at least.

From this we are able to summarise that multifibre tilt errors that vary from ring to ring and as a function of the azimuth angle about the optical axis are to blame for the reduced efficiency of radially-packed optics. Figure 6.13 shows how the packing of square multifibres in a radial pattern leads to different size voids between the multifibres in each ring. It is possible that during the fusion process these lead to different alignment errors being induced in each ring. After etching, stresses incurred as a result of this could give rise to the azimuthal warp observed.

These problems are compounded during the slumping process where multifibres towards

Diameter	210mm
Focal length	1m
First MPO slump radius	4m
Second MPO slump radius	4/3m
Field of view	2°
Angular resolution	$2'$
Mass	< 500g

Table 6.7: The proposed characteristics of the microchannel Wolter optic required for the HERMES-X spectrometer on the ESA mission to Mercury, BepiColombo.

the edge of the MPOs shear instead of being tilted to point to a common centre.

6.7 The BepiColombo microchannel Wolter optics

The HERMES-X spectrometer for the BepiColombo mission, introduced and discussed in section 1.5.2, proposes to use a microchannel Wolter optic in a remote sensing capability. The proposed characteristics of this optic are listed in Table 6.7.

To increase the effective area for on-axis sources, it is possible to profile the MPOs post-slumping so that the aspect ratio of the channels varies as a function of the channel's position on the MPO. In the most efficient on-axis microchannel Wolter optic, each ray would suffer only one reflection in each MPO. In a perfect slumped optic, where all channels point to a common centre, we can calculate their angle to the optical axis, as shown in Figure 6.14.

The slump angle of a channel a distance r from the optical axis of the system is approximated as

$$\theta_1 = \frac{r}{R_1} \tag{6.1}$$

$$\theta_2 = \frac{r}{R_2} \tag{6.2}$$

where R_1 and R_2 are the slump radii of the MPOs. The grazing angle of incidence of a

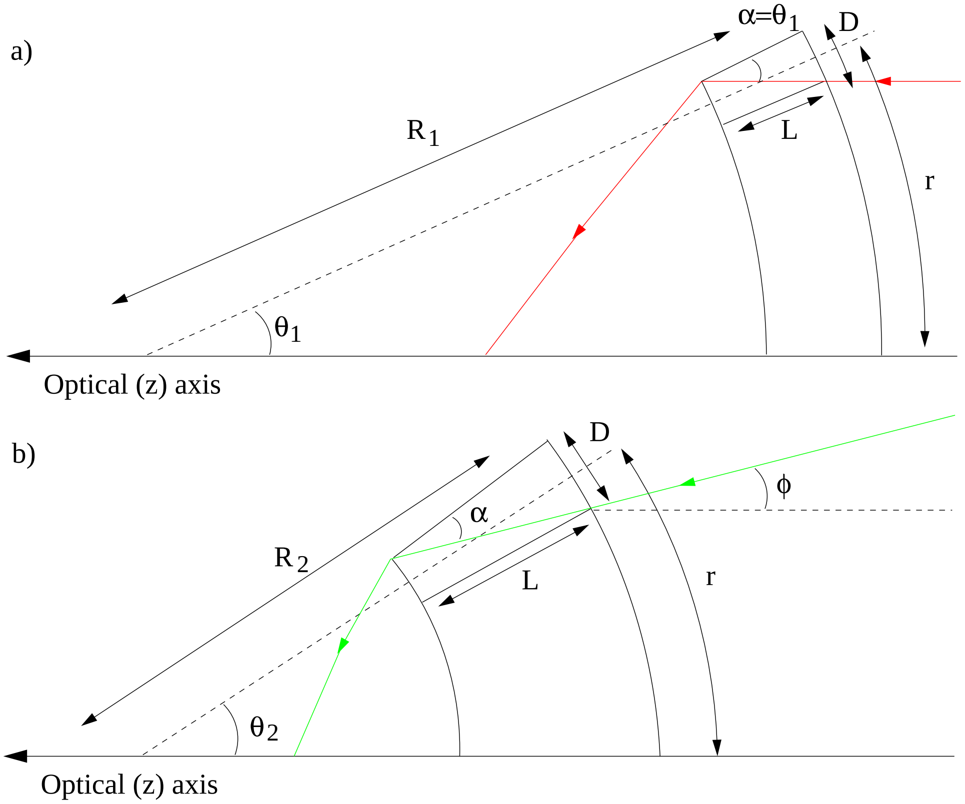

Figure 6.14: The most efficient reflections through an MPO will occur when the grazing angle of incidence is equal to D/L. (a) illustrates this condition for the front MPO in a microchannel Wolter optic, (b) in the second, where ϕ is the ray's emergent angle from the front MPO.

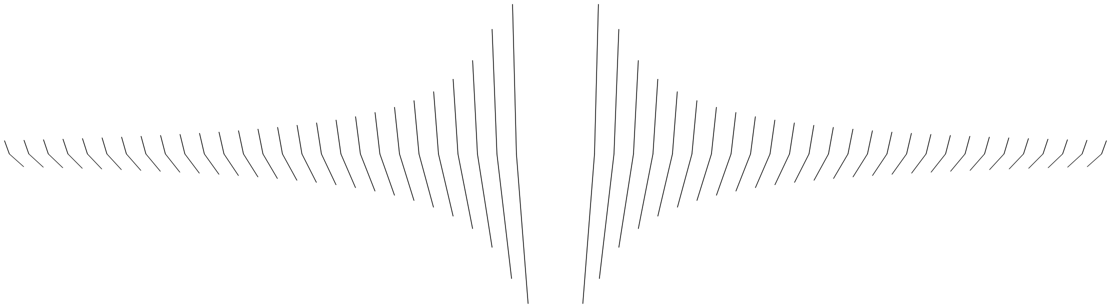

Figure 6.15: A profiled microchannel Wolter optic. The first MPO follows the profile of equation (6.4), the second that of equation (6.6).

ray from infinity will be the same as the channel's slump angle (Figure 6.14(a)). If the ray is to suffer only one reflection in the channel, the channel length L must be exactly

$$L = \frac{D}{\theta_1} \tag{6.3}$$

where D is the channel diameter. The channel profile on the first MPO in a Wolter optic is thus written as

$$\frac{L}{D} = \frac{R_1}{\sqrt{x^2 + y^2}} \tag{6.4}$$

where x and y are the distance of the channel from the optical axis in the respective directions.

To calculate the profile of the second MPO, the angle to the optical axis, ϕ, of the emergent ray from the first MPO must be considered (Figure 6.14(b)). According to equation (5.16) of section 5.2.2, if the ray comes from an on-axis source at infinity, this angle would be $\phi = 2\theta_1$. Consequently the grazing angle to the channel wall in the second optic is

$$\alpha = \theta_2 - \phi = \theta_2 - 2\theta_1 \tag{6.5}$$

To satisfy the Wolter approximation described in section 5.2.2; $\theta_1 = \theta_2/3$. Equation (6.4) can then be written

$$\frac{L}{D} = \frac{3R_2}{\sqrt{x^2 + y^2}} = \frac{R_1}{\sqrt{x^2 + y^2}} \tag{6.6}$$

for the second MPO. A diagram of an MPO profiled in this manner is shown in Figure 6.15.

These profiles can be included in the raytrace model described in section 3.6. For a perfectly aligned set of Wolter MPOs with the parameters described in Table 6.7, Figure

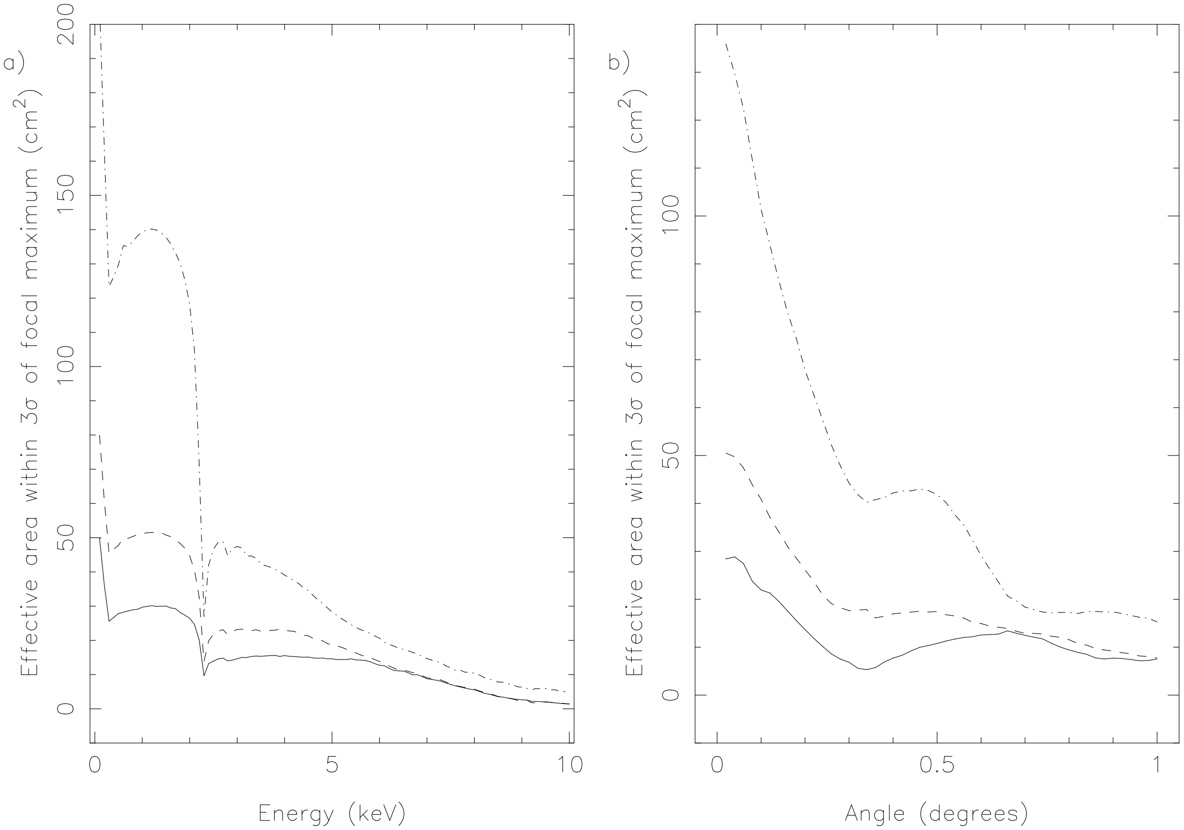

Figure 6.16: The effective area as (a) a function of energy and (b) off-axis angle at 1keV for the HERMES-X microchannel Wolter optic. The solid lines correspond to a pair of standard 100:1 aspect ratio plates; the dashed lines to having the front MPO profiled; the dash-dot lines to having both MPOs profiled according the equations (6.4) and (6.6). The open area fraction of the MPO is 0.76 ($D = 50\mu$m, $p = 55\mu$m).

6.16 shows both the on-axis effective area as a function of energy and the off-axis effective area at 1keV. The MPOs have 50μm channels on a 55μm pitch and have a 150Å gold coating. The solid line shows the effective area for a standard, unprofiled 100:1 Wolter pair. The dashed line has the front MPO profiled according to equation (6.4) and a standard rear plate; the dash-dot line also has the rear MPO profiled according to equation (6.6).

The data in Figure 6.16 clearly shows that for perfectly aligned micropore optics, profiling increases not only the on-axis effective area, but also the off-axis response. Profiling a slumped MPO will not be without problems, the MPOs will have to be much thicker in the first place (and hence more difficult to slump) and shaping the optic post-slump can be easily envisaged as incurring many alignment errors. If, however, this can be achieved, an optic with an equivalent effective area to the RoSAT X-ray telescope ($\sim 100\text{cm}^2$ at 2keV (Aschenbach, 1987)) can be created with a more compact focal length and very low mass.

An alternative to profiling the MPOs is to maintain a constant channel length, but vary the channel side length as a function of radial position. The aspect ratio would still vary as in equations 6.4 and 6.6, but it would not be necessary to physically grind the MPOs. A new TRP contract, discussed in section 8.2, is to investigate both approaches.

6.8 Conclusions

The concept of using micropore optics to provide Wolter imaging with high effective area and good resolution at a low mass cost has been proven. Although the effective area has been a fraction of that calculated for a perfect optic, a *peak* channel gain of greater than unity has been demonstrated.

The source of the imperfections has been identified as multifibre stacking errors, compounded when the MPOs are slumped by shearing of the channels near the MPO edge. Work thus needs to be done in reducing the large scale distortions introduced in the stacking and fusing of multifibres into boules, and also in the slumping process to prevent the shearing of channels. A new TRP programme has been approved to address these problems, however, so working optics could well be a reality in the time-frame necessary for their use in the currently proposed BepiColombo mission and the possible high energy extension to the XEUS mission profile.

Chapter 7

Lobster: An X-ray All Sky Monitor

7.1 Introduction

The need for an All Sky Monitor (ASM) in X-ray astronomy has long been recognised (Holt and Priedhorsky, 1987). While Chandra and XMM-Newton have brought a new era of sensitive high resolution imaging and spectroscopy to X-ray astronomy, the behaviour of hot astrophysical objects as a function of time has been neglected.

Monitoring the temporal nature of the X-ray sky will not only provide an archive of light curves for all resolvable sources, it will also provide a transient event alert facility for more powerful observatories such as Chandra and XMM. Holt and Priedhorsky (1987) have specified the ideal ASM in terms of:

i) As large an instantaneous field of view (FOV) as possible. This should be as close to 4πsr as possible, avoiding only a zone centred on the sun.

ii) An angular resolution that will allow the identification of sources within the FOV of a larger telescope. This points to an ASM resolution of around $\leq 10'$.

iii) A temporal resolution high enough to be able to identify transient events. Hence a resolution of the order of hours should be acceptable, much higher resolution measurements can be made with pointed instruments.

iv) Energy resolution is not important due to the fact that, as for temporal resolution, pointed telescope observations will provide far higher resolution than could be reasonably within the scope of an ASM. At the edge of the detection threshold spectral information would be statistically insignificant, because a source would typically be identified by a few counts.

The instrument should also be as sensitive as possible to allow the cataloguing of extragalactic sources. The $\sim$ 30 brightest Active Galactic Nuclei (AGN) in the sky have a flux of a few mCrab in the 0.5keV$\rightarrow$ 3.5keV band (1Crab= 14photons/cm^2/s at 1keV), the next brightest $\sim$ 1000 AGN having a flux of a few$\times$0.1mCrab (RoSAT All Sky Survey Bright Source Catalogue - RASSBSC; Fraser *et al.* 2000).

The Rossi X-ray Timing Explorer (RXTE) (Bradt *et al.*, 1991) is the most sensitive ASM to date with an angular resolution of $15' \times 3'$ provided by a coded mask aperture, and a detection threshold of 8mCrab in a one day observation. Awaiting launch are the Monitoring X-ray Experiment (MOXE) on board the Russian Spectrum X-Gamma high energy observatory (In't Zand *et al.*, 1994) with a daily sensitivity of 2mCrab and the NASDA Monitor of All-sky X-ray Image (MAXI), itself an attached International Space Station (ISS) payload due for launch in 2005 (one day sensitivity $\sim$ 2mCrab; Matsuoka *et al.* 1997). The relatively low sensitivity of the RXTE ASM means that the majority of observable sources are galactic X-ray binaries, whilst MOXE and MAXI are non-imaging and use simple collimation to identify sources with poor angular resolutions of $2.4^\circ \times 9.7^\circ$ and $1.1^\circ \times 1.1^\circ$ respectively.

The Lobster-ISS mission (Fraser *et al.*, 2000) proposes to use lobster eye micropore optics (section 4.2) to observe the soft X-ray (0.2keV$\rightarrow$ 3.5keV) sky. The imaging capability of these optics will provide not only an order of magnitude better sensitivity ($\sim$ 0.15mCrab in 1 day), but also an angular resolution of the order of $4'$. An instantaneous $162^\circ \times 22.5^\circ$ FOV will map almost the entire sky once every 90 minute ISS orbit. Lobster-ISS thus fulfils, and in many cases surpasses, the requirements for an ASM laid down by Holt and Priedhorsky.

7.2 The Lobster-ISS Concept

Once it was realised that micropore optics could be used to construct a lobster eye ASM, a conceptual telescope design based on these devices was proposed by Fraser *et al.* (1991b) and subsequently studied in detail by Priedhorsky *et al.* (1996). These led to the proposal of Lobster in the NASA Small Mission EXplorer (SMEX) round of opportunity in 1997 (Priedhorsky *et al.*, 1997) where the science case was approved, but the mission rejected on grounds of the technical immaturity of the optics and detector. Following the ESA TRP programme, where lobster eye MPOs approaching the required specification were demonstrated (section 4.5.3), the instrument was proposed again to the ESA F2/F3 call for proposals in January 2000, this time as an attached ISS payload (Fraser *et al.*, 2000). Following technical reviews and an accommodation study, the mission was approved for a Phase A study which will run to December 2002.

The large field of view is provided via six identical modules, each with a $27° \times 22.5°$ FOV. The slump radius of each 'lobster eye' is 0.75m, originally chosen for the SMEX proposal so that the satellite would fit within a Pegasus rocket shroud and kept so that the instrument can be accommodated on an Express Palette Adapter (ExPA) (experiment volume $\sim 1\text{m}^2$) used to interface external experiments with the ISS. With such a slump radius, an optic of 0.4m side would be required to provide the necessary FOV. As it is unrealistic to manufacture a micropore optic of these dimensions, a high conductivity Carbon Fibre Reinforced Plastic (CFRP) frame is populated with co-aligned 40mm^2 lobster eye MPOs.

The instrument will be on the zenith exposed payload facility of the ESA Columbus module of the ISS (Figure 7.1). Using computer models of the completed ISS, a configuration of the mirror modules has been arrived at that provides the minimum obscuration of the FOV from the ISS superstructure, moving elements (solar panels and radiators) and

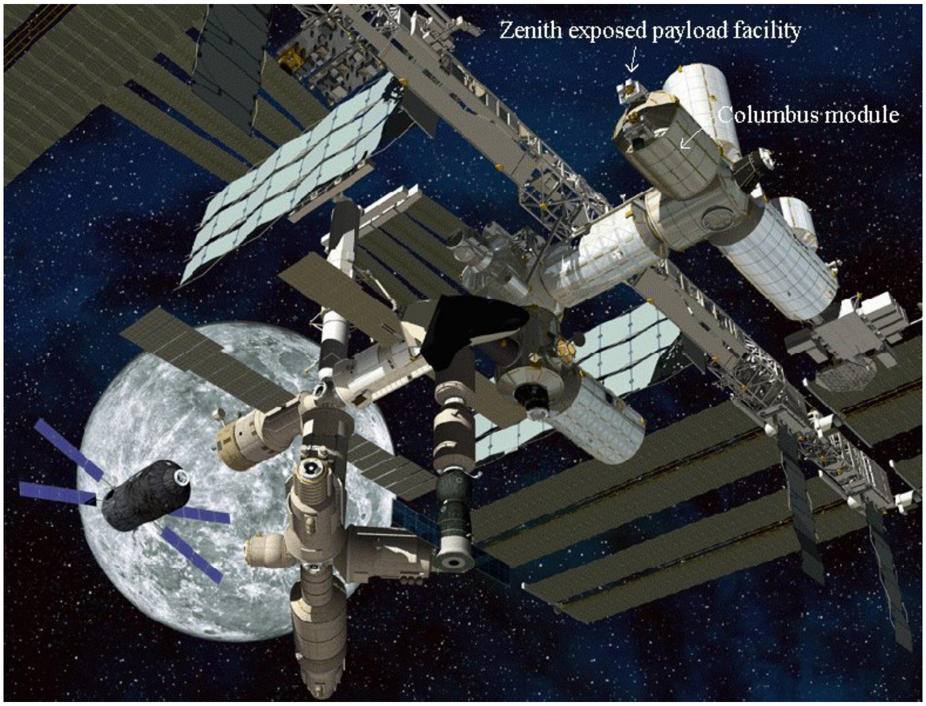

Figure 7.1: Image of the ISS showing the Columbus module and the position of the zenith exposed payload facility where Lobster-ISS will be accommodated.

docked orbiters (Smith *et al.*, 2001). The current design of the instrument is shown in Figure 7.2, the FOV of the six modules is shown with respect to the ISS in Figure 7.3.

As demonstrated in previous chapters, X-rays from infinity will be focused by a lobster eye optic onto a spherical surface of radius $R_{slump}/2$ centred on the slump origin. Ideally a detector with a focal plane curved to this radius would be used to image the incident photons. An approximation to a spherical detector is provided by a pyramid arrangement of position sensitive microwell proportional counters (Jahoda *et al.*, 2000).

The microwell proportional counter has a xenon and carbon dioxide multiplier gas at a pressure of 1.5 atmospheres and provides a signal though an electron avalanche, as for a traditional proportional counter. The high field avalanche regions of the detector, however, are within laser machined microwells. In the Lobster-ISS detector, the microwells are in an array with a pitch of 400μm, providing a spatial resolution of $\leq 400\mu$m.

Figure 7.4 shows the effective area of the Lobster-ISS instrument. The telescope effective area was calculated with the raytrace software described in section 3.6. The transmission

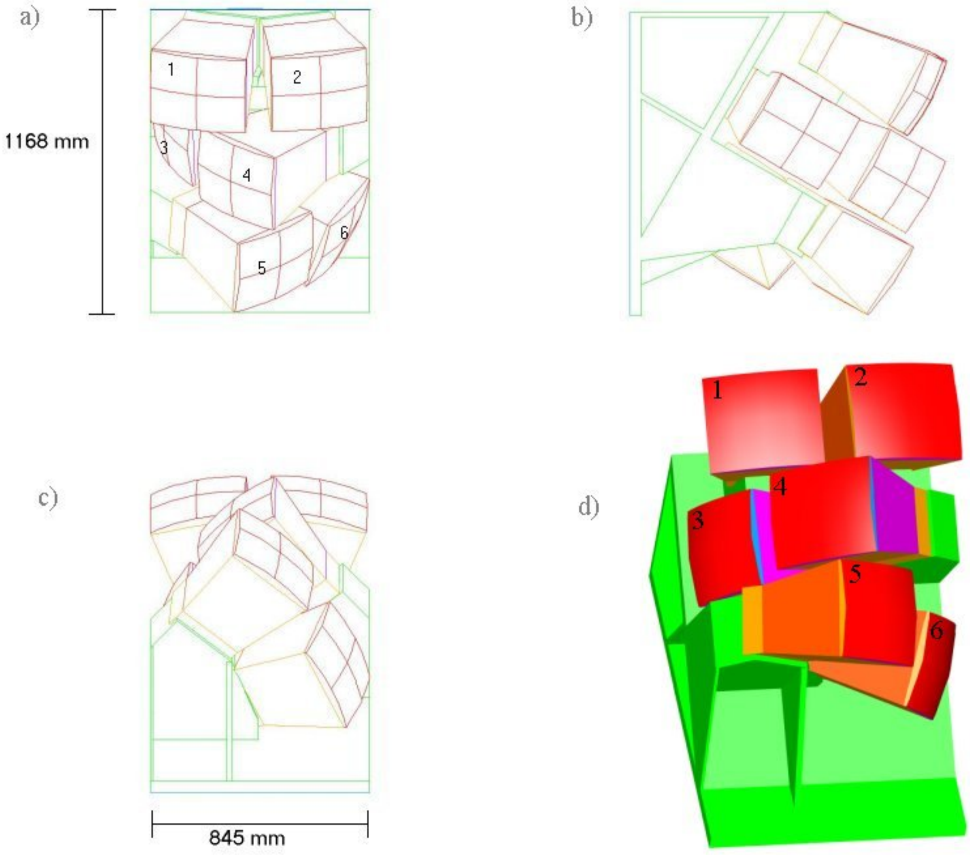

Figure 7.2: The current configuration of the Lobster-ISS mirror modules (a) plan view, (b) side view showing the $30°$ tilt towards ram, (c) front view and (d) solid model. This arrangement was reached considering the size constraints of the express palette adaptor and FOV obscuration from ISS elements (providing the requirement for the $30°$ tilt towards ram.).

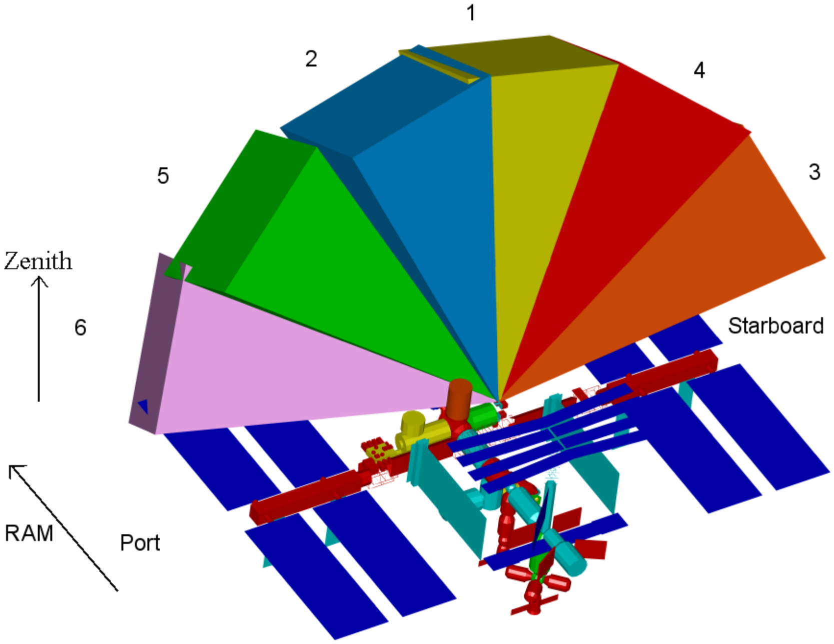

Figure 7.3: Lobster-ISS field of view. The 30° tilt towards RAM (the direction of ISS motion) with subsidiary tilts of modules 5 and 6 is to provide the most unobscured FOV possible.

of a 0.2μm silicon nitride (Si_3N_4), 400Å aluminium window is included to represent the detector window (Fraser *et al.*, 2001a). The quantum efficiency of the detector is modelled as the absorption of 1.5 atmospheres of xenon (unity up to 2keV, 0.64 at 3.5keV).

7.3 The Lobster optics

Lobster-ISS is a soft X-ray telescope with an energy bandpass of 0.2keV→ 3.5keV (Figure 7.4). Consequently the critical reflection angle θ_c is relatively large ($\theta_c = 2.4E^{-1.04}$ for lead glass, where E is the energy in keV and θ_c is in degrees; Willingale *et al.* (1998)) and the most efficient MPOs will have low aspect ratios. An L/D ratio of 50:1 was chosen on the basis of detailed raytracing simulations carried out by Priedhorsky *et al.* (1996). In order to maintain mechanical strength in such low aspect ratio plates, 20μm channel side lengths were chosen (this results in 1mm thick MPOs). The larger channel would result in an increased focus size in a perfect MPO. This, however, is negligible in Lobster-ISS

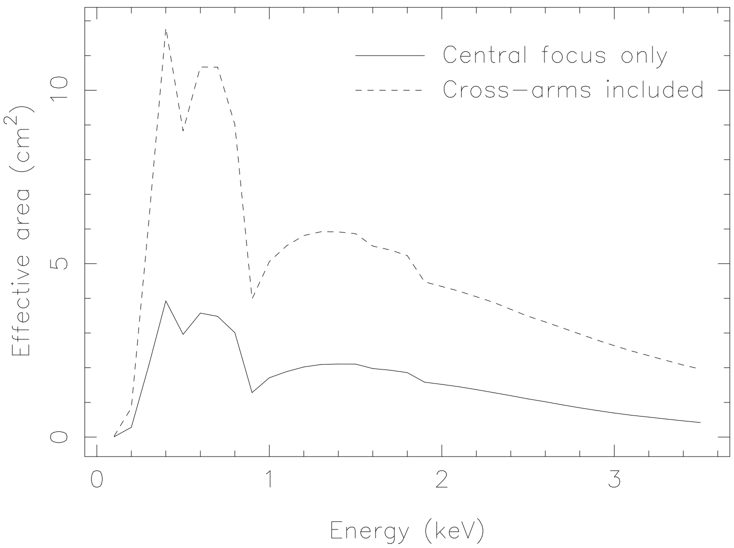

Figure 7.4: The effective area of the Lobster-ISS, including detector quantum efficiency and detector window transmission (0.2μm Si_3N_4, 400Å Al). In this calculation, the MPO walls are coated with nickel to improve reflectivity. The cruxiform point spread function will be deconvolved and hence counts in both the central focus and cross-arms (dashed line) will be included for all sources.

where the 400μm FWHM spatial resolution of the detectors translates to a maximum angular resolution of $\sim 3'$ FWHM. The channels will be on a pitch of 24μm to provide a 70% open area fraction. The MPOs are to be manufactured in Philips 297 glass by Photonis SAS, building on the expertise gained by the company during the ESA TRP contract.

7.4 Co-alignment of lobster eye optics

In order to co-align the ~ 60 MPOs required to fill one mirror module, an alignment jig has been constructed in the Space Research Centre, this takes advantage of the behaviour of MPOs at optical wavelengths. The jig is shown in Figure 7.5.

If illuminated with coherent light, the MPO channels are sufficiently small ($\lambda/D \simeq 0.03$) that they act as a two dimensional diffraction grating. The diffraction properties of micropore optics and the proposed method of using those properties to co-align many individual MPOs are discussed in the following sections.

Figure 7.5: The Lobster MPO alignment jig and associated hardware designed to co-align many individual lobster eye MPOs to create the large mirror modules required for the Lobster-ISS instrument.

7.4.1 Lobster eye micropore optic diffraction

There are two methods of forming a diffraction pattern from a micropore optic using a coherent source. The first is to use the channels as collimators so that the exit of each illuminated channel acts as a coherent square source. The second is to reflect light from the inter-channel web. Here the opposite of the transmitted source pattern is created, a coherent source with a regular array of non-emitting squares throughout it.

Providing that the source array is known, Fourier analysis can be used to predict the resulting Fraunhofer diffraction pattern (Hecht, 1987). The Fourier transform of the aperture function, $A(x, y)$, will yield its diffraction pattern in terms of spatial frequencies, k_x and k_y

$$E(k_x, k_y) = \int\int_{-\infty}^{\infty} A(x, y) e^{i(k_x x + k_y y)} dx dy \tag{7.1}$$

The pattern can be expressed in angular terms by substituting for the spatial frequencies (defined as $k_x = k \sin\theta_x$ and $k_y = k \sin\theta_y$, where θ is the angle subtended by an image point on the optical (z) axis at the aperture and $k = 2\pi/\lambda$).

A regular array of identical sources can be written as the convolution of the aperture function and an array of Dirac delta functions. The diffraction pattern is then found, as stated by the convolution array theorem, from the product of the Fourier transforms of these two functions.

Figure 7.6 shows both (a) a regular array of 20μm side square sources on a 24μm pitch and (c) a source with corresponding dark areas. Areas emitting coherent light have a value of 1 in these arrays, dark areas a value of 0. The Fast Fourier Transform (FFT) diffraction pattern of the two sources are shown in (b) and (d) respectively, the diffraction patterns are identical.

A reflection diffraction pattern from a Lobster specification planar MPO, captured using the alignment jig cameras (section 7.4.2) is shown in Figure 7.7. The angular separation of the secondary maxima from the principal maximum (distances a and b) is $1.6 \pm 0.1°$. This shows strong agreement with the calculated pattern in Figure 7.6(d). The ratio of

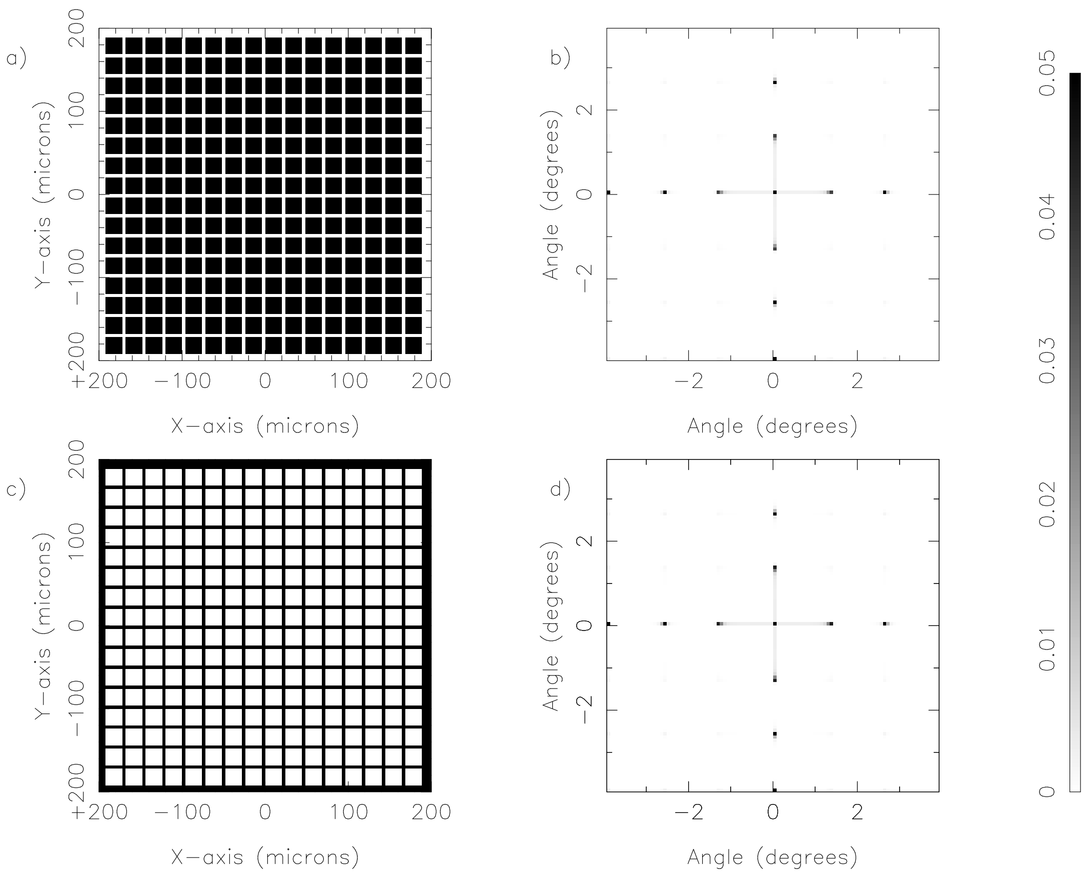

Figure 7.6: Fast Fourier Transforms in transmission (*b*) and reflection (*d*) of the source arrays created when coherent light (*a*) shines through an ideal square-pore MPO and (*b*) reflects from the inter-channel webbing of the same MPO.

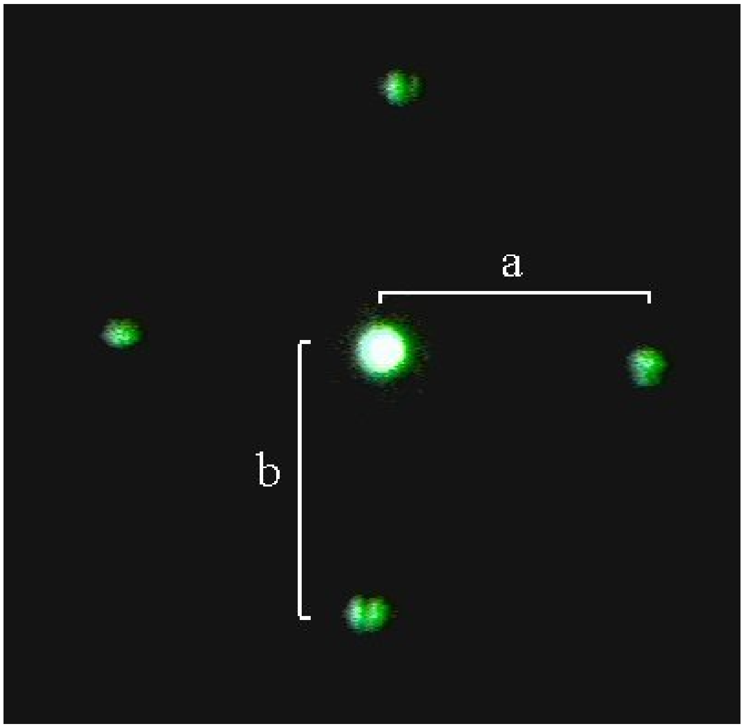

Figure 7.7: Reflection diffraction pattern from a Lobster specification planar micropore optic, captured using the webcams mounted on the alignment jig. The angular separation of the secondary maxima from the principal maximum ($a = b$) is $1.6 \pm 0.1^\circ$. Note the agreement with Figure 7.6(d). The intensity ratio of the principal maximum to a secondary is measured to be 19.0 ± 0.1 c.f. an FFT calculated value of 44.0.

the principal maximum intensity to that of a secondary is measured (section 7.4.2) to be 19.0 ± 0.1 compared to an FFT calculated value of 44.0. The discrepancy is probably a result of imperfections in the MPO lattice, the divergence ($2.8'$) of the laser beam and the circular cross-section of the illuminated area.

The coherent light is provided by a laser and hence the illuminated area on the MPO is small (beam diameter 0.86mm ($1/e^2$) at laser face). A slumped MPO is thus considered to be locally flat and exhibits the same pattern as a planar MPO of the same specification.

When laser light is reflected from the inter-channel webbing of an MPO, it acts as a reflection diffraction grating, a diffraction pattern being formed in the reflected light with the principal maximum in the specular direction. This is illustrated in Figure 7.8.

It is possible to align individual MPOs using this property so that each optic's surface

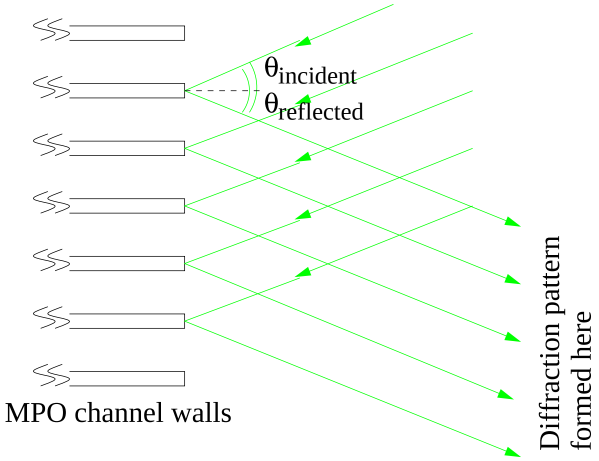

Figure 7.8: MPO channel walls acting as a reflection diffraction grating.

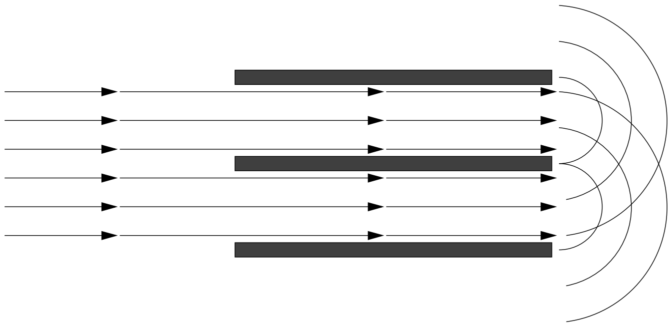

Figure 7.9: Microchannels acting to collimate an on-axis laser beam, producing an array of sources that exhibit a diffraction pattern.

lies on the same sphere. However, during the process where individual channel plates are cut from the block (section 1.4), small bias angles may unknowingly be introduced to each plate. A lobster eye optic requires that all channel axes should point to a common centre; one composed of many MPOs having slightly different bias angles would violate this condition and not be confocal. In order to align the channels of each optic normal to a common sphere, transmission measurements must also be made.

If an array of channels lie with their axes parallel to the incident laser beam, they will simply act as collimators and a single diffraction pattern is seen (Figure 7.9). However, as soon as the laser moves off-axis, reflections are introduced from the channel walls and the channel 'sources' emit coherent light in two directions, as shown in Figure 7.10. The result of this is that two diffraction patterns are produced, one in the direction of the laser beam, and the other at an angle of 2θ to this, where θ is the angle between the laser beam and the channel axes.

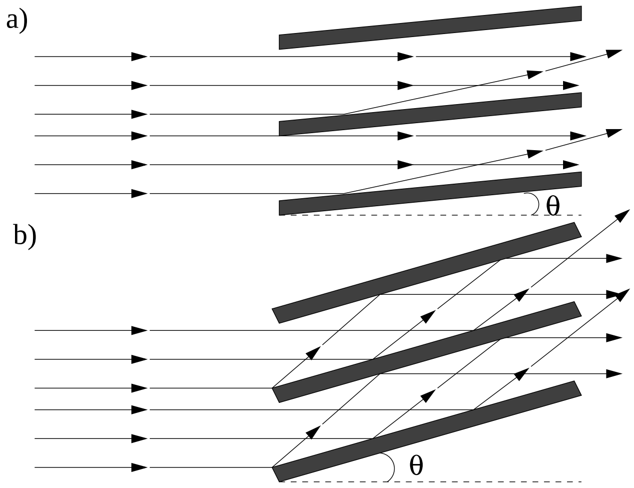

Figure 7.10: As the incident laser beam makes an off-axis angle, θ, with the channel walls, reflections of the laser light will be introduced. This will result in coherent light emerging from the channels in two directions and consequently two distinct diffraction patterns will be observed (a). As the angle increases, more than one reflection can occur from opposite walls, the result, however, is still two patterns, one in the direction of the beam and one at an angle of 2θ to it (b).

In a square cross-section channel there are of course, four walls and so light will emerge in the original incident direction plus three others. There will thus be four diffraction patterns observed when the incident beam is off-axis in both x and y directions. A pattern recorded with the alignment jig cameras (section 7.4.2) is shown in Figure 7.11.

The channel axis direction of an MPO can be determined by observing the principal maximum of the pattern formed in the incident direction of the laser beam. As the plate is tilted, some of the flux that originally contributed to the principal maximum is redirected to the other patterns. Hence by manipulating the MPO until a peak intensity is observed in the original principal maximum, we can align the illuminated channels with the laser beam. In reality the peak will be blurred out slightly by the imperfections in the MPO.

A minimum will be seen at $\theta = D/L$ as all rays will undergo one reflection and it is only just possible for two to occur (and hence continue in the original direction). This will result in nearly all of the flux being diverted from the original principle maximum to the other diffraction patterns. This should not be an issue as the MPO bias angles should be

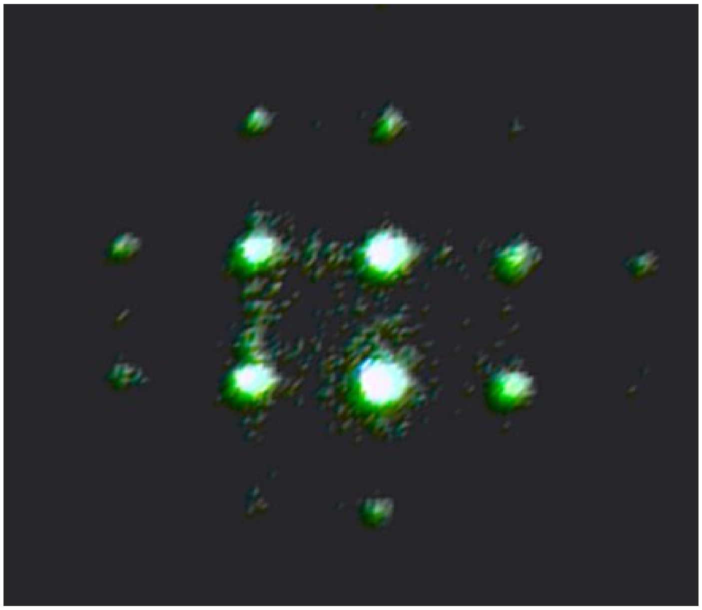

Figure 7.11: A camera image of the transmitted diffraction pattern observed with a tilted MPO. Four principle maxima can be observed with lower intensity secondary maxima surrounding them.

significantly smaller than $D/L = 1/50\text{rads} = 1.15°$.

7.4.2 The Lobster alignment jig

A manipulation jig has been designed and constructed in the Space Research Centre that can exploit the diffraction properties of micropore optics described above to co-align individual MPOs in the Lobster mirror matrix. The jig is shown in Figures 7.5 (photo) and 7.12 (diagram).

The mirror matrix is mounted so that it can be pivoted around the centre of curvature. This allows each point where an MPO will be positioned to be rotated so that it is on the vertical axis of the jig. The transmission laser is aligned along this vertical axis. The reflection laser is mounted to the side of this and is aligned so that it is incident on the lobster eye's surface of curvature at the same point as the transmission laser. The reflected beam is displayed on a ground glass screen along the reflected beam's axis.

The laser beam axes are calibrated through reflections from a spherically concave fused

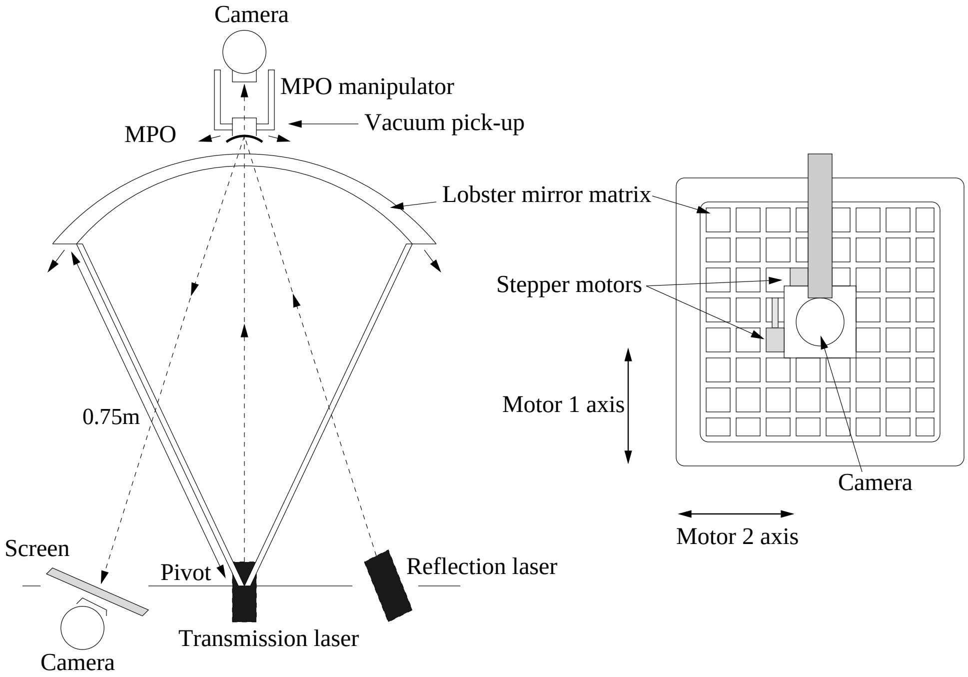

Figure 7.12: The Lobster mirror alignment jig. The MPO matrix pivots about the centre of curvature so that individual MPOs can be fitted in the correct positions. The manipulator then rotates the MPO about two perpendicular axes until transmission and reflection measurements determine it is correctly aligned, when it is glued to the frame.

silica mirror of 0.75m focal length (figure manufactured to a tolerance of $\lambda/10$). The mirror is of the same radius of curvature as the lobster eye optic and can thus sit on the MPO mirror matrix. The vertical of the system can then be defined by reflecting the transmission laser beam back to its origin. The absolute reflection centre can be defined by measuring the specular reflection position on the screen.

The transmitted intensity and reflected position are recorded by Logitec webcams mounted directly above the MPO and behind the screen respectively. The cameras record images as 24 bit 640 × 480 pixel bitmaps, composed of red, blue and green 8 bit colour table arrays. The reflected position is determined by centroiding the reflected diffraction pattern's principal maximum. The transmitted intensity is found by adding the colour table values within a 100 × 100 pixel box centred on the transmitted (original) principal maximum. The transmitted intensity is normalised to the maximum possible intensity in the region of interest (I_{max} = 100 × 100 pixels × 3 colour tables × 2^8 colour table values = 7.68×10^6 colour table units). The RGB (red, blue and green) gains and exposure time levels are adjusted, and neutral density filters inserted in the beam paths to prevent saturation of the images. The webcam is calibrated so that 1mm on the reflection screen corresponds to 11.5 pixels. This gives a theoretical resolution for reflection measurements of $1/(11.5r_{screen})$rads, where r_{screen} is the distance from the matrix surface to the screen. This is currently set at 455mm, giving $39''$ resolution with a $7.0° \times 5.3°$ FOV.

The supporting frame of the system is solidly constructed in stainless steel to dampen vibrations that may perturb measurements, the manipulator and other pieces that form part of the optical system are fabricated in aluminium, anodised black to prevent reflection. The current mirror matrix was machined, in house, to a high tolerance (±0.5mm) from a solid block of glass-fibre. The lasers (543.5nm HeNe) were purchased from Coherent Ltd.

The MPO is attached to the manipulator via a vacuum pick-up with a transparent top to allow the transmitted beam to the camera. The PTFE pick-up uses a water aspirated filter pump to provide a pressure differential that keeps the MPO in place. In this manner the MPO is under as little stress as possible when being aligned. The pick-up is manipulated in orthogonal axes by two geared down computer controlled stepper motors.

The software used to control the stepper motors and cameras was written in house and interfaced to IDL in order to analyse the images. When production of the mirror modules begins, the cameras, analysis package and stepper motors will be connected in a feed-back loop, allowing the automatic alignment of each MPO. The MPOs will be bonded to the matrix with a small amount of a fast U.V. cured glue before the matrix is rotated to allow the positioning of the next MPO ‘tile’.

7.5 Determining the residual bias angle of Lobster MPOs

As an initial trial of the alignment jig, it was decided to determine the bias angles of several planar MPOs of the Lobster specification (40mm square plates with 20μm side square channels on a 24μm pitch and with aspect ratios of 50:1). This has relevance not only to testing the apparatus, but is also an important measurement to be fed back to the MPO manufacturer, as planar MPOs with large bias angles will result in severely misaligned slumped optics.

If the reflection position and transmitted intensity are recorded simultaneously, then the angle between the position of maximum transmitted intensity and the absolute centre of reflection from the mirror module's surface of curvature can be determined. When done in both motor axes, corresponding to the normals of the orthogonal channel walls, the components of the bias angle in each axis are determined. The orientation of the MPO in relation to the motor drive axes can be easily found by analysing the 'axes' of the diffraction patterns. It should be noted that the system FOV is far larger than the bias angles, quoted by Photonis, for the MPOs of $< 0.1°$.

First the reflected principal maximum is moved to the absolute reflection position defined by the reflection from the spherical mirror. The MPO is then tilted $\sim 0.5°$ along one motor axis and scanned in small increments to a similar distance the other side of the reflected centre. This is repeated in the other motor axis. At each angular increment the reflected beam position and transmitted intensity are recorded.

This enables plots of the transmitted principal maximum intensity as a function of the off-axis angle (calculated as the deviation of the reflected spot from the absolute reflection centre) to be made. Figure 7.13 shows the measurements taken with the planar Lobster MPO HC-001-A5.

Uncertainty in the off-axis angle arises from the accuracy of the centroiding technique and in the knowledge of the absolute reflection centre, the intensity reading having a standard Poissonian counting error. A fifth degree polynomial fit is calculated for the points. This function can be differentiated and solved to provide us with the point of inflection (i.e. the angle of maximum transmitted intensity). By repeating this calculation for the maximum and minimum possible angles, an uncertainty in the accuracy of the interpolated point can be found. The data shown in Figure 7.13 gives a maximum transmitted intensity at

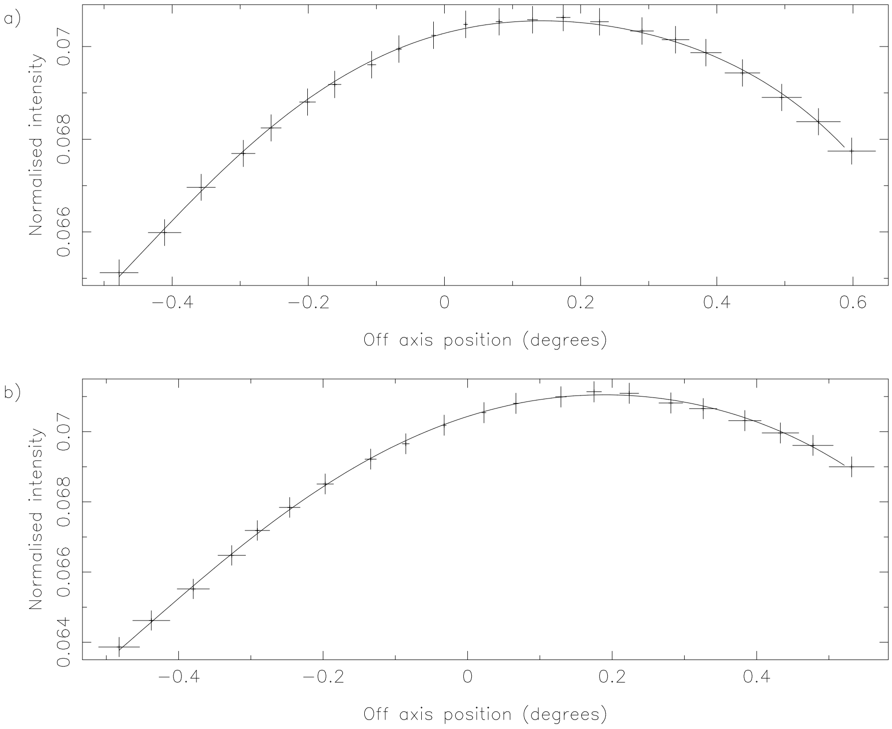

Figure 7.13: The variation in transmitted intensity as a function of angle from the reflection centre, as defined by the spherical mirror, for MPO HC-001-A5. In (a) the MPO has been driven in the motor 1 axis, (b) in the motor 2 axis. The solid line is a fifth degree polynomial fit to the data.

$+0.141 \pm 0.01°$ and $+0.182 \pm 0.01°$ along the motor 1 and motor 2 axes respectively.

In order to be able to tilt the MPO, the vacuum pick-up must be moved away from the surface of the mirror matrix. This introduces a systematic error to any measurements made in this manner. Figure 7.14 shows how the perturbation from the absolute reflection centre as seen on the screen, Δs varies as a function of the MPO distance above the matrix surface of curvature Δz ($\Delta s = 2\Delta z \sin\theta_{laser}$). Under analysis, the variation Δs shows up as an offset angle, θ_{offset}. Δz is typically of the order of several mm.

The measured angle can be written as a sum of the bias angle, θ_{bias} and the offset angle, θ_{offset}

$$\theta_{totalA} = \theta_{offset} + \theta_{bias} \tag{7.2}$$

If another measurement is made with the MPO rotated 180° about the vertical axis of the system, with Δz remaining constant, then the bias angle will be reversed with the

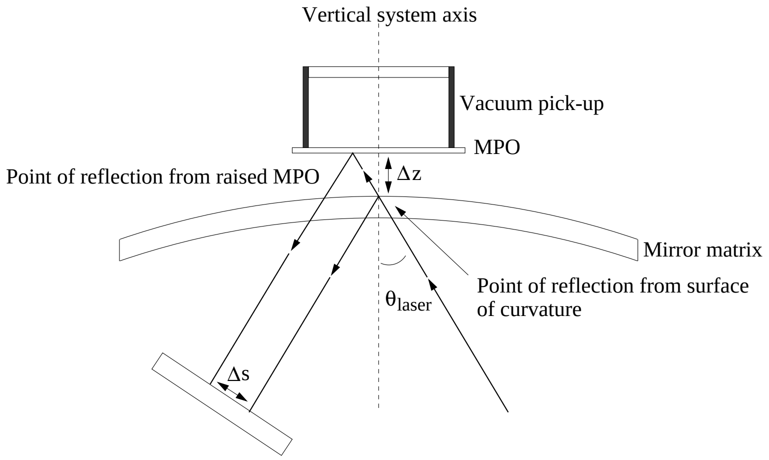

Figure 7.14: As the MPO is raised from the surface of curvature of the mirror matrix, a systematic error is introduced in the reflected position. The error varies as a function of the height of the MPO above the matrix.

offset remaining the same

$$\theta_{totalB} = \theta_{offset} - \theta_{bias} \tag{7.3}$$

This enables the offset angle to be eliminated and the bias angle found

$$\theta_{bias} = \frac{\theta_{totalA} - \theta_{totalB}}{2} \tag{7.4}$$

Figure 7.15 shows the data from the scans of MPO HC-001-A5 once it has been rotated about the system's vertical axis by 180°. This analysis yields off-axis angles of $+0.0154 \pm 0.0005°$ and $+0.223 \pm 0.02°$ along the motor 1 and 2 axes respectively. Using equation (7.4) with the two sets of results (Figures 7.13 and 7.15) allows us to calculate the actual residual bias angles of the MPO to be $-0.063 \pm 0.005°$ and $+0.0205 \pm 0.002°$ in the respective axes. This has a total magnitude of $0.0663 \pm 0.01°$, well within the $\pm 0.1°$ error quoted by Photonis.

A check of these results would be to flip the MPO over and repeat the measurements. If the flip is made about the motor 2 axis, then the bias angle component to the motor 2 axis is expected to remain the same while that to the motor 1 axis will be reversed. Figure 7.16 shows the scans for both motors with the MPO inverted.

Analysis of this data yields bias angles of $+0.0633 \pm 0.003°$ and $+0.0205 \pm 0.001°$ in the motor 1 and 2 axes. This is exactly the expected result. The measured angles must,

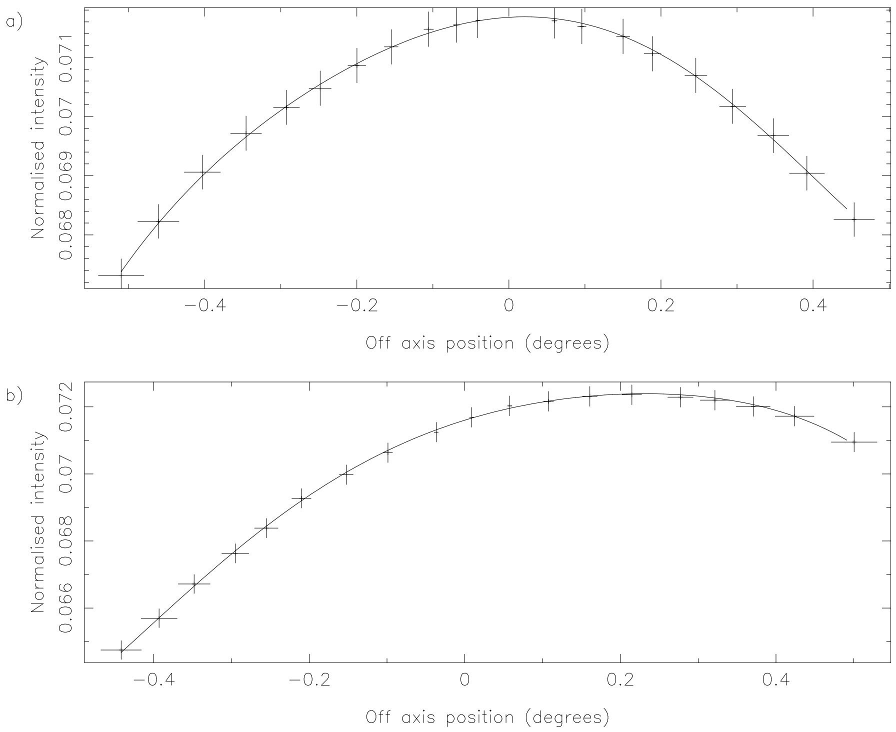

Figure 7.15: **The variation in intensity as a function of angle from the reflection centre for MPO HC-001-A5 when it has been rotated by** $180°$ **about the systems vertical axis.** (a) **shows the motor 1 scan and** (b) **that of motor 2.**

therefore, be real and the surfaces of the MPO must be parallel planes.

Figure 7.17 shows the full face illumination Cu-L (0.93keV) X-ray image of MPO HC-001-A5 taken in the VTF (section 3.2.1). It should be noted that the geometry of planar Lobster plates in the VTF is very similar, in terms of grazing angles, to that of their slumped sister plates viewing X-rays from infinity. The maximum grazing angle of incidence at the edge of the MPO is 1.53° for the slumped plate and 1.64° in the VTF. Unreflected transmission is possible, in the present experimental set-up, to a distance of $(1/50) \times 691$mm=13.8mm from the optical axis and $(1/50) \times 750$mm=15.0mm for a slumped MPO illuminated by a source at infinity.

The FWHM resolution of the MPO is $7'$ square with an effective area (within 3σ of peak channel) of $3.08 \pm 0.35\text{cm}^2$ and a peak channel gain of 86 ± 10. These values were calculated in the same manner as for all other images in this thesis (section 3.5). The MPO can be modelled, as for the square-packed MPOs in chapter 4, using the raytrace

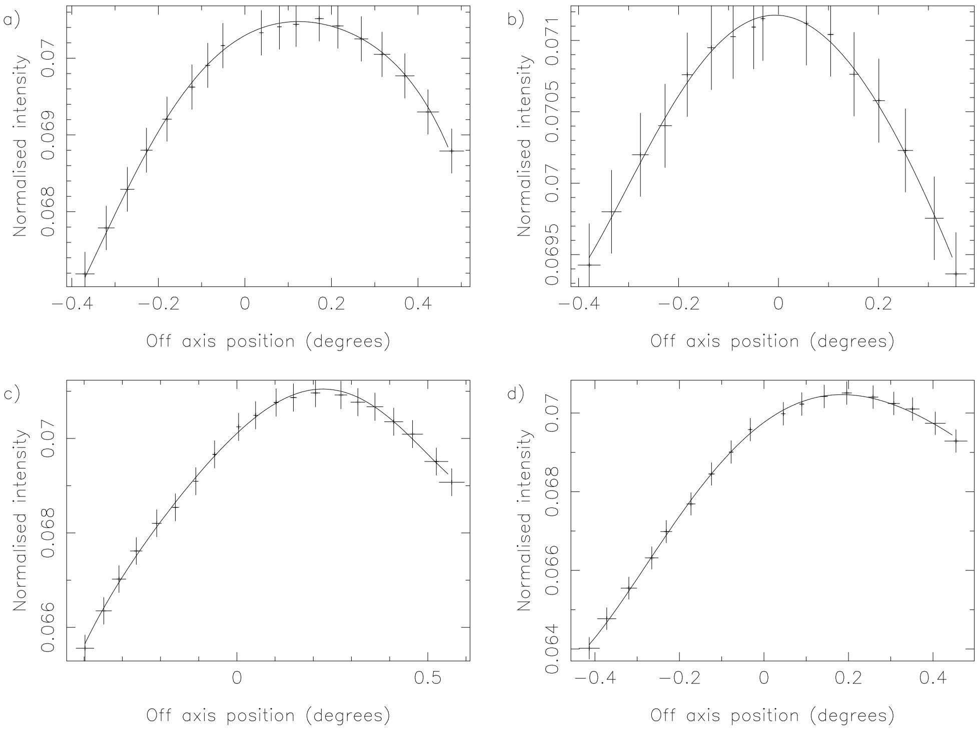

Figure 7.16: The variation in intensity as a function of angle from the reflection centre for MPO HC-001-A5 when it has been flipped over about the motor 2 axis. (a) and (b) show the motor 1 scans for the normal and rotated positions respectively, (c) and (d) the motor 2 scans.

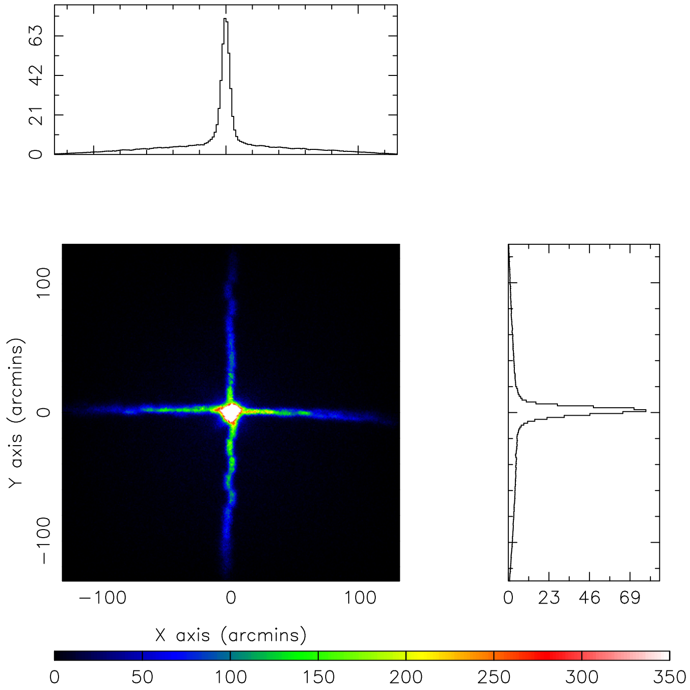

Figure 7.17: The full face illumination image of MPO HC-001-A5 with Cu-L (0.93keV) X-rays in the VTF. The focus resolution is $7'$ square FWHM with an effective area of 3.08 ± 0.35cm^2 and a peak channel gain of 86 ± 10. These values were measured as for all other images (section 3.5).

software. Using the same inter-channel alignment errors as determined during the ESA TRP programme (15Å rms wall roughness on a correlation length of 1μm and 20$''$ rms tilt errors; Beijersbergen *et al.* 1999), the inter-multifibre tilt errors required to model the MPO have an rms magnitude of $\sim 1.5'$.

Although the MPOs are of a relatively poor resolution, it should be remembered that HC-001-A5 and its sister plates come from the first block to be manufactured with 20μm pores and so teething problems are to be expected. The bias angle control seems to be well within quoted values and approaching zero ($4 \pm 1.5'$ taking into account inter-multifibre alignment errors).

The resolutions and bias angles from the planar sister MPOs to HC-001-A5 are of the same order of magnitude.

7.6 Conclusion

The technique that has been proposed to align the individual MPOs in the Lobster mirror matrices has been tested. The bias angles of several Lobster specification micropore optics have been measured and demonstrated to be within the $\pm 0.1°$ from zero limits quoted by Photonis. The angles are of such a level ($\sim 4'$) that they are nearly at the level of tilt error that would be expected for the baselined $2' \rightarrow 3'$ resolution Lobster MPOs. If the bias can be reduced to such a level during the cutting process, the transmission measurements can be abandoned during the mirror matrix assembly, making the whole process more streamlined.

The next step to be taken will be the co-alignment of two MPOs slumped to the correct radius on the glass-fibre matrix shown in Figure 7.12. The TTF (section 3.2.2) has been modified so that the matrix can be accommodated in the tank at the correct distance from the detector. This is expected to take place within the next few months. A full time-line for the Lobster-ISS project can be found in the final chapter of this thesis.

Chapter 8

Conclusions and future work

8.1 Summary of results

This thesis has described progress in the fields of microchannel plate detectors and their offspring, micropore optics.

Chapter 2 described a Monte Carlo model developed to calculate the electron energy and angular distributions in the output charge cloud of an MCP detector. The model was validated through comparison with published experimental data and was shown to be a useful tool in the evaluation of channel structure modifications.

The rest of the thesis has been concerned with the assessment of the micropore optic deliverables from the ESA TRP programme and with the status of planned (UK) astronomical missions in light of the results.

Point-to-point hard X-ray (50keV→ 65keV) imaging and the best ever ($5'$ FWHM) large format planar and slumped plate foci have been demonstrated with square-pore, square-packed micropore optics. True Wolter imaging with a peak channel gain of greater than unity has been observed in a microchannel conic approximation to the Wolter II geometry.

In all cases, however, the resolution, effective area and gains have been recorded at far lower levels than expected from a perfect MPO. Most of the alignment error responsible for the reduced quality of the MPOs has been shown to lie between multifibres. Furthermore, these misalignments are systematic, not random in nature and are thought to be induced during the fusion of individual multifibres in to a boule/block.

i) In the case of radially-packed boules, it has been suggested that the voids that result from the packing of square multifibres in a radial pattern could be the source of the observed distortions.

ii) The deformation or thermal mismatch to MPO glass of the of the moulds used during ram fusion has been proposed as a possible mechanism for the production of the alignment errors found in square-packed blocks.

The slumping of large format, small pore MPOs has been found to have demanding problems associated with it. Large aspect ratio plates (L/D=500:1) have shown evidence of channel shearing occurring towards their edges and MPOs with smaller aspect ratios have been shown to have different radii of curvature in orthogonal directions. A new method of post-etch slumping MPOs has been tried, the resulting lobster eye MPOs are currently at Leicester awaiting testing.

The TRP programme has developed square-packed MPOs from immaturity to the point where they are very close to the quality necessary for their first astronomical application in the Lobster-ISS experiment. Another TRP programme has been approved (0.8MEuro) to start at the end of 2001. This programme is to be dedicated to the microchannel Wolter optic and will hopefully bring it to a similar state of technical evolution.

The current status of micropore optics is summarised in Table 8.1, reproduced, in part, from the ESA TRP summary report (Boutot *et al.*, 2000).

Characteristic	TRP goal	TRP results
Focused energy range	$10 \rightarrow 50$keV	$1 \rightarrow 65$keV (limited high energy response)
Channel surface roughness	< 10Å	$5 \rightarrow 15$Å
Channel aspect ratios	1000:1	500:1
Channel side length	10μm	10μm
Corner radiusing	$< 4\%$ channel perimeter	$< 4\%$ channel perimeter
Open area fraction	$> 50\%$	69% (Square-packing) 65% (Radial-packing)
Alignment errors	$< 100''$	$20''$ (Inter-channel) $60 \rightarrow 420''$ (Inter-multifibre) with additional systematic errors dependent upon stacking pattern

Table 8.1: ESA TRP micropore optic technical specification goals and results.

8.2 Status of microchannel Wolter optics for astronomy

The ESA TRP2 programme, as mentioned above, is to be dedicated to the realisation of functional microchannel Wolter optics. The contract (again with Photonis SAS) will run for 30 months and has listed as its aims (Bavdaz, 2001):

i) The improvement in quality of single fibres and multifibres to the level required for practical X-ray optic applications.

ii) The stacking of square multifibres into radially-packed arrays with diameters up to 400mm.

iii) The coating of channel walls with an appropriate heavy metal to improve high energy reflectivity.

iv) The production of an optic of the HERMES-X specification (section 6.7). This is to be made in several segments for each Wolter MPO (e.g. quadrants).

v) The demonstration of high aspect ratio channel etching in silicon (Si-)MPOs.

New stacking techniques are to be developed including the use of appropriate feedback metrology and mechanisation to ensure the accurate alignment of multifibres during stacking into boules. This process may use a similar technique to that used to co-align Lobster-ISS MPOs (section 7.3). A cold gluing method of bonding the multifibres together will be explored alongside the traditional hot fusion process in an attempt to eliminate the tilt errors induced during this stage of manufacture. The profiling of MPOs to increase effective area, discussed in section 6.7, is also to be implemented.

An intensive campaign of this nature will certainly increase the efficiency of microchannel Wolter optics, hopefully to a level where the HERMES-X telescope for BepiColombo can be considered a realistic prospect. Should the results of the TRP2 contract be of sufficient quality then "a high energy extension module for the XEUS telescope becomes an attractive option" (Bavdaz, 2001).

8.3 Lobster-ISS micropore optics

Following the ESA TRP contract, Leicester commissioned another square-packed MPO block. This block was produced to the Lobster specifications described in section 7.3. The initial results from the planar MPOs cut from this block are promising, with observed focus and gain (Figure 7.17) of the same order as the best optics tested to date, despite problems related to the first draw attempt with an increased fibre size (Fairbend, 2001). MPOs from this block, slumped using a new post-etch method, are currently at Leicester awaiting evaluation.

Following the testing of individual Lobster MPOs, the alignment jig (section 7.4.2) will be used to co-align first several, then many MPOs on the Lobster mirror matrix. At each stage, the focus and effective area of the growing telescope will require testing in the TTF. A fixture has now been installed in the test chamber to hold the mirror matrix in the X-ray beam. When production of the flight modules occurs, the process will require automating to some degree as the six mirror modules each have ~ 60 MPOs to be co-aligned.

The MPOs proposed for Lobster-ISS have nickel coated channels to increase their reflectivity. Nickel coating is a process that has been looked into before (Martin, 2000) but will require intensive study in the near future.

A thermal study of the Lobster-ISS instrument in the environment of the ISS (Renouf *et al.*, 2001) found that the low thermal conductivity and heat capacity of MPOs resulted in large fluctuations in their temperature as Lobster-ISS moves in and out of eclipse. A solution to this is to use filmed MPOs, where a thin aluminium film covers one side of the plate (Renouf, 2001). This decreases the thermal absorptivity of the optics and thus their temperature fluctuations. MCPs with films of this type are currently used in so called "Gen 3" image intensifiers to prevent ion feedback. The use of this technology with square-pore MPOs has to be explored.

In addition to the above points, the MPOs need to be space qualified (i.e. vibration, thermal cycle and radiation tested). This should occur before the instrument assembly phase. Plans to fly MPO witness samples to the ISS early in 2002 for exactly this purpose have been implemented.

Although there are still many technological obstacles to be overcome before the Lobster-ISS requirements are fully met, the basic optics are very close. Given the time available and the rapid evolution of micropore optics thus far, the proposed characteristics seem entirely reasonable. The Lobster-ISS time-line is shown in Table 8.2.

2000	31 Jan	F2/F3 proposal deadline
	7 Mar	ISS selection
	23 Mar	Study kick-off meeting at ESTEC
	23 May	
	11 Jul	Study progress meetings (Leicester)
	16 Nov	
	20 Dec	Accommodation study report issued
2001	22 Jan	ESA Astronomy Working Group (AWG) approval
	30 Jan	ESA Space Science Advisory Committee approval
	14 Feb	ESA ISS Utilisation Board approval
	27 Feb	ESA Scientific Programme Committee (SPC) approval (no further science approvals required)
	1 Mar	ESA ISS Programme Board approval → *Phase A study commitment*
	1 Oct	Release of Invitation to tender for Phase A
2002	1 Jan	Industrial Phase A study start
	Jan (TBC)	Launch of MPO witness sample to Russian module of ISS for 1 year exposure
	31 Dec	Industrial Phase A study ends
2003	Apr	*Commitments from national agencies to Instrument Phases B,C,D*
2005		ISS operational (NASDA MAXI X-ray All Sky Monitor)
2007		Delivery of flight instrument
2009		Lobster-ISS launch on Shuttle and deployment on Columbus Exposed Payload Facility
2012		End of mission, retrieval and return to Earth

Table 8.2: The Lobster-ISS time-line.

Bibliography

J. Adams and B.W. Manley. The channel electron multiplier. *Electron.Eng.*, **37**, 180, 1965.

J. Adams and B.W. Manley. The mechanism of channel multiplication. *IEEE Trans.Nucl.Sci.*, **NS-13**(3), 100, 1966.

J. Adema. UV auroral imager for the Freja project, 1993. Delft Electronic Products.

J.R.P Angel. Lobster eyes as X-ray telescopes. *Astrophys.J.*, **233**, 364, 1979.

A .V. Antonov, V. V. Apanasovich, and E.G. Novikov. Analytical and simulation model of electron multiplication in microchannel plate. *Proc. SPIE.*, **2859**, 281, 1996.

B. Aschenbach. Design, construction and performance of the RoSAT high-resolution mirror assembly. *Proc. SPIE.*, **830**, 152, 1987.

A. Authinarayanan and R.W. Dudding. Changes in secondary electron yield from reduced lead glass. *Adv. Electronic. Electron. Phys.*, **40A**, 167, 1976.

G. Bale. *CdZnTe radiation detectors for hard X-ray astronomy.* PhD thesis, University of Leicester, 2001.

N.P. Bannister, M.A. Barstow, and G.W. Fraser et al. The Joint astrophysical Plasmadynamic EXperiment (JPEX). In *ASP Conf. Ser. 169: 11th European Workshop on White Dwarfs*, page 188, 1999.

M.A. Barstow, J.E. Lees, and G.W. Fraser. Observation of microchannel plate multifibre structure in soft X-ray images. *Nucl.Instr.Meth.A*, **286**, 350, 1990.

M.A. Barstow and A.E. Samsom. The RoSAT WFC imaging detectors. *Proc. SPIE.*, **1344**, 244, 1990.

M. Bavdaz. Technical assistance for support in the study of high energy optics: Statement of work. ESA Internal report MB/SSD/01/01, 2001.

M. Bavdaz, M. Beijersbergen, A. Peacock, B. Aschenbach, H. Bräuninger, and R. Willingale. Status of the optics for the X-ray Evolving Universe Spectroscopy Mission (XEUS). *Proc. SPIE.*, **4138**, 69, 2000.

M. Bavdaz, J.A.M Bleeker, G. Hasinger, H. Inoue, G. Palumbo, A. Peacock, A. Parmar, M.J. Turner, J. Truemper, and J. Schiemann. The X-ray Evolving Universe Spectroscopy Mission (XEUS). *Proc. SPIE.*, **3766**, 82, 1999.

P. Beckmann and A. Spizzichino. *The scattering of electromagnetic waves from rough surfaces.* Pergamon Press, 1963.

C.P. Beetz, R. Boerstler, J. Steinbeck, B. Lemieux, and D.R. Winn. Silicon-micromachined microchannel plates. *Nucl.Instr.Meth.A*, **442**, 443, 2000.

M. Beijersbergen, M. Bavdaz, A. Peacock, E. Tomaselli, G. Fraser, A. Brunton, E. Flyckt, R. Fairbend, M. Krumrey, and A. Soouvorov. Microchannel plate based X-ray optics. *Proc. SPIE.*, **3765**, 452, 1999.

M.W. Beijersbergen. Roughness measurements on four sides of channels in a square-pore square-pack micropore optic. Technical report, ESA, January 2000a.

M.W. Beijersbergen. X-ray measurements of final deliveries of micropore optics at Bessy. Technical report, ESA, June 2000b.

M.W. Beijersbergen, M. Bavdaz, A. Peacock, E. Tomaselli, R. Fairbend, J-P. Boutot S.O. Flyckt, A. Brunton, G. Price, G. Fraser, C. Herrmann, M. Krumrey, E. Zeigler, and A. Freund. High-resolution micro-pore X-ray optics produced with microchannel plate technology. *Proc. SPIE.*, **4145**, 188, 2000a.

M.W. Beijersbergen, M. Bavdaz, A. Peacock, E. Tomaselli, G. Fraser, A. Brunton, G. Price, M. Krumrey, C. Herrmann, A. Freund, E. Zeigler, A. Souvorov, R. Fairbend, J-P. Boutot, and S.O. Flyckt. Novel micro-pore X-ray optics produced with microchannel plate technology. *Proc. SPIE.*, **4012**, 218, 2000b.

C. Bouchard and J.D. Carette. Secondary electron emission and ion feedback in a straight semiconduction channel. *J.Appl.Phys*, **50**(11), 7168, 1979.

J.P. Boutot, P. Clauzel, R. Fairbend, S.O. Flyckt, and J.L. Mutz (Photonis SAS). Summary Report: Development of microchannel plates for UV and X-ray imaging systems. Technical report, ESA/ESTEC, June 2000.

H.V. Bradt, J.H. Swank, and R.E. Rothschild. The X-ray Timing Explorer. *Adv.Space.Res.*, **11**, 243, 1991.

I.M. Bronshteyn, A.V. Yevdokimov, and A.M. Tyutikov V.M. Stozharov. Differential secondary-emission characteristics of microchannel plates. *Radio Eng. Elec. Phys.*, **24**, 150, 1979.

A.N. Brunton. *MCP optics.* PhD thesis, University of Leicester, 1994.

A.N. Brunton. XRF imager for BepiColombo, 2001. Leicester University internal report.

A.N. Brunton, G.W. Fraser, J.E. Lees, W.B. Feller, and P.L. White. X-ray focusing with 11μm square pore microchannel plates. *Proc. SPIE.*, **2519**, 40, 1995.

A.N. Brunton, G.W. Fraser, J.E. Lees, and I.C.E. Turcu. Metrology and modeling of microchannel plate X-ray optics. *Appl.Opt.*, **36**, 5461, 1997.

A.N. Brunton, A.P. Martin, G.W. Fraser, and W.B. Feller. A study of 8.5μm microchannel plate X-ray optics. *Nucl.Instr.Meth.A*, **431**, 356, 1999.

A.N. Brunton, G.J. Price, and R. Fairbend. Summary of square-packed optics results, 2000. Leicester University internal report.

E. A. Burke. Soft X-ray induced electron emission. *IEEE Trans.Nucl.Sci.*, **NS-24**, 2505, 1977.

H.N. Chapman, K.A. Nugent, and S.W. Wilkins. X-ray focussing using square channel-capillary arrays. *Rev.Sci.Instrum.*, **62**, 1542, 1991.

Y.S. Choi and J.M. Kim. Monte carlo simulations for tilted-channel electron multipliers. *IEEE Trans.Elec.Dev.*, **47**, 1293, 2000.

E.L. Church, H.A. Jenkinson, and J.M. Zavada. Relationship between surface scattering and microtopographic features. *Opt.Eng.*, **18**, 125, 1978.

S.W.H. Cowley, M. Lester, and G.W. Fraser. A wide field FUV auroral imager for low earth orbit missions: A response to PPARC panel and referee comments, 2000.

T.A. Crabb, P.N. Gibson, and K.J. Roberts. Rex - a least squares fitting program for the simulation and analysis of X-ray reflectivity data. *Comp.Phys.Commu.*, **3**, 441, 1993.

D.T. Cromer and D. Liberman. Relativistic calculation of anomolous scattering factors for X-rays. LASL report LA-4403, Los Alamos Laboratory, 1970.

I.P. Csorba. Current gain parameters of microchannel plates. *Appl.Opt.*, **19**, 3863, 1980.

D. de Chambure, R. Laine, K.v. Katwijk, J.v. Casteren, and P. Glaude. The status of the X-ray mirror production for the ESA XMM spacecraft. *Proc. SPIE.*, **2808**, 362, 1996.

D. de Chambure, R. Laine, and K. van Katwijk. The X-ray telescope for the ESA XMM spacecraft. *Proc. SPIE.*, **3444**, 313, 1998.

A.J. Dekker. *Solid State Physics: secondary electron emission.* Academic Press, New York, 1958.

E. H. Eberhardt. Gain model for microchannel plates. *Appl.Opt.*, **18**, 1418, 1979.

E. H. Eberhardt. An operational model for microchannel plate devices. *IEEE Trans.Nucl.Sci.*, **NS-28**, 712, 1981.

M.L. Edgar, R. Kessel, J.S. Lapington, and D.M. Walton. Spatial charge cloud distribution of microchannel plates. *Rev.Sci.Instrum.*, **60**, 3673, 1989.

W. Ehrenberg. X-ray optics: The production of converging beams by total reflection. *J.Opt.Soc.Am.*, **39**(9), 741, 1949.

D.L. Emberson. Summary of square channelled MCP development for scientific applications 1990-1993, 1994. Philips internal report.

ESA Internal report. Statement of work for the development of a microchannel plate imaging system for hard X-rays., 1995. ESA TRP contract 12193/96/NL/SB.

R. Fairbend. (Photonis SAS). Private communication to A. Brunton, 2001.

Farnsworth, 1930. U.S. Patent number 1,969,399.

W.B. Feller, R.G. Downing, and P.L. White. Neutron field imaging with microchannel plates. *Proc. SPIE.*, **4141**, 2000.

R.F. Floryan. Focussed output microchannel plate for image intensifier tube, 1996. U.S. Patent number 5,563,653.

L.A. Frank, J.B. Sigworth, J.D. Craven, J.P. Cravens, J.S. Dolan, M.R. Dvorsky, P.K. Hardebeck, J.D. Harvey, and D.W. Muller. The visible imaging system (VIS) for the POLAR spacecraft. *Space Sci.Rev.*, **71**, 297, 1995.

G. W. Fraser. *X-ray detectors in astronomy.* Cambridge University Press, 1989.

G. W. Fraser, M.A. Barstow, J. F. Pearson, M.J. Whiteley, and M. Lewis. The soft X-ray detection efficiency of coated microchannel plates. *Nucl.Instr.Meth.A*, **224**, 272, 1984.

G. W. Fraser, J. F. Pearson, and J. E. Lees. Caesium bromide X-ray photocathodes. *Nucl.Instr.Meth.A*, **256**, 401, 1987.

G. W. Fraser, J. F. Pearson, J. E. Lees, and W.B. Feller. Advances in microchannel plate detectors. *Proc. SPIE.*, **982**, 98–107, 1988.

G. W. Fraser, J. F. Pearson, G. C. Smith, M. Lewis, and M. A. Barstow. The gain characteristics of microchannel plates for X-ray photon counting. *IEEE Trans.Nucl.Sci.*, **NS-30**, 455, 1983.

G.W. Fraser. The characteristics of soft X-ray photo-cathodes in the wavelength band 1-300$\mathring{A}$ 1. lead glass, lithium flouride and magnesium flouride. *Nucl.Instr.Meth.*, **206**, 251, 1983.

G.W. Fraser. Microchannel plate X-ray optics. In: The next generation of X-ray observatories, M.J.L. Turner and M.G. Watson eds., XRA97/02, Leicester X-ray Astronomy Group Special Report, 191, 1997.

G.W. Fraser. Angle and energy distributions of output electrons in microchannel plate (MCP) multipliers. Technical report, Leicster University internal report XRA/Ebeam-1, 1998.

G.W. Fraser, A.N. Brunton, N.P. Bannister, J.F. Pearson, M.J. Ward, T. Stevenson, D.J. Watson, B. Warwick, S. Whitehead, P.T.O'Brian, N. White, K. Jahoda, K. Black, S.D. Hunter, P. Deines-Jones, W.C. Priedhorsky, S.P. Brumby, K.N. Borozdin, T. Vestrand, A.C. Fabian, K. Nugent, A. Peele, T.H. Irving, S. Price, S. Eckersley, I. Renouf, M. Smith, A. Parmar, I.M. McHardy, P. Uttley, and A. Lawrence. Lobster-ISS: An imaging X-ray sall-sky monitor for the International Space Station. *Proc. SPIE.*, **4497**, page number TBA, 2001a.

G.W. Fraser, A.N. Brunton, J.E. Lees, and D.L. Emberson. Production of quasi-parallel X-ray beams using microchannel plate 'X-ray lenses'. *Nucl.Instr.Meth.A*, **334**, 579, 1993a.

G.W. Fraser, A.N. Brunton, J.E. Lees, J.F. Pearson, and W.B. Feller. X-ray focusing using square-pore microchannel plates: First observation of cruxiform image structure. *Nucl.Instr.Meth.A*, **324**, 404–407, 1993b.

G.W. Fraser, A.N. Brunton, D. Ramsden, J. Zarnecki, M.G. Pia, J. Huovelin, and S.O. Flyckt. High Energy Remone-sensing of Mercury's Surface (HERMES). Technical report, Intent to propose an instrument for BepiColombo, 2001b.

G.W. Fraser, J.E. Lees, J.F. Pearson, and M.A. Barstow. The operation of microchannel plates with square pores. *Nucl.Instr.Meth.A*, **310**, 292, 1991a.

G.W. Fraser, J.E. Lees, J.F. Pearson, M.R. Sims, and K. Roxburgh. X-ray focusing using microchannel plates. *Proc. SPIE.*, **1546**, 41, 1991b.

G.W. Fraser and E. Mathieson. Signal location by uniform resistive anodes. A: Square anodes in the D.C. limit. *Nucl.Instr.Meth.A*, **179**, 591, 1981.

G.W. Fraser, M.J. Ward, R. Warwick, A.N. Brunton, R.E. Cole, M.G. Watson, P.O'Brien, W.C. Priedhorsky, S. Brumby, K. Borozdin, T. Vestrand, N.E. White, K. Jahoda ans K. Black, R. Petre, S. Hunter, W. Zhang, A.C. Fabian, K. Nugent, and A. Peele. LOBSTER-ISS: An imaging all-sky monitor (ASM) based on lobster eye X-ray optics. Technical report, An International Space Station (ISS) attached payload submitted in response to the ESA call for mission proposals for the flexi-missions F2 and F3, 2000.

G.W. Fraser, R. Willingale, M.J.L. Turner, R.E. Cole, A.M. Cruise, and Yu.N. Gnedin. Hard X-ray Telescope HXT: a proposal for the ESA M3 mission opportunity. Technical report, Leicester University, 1993c.

H.O. Funsten, D.M. Suszcynsky, and R.W. Harper. Mean secondary electron yield of avalanche electrons in the channels of a microchannel plate detector. *Rev.Sci.Instrum.*, **67**, 3478, 1996.

R. Giacconi, H. Gurskey, F.R. Paolini, and B.B. Rossi. Evidence for X-rays from sources outside the solar system. *Phys.Rev.Let.*, **9**, 439, 1962.

R.F. Goff and C.F. Hendee. Studies of the secondary electron emission yield, energy and angular distribution from high resistance targets at grazing angles of incidence. *Proc. 27th Ann. Conf. Phys. Elec.*, 1967.

Ph. Gondoin, D. de Chambure, K. van Katwijk, Ph. Klezkine, D. Stramaccioni, B. Aschenbach, O. Sitterio, and R. Willingale. The XMM telescope. *Proc. SPIE.*, **2279**, 86, 1994.

G.W. Goodrich and W.C. Wiley. Continuous channel electron multiplier. *Rev.Sci.Instrum.*, **33**, 1962.

R.A. Greenwald, K.B. Baker, J.R. Dudeney, M. Pinnock, T.B. Jones, E.C. Thomas, J-P. Villan, J-C. Cerisier, C. Senior, C. Hanuise, R.D. Hunsucker, G. Sofko, J. Koehler, E. Nielsen, R. Pellinen, A.D.M. Walker, N. Sato, and H. Yamagishi. DARN/SuperDARN a global view of the dynamics of high lattitude convection. *Space Sci.Rev.*, **71**, 761, 1995.

A. J. Guest. A computer model of channel multiplier plate performance. *Acta Electronica*, **14(1)**, 79, 1971.

A. Haar. Array software boost electon beam lithography throughput. *BMDO Update*, **38**, 1, 2001.

L.A. Harris. Saturation in continuous channel electron multipliers. *Rev.Sci.Instrum.*, **42**, 987, 1971.

E. Hecht. *Optics 2^{nd} ed.* Addison-Wesley, 1987.

B.L. Henke. Low energy X-ray interactions: photoionization, scattering, specular and bragg reflection. In D.T. Attwood and B.L. Henke, editors, *Topical conference on low-energy X-ray diagnostics*, volume 75, page 146. AIP, 1981.

G.E. Hill. Secondary electron emission and compositional studies on channel plate glass surfaces. *Adv.Electron.Electron Phys.*, **40A**, 153, 1976.

S.S. Holt and W. Priedhorsky. All sky monitors for X-ray astronomy. *Space Sci.Rev.*, **45**, 269, 1987.

J.J.M. In't Zand, W.C. Priedhorsky, C.E. Moss, and E.E. Fenimore. The MOXE X-ray all sky monitor for Spectrum-X-Gamma. *Proc. SPIE.*, **2279**, 458, 1994.

K. Jahoda, K. Black, and P. Deines-Jones. Lobster-ISS detector description document. Technical report, GSFC, 2000.

P. Kaaret and P. Geissbuhler. Lobster eye X-ray optics using microchannel plates. *Proc. SPIE.*, **1546**, 82, 1991.

J. Kawarabayashi, H. Takahashi, I. Iguchi, M. Nakazawa, A. Takahashi, and R. Tokue. New array type electron multiplier as a two dimensional position sensitive detector. *Nucl.Instr.Meth.A*, **353**, 172, 1994.

J. Kawata and K. Ohya. Energy and angular distributions of kinetic electrons emitted from a solid surface due to grazing incidence of protons. *Jap.J.Appl.Phys*, **36**, 2325, 1997.

J. Kawata, K. Ohya, and I. Mori. Direct Monte Carlo simulation of incident angle dependence of secondary electron emission from aluminium. *Jap.J.Appl.Phys*, **31**, 1453, 1992.

H. Kiessig. Interferenz von Röntgenstrahlen an dünnen Schichten. *Ann.Physik*, **10**(5), 769, 1931.

P. Kirkpatrick and A.V. Baez. Formation of optical images by X-rays. *J.Opt.Soc.Am.*, **38**(9), 766, 1948.

O. Klemperer and M.E. Barnett. *Electron Optics.* Cambridge University Press, 1971.

N. Koshida. Effects of electrode structure on output electron energy distribution of microchannel plates. *Rev.Sci.Instrum.*, **57**, 354, 1986.

N. Koshida and M. Hosobuchi. Energy distribution of output electrons from a microchannel plate. *Rev.Sci.Instrum.*, **56**, 1329, 1985.

N. Koshida, M. Kunii, and S. Yoshida. Narrow energy distribution of output electrons from modified single channrl electron multiplier. *Rev.Sci.Instrum.*, **51**, 365, 1980.

N. Koshida, M. Midorikawa, and Y. Kiuchi. Output energy distribution of a microchannel plate. *Adv.Electron.Electron Phys.*, **64B**, 337, 1985.

N. Koshida and S. Yoshida. Energy distribution of output electrons from a single channel electron multiplier. *Rev.Sci.Instrum.*, **50**, 177, 1979.

M.F. Land. Animal eyes with mirror optics. *Scientific American*, **239**, 126, 1978.

J.S. Lapington. The effects of secondary electron emission on the operation of position sensitive anodes. *Nucl.Instr.Meth.A*, **392**, 336, 1997.

J.S. Lapington, B. Sanderson, and L.B.C. Worth. The vernier electronic readout - high resolution and image stability from a charge division readout for microchannel plates. *Proc. SPIE.*, **3445**, 535, 1998.

J.S. Lapington and L.B.C. Worth. The effect of anode composition on secondary electron mediated charge redistribution in charge division anodes. *Proc. SPIE.*, **3445**, 546, 1998.

J.E. Lees, G.W. Fraser, M.R. Sims, A.N. Brunton, R.E. Cole, and J.F. Pearson. A wide field FUV auroral imager for low earth orbit missions, 1999. RSPP study - final report.

J.E. Lees and J.F. Pearson. A large area MCP detector for X-ray imaging. *Nucl.Instr.Meth.A*, **384**, 410, 1996.

M. Lester, S. Milan, J. Thornhill, C. Thomas, J. Wild, and T. Yeoman. CUTLASS tutorial, 1998. CUTLASS workshop University of Leicester.

J.D. Mangus and J.H. Underwood. Optical design of a glancing incidence X-ray telescope. *Appl.Opt.*, **8**, 94, 1969.

A.P. Martin. *Exploitation of microchannel plates.* PhD thesis, University of Leicester, 2000.

M. Matsuoka, N. Kawai, T. Mihara, A. Yoshida, H. Kubo, T. Kotani, H. Negoro, B.C. Rubin, H.M. Shimizu, H. Tsunemi, K. Hayashida, S. Kitamoto, E. Miyata, and M. Yamauchi. MAXI (Monitor of All sky X-ray Image) for JEM on the space station. *Proc. SPIE.*, **3114**, 414, 1997.

P.K. Oschepkov, B.N. Skvortsov, B.A. Osanov, and I.V. Siprikov. Application of a continuous secondary electron multiplier for amplifying small currents. *Pribory.Tekh.Eksper.*, **4**, 89, 1960.

A. Owens, M. Bavdaz, M. Beijersbergen, A. Brunton, G. Fraser, P. Nieminen, A. Peacock, and M.G. Pia. A new planetary imaging fluoresecent spectrometer for the BeppiColombo Mercury mission. *Proc. SPIE.*, **4506**, TBA, 2001.

L.G. Parratt. Surface studies of solids by total reflection of X-rays. *Phys.Rev.*, **95**, 1593, 1954.

J.F. Pearson. *Advances in soft X-ray performance of microchannel plate detectors.* PhD thesis, University of Leicester, 1984.

J.F. Pearson, A.N. Brunton, A.P. Martin, G.W. Fraser, J.E. Lees, J.P. Boutout, R. Fairbend, and S.O. Flyckt. Characteristics of Photonis 6μm pore microchannel plates. *Proc. SPIE.*, **4140**, 217, 2000.

A. Peele, G.W. Fraser, A.N. Brunton, A.P. Martin, R.M. Rideout, W. Zhang, N. White, and R. Petre. Recent studies of lobster-eye optics. *Proc. SPIE.*, **3444**, 404, 1998.

A.G. Peele, K.A. Nugent, A.V. Rode, K. Gabel, M.C. Richardson, R. Strack, and W. Siegmund. Towards X-ray focusing using lobster-eye optics: A comparison of theory with experiment. *Appl.Opt.*, **35**, 4420, 1996.

P.A. Pella, L.Feng, and J.A. Small. An analytical algorithm for calculation of spectral distributions of X-ray tubes for quantitative X-ray fluorescence analysis. *X-Ray Spectrometry*, **14**, 125, 1985.

P.A. Pella, L.Feng, and J.A. Small. Addition of M and L series lines to NIST algorithm for calculation of X-ray tube output spectral distributions. *X-Ray Spectrometry*, **20**, 109, 1991.

R. Petre, P.J. Serlemitsos, F.E. Marshall, K. Jahoda, and H. Kunieda. In-filght performance of the Broad Band X-Ray Telescope. *Proc. SPIE.*, **1546**, 72, 1991.

I.R. Petrovna and Yu.A. Flegontov. Measurement of the characteristics of a channel multiplier for the amplification of an electron beam in the presence of a magnetic field. *Sov. J. Opt. Tech.*, **55**, 210, 1988.

B. Praček and M. Kern. AES studies of active intrachannel surface in microchannel plates. *Appl.Surf.Sci.*, **70/71**, 169, 1993.

W.C. Priedhorsky, J. Bloch, A.N. Brunton, S.A. Drake, D. Roussel-Dupre, R.I. Epstein, E.E. Fenimore, G.W. Fraser, J.T. McGraw, K. Mukai, K.A. Nugent, P.T.O'Brien,

A. Peele, R. Petre, W.T. Sanders, M. Ward, R.S. Warwick, R.L. Webster, N. White, and B. Wong-Swanson. The LOBSTER all-sky X-ray monitor. Technical report, Proposal to NASA SMEX opportunity, 1997.

W.C. Priedhorsky, A.G. Peele, and K.A. Nugent. X-ray all-sky monitor with extraordinary sensitivity. *Mon.Not.R.A.S.*, **279**, 733, 1996.

I. Renouf. (Astrium UK). Presentation at Lobster-ISS study progress meeting, 2001.

I. Renouf, S. Price, and I. Honstvet (Astrium UK). A study of the thermo-mechanical properties of the Lobster microchannel plates, 2001. Astrium report number LOB-AST-0001.

D.J Ruggieri. Microchannel plate imaging detectors. *IEEE Trans.Nucl.Sci.*, **NS-19**, 74, 1972.

W.K.H Schmidt. A proposed X-ray focussing device with a wide field of view for use in X-ray astronomy. *Nucl.Instr.Meth.A*, **127**, 285, 1975.

P.M. Shikhaliev. A novel gamma-ray imaging concept using "edge-on" microchannel plate detector. *Nucl.Instr.Meth.A*, **460**, 465, 2001.

S.H. Siddiqui. An investigation of active surfaces of microchannel plates using auger electron spectroscopic techniques. *J.Appl.Phys*, **48**, 3053, 1977.

S. Smith, R. Willis, G.W. Fraser, and N.P. Bannister. Lobster-ISS field obscuration study. Technical report, Leicester University, 2001.

S. Suzuki and T. Konno. A computer simulation on electron multiplication of parallel-plate electron multipliers. *Rev.Sci.Instrum.*, **64**, 436, 1993.

Y. Tanaka, I. Hojime, and S. Holt. The X-ray astronomy satellite ASCA. *Publ. Astron. Sco. Jap.*, **46**, 37, 1994.

M.J.L. Turner and A. Smith. The medium energy instrument on EXOSAT. *Space Sci.Rev.*, **30**, 513, 1981.

A.M. Tyutikov and L.B. Tsoi. The distribution, in energy and direction, of the electrons leaving microchannel plates. *Sov. J. Opt. Tech.*, **43**, 86, 1976.

J.H. Underwood. X-ray optics. *American Scientist*, **66**, 476, 1978.

L.P. VanSpeybroeck and R.C. Chase. Design parameters of parabaloid-hyperberloid telescopes for X-ray astronomy. *Appl.Opt.*, **11**, 440, 1972.

P. Verhoeve, A. Peacock, M. Bavdaz, Martin D, N. Rando, A. Poelaert, R. den Hartog, and L. Duband. The X-ray Evolving Universe Spectroscopy Mission (XEUS) : The narrow field imaging high resolution spectrometer. *Proc. SPIE.*, **3766**, 82, 1999.

U. Von Gemmingen. Ion induced secondary electron emission from single crystal surfaces. *Surf.Sci.*, **120**, 334, 1982.

A. Wells. The XUV Wide Field Camera on RoSAT. *Proc. SPIE.*, **597**, 146, 1985.

S.W. Wilkins, A.W. Stevenson, K.A. Nugent, H. Chapman, and S. Steenstrup. On the concentration, focussing and collimation of X-rays and neutrons using microchannel plates and configurations of holes. *Rev.Sci.Instrum.*, **60**, 1026, 1989.

R. Willingale. The grazing incidence telescope. *Nucl.Instr.Meth.A*, **221**, 1, 1984.

R. Willingale. The Q reference manual. Technical report, Leicester University, 1994.

R. Willingale, G.W. Fraser, A.N. Brunton, and A.P. Martin. Hard X-ray imaging with microchannel plate optics. *Experimental Astronomy*, **8**, 281, 1998.

C. E. Winkler, N. P. Cumings, J. L. Randolph, and D. H. Talley. Science instruments for the advanced X-ray astrophysics facility (AXAF). *Proc. SPIE.*, **1948**, 63, 1993.

J.L. Wiza. Microchannel plate detectors. *Nucl.Instr.Meth.A*, **162**, 587, 1979.

H. Wolter. Spiegelsysteme streifenden einfalls als abbildende optiken für Röntgenstrahlen. *Ann.Physik*, **10**, 94, 1952.

M.V. Zombeck, J.H. Chappell, A. Kenter, R.W. Moore, S.S. Murray, G.W. Fraser, and S. Serio. The High Resolution Camera (HRC) on the Advanced X-ray Astrophysics Facility (AXAF). *Proc. SPIE.*, **2518**, 96, 1995a.

M.V. Zombeck, L.P. David, F.R. Harnden Jr, and K. Kearns. Orbital performance of the High Resolution Imager (HRI) on RoSAT. *Proc. SPIE.*, **2518**, 304, 1995b.